UNIVERSITÉ CATHOLIQUE DE LOUVAIN
École polytechnique de Louvain
CERMIN

Advanced fabrication of nanowire arrays and three-dimensional nanostructures

Dissertation présentée en vue de l'obtention du grade de
Docteur en Sciences de l'Ingénieur
par

Alexandru Vlad

Promoteur:
Dr. Sorin Melinte

Septembre 2009

UNIVERSITÉ CATHOLIQUE DE LOUVAIN
École polytechnique de Louvain
CERMIN

Advanced fabrication of nanowire arrays and three-dimensional nanostructures

Dissertation présentée en vue de l'obtention du grade de
Docteur en Sciences de l'Ingénieur
par

Alexandru Vlad

Membres du jury:

Dr. Sorin Melinte, promoteur
Prof. Jean-François Gohy
Prof. Vincent Bayot
Dr. Stefan Mátéfi-Tempfli
Prof. Paul Heremans
Prof. Ulf Södervall
Prof. Pulickel M. Ajayan
Prof. Jean-Pierre Raskin, président

Septembre 2009

Abstract

Faster, smaller, cheaper are the three magic words that define the goal of modern semiconductor manufacturing industry. While speed and price behave satisfactorily, downscaling is the culprit. The "More than Moore" era pushes the scientist to dream about innovative devices, performing more operations at smaller and smaller scales and based on different physical principles. Molecular and organic electronics, spintronics and quantum computing as well as carbon nanotubes and "Graphenium Inside" exponentially emerging fields are only few to be cited. These concepts for sure will have their place in the tomorrow technologies. What we don't know is how they will perform.

One typically thinks that sizing down or changing the structural and operating philosophy of the electronic circuit elements will allow us to continue the progress. This is essentially true and remains the major tendency in advancing the information technology. Vertical stacking of multiple active components, providing identical functionality, can be regarded as a relatively long term option. Instead of shrinking, we can pile them up at their nominal size and fit the same number of active elements on a given surface area. Technologically, both approaches could require the same degree of processing complexity. Other option is to use photons instead of electrons to manipulate, store and transmit data. The electrons are operated at a few GHz for everyday computing and the increase of the operation frequency can seriously complicate the fabrication tasks; the visible and infrared spectrum range photons are already "operating" at hundreds of terahertz. In this thesis, we bring together these two fields, which are closely related in their fabrication methodology. Nanoporous templates have been found to be excellent candidates for this study since their peculiar morphology is well suited for both purposes. Ordered, modulated dielectric media could be directly employed to mold the flow of light. Indirectly, they can be used to confine and stack various electronic components in the nanoscale channels. By combining them novel optoelectronic devices could be advanced.

Two types of porous materials have been extensively exploited. First,

we consider the nano- to macro-scale manipulation of self-organized, anodic aluminum oxide templates. Parallel integration of single nanowires is highlighted. We provide a full processing technology, starting from a bulk silicon substrate and finishing with a cross-bar latch having at its heart single, template-embedded nanowires. A novel statistical protocol for template processing is put forward. The comprehensive explanation of the experimental and simulated stochastic behavior relies on a straightforward analytical formalism and the technology is interpreted in terms of surface and packing optimization. The method is scalable and can be generalized to virtually any type of templates.

Simultaneously, high resolution electron beam lithography was used to generate highly ordered 2D and 3D templates. A novel type of resist- and dose-modulated electron beam lithography (RDM-3D-EBL), extensively exploiting the intrinsic properties of resist-electron beam interaction was developed. Surface initiated and template confined aniline polymerization was then used to provide a genuine method for controlled nanoscale processing of polyaniline, a prototypical conjugated polymer that definitively settled the concept of synthetic metals. Using nanoscale polymerization reactors, ultimate resolution patterning and processing control of single polyaniline nanostructures was feasible. Near teradot/inch^2 pattern transfer technology, complex 3D structuring and physico-chemical functionalization of polyaniline have been subsequently harnessed to build a large variety of architectures with potential for emerging optoelectronic technologies. This allowed the implementation of a simple scheme for single polyaniline nanowire fabrication, processing and device integration.

Contents

Abstract i

Symbols and abbreviations vii

List of Figures ix

List of Tables xiii

Preface 1

1 Nanoporous Materials 7
- 1.1 Introduction . . . 7
- 1.2 Classification . . . 9
  - 1.2.1 Zeolites and mesoporous materials . . . 10
  - 1.2.2 Nanoporous templates . . . 11
  - 1.2.3 Macroporous membranes . . . 14
- 1.3 General applications . . . 15

2 Porous materials for nanotechnology 19
- 2.1 General overview . . . 19
- 2.2 Photonics . . . 20
  - 2.2.1 Photonic crystals . . . 20
    - 2.2.1.1 Theoretical consideration . . . 21
    - 2.2.1.2 2D and 3D systems . . . 27
  - 2.2.2 Plasmonics . . . 39
- 2.3 Nanowire electronics . . . 42
  - 2.3.1 Template confined fabrication . . . 42
  - 2.3.2 Characterization techniques . . . 44
    - 2.3.2.1 Template-embedded methods . . . 44
    - 2.3.2.2 Template-free approaches . . . 47
- 2.4 Nanowire-based photonics . . . 48

3 AAO templates **49**
3.1 Overview . . . 49
3.2 Anodic oxidation of aluminum . . . 50
3.2.1 Nonporous anodization . . . 51
3.2.2 Porous anodization . . . 51
3.3 AAO microstructuring . . . 54
3.3.1 Supported AAO fabrication . . . 56
3.3.2 Nanowire decorated microelectrodes . . . 57
3.3.3 AAO patterning . . . 64
3.4 AAO nanostructuring . . . 67
3.4.1 Silicon nitride deposition and etching . . . 68
3.4.2 Selective electroplating . . . 74
3.4.3 Statistical interpretation . . . 76
3.4.4 Analytical modeling . . . 85
3.4.5 Counting threshold and process reliability . . . 89
3.4.6 Statistical processing . . . 94
3.5 Single nanowire crossbar devices . . . 97
3.5.1 Self-contacting layer definition . . . 98
3.5.2 Top contact definition and SCL statistics . . . 100
3.6 Conclusion . . . 102

4 Polymer templates **103**
4.1 Why EBL templates? . . . 103
4.2 Electron beam lithography . . . 105
4.2.1 General considerations . . . 107
4.2.1.1 High vs. low electron energy . . . 108
4.2.1.2 Resist types . . . 112
4.2.1.3 Substrate influence . . . 116
4.2.2 High-resolution lithography . . . 116
4.2.3 Resist and dose modulated 3D EBL . . . 118
4.2.3.1 Resist composition modulation . . . 120
4.2.3.2 Dose modulation . . . 124
4.2.3.3 When 1+2=3 . . . 126
4.3 Polyaniline . . . 128
4.3.1 Historical background . . . 128
4.3.2 Redox states and associated applications . . . 130
4.3.3 Synthesis and nanoscale structuring . . . 132
4.3.4 Aniline electroless polymerization . . . 136
4.3.4.1 Intrinsic advantages . . . 137
4.3.4.2 Growth mechanism . . . 138
4.3.4.3 Optoelectronic properties . . . 144
4.3.5 Nanoscale chemistry . . . 148

4.4 Template confined polymerization 155
4.4.1 2D structuring 156
4.4.2 3D structuring 167
4.4.3 Nanocomposites and macroassemblies 171
4.5 Single PANI nanowire electronics 176
4.5.1 Fabrication approach in 4-steps 180
4.5.2 Polyaniline nanowire crossbar devices 183
4.6 Conclusion 192

5 Porous silicon and colloidal mask lithography 193
5.1 Metal assisted chemical etching of silicon 193
5.2 Colloidal mask lithography 199

Conclusions and perspectives 205

A Process sheet 209

B Statistical patterning simulation protocol 215

Bibliographie 219

Symbols and abbreviations

μCP	Micro-Contact Printing
2D	Two Dimensional
3D	Three Dimensional
AAO	Anodic Aluminum Oxide
AC	Alternative Current
AFM	Atomic Force Microscopy
ALD	Atomic Layer Deposition
BE/TE	Bottom/Top Electrode
BSE	BackScattered Electrons
CPD	Critical Point Dryer
CVD	Chemical Vapor Deposition
DC	Direct Current
DI	DeIonized Water
EBL	Electron Beam Lithography
EUVL	Extreme Ultra-Violet Lithography
FWHM	Full Width at Half Maximum
IPA	IsoPropyl Alcohol
LOL	LiftOff Layer
LOR	LiftOff Resist
MEMS	Micro Electro Mechanical Systems
MIBK	Methyl Isobutyl Ketone
MIMIC	MIcroMolding In Capilaries
MSE	Mean Squared Error
NEMS	Nano Electro Mechanical Systems
NIL	NanoImprint Lithography
PANI	PolyANIline
PBG	Photonic Band Gap
PBS	Poly(Butene-1-Sulfone)
PECVD	Plasma Enhanced Chemical Vapor Deposition
PMGI	PolydiMethyl GlutarImide
PMMA	PolyMethyl MethAcrylate

PMMA(8.5)MAA	PolyMethyl MethAcrylate MethAcrylic Acid
RF	Radio Frequency
RIE	Reactive Ion Etching
ROI	Region Of Interest
RT	Room Temperature
SCALPEL	SCattering with Angular Limitation in Projection Electron-beam Lithography
SCL	Self-Contacting Layer
SE	Secondary Electrons
SEM	Scanning Electron Microscope
SPM	Scanning Probe Microscope
SPP	Surface Plasmon Polaritons
SRR	Split-Ring Resonator
STM	Scanning Tunneling Microscopy
TE	Transverse Electric
TEM	Transmission Electron Microscope
TM	Transverse Magnetic
XRL	X-Ray Lithography

List of Figures

1.1 Convergence of traditional sciences. 8
1.2 M41S group classification. 11
1.3 Block copolymer self-organized superlattices. 13
1.4 Track etched membranes. 14

2.1 Photonic band structure for a square lattice of silicon pillars. 29
2.2 Photonic band structure for a triangular lattice of silicon pillars. 30
2.3 Photonic band gap of a triangular lattice of polyaniline pillars. 32
2.4 Photonic band structure for a triangular lattice of air holes in silicon. 33
2.5 Photonic band structure of AAO and waveguiding in photonic crystals. 34
2.6 Photonic band structure for cubic symmetry lattices. . . . 38
2.7 State of the art for single nanowire electronics. 45

3.1 Idealized structure of anodic porous alumina. 53
3.2 Surface morphology of Al deposited in different conditions. 56
3.3 Substrate pre-fabrication for AAO. 59
3.4 Circuit integrated AAO fabrication. 60
3.5 Defectuous anodization and electroplating. 61
3.6 Nanowire decorated microscale metallic electrodes. 63
3.7 AAO patterning. 66
3.8 Alumina and silicon nitrides surface morphologies. 70
3.9 SiN_x and PMMA etch rate and selectivity. 73
3.10 Nanoscale confined electroplating. 75
3.11 SEM views of patterned masks and obtained resolution. . 77
3.12 Experimental and simulated probability dispersion for the statistical patterning. 79
3.13 Simulated probability distribution for different morphology of AAO. 81

3.14 Simulated probability distribution using a square mask. . 83
3.15 Analytical representation of the statistical structuring methodology. 86
3.16 Self-repaired masks. 90
3.17 Counting threshold *vs* process reliability. 93
3.18 SPM interrogation techniques. 95
3.19 SCL definition. 99
3.20 Single-nanowire crossbar devices. 101

4.1 Schematic view of a typical EBL system. 106
4.2 High energy *vs*. low-energy EBL. 109
4.3 Interactions of the electron beam with the resist and the substrate. 110
4.4 Characteristic gradation curves for positive and negative resists. 114
4.5 Substrate influence on the EBL parameters. 117
4.6 Examples of multilayered resist templates. 121
4.7 Stress-induced cracking in the resist film. 123
4.8 PMMA and PMMA(8.5)MAA contrast curves. 125
4.9 Substrate-induced resist structuring. 126
4.10 RDM-3D-EBL: how it works. 127
4.11 Redox states of polyaniline. 131
4.12 State of the art in the polyaniline nanostructuring. 133
4.13 Mechanism of the aniline polymerization reaction. 140
4.14 Polyaniline growth kinetics. 142
4.15 Modulating the opto-electronic properties of PANI. 147
4.16 Micro- and nano-scale PANI chemistry using miniaturized reactors. 149
4.17 Micro- and nano-scale PANI chemistry using dual-metal miniaturized reactors. 150
4.18 Polyaniline induced growth on silicon and porous silicon. . 153
4.19 Hierarchical approach for polyaniline patterning. 156
4.20 High-areal density polyaniline patterning. 159
4.21 Aspect ratio *vs*. patterning density. 160
4.22 High-resolution, high-aspect ratio polyaniline patterning. . 162
4.23 Ultra high-resolution polyaniline patterning. 164
4.24 Flooded polyaniline structures. 165
4.25 *Ultimate* resolution patterning and growth of PANI nanostructures. 167
4.26 Axially modulated polyaniline nanopillars. 168
4.27 Polyaniline 3D lattices. 169
4.28 Gold - polyaniline nanocomposites. 173

4.29 Guided 2D assembly of PANI nanowires. 174
4.30 Geometry locked assembly of PANI nanoarchitectures. . . 175
4.31 Polyaniline circuits fabrication pathways. 177
4.32 Thin film electrical properties. 178
4.33 Nanowire decorated microelectrodes. 182
4.34 Polyaniline nanowire crossbar devices I. 185
4.35 Polyaniline nanowire crossbar devices II. 186
4.36 Single polyaniline nanowire devices. 189

5.1 Silicon etching with gold nanoparticles. 195
5.2 "Metal-free" silicon etching. 197
5.3 $AgNO_3$ assisted formation of silicon nanowires. 197
5.4 2D colloidal monocrystal. 200
5.5 Colloidal mask lithography. 201
5.6 3D colloidal assembly. 203

B.1 Gray-scale and corresponding binarized SEM image. . . . 216

List of Tables

3.1 Silicon nitride properties as a function of deposition temperature. 69
3.2 Gaussian fit coefficients for the simulated probability plots function of ζ. 92

4.1 Overview of modern lithographic techniques. 105
4.2 Influence of electron energy on porous templates manufacturing. 112

A.1 Process sheet for the micro- and nano-fabrication of AAO embedded single nanowire devices. 214

Preface

Les enfants seuls savent ce qu'ils cherchent.

Antoine de Saint-Exupéry

Nanoporous materials and templates have definitively settled the concept of mass production of low dimensional structures in the nanotechnology field. While the process simplicity, the variety of synthesized systems, and the order control over large areas have boosted them to the top of nanopatterning techniques, the major drawback that restricts their pervasive integration into real working devices is the mismatch between their dimensionality and today's technological ability. A careful review of the literature reveals that the porous templates have led to amazing discoveries in the field of nanotechnology. However, it also discloses that mainly their specific dimensionality was extensively exploited, in occurrence, the nanoscale dimensions of the open channels. Large area ordered structuring, high-density parallel patterning, vertical manufacturing as well as their intrinsic properties such as periodic modulation of dielectric properties and high surface-to-volume ratio with very versatile composition and chemistry are only modestly considered. Pervasive integration into modern semiconductor manufacturing and device fabrication is conspicuously missing. Hence, nanoporous template processing technologies are continuously developed and tested.

Two concepts, closely related in their design and fabrication methodology, were tested throughout this work. The first one is directly related to the intrinsic structure and properties of porous materials. In analogy to the electron flow in a conducting crystal where the periodic potential of the lattice dictates the conduction properties, the propagation of light in a periodically modulated dielectric lattice (or equivalently, a periodic index of refraction) could be also allowed or prohibited. If the dielectric contrast of the crystal constituents is sufficiently high and the absorption of waves is minimal, then the reflection/refraction of light from all of the interface configurations can produce many of the same phenomena for

photons. Thus, photonic crystals represent one of the most advanced solutions for optical control and light manipulation. The operating scales of electronic and photonic crystals are different. The first one occurs at atomic level (Å scale) while the latter depends on the used wavelength. For the visible and infrared parts of the electromagnetic spectrum this corresponds to few hundreds of nanometers[1] and matches the characteristic length scale of nanoporous materials. Hence, taking into account their vast composition and easy structural control, they seem to be the perfect candidates for such applications. Though we know to manufacture them at ultra large scales, technological requirements are striking again. In the same way as blocks of metallic aluminum and semiconducting silicon are to be fashioned in order to compute your everyday tasks, a periodic photonic lattice needs as well to be reworked to be able to bend the light at straight corners, control and switch its intensity. This is where the use of porous materials starts to be discouraging. Solutions exist and can be categorized either as pre-synthesis (one induces the pattern during the template fabrication) or post-synthesis (one processes a uniform template in order to obtain the desired pattern) structuring.

The second concept uses indirectly the porous templates. Air channels were found to be excellent hosts for different types of confined growth and deposition techniques. Various multidimensional metallic, semiconducting and organic as well as heterogeneous systems have been fabricated and studied using template confined methods. To this miscellaneous compositional and size diversity we can add the ability of vertical multifunctionality (for example, building a bistable electrical element and a rectifying structure along a nanowire will eliminate cross-talking in cross-bar latch devices). General approaches to date consisted in studying large assemblies of nanostructures fabricated inside templates or employing allied techniques to localize and analyze single nano-objects. We stress out that these procedures exploit only the reduced dimensionality and not the high-density imposed by the nanoporous templates: parallel integration of template embedded nanostructured devices is prominently missing. By integrating both concepts, one can imagine visionary devices where light-emitting nanowires are build inside a porous materials photonic slab to guide the emitted light and perform as hybrid optoelectronic devices. This work tried to advance both fields.

[1] The Yablonovite structure was the first experimental photonic crystal demonstrating the existence of a complete photonic band gap. It consisted of a dielectric medium, mechanically drilled along the three lattice vectors of the fcc lattice on the centimeter scale for measurements of microwave propagation. With the subsequent development of micromachining and nanoscale processing it was possible to build smaller and smaller photonic crystals and to probe other wavelength scales.

In the first Chapter, we offer a simple description of nanoporous templates. A classification by composition, fabrication methods and characteristic sizes is given. As the field is very broad, the discussion is mainly centered on potentially useful materials. A brief overview of general applications is also provided.

Chapter 2 details their specific applications for nanotechnology. Emphasis is put on their use in photonics and in nanowire electronics. General concepts of photonic crystals and plasmonic structures are given in order to facilitate further comprehension. Though, due to limited experimental capabilities, optical characterization of fabricated architectures remained qualitative, the expected behavior was theoretically predicted. Instead of presenting general cases, we have chosen to work by the way of examples. For the fabricated 2D and 3D photonic crystal like structures, we have calculated and optimized the structural parameters in order to maximize the band gap and minimize the looses. An overview of plasmonic structures obtained using template methods is presented. A brief description including theory and applications of surface plasmons in several rapidly developing areas of nanotechnology (biophotonics, biosensing, biochemistry and medicine) is also given. Recent trends in the field of nanowire electronics (especially those fabricated in nanoporous templates) will try to convince the reader that further optimization methods are indeed required. The reader will be indeed persuaded that the present work fits well to the latest advances in this field.

Porous anodic aluminum oxide is the main concern of Chapter 3. We shall not insist on the fabrication methods and applications of AAO templates. The topic is well studied and an exhaustive description in literature exists. The focus is put on the newly developed micro- and nanostructured techniques. A full processing technology, starting from a bulk silicon substrate and finishing with a cross-bar latch having at its heart single, template-embedded nanowires is provided. First, AAO microstructuring techniques are presented, detailing supported membrane fabrication, nanowire decoration of microelectrodes and alumina patterning. Nanostructuring is used to further confine the growth with ultimate single-nanowire resolution. At the same time, a statistical interpretation is given. We present a systematic study on the number of accessed nanopores using selective mask processing of anodic aluminum oxide [1, 2]. Modulating the size and geometry of the mask enables statistical, yet accurate control over the achieved resolution. A well-defined probability dispersion, with distinct maxima at integer number resolution it is found to exists for a given circular mask diameter range. We propose a simple image analysis procedure to simulate the experimental data, enabling fast screening of the processing reliability. The method

generalizes to virtually any type of templates. While the comprehensive explanation of the experimental and simulated stochastic behavior relies on a straightforward analytical formalism, the technology is interpreted in terms of surface and packing optimization.

Organic materials are at the heart of Chapter 4. Essentially, polymethylmethacrylate templates are used to confine polymer nanowires. In contrast with the previous Chapter, where the nanoporous structures are mass-generated and then processing techniques are used to isolate single features, here this is done solely by using electron beam lithography. Though it is generally considered as a slow and costly technique, EBL still remains the foundation for high-resolution, high overlay accuracy, relatively large area nanoscale patterning and next generation device process development, at least at research and development level and for small batch production. Using EBL defined templates, a novel protocol for patterning the semiconducting polyaniline with an unprecedented areal patterning order and density exceeding 0.25 teradot/inch^2 is presented [3]. A simple two-step process is put forward to hierarchically build a large variety of functional PANI nanostructures on virtually any type of flexible or rigid substrates. Using template confinement, through platinum catalyzed electroless growth, highly-ordered arrays of distinct PANI nanowires are produced with a typical diameter of $\sim$ 15 nm and aspect ratio higher than 20. Complex three-dimensional structural control is achieved through a direct pattern transfer using a novel type of resist- and dose-modulated electron beam lithography. The method is scalable and provides a generic approach for nanopatterning surfaces with functional polymers. Aspects of the PANI growth mechanism at nanoscale are discussed and sub-picogram scale fabrication is emphasized. The tunable optoelectronic properties achieved through a simple doping/dedoping scheme are considered. A simple scheme for the single PANI nanowire fabrication, processing and device integration is presented.

Alternative methods for the template fabrication were also studied and are presented in Chapter 5. They mainly concern the porous structuring of silicon. Due to its excellent properties and very well established nano- and micro-structuring techniques, silicon represents the main component for various optoelectronic applications. Metal assisted chemical etching is a simple way to fabricate silicon nanowires or nanoporous silicon. Colloidal lithography was the second studied alternative method. Here 3D assembly provides direct template structuring, while 2D assembly is used for masking purposes: via shadow physical vapor deposition or reactive ion etching arrays of nanoscale elements are produced. Nanostructuring at centimeter scale highlights the enormous potential provided

by this method.

The exhaustive description of the operating principle for used experimental equipments was left aside. Instead, when appropriate, short descriptions of the unusual experimental approaches and findings were presented. Only the electron beam lithography, as being an important tool for this work, and the associated processes and developments have been extensively described.

Finally, even if some parts of this work still need a more profound experimental characterization to fully approve their intended utility, they may provide "débouchées" for further research in the field. Proposed protocols for alumina patterning could be used for purposes other than single nanowire electronics: surface functionalization, single channel filters, statistical "gambling" with other types of templates and so on. Polymethylmethacrylate templates could be used to structure other materials than polyaniline. Reversely, polyaniline electroless growth could be confined using other, more "innovative" templates and on more sophisticated "substrates". So, even if skeptics will consider this work as never being able to reach an industrial production level, we shall not forget the philosophy behind "curiosity driven" research. A large part of the modern scientific research is very often justified by its potential use in everyday applications, though, it will remain at the stage of published papers and laborious reports for funding agencies. Moving researchers from "curiosity-driven" science, for example space exploration and particle physics, into "driven" science does not make sense and it is certainly not how scientists are motivated. The history of science has shown that many hot topics (that were considered perfectly suited for high social and technological impact) were eventually left aside while others, after being long time considered as fundamental, have emerged as valuable technological solutions. Hence, studying and understanding the mater behavior at the nanoscale in the adventurous beginning century of "all-nano" should remain the key motivation, especially for young researchers, who seek the fascination of Nature.

Chapter 1

Nanoporous materials

> Le trop de quelque chose est un manque de quelque chose.
>
> *Proverbe arabe*

1.1 Introduction

The concept that matter is composed of discrete units and cannot be divided into arbitrarily tiny quantities has been around for millennia, but these ideas were founded in abstract, philosophical reasoning rather than on experimentation and empirical observation. The nature of atoms in philosophy and physical sciences varied considerably over time and between cultures and schools. A lot of work has been done to study and to understand the properties of these tiny objects constituting the matter. The past two centuries abounded in various experimental confirmations and theoretical models correlating the bulk properties with the atomistic behavior of materials. Nevertheless, only in the past 3 decades, with the advent of technology at small scales, it was possible to truly visualize and manipulate atoms [4, 5]. This fruitful period in science has been marked by the onset of nanotechnology dealing with the study and control of matter at atomic and molecular scale. In principle, nanotechnology refers to structures with a typical size smaller than 100 nm and involves developing materials or devices within that size (Fig. 1.1).

Nanoporous materials possess unique surface, structural, and bulk properties that underline their important uses in various fields such as ion exchange, separation, catalysis, sensor, biological molecular isolation. Nanoporous materials abound in nature, both in biological systems and

natural minerals. Some nanoporous materials have been used industrially for a long time. Recent improvements in our ability to see and manipulate on the nanoscale are transforming our use of these materials from merely opportunistic to directed design. This is most strikingly true for the creation of a wide variety of membranes, where control over the pore size is increasing dramatically, often to atomic levels of perfection.The theoretical space of possible engineering permutations for such materials is vast and will present many opportunities for the control of substances at the molecular and atomic levels for years to come.

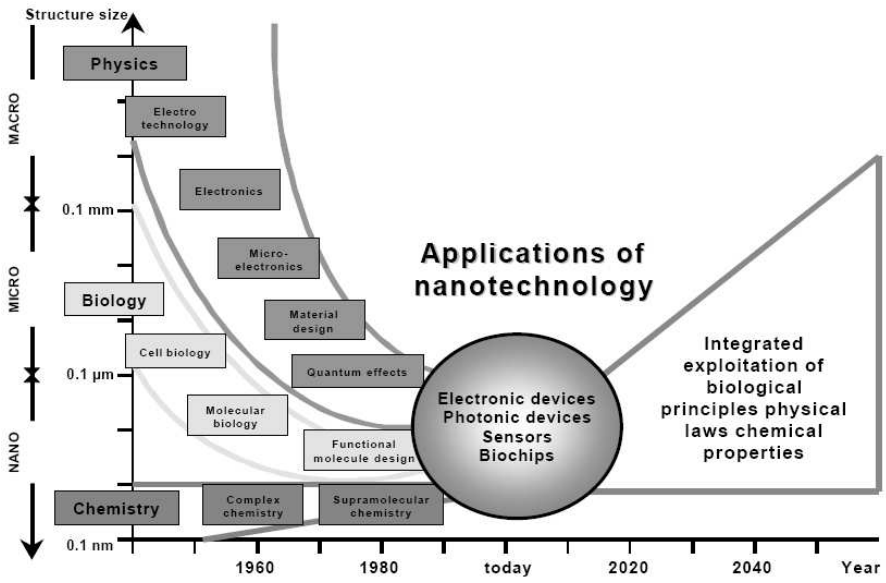

Figure 1.1: Threshold of nanotechnology as basic sciences converge at nanoscale [6].

Much effort has been undertaken to develop methods for the synthesis of nanostructures over macroscopic surface areas. Template synthesis has proved to be an elegant, inexpensive and technologically simple approach for the fabrication of various nanoscale sophisticated materials. It consist in confined structuring of the desired material inside the void channels of a porous matrix. This alternative method overcomes many of the drawbacks of lithographic techniques, and exploit templates which differ in material, pattern, range of order and periodicity, feature size and overall dimensions. Templating methods employing a variety of porous membranes are commonly used for the synthesis of high-density, ordered arrays of nanodots, nanotubes and nanowires. The origin of the tem-

plate used for nanofabrication may also be lithographic; the relatively high cost of its preparation may limit the application. Although the aspect ratio achievable is not high, lithographically prepared templates have the undeniable advantage of exploiting a much wider spectrum of substrate choices than do porous membranes. The most significant drawback of membrane-templating methods is the poor long-range order in the formed nanostructures, even though a short-range order is maintained satisfactorily. An important discriminating factor comes from the intended application. If one desires to fabricate, analyze and characterize bulk quantities of nanostructures then a self-organized (or self-arranged) template is more suitable. Working on distinct single nanostructures may be troublesome doing so and may require additional processing complexity. Lithography approaches directly solve this issue as the number and position of nano-objects can be easily controlled. Basically, the choice for using a given porous material or template will be given by the intended application, available technology and process simplicity.

1.2 Classification

Nanoporous materials are all about holes and channels that are less than 100 nm, although there are some interesting porous materials with voids above this size; this work will not be too strict about the "arbitrary" 100 nm limit [7]. Like many nanostructured materials, nanoporous materials abound in the natural world. The walls of our cells are nanoporous membranes, although with a lot of added complexity. The same way as biological membranes are designed to perform and act in a specific way, the scientists are looking for synthetic "intelligent" membranes engineered to accomplish dedicated tasks.

In principle, any solid material which contains cavities, channels or interstices may be regarded as porous, though in a particular context a more restrictive definition may be appropriate. Thus, in describing a porous solid, care must be exercised in the choice of terminology in order to avoid ambiguity. A strict classification of porous materials based on their specific size, morphology, chemical composition and fabrication method is difficult to draw. Sizes can span form few nanometers up to micrometers with 1D to 3D morphology. Sorting by application is also difficult as the same material can behave differently upon specific requirements. For example, the same porous matrix can be used as catalyst (due to its increased specific area), filtering media or confining environment for nanomaterial structuring. As the primary intent in this work was the use of porous materials for nanostructuring, in the following, a coarse

classification based primarily on the characteristic dimensions is given. Worth mentioning is the fact that the 2D porous materials are also called channeled (or nanochanneled if the size goes below 100 nm) materials as they can be regarded as a network of parallel channels "drilled" in a solid matrix. Both definitions are correct to some extent and which of them is to be used is mainly a subjective question. This kind of materials are at the heart of this work. Namely, nanoporous alumina and nano- to macro-porous PMMA systems have been studied and detailed in following chapters. It may be also convenient to divide nanoporous materials into bulk materials and membranes (or films). While bulk materials are predominantly used for storage, filtering and catalysis applications the porous membranes have found utility in nanofabrication due to the flexibility to integrate them on a substrate and our actual possibility to process 2D rather than 3D geometries.

1.2.1 Zeolites and mesoporous materials

Zeolites (also known as molecular sieves) are a class of aluminosilicate minerals with pore size of ~ 15 Å. In zeolites the template refers to a single molecule or ion. They have a porous structure that can accommodate a wide variety of cations such as Na^+, K^+, Ca^{2+}, Mg^{2+}. These positive ions are rather loosely held and can readily be exchanged for others in a contact solution. Some of the more common mineral zeolites are analcime, chabazite, clinoptilolite, heulandite, natrolite, phillipsite, and stilbite. Other types of materials that can be included in this class are the metal-organic frameworks and aggregated surfactant structures.

Porous materials having pores with diameters between 2 and 50 nm are usually classified as mesoporous materials[1]. They have huge surface areas, providing a vast number of sites where sorption processes can occur. The synthesis of these materials is of considerable interest and is constantly being developed to introduce different properties. A typical example is MCM-41, composed of rod like surfactant aggregates (Fig. 1.2 (**a**)) [8–13]. The pore size distribution in MCM-41 is usually quite narrow (~ 40 Å) but it is not as tightly defined as that for a zeolite. 3D porous networks can also be prepared (MCM-48) (Fig. 1.2 (**b**)) [8, 14, 15]. A variety of different layered structures can be formed. These data apply to MCM-50, a stabilized layered structure (Fig. 1.2 (**c**)). Stabilized structures contain surfactant bilayers and collapse when the surfactant is removed. Typical synthesis consists in the self-assembly of surfactant

[1] According to IUPAC notation, microporous materials have pore diameters of less than 2 nm and macroporous materials have pore diameters of greater than 50 nm and the mesoporous category lies in the middle.

micelles modified with silicate species and then calcinated to obtain the porous silica matrix [16].

Figure 1.2: M41S group phases. (**a**) MCM-41 with the unidirectionally non-interconnected hexagonally arranged pores. (**b**) 3D cubic structure of MCM-48. (**c**) Lamella structures of MCM-50.

Though they display extremely reduced channels dimensions, the high specific area rather than the confinement properties are mainly exploited in these materials. Even when the confinement of active materials was possible the characterization was performed on bulk architectures and not on single nanoobjects. For example, Wu and Bein have synthesized the smallest ever made (3 nm in diameter) conducting polyaniline filaments using the channel system of the aluminosilicate MCM-41 [17, 18]. Authors noted that about 20 aligned polyaniline chains could fit in the respective volume. It would be extremely interesting to perform electrical transport measurements on this type of systems, where the intra- or inter- molecular charge transfer may have the same contribution to the electrical performance. Yet, even nowadays it would be difficult to realize an adequate experimental set-up for this kind of measurements [2]. The main constraint is that the characteristic sizes, morphology and properties of this class of porous materials are well above our modern processing capabilities.

1.2.2 Nanoporous templates

A special class of porous materials are the so called nanoporous templates. The main specificity of this category is that they can be processed in the form of films with 1D, 2D and 3D morphology. The class is very broad and some representative groups are described in the following.

[2]The authors used contact less microwave absorption technique to probe the charge transport on bulk quantities of polyaniline nanofilaments, obviously, averaging the data.

Block copolymers are made up of blocks of different polymerized monomers [19–23]. Due to the inherent immiscibility of the majority of polymer blocks, phase separation is usually observed in block copolymers. Because the polymer blocks are strongly linked to each other, macroscopic phase separation cannot occur and a structural organization appears with domain periodicities in the range of tens of nanometers, either in the melt, bulk state or in solution. As prepared, these materials present no porosity. Only after a selective removal of one of the components, void spaces (or the porous structure) can be obtained. Selective removal methods (inherent to the chemical properties of the constituents or of the linker groups) are as vast as the chemical nature of the constituents making this class of materials almost limitless in their design and applications. Moreover, the morphology of the accessed hierarchical architectures extends (or can be virtually extended) to any desired superlattice with characteristic dimensions in the range of a few nanometers up to several micrometers (Fig. 1.3). The main microstructures observed in solid state are lamellar (LAM), hexagonally packed cylinders (HEX), a body centered cubic array of spheres (BCC) and a gyroid structure (GYR).

Amongst these structures the HEX is the most interesting for use as template for high density nanowire arrays growth [25, 26]. Applying an electric field during segregation of the A block in hexagonally ordered cylinders from the B block (in which they are embedded) their axes could be aligned parallel to the applied field and perpendicular to a conducting substrate. By selective removal of the constituent A, a hexagonally ordered nanoporous template of B constituent could be obtained. The main advantages of this template are the mild preparation conditions and the ordered arrangement of nanopores in a high density structure of typically 10^{11} - 10^{12} pores/cm^2.

Nanochanneled inorganic oxides. Porous materials obtained mainly from electrochemical anodic etching of various metals. Characteristic sizes are typically higher than for the block copolymers. Densities as high as 10^{11} pores/cm^2 can be achieved. A brief description of nanochanneled anodic aluminum oxides is given in Chapter 3.

Track etched membranes. When an energetic particle crosses a certain material it leaves a trail of radiation damage which shows up as a track. Such tracks were first observed in the 50's in mica exposed to fission fragments from uranium [27]. Upon etching in a suitable reagent it has been found that the tracks are very selectively attacked and hollow channels are formed along the particle paths, while the remaining material is mainly unaffected (Fig. 1.4 (**a**)). Various inorganic and organic materials were tested and studied [28]. In fact, it has been found that

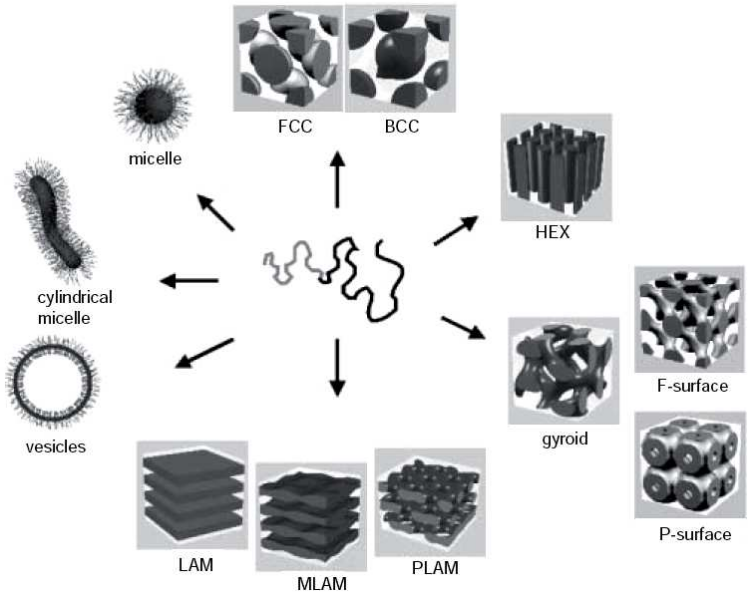

Figure 1.3: Spherical micelles, cylindrical micelles, vesicles, fcc- and bcc-packed spheres (FCC, BCC), hexagonally packed cylinders (HEX), various minimal surfaces (gyroid, F surface, P surface), simple lamellae (LAM), as well as modulated and perforated lamellae (MLAM, PLAM) morphologies can be designed and produced. From [24].

this effect could be efficiently used for charged particles detection. Only much later, in the mid 90's, it was recognized that track etched polymers could be used also as templates for nanowires fabrication [29–31]. Such track etched templates are fabricated by irradiating polymer membranes such as bisphenol-A polycarbonate (PC) with heavy ions [32] produced by a particle accelerator in the MeV - GeV range. The ion irradiated PC film is then UV irradiated to increase the selectivity of the subsequent chemical etching. Etching is performed with a NaOH aqueous solution to form nanopores (nanochannels) with a desired diameter. A typical PC nanoporous membrane could be seen in Figure 1.4 (**b**). The main characteristics of this kind of templates are: random pore distribution; pore diameters from 10 nm to a few μm tunable by the etching time; and densities ranging from 10^5 to 10^{10} pores/cm^2 controlled by the irradiation flux and time.

Porous silicon. Porous material made out of silicon by electrochemical or metal assisted chemical etching. A recent metal assisted method has gained much interest due to its specificity and selectivity during the

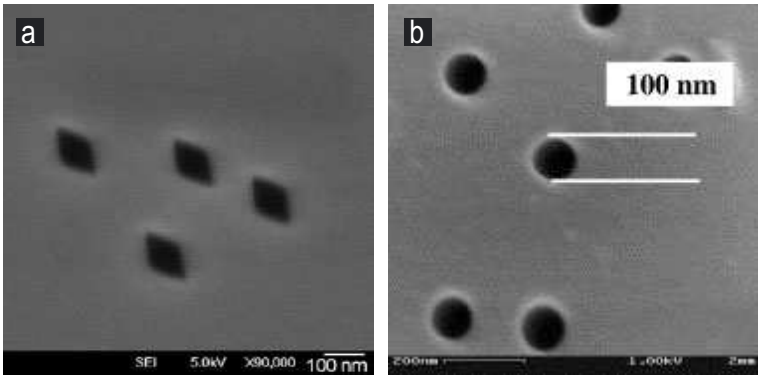

Figure 1.4: SEM images of the surfaces of track-etched membranes. (**a**) Muscovite mica exposed to U^{+25} ions. The crystalline structure of mica imposes different etch rates for different directions relative to the crystal axes. The slowest etching planes are those terminated by oxygen. As a result of this etch-rate anisotropy, pores etched in mica have a diamond-shaped cross section. From [33]. (**b**) Circular pores are obtained using an amorphous ion bombarded material, in occurrence, a polycarbonate membrane.

etching of silicon. Details on this approaches will be given in Chapter 5. The porosity can range from 4% to 95% depending on the fabrication conditions. The pore size can be tunned as well: from less than 2 nm to few micrometers (going actually into the macroporous range) upon appropriate etching conditions and surface treatments.

1.2.3 Macroporous membranes

This class is characterized by materials having pores larger than 100 nm. In principle it can be divided into 2 subclasses: self-assembled and lithographically defined porous structures. Self-assembled macroporous materials are mainly composed of crystallized colloidal structures (silica, PMMA or polystyrene spheres). The 2D or 3D porous structure originates from the spherical shape of constituents and hence, formation of void spaces between the packed structure. The second subclass materials are actually the patterned resist films using various lithographic exposure techniques. It is one of the most simple and flexible methods, in terms of characteristic sizes and lattice geometry, for the fabrication of 2D and 3D templates. The lower pore size limit is around 5 nm while the higher limit is virtually infinite. Thus, lithographically defined templates can cover all of the classes upon considering the pore size as the main classification criterion. Pattern shape and positioning can be controlled with

single-feature resolution. The main drawbacks that are usually evoked are the low aspect ratio and fabrication throughput combined with the high processing costs. More details on these types of templates will be given in Chapters 4 and 5.

These type of templates can be used as fabricated or post-processed to yield new types of macroporous materials. 2D structures, or channeled templates, are either inverted to obtain post type structures or used at etch masks to transfer the porous matrix to the substrate. The later approach is intensely used in silicon technology for the fabrication of photonic devices (waveguides, photonic crystals and wires). For 3D structures it is difficult to transfer the pattern to the substrate due to the internal shadowing elements. Typically, conformal coating techniques (chemical and electrochemical as well as various physical deposition methods) are used. If the original material is removed, then a new macroporous material is obtained which is an inverted replica of the initial one.

1.3 General applications

Porous materials are expected to play an increasingly important role in our daily life. There are plenty of advantages offered by these materials. Without being redundant, some of them are listed below. As there is always pay off for the benefit, the disadvantages are also mentioned. Applications regarding their use as light modulating materials (or photonic crystals) and their use as growth templates are skipped here. The respective methodologies are detailed in the next Chapter.

- Filtering medias. As the regulatory limits on environmental emissions become more and more stringent, industries have become more active in developing separation technologies that could remove contaminants and pollutants from waste gas and water streams. Adsorbent materials and membranes (typically mesoporous and nanoporous) are increasingly being applied and new adsorbents and membranes are constantly being invented and modified for various environmental applications. Traditional types of commercial adsorbents are activated carbons, zeolites, silica gels and activated alumina. The main advantages are the high surface area and the void volume fraction per unit mass of porous materials. Smaller are the characteristic dimensions, better are the performances. In turn, decontamination or release of trapped species can be difficult.

- Energy production and storage. Future energy supply is dependent

on hydrogen as a clean energy carrier. It can be produced from fossil fuels, water electrolysis and biomass. Porous materials can be very useful during the fabrication, separation, storage and efficient energy conversion of hydrogen fuels. Currently there are no optimal systems for hydrogen storage. It can be stored in gaseous, liquid and more recently in solid forms. Despite many controversial reports in the literature, hydrogen storage in carbon nanotubes (that can be also treated as mesoporous materials) may one day become competitive and usefull. Another type of nanostructured carbon is templated using 3D ordered mesoporous silicates. Metal-organic frameworks represent another class of synthetic porous materials that store hydrogen. Efficient and secured storage - release processes need still to be optimized.

- Catalysis and photocatalysis. More efficient catalytic processes require improvement in catalytic activity and selectivity. Both aspects will relly on the tailor-design of catalytic materials with desired microstructure and active site dispersion. The traditional methods of impregnating metal ions in nanoporous supports are as not as effective in achieving high dispersion of active centers. Incorporation in template or intercalation are more advanced techniques rendering a high activity owing to the high surface area of the active components and selectivity due to the narrow pore size distribution. Transition metal oxides exhibit a wide range of physical, chemical and optical properties appropriate for such applications. One of the most studied metal oxide is semiconducting TiO_2. Titania in anatase form exhibits a strong photocatalytic effect. Regeneration of contaminated catalysts can be difficult.

- Sensors and actuators. Gas sensing relies on the detection of the electric resistivity change upon modification in gas composition or concentration and the sensitivity is normally dependent on the surface area. Gas sensors based on nanoporous metal oxides such as SnO_2, TiO_2, ZrO_2 and ZnO are being developed and applied in detectors of combustible gases, humidity, ethanol and hydrocarbons. Zirconia is typically a good sensor material for oxygen. Disadvantages are related to the selectivity as well as to regeneration of the sensing surfaces.

- Biological applications. Nanomaterials that are assembled and structured on the nanometer scale are attractive for biotechnology applications because of the potential to use materials topography and the spatial distribution of functional groups to control proteins,

cells, and tissue interactions, and also for bioseparations. Bionanotechnology is all about creating nanomaterials or biomaterials for biological applications. Nanoporous materials being porous and bio-compatible afford the capability to build enzymatic systems that mimic natural biological reactions. Immobilizing recombinant enzymes into nanoporous materials can be useful for long-lifetime biological reactors for a variety of applications. The possibilities for using enzymes in small-scale reactors for producing drugs, energy, decontaminating wastes, and creating complicated synthetic reactions are limitless. Nanopores embedded in an insulating membrane fabricated by physical methods have been demonstrated useful to examine biomolecules one by one, achieving single-molecule analysis [34]. The passage of individual molecules through nanosized pores in membranes is central to many processes in biology. Previous experiments have been restricted to naturally occurring nanopores, but advances in technology now allow artificial solid-state nanopores to be fabricated in insulating membranes. By monitoring ion currents and forces as molecules pass through a solid-state nanopore, it is possible to investigate a wide range of phenomena involving DNA, RNA and proteins. The solid-state nanopore proved to be a surprisingly versatile new single-molecule tool for biophysics and biotechnology [35]. The most supervising result of this field was that the DNA molecules do not thread meekly through these nanopores like a noodles, but instead come through the pores in several configurations. This is an important breakthrough towards DNA sequencing, demonstrating the potential applications of nanoporous materials in bioengineering.

Chapter 2

Porous materials for nanotechnology

> Il faut faire partie d'un groupe. Seul, vous ne valez rien. Que vous apparteniez, cela vous grandit et rassure en même temps ceux qui, loin, ne peuvent aller vérifier votre qualité.
>
> *Jacques Folch-Ribas*

2.1 General overview

In the previous Chapter we offered a condensed view on types, characteristics and utilities of porous materials. In this Chapter we will try to a give a more detailed picture of only two potential applications: photonics with an emphasis on PBG materials and template confined growth. In principle, every material having a structural periodicity along one or more directions can behave as a PBG material, if properly dimensioned and engineered. The operation spectrum range will depend on the characteristic dimensions. As it will be shown further, nano- and macro-porous materials can be designed to affect the electromagnetic waves in the useful, visible and infra-red spectral ranges. Template confined growth exploits the structure of porous materials to produce new structures which preserve the morphology of the initial building block. Compared to other applications (such as catalysis, storage, sensing or actuation) these applications are truly benefiting from the intrinsic structure of the porous materials. On one hand, catalysis, storage and sensing can be done using non-porous materials. On the other hand, shaping ma-

terials to possess a PBG will be impossible otherwise than structuring them.

2.2 Photonics

The term "Photonics" appeared in the late 1960s to describe a research field whose goal was to use light to perform functions that traditionally fall within the typical domain of electronics, such as telecommunications and information processing. Generally, the science of photonics[1] includes the emission, transmission, amplification, detection, and modulation of light. The power of photonics is based on the simple fact that the energy of light quanta lies in the energy range of electronic and vibrational transitions in matter. This fact is at the core of our abilities for visual perception and is the reason why experiments with light are very close to our intuition. In recent years, relying on the momentum of flowering nanosciences and the understanding of optical phenomena on the nanometer scale, researchers started to tailor nanomaterials with novel optical properties. Photonic crystals, single-photon sources and optical microcavities are the products of this effort. The strong interest in near-field optics gave birth to the fields of single-molecule spectroscopy and plasmonics, and inspired new theoretical work associated with the nature of optical near-fields.

2.2.1 Photonic crystals

Photonic crystals are periodic optical structures that are designed to affect the motion of photons in a similar way that periodicity of a semiconductor crystal affects the motion of electrons. In analogy with the well-known Bragg reflection and diffraction of X-rays from crystals, these "optical" crystals show Bragg resonances, that is, certain frequencies or wavelengths are completely reflected whereas others are transmitted. It is possible to create "optical" crystals that exhibit a periodicity in either 1, 2 or 3 dimensions and in general we talk of photonic band gap crystals, indicating the existence of certain frequency regions in which

[1] Photonics is closely related to optics. Photonics is also approximately synonymous with quantum optics, quantum electronics, electro-optics, and optoelectronics. However each term is used with slightly different connotations by scientific and governmental communities and in the marketplace. The term photonics more specifically addresses the particle like properties of light, the potential of creating signal processing device technologies using photons as well as the quantum optical technologies which are easily manufacturable and can be low-cost.

transmission of light is prohibited. Photonic crystals provide the unique ability to guide light around very tight bends and along narrow channels.

2.2.1.1 Theoretical consideration

Many basic ideas are common to both solid-state and photonic crystals and they have been utilized to build fundamental theories of the photonic crystals. The difference between them is the scale of the lattice constant, which is of the order of the wavelength of the relevant electromagnetic radiation in photonic crystals, while it is few angstroms in the other case. The theoretical solution for photonic crystals is based on Maxwell's equations in form of an eigenvalue problem for the harmonic Fourier components of the electric and magnetic fields[2]. This makes an analogy of the electromagnetic problem with the Schrödinger equation, and allows one to take advantage of some well-established results from quantum mechanics, such as the orthogonality of modes, the variational theorem and the perturbation theory. In the following, a very short description of the concepts applied to this field will be given with an emphasis on the employed materials in this work and their potential use as photonic materials. For a more complete theoretical description the reader can refer to Joannopoulos [36] and Novotny [37] books that inspired this part.

Maxwell's equations govern the electromagnetism, including the propagation of light in a photonic crystal:

$$\nabla \cdot D(r,t) = \rho \qquad \nabla \cdot B(r,t) = 0$$

$$\nabla \times E(r,t) = -\frac{\partial B(r,t)}{\partial t} \qquad \nabla \times H(r,t) = J + \frac{\partial D(r,t)}{\partial t} \ ,$$

where D is the electric displacement, B - the magnetic induction, E - the electric field, H - the magnetic field and J, t and ρ are the current density, time and charge density, respectively. For perfect dielectric materials (i.e. with relative permeability $\mu_r = 1$), by assuming a source-free region ($J = 0$ and $\rho = 0$) in which the structure does not vary with time, Maxwell's equations can be reduced to four relations, each involving only one type of field. The representation can be simplified by relating B to H and D to E. The components D_i of the displacement field can be related to the electric field components E_i via power series:

$$D_i/\epsilon_0 = \sum_j \epsilon_{ij} E_j + \sum_{j,k} \chi_{ijk} E_j E_k + O(E^3) \ .$$

[2]Maxwell's equations, being scale invariant provide a secure basis.

For many dielectric materials it is convenient to use the following assumptions: (i) linear regime, the field strengths are small enough so that χ_{ijk} can be neglected; (ii) macroscopic and isotropic materials, the dielectric constant can be approximated by a scalar dielectric function $\epsilon(r, w)$; (iii) ignoring any frequency dependence of the dielectric function (in the subsequent, we will simply choose the value of the dielectric constant appropriate to the frequency range of the studied systems) and (iv) consider low-loss, transparent materials, $\epsilon(r)$ is real and positive. Thus, the electric displacement is given by $D_i = \epsilon_0\epsilon(r)E(r,t)$ and considering that the photonic crystals are not realized in magnetic materials ($\mu_r = 1$), the magnetic induction can be written as $B = \mu_0 H(r,t)$. A new set of equations is obtained:

$$\nabla \cdot H(r,t) = 0 \qquad \nabla \times E(r,t) + \mu_0 \frac{\partial H(r,t)}{\partial t} = 0$$

$$\nabla \cdot [\epsilon_0\epsilon(r)E(r,t)] = 0 \qquad \nabla \times H(r,t) - \epsilon_0\epsilon(r)\frac{\partial E(r,t)}{\partial t} = 0 \ .$$

The field functions E and H are complicated functions of both space and time. Due to the linearity of Maxwell's equations it is easier to separate the time dependence from the spatial dependence by expanding the fields into a set of harmonic modes:

$$E(r,t) = E(r)e^{-i\omega t} \qquad H(r,t) = H(r)e^{-i\omega t} \ .$$

We can rewrite the new set of equations in an eigenvalue problem having w^2/c^2 as eigenvalues and the fields $E(r)$ and $H(r)$ as eigenfunctions:

$$\nabla \cdot H(r) = 0 \qquad \nabla \times \Big(\frac{1}{\epsilon(r)}\nabla \times H(r)\Big) = \frac{\omega^2}{c^2}H(r)$$

$$\nabla \cdot [\epsilon(e)E(r)] = 0 \qquad \nabla \times [\nabla \times E(r)] = -\frac{\omega^2}{c^2}E(r) \ ,$$

where $c = 1/\sqrt{\epsilon_0\mu_0}$ is the vacuum speed of light. As it can be observed, the right-hand equations are eigenfunctions and the equation defined in $H(r)$ is called the **master equation** as combined with the fact that the magnetic field is transverse ($\nabla \cdot H = 0$) offers a more convenient way to solve the electromagnetic problem using this representation. A generally adopted representation, using a differential operator Θ is:

$$\Theta H(r) = \frac{\omega^2}{c^2}H(r) \ , \qquad where \qquad \Theta = \nabla \times \Big[\frac{1}{\epsilon(r)}\nabla \times\Big] \ .$$

One interesting aspect of electromagnetism is that there is no fundamental length scale. In atomic physics, the spatial scale of potential

functions is generally set by the fundamental length scale of Bohr radius. Hence, configurations of materials that differ only in their overall spatial scale have very different physical properties. For photonic crystals the solution of the problem at one length scale determines the solution at all other length scales. This simple fact is very important for practical considerations. The fabrication of complex micrometer-scale photonic-crystals can be difficult. Yet, models can be easily made and tested in the microwave regime, at the much larger length scale of centimeters, if materials can be found that have nearly the same dielectric constant[3].

To solve the problem for a photonic crystal, it is necessary to impose that the dielectric function is periodic. In real space this can be in one, two or three-dimensions corresponding accordingly to 1D, 2D and 3D photonic crystals. The periodicity can be reduced to two concepts: the basis - defining the spatial arrangement of the unit cell and the lattice - the confinement of the unit cell. Photonic crystals (like traditional crystals of atoms or molecules) do not have continuous translational symmetry. Instead, they have discrete translational symmetry, that is, they are not invariant under translations of any distance, but rather, only distances that are multiple of some fixed step length. For a system with lattice constant a, because of the discrete symmetry, we will have $\epsilon(r) = \epsilon(r \pm a)$ or, by repeating this translation, we can see that $\epsilon(r) = \epsilon(r + R)$ for any R which is a linear combination of a_i: $R = \sum_i n_i a_i$ for $(i = 1, 2, 3 ...)$.

A system with translational symmetry is unchanged by a translation through a displacement d. We can then define an operator T_d associated with an arbitrary displacement d and when applied on a function $f(r)$ shifts the argument by d. In a continuous dielectric medium $T_d\epsilon(r) = \epsilon(r \pm d) = \epsilon(r)$, or equivalently $[T_d, \Theta] = 0$. The eigen-functions of the T_d operator must have the functional form of a plane wave:

$$T_d H_0 e^{ik\cdot r} = H_0 e^{ik\cdot(r+d)} = (e^{ik\cdot d}) H_0 e^{ik\cdot r} \quad ,$$

where H_0 is any constant vector and $e^{ik\cdot d}$ is the corresponding eigenvalue. This equation shows that for continuous dielectric media, the solution of master equation must have the form of plane waves. Imposing the transversality condition ($\nabla H(r) = 0$), the dispersion relation of photons in a medium with dielectric permitivity ϵ (or refraction index $n = \sqrt{\epsilon}$) can be obtained: $\omega = c|k|/\sqrt{\epsilon}$.

[3]You will ascertain a similar scale invariant approach in Chapter 3. You will see that in the same way as photonic crystals can be tested at the centimeter scale and then transposed at the nanometer scale without any fundamental differences, the reliability of the statistical patterning can be verified as well using macroscale objects.

Photonic crystals are invariant under discrete translational symmetry defined by the vector R described previously. Being $\hat{T}_R$ the unitary operator associated with the discrete translation R, the rule for the transformation in the basis defined by eigenfunctions of $\hat{T}_R$ states:

$$\hat{\Theta}'_H = \hat{T}_R \hat{\Theta}_H \hat{T}_R^{-1} \qquad \epsilon^{'} = \hat{T}_R \epsilon \hat{T}_R^{-1} \qquad H^{'}(r) = (\hat{T}_R H)(\hat{T}_R^{-1} r) \ .$$

Photonic crystal invariance under T_R means that the operator Θ_H and the dielectric function ϵ are left unchanged. The application of T_R to the master equation yields a new eigenvalue problem for the transformed $H^{'}$. However, since $[\Theta_H, T_R] = 0$, it can be showed that $H^{'}$ must satisfy the same equation that holds for H, and fulfilled if equal to $H^{'}$ within a multiplication factor:

$$\hat{\Theta}_H H = \frac{\omega^2}{c^2} H \quad <=> \quad \hat{\Theta}_H \hat{T}_R H = \frac{\omega^2}{c^2} \hat{T}_R H \ .$$

Consequently, H is a linear combination of degenerate eigenfunctions of the translation operator $\hat{T}_R$: $\hat{T}_R H(r) = \alpha H(r)$, the eigenfunctions of $\hat{T}_R$ are plane waves and the eigenvalues are complex numbers of unitary modulus:

$$f_k(r) = f_0 e^{ik \cdot r} \qquad \hat{T}_R f_k(r) = e^{-ik \cdot R} f_k(r) \qquad \alpha = e^{-ik \cdot R} \ .$$

Using symmetry and operator formalism we can find the general form for the solution of Maxwell's equation in a photonic crystal. The discrete periodicity in the r direction leads to a r dependence for H that is simply the product of a plane wave with a r-periodic function (detailed calculations can be found in the cited books). This result is commonly known as the Bloch-Floquet theorem which states that the general solution of a master equation invariant under a translational symmetry operation $\hat{T}_R$ is a periodic function $u_k(r)$ multiplied by a phase factor $e^{ik \cdot r}$:

$$\hat{T}_R H_k(r) = H_k(r - R) = e^{-ik \cdot R} H_k(r) \ ,$$

or in a more compact form :

$$u_k(r) = e^{-ik \cdot r} \sum c(k + B) f_{k+B}(r) \quad \longrightarrow \quad H_k(r) = e^{ik \cdot r} u_k(r) \ .$$

Without going to much into the mathematical details, we shall recall briefly the notions related to the reciprocal lattice and the Brillouin zone. The Bloch's theorem is used to express an electromagnetic mode as a plane wave that is modulated by the periodic function $u(r)$. The function u shares the same periodicity with the crystal. In principle, we need only to consider the wave vectors k that lie in a certain region of

the reciprocal lattice known as the Brillouin zone. If we are working with a lattice-periodic function out of plane wave (with period or the lattice vector R), we need only to consider the plane waves with wave vectors q such that $e^{iq\cdot R} = 1$ for all the lattice vectors. The vectors that satisfy the relation $e^{iq\cdot R} = 1$ or equivalently $q \cdot R = 2\pi N$ are called reciprocal lattice vectors. They span the so-called reciprocal space $\mathbb{K}^3$ which is the dual space of the Euclidean space $\mathbb{R}^3$. For a given set of lattice vectors R, the lattice vectors are determined by the equation $q \cdot R = 2\pi N$. If we represent the lattice vectors R in terms of the primitive lattice vectors ($R = la_1 + ma_2 + na_3$, where l, m, n integers, and a_1, a_2 and a_3 are the smallest vectors pointing from the lattice point to another) then the primitive lattice vectors are expressed as follows:

$$b_1 = \frac{2\pi}{|a_1|}\hat{a}_1; \qquad b_i = 2\pi[\text{lim}]\frac{a_j \times \delta\hat{k}}{a_i \cdot (a_j \times \delta\hat{k})}; \qquad b_i = 2\pi\frac{a_j \times a_k}{a_i \cdot (a_j \times a_k)}$$

in 1D, 2D and 3D space, respectively, where $\hat{k}$ gives the direction of the z axis and i, j, k label the primitive vectors. As such, when we take the Fourier transform of a function that is periodic on a lattice, we need only to include terms with wave vectors that are reciprocal lattice vectors. To construct the reciprocal lattice vectors, we take the primitive lattice vectors and perform the operations depicted above. Further, the Brillouin zone is the region delimited by cutting the reciprocal space with planes perpendicular to the primitive vectors at $|b_i/2|$ from the origin. For a cubic (3D) or square (2D) lattice the reciprocal primitive vectors are simply $b_i = \frac{2\pi}{|a_i|}\hat{a}_i$. This is not the case for other lattices as will be discussed further for the triangular lattice.

Two more concepts are needed and exemplified further: the band structure and the photonic bandgap. As mentioned, the electromagnetic modes of a photonic crystal with discrete periodicity in three dimensions can be written as Bloch states: $H_k(r) = e^{ik\cdot r}u_k(r)$. By inserting the Bloch state into the master equation we can solve $u_k(r)$:

$$(ik + \nabla) \times \frac{1}{\epsilon(r)}(ik + \nabla) \times u_k(r) = \Big(\frac{\omega(k)}{c}\Big)^2 u_k(r).$$

The mode profiles are determined by the eigenvalue problem subject to transversality $(ik + \nabla) \cdot u_k = 0$ and the periodicity condition $u_k(r) = u_k(r + R)$. Because of this periodicity condition, we can treat the eigenvalue problem as being restricted to a single unit cell of the photonic crystal. Since k enters as a continuous parameter, the frequency of each band will vary continuously as k varies. In this way we have a description of the modes of a photonic crystal: a family of continuous functions

$\omega_n(k)$ indexed in order of increasing frequency by the band number. The information contained in these functions is called the band structure of the photonic crystal. Because of the boundary condition, we can regard the eigenvalue problem as restricted to a single unit cell of the photonic crystal. The situation is similar to the quantum mechanics problem of the "electron in a box" where the restriction of the eigenvalue problem to a finite volume leads to a discretization of the energy spectrum.

In addition to the Bloch vector and the index n, there is also another important degree of freedom that characterizes the solution of the master equation, namely, the polarization σ. Hence, for each choice of (k, n) there are two independent solutions with different polarizations. In general, it is found that the polarization is not independent of the Bloch vector $\sigma = \sigma(k)$. Therefore, it is convenient to absorb the polarization degree of freedom in the band index n. Only for some specific cases, where at least one polarization is independent of the Bloch vector, the index σ is used to label the eigenfunctions and eigenfrequencies. As it will be shown further, this happens for the in-plane propagation in 2D photonic crystals.

It is worth mentioning that the spectrum ω can be further classified by considering other symmetry properties of the photonic crystals (other than translational). For example, a given photonic crystal can be left invariant after a rotation, a mirror reflection or inversion operation. It can be shown that whenever a photonic crystal will have one of the mentioned symmetries, the $\omega(k)$ functions will have that symmetry as well. This particular collection of symmetry operations is called the point group of the crystal. Since the functions $\omega(k)$ possess the full symmetry of the point group, we don't need to consider them at every k point in the Brillouin zone. The smallest region within the Brillouin zone for which the $\omega(k)$ is not related by symmetry is called the irreducible Brillouin zone. Other symmetry aspect is the time-reversal invariance yielding $\omega(k) = \omega(-k)$. The above relation holds for almost all photonic crystals, with the exception of magneto-optical materials. The frequency band has the inversion symmetry even if the crystal does not.

A photon with energy ω will propagate in a photonic crystal only if $\exists(k, n) : \omega = \omega(k)$. Thus, we can define the photonic bandgap as the spectral region $[\omega_1, \omega_2]$ for which $\forall\omega \in [\omega_1, \omega_2], \nexists(k, n) : \omega = \omega(k)$. Photonic bandgap means that in the frequency window $[\omega_1, \omega_2]$ there is a null DOS $\rho(\omega)$ which for a photonic crystal is defined as:

$$\rho(\omega) = \sum_n \sum_{k \in BZ} \delta(\omega - \omega_n(k))$$

Contrary to the smooth DOS for a homogeneous medium, in a photonic

crystal DOS presents peaks and dips around a mean value given by the effective medium theory.

To conclude, for a given photonic crystal $\epsilon(r)$ we can calculate the band structure functions $\omega(k)$. For that, various computational techniques are available. In the next section, the band structures of some photonic crystals was calculated using MPB (MIT Photonic Bands *AbInitio*)[4] [38]. To avoid solving the master equation for every point of the irreducible Brillouin zone, it is often enough to do it along the symmetry lines, because they correspond to higher degree of symmetry with respect to the internal point and for this reason they are more representative.

2.2.1.2 2D and 3D systems

In the following we will discuss the cases for 2D and 3D photonic crystals. To avoid redundancy, we will analyze the particular systems used throughout this work. Going back to the porous materials their architectures can be treated as a 2D photonic crystal of air columns in a dielectric substrate or by inverting them, as an array of dielectric columns in an air matrix. The square and the triangular (or hexagonal) lattices are the most representative of the 2D class. By making a porous film "suspended", we can obtain a new hybrid structure, known as photonic-crystals slabs or planar photonic crystals. For the 3D structures we will limit to the case of a simple cubic lattice. As for the dielectric nature, the polyaniline in both, doped and dedoped states, silicon, alumina and PMMA will be the materials of interest.

A 2D photonic crystal is periodic along two of its axes and homogeneous along the third axis. For the simplicity, the size in the third axis is considered to be infinite[5]. Photonic band gaps appear in the plane of periodicity. For light propagating in this plane, the harmonic modes can

[4]The MIT Photonic-Bands (MPB) package is a free program for computing the band structures (dispersion relations) and electromagnetic modes of periodic dielectric structures, on both serial and parallel computers. It was developed by Steven G. Johnson at MIT along with the Joannopoulos Physics group. This program computes definite-frequency eigenstates (harmonic modes) of Maxwell's equations in periodic dielectric structures for arbitrary wavevectors, using fully-vectorial and three-dimensional methods. It is especially designed for the study of photonic crystals (a.k.a. photonic band-gap materials), but is also applicable to many other problems in optics, such as waveguides and resonator systems.

[5]In reality it is experimentally impossible to realize such structures. For a finite size in the z direction the out of plane propagation has to be taken into account. The states with wavevectors with nonzero component in the vertical direction will fill completely the 2D band structure. A solution to this problem is the concept of finite height 2D photonic crystal: structuring the 2D crystal in a planar dielectric **waveguide** so that the in-plane confinement is provided by the photonic crystal, while the vertical confinement is obtained through total internal reflection. However,

be divided into two independent polarizations, each with its own band structure. TE modes have H normal to the plane, $H = H(\rho)\hat{z}$ and E in the plane $E(\rho) \cdot \hat{z} = 0$ and TM modes have just the reverse. The band-structure for TE and TM modes can be completely different and it is possible to have a band-gap for one polarization but nor for the other one.

We will begin with the simplest case[6], the square lattice made out of "transparent" pillars with high ϵ. Silicon is an excellent candidate as it has $\epsilon \sim 12 - 14$ with low absorption coefficients over a wide spectrum range (900 to 9000 nm). It is one of the most attractive material for constructing photonic band gap materials for the telecomunication wavelengths (1550 nm). Although it is not considered practical for the visible range because it absorbs light, silicon is an indirect band gap semiconductor with weak absorption in the submicrometer wavelength range: $\alpha \sim 10^2 cm^{-1}$ at 1.25 eV ($\sim$ 1000 nm) and $\alpha \sim 10^3 cm^{-1}$ at 1.6 eV ($\sim$ 775 nm). Hence, the absorption of light can be insignificant in a photonic crystal if the volume fraction of silicon is low, low enough for high transparency in the visible range and high enough for opening a rather large photonic band gap [39]. For the simplicity, we will not take into account these aspects. Other important parameter is the dimensionless lattice constant. The lattice period a as well as the pillar radius (a more general parameter is the ratio between the pillar radius to lattice period r/a) can modify the photonic band appearance. Obviously, there is a optimum value of r/a for which the band gap is maximized. In the following, we will restrict to this condition.

Figure 2.1 shows the photonic band structure for the discussed structure. The frequency (left axis) is expressed as the dimensionless ratio $\omega a/2\pi c$. For the simplicity, further we will use f for the frequency. This is equivalent to a/λ, where λ is the vacuum wavelength ($2\pi c/\omega$) or, expressed in terms of photon energy to $1241.25/a$. As it can be observed, a large band gap is opened only for the TM mode (shaded gray region) between the band 1 and 2. The band gap size is defined as the gap-midgap ratio $\Delta\omega/\omega_m \times 100\%$ (scale independent value), where $\Delta\omega$ is the frequency width of the gap and ω_m is the frequency at the middle of the gap. Thus, we have a 39% TM gap centered at $0.354 \cdot f$. There is also a smaller (3.9%) TM gap at $0.732 \cdot f$ as well as an apparent TE gap (0.27

this does not simplify so much the problem as the introduction of the waveguiding component in the photonic crystal modify the 2D band structure and not transposable out of plane losses appear.

[6]Simple because of geometry: a square lattice has a square reciprocal lattice, pointing in the same directions.

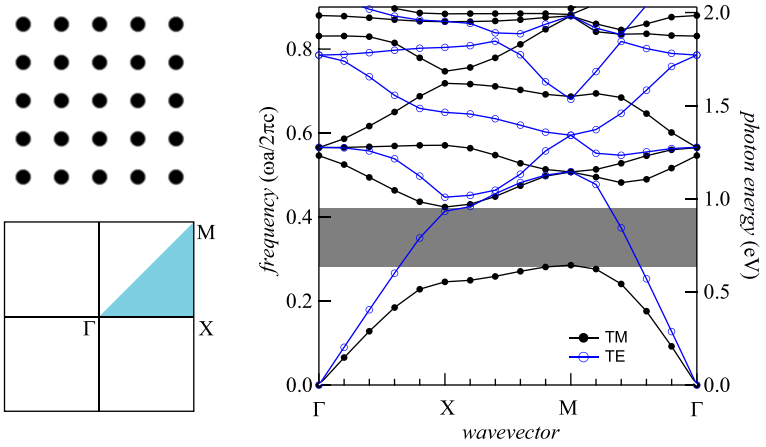

Figure 2.1: Left: the dielectric function of a square lattice of rods and the Brillouin zone (with the irreducible zone shaded in blue). Right: the photonic band structure of a square lattice of silicon rods in air with r/a=0.194, as obtained by maximizing the TM gap, shown as the shaded gray area.

%) at $0.881 \cdot f$[7]. Due to the scale independence, the band structure is valid for all the range where ϵ was considered to be constant (900 - 9000 nm or 1.38 - 0.138 eV, respectively). This means that you can center the band gap (without affecting the band structure or the gap size) in this range by adjusting a. For example, centering the band gap at 0.8 eV (or 1550 nm) it is possible for a lattice with a=550 nm. Now, the right axis in Figure 2.1 is a plot of f in eV units only for a= 550 nm. Technically, a 550 nm lattice constant and 206 nm pillar diameter (or r/a=0.194) are is easily feasible. Combined with the high transparency of silicon in the infrared region explains why Si still remains one of the most used materials in photonics for the telecommunication applications. It is possible to design band gaps in visible as well, though with some modifications. First, the increase in ϵ will slightly modify the band structure. Second, as mentioned, low filling fraction crystal will be needed in order to minimize the absorption. Poborchii *et al.* used a square lattice of silicon pillars with a= 270 nm and r= 32 nm to demonstrate a green light band gap (2.23 eV).

Using a triangular lattice it is possible to open even a larger band gap. Again, we have computed the band structure of a triangular lattice of silicon pillars (ϵ = 13, band gap optimized geometry) and the results

[7]The sources of "false positive" band gaps are explained in details in the MPB manual.

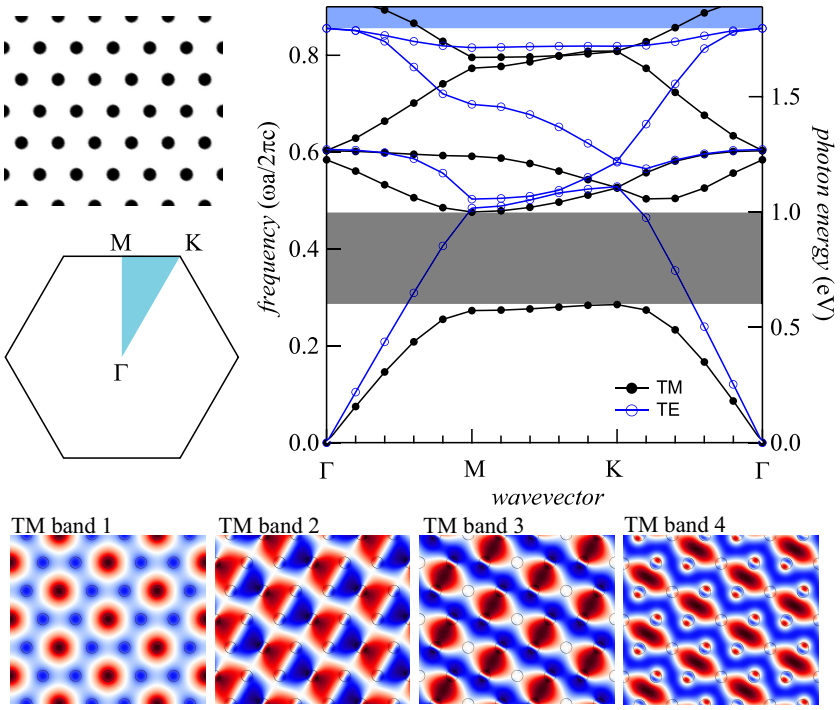

Figure 2.2: Left: the dielectric function of a triangular lattice of rods and the Brillouin zone (with the irreducible zone shaded in blue). Right: the photonic band structure of a triangular lattice of silicon rods in air with r/a=0.176, obtained by maximizing the TM gap, shown as the shaded gray area. A TE gap opens as well in this case displayed by the shaded blue area. Bottom: Electric-field distribution for the first 6 TM bands at the K-point. For the clarity, only the contour of the dielectric function is represented. The colors indicate the amplitude of the displacement field pointing in the z direction (blue - negative, red - positive).

are shown in Figure 2.2. Now the size of the TM gap is 50.2%, centered at $0.38 \cdot f$. We can observe that there is also a TE gap of about 8.36% centered at $0.89 \cdot f$. If centering the band gap at 0.8 eV we obtain the value for $a = 590$ nm (and hence, a modified right axis). Using the MPB data analysis tools it is also possible to examine the real part of the z component for the displacement fields inside the lattices (bottom plots in Fig. 2.2). The real part representation shows us the field intensities of the modes at a given instant in time. We can learn several things from these plots. The first band has most of its energy in the dielectric regions and has a low frequency. The second band must have a nodal plane in order to

be orthogonal to the first and thus, has most of its energy in the air region with a corresponding higher frequency. Successive bands have more and more complex nodal structures in order to maintain orthogonality. As such, we can see that a triangular lattice can open a bigger TM band gap than a square lattice, though, in both cases, a full band gap for both, TM and TE modes is absent. It will be shown further that this is possible using a different lattice configuration, namely, a triangular lattice of air holes in a dielectric. Nevertheless, the post-type structure can be sometimes useful. As mentioned, working with an absorbing material requires low material filling fraction. From sterical considerations it can be shown that a triangular lattice of air holes can has a minimum filling fraction of ~ 0.1[8] while for the post-type structures the filling fraction can be made much smaller.

Before going further, we will analyze the case of a crystal made out of polyaniline pillars (see more details in Chapter 4). Silicon and most of materials have a definite constant refractive index (or dielectric constant) at a given wavelength[9]. Hence, to modify the band structure of an already fabricated photonic crystal you can either modify the lattice parameters (very often difficult to do that) or, change the surrounding medium dielectric constant (also, not so practical). As it will be shown in Chapter 4, polyaniline has very interesting optoelectronic properties. Protonation/deprotonation or other chemical modifications induce strong changes in the electric conductivity as well as in the dielectric constant. Hence, it could be possible to fabricate a photonic crystal with tunable properties by chemically modifying the material dielectric properties. But there are other problems to solve before doing that. For instance, polyaniline has strong absorption bands in the visible spectrum range, property which may alter the photonic band gap properties. As pointed out previously, by reducing the material filling fraction in the crystal, it is possible to render it "transparent". However, polyaniline has a low dielectric constant, which may be insufficient to open a band gap in a low filling fraction structure. In turn, in the near-infrared region, it has low absorption for both, protonated and deprotonated states, with relatively high and still tunable dielectric constants (ϵ= 5.2 and ϵ= 2.8 for protonated and deprotonated phases, respectively). The results are shown in Figure 2.3.

First, the band structure was calculated for the protonated polyaniline, again maximizing and centering the TM gap at 0.8 eV (left plot

[8]You can also calculate that. Take a look at Figure 3.15 and at the afferent text descriptions and you will find rapidly the answer.

[9]We exclude non-linear optical media; for example, affecting the refractive index using static electric fields (Pockels effect) or using acoustic waves.

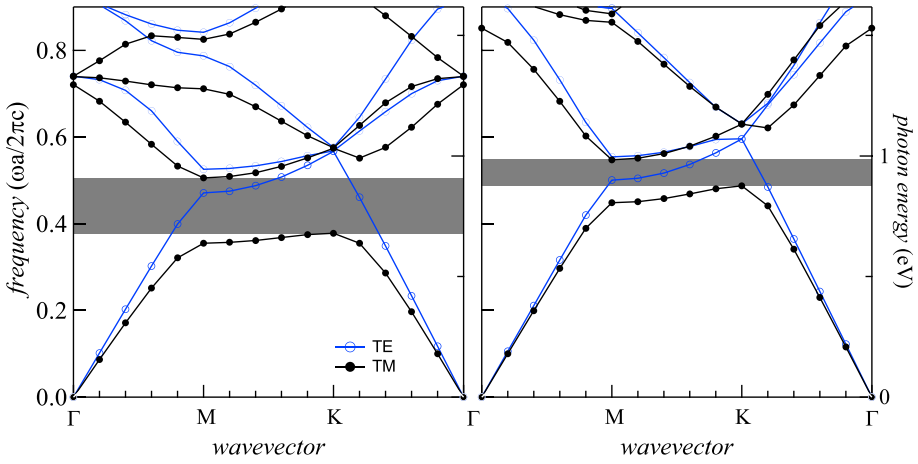

Figure 2.3: Band structure of a triangular lattice of polyaniline pillars in the protonated (left) and deprotonated (right) state.

in Fig. 2.3). A relatively large band gap (28.86%) opens at $0.44 \cdot f$. Here, $0.44 \cdot f$ represents 0.8 eV for a lattice having the constant a= 690 nm. The gap maximizes for a/r= 0.2236 or, for pillars having the diameter of 310 nm. As it will be shown in Chapter 4 the fabrication of such lattice is relatively a simple task. Deprotonation leads mainly to a change in the dielectric constant of polyaniline[10]. The same structure with a new ϵ has a different band structure. The band gap is narrower (11.6%) and centered at a higher frequency $0.52 \cdot f$. Thus, it is possible to chemically tune the optical properties of a polyaniline photonic crystal. What is more interesting is that the process is reversible and we can switch between the states by simply dipping the structures into a given pH solution. Probably, the approximations that were made are too severe (rough estimation of the ϵ, neglecting the absorption, etc.). What is sure is that there is a change in the dielectric constant between the two states (and probably with some intermediate states) and fine chemical tuning of polyaniline photonic structures is possible [40]. There is still some work to do but this could be further exploited to build chemically tunable optical switches as well for in optical sensing.

Up to now we have reviewed the post-type photonic structures, which are the inversed replicas of porous materials. To recall, a porous material consists of air-holes in a solid matrix (usually dielectric). Making them

[10]Polyaniline films "shrinks" upon deprotonation and presumably, there will be also a change in the pillar diameter. We will neglect that here.

ordered will result in a periodically modulated dielectric structure or a photonic crystal. In the following we will shortly review only the triangular lattice of air holes as this geometry is the most encountered in self-organized systems (AAO, self-assembled colloids). We will focus only on silicon, AAO and PMMA structures and we will reduce the analysis mainly from the technological point: whether is possible or not to make them operational in the visible and infrared spectrum ranges.

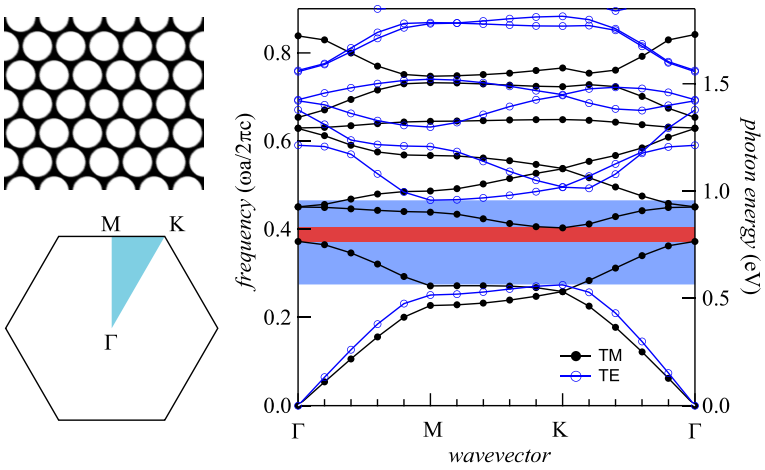

Figure 2.4: Left: the dielectric function of a triangular lattice of air holes and the Brillouin zone (with the irreducible zone shaded in blue). Right: the photonic band structure. The right axis corresponds to a=600 nm where the complete gap is centered at 0.8 eV.

Using this geometry it is possible now to obtain a complete band gap for both TE and TM modes. The band structure for a lattice of air holes drilled in silicon with r/a=0.44 is shown in Figure 2.4. As it can be observed, there is a large TE gap (shaded blue region, 51.9 %) and a small TM gap which actually is the complete gap for both TE and TM modes (shaded red region, 7.8%). Making this structure to operate in the infrared range (for example centering its band gap at 0.8 eV) requires a lattice constant of 600 nm and hole diameter of 530 nm. These dimensions are easily accessible using standard top-down microprocessing techniques as well as using bottom-up self-assembled approaches. For example, arranging 620 nm PS spheres (see Figure 5.5 (**a**)) on a silicon substrate we can then etch holes arranged in a triangular lattice and obtain the "telecomm-operating" photonic crystal. It is possible to further augment the size of the band gap, yet this will require an increase in the hole radius and the fabrication of such structure may become trou-

blesome. It is worth mentioning that the air-holes structures are more used for the photonic structures than the post-type structures from the application and fabrication points of view. First, as we saw, it is possible to open complete band gaps. Second, we have treated crystals with infinite z axis that will be difficult to realize. In practice, finite height architectures are used, namely, the photonic-crystal slabs combining the 2D periodicity with the total internal reflection vertical confinement. We will not discuss them here, the domain is intensely studied and a vast literature on this topic exists [41].

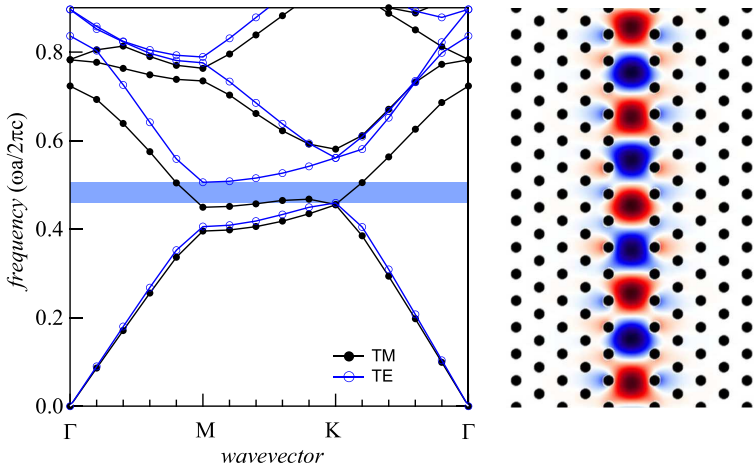

Figure 2.5: Left: band structure of porous alumina photonic crystal. Right: waveguide mode propagating along a linear defect in a triangular lattice of rods. This structure supports a single guided band within the band gap.

Let's consider now the cases of AAO and PMMA photonic crystals. Both are known to have very low absorption coefficient (then we can approximate ϵ to n^2) in the visible range of spectrum and to have optoelectronic properties sensitive (at different extents) to the preparation conditions. For the PMMA, small variations are observed for different molecular masses though, the differences are so small that they can be neglected (for example n= 1.495 and 1.506 for 950k and 495k PMMA). For alumina the variations are larger (ϵ varies between 2 and 2.8) and are sensitive to the preparation conditions. For example, the *e-beam* evaporated alumina has $\epsilon = 2.7$ while the sputter deposited alumina has $\epsilon = 2.5$ at 631 nm wavelength. The dielectric behavior of AAO is even more complicated because it depends on the anodization chemistry and species that are incorporated during the oxidation of aluminum [42].

Moreover, it was found that the porous alumina structure is composed of a duplex oxide layer: an inner oxide layer consisting of pure alumina oxide ($\epsilon \sim 2.8$), and an outer oxide layer of a nonuniform refractive index ($\epsilon \sim 2.4$ - 2.7 in near-IR) [43]. The authors suggested that the nonuniform refractive index of the outer oxide arises from an inhomogeneous distribution of anion species concentrated in the intermediate part of the outer oxide. They've used a composite dielectric structure to model the experimental observations. We will neglect these aspects and focus on photonic structures that will operate in the visible range (assuming ϵ=2.2 for PMMA and ϵ=2.8 for AAO at 631 nm). As the difference in the dielectric constant of these materials is relatively small, the band structure is not significantly modified and the same discussion is valid for the 2 structures.

The "optimized" band structure, obtained for r/a= 0.4 is shown in Figure 2.5 left panel. Only a relatively small band gap (TE mode, gap size 9.7%, centered at $0.48 \cdot f$) is observed. It can be shown that the gap is further diminished for decreased values of ϵ and eventually disappears for ϵ= 2. In practice, it would be difficult to measure such small band gaps as we have to take into account the processing defect that will alter the band structure (as well as the fact the for alumina ϵ will be smaller in reality). Instead, it can be measured the Γ - M direction and as calculated, a band gap centered around $0.42 \cdot f$ is expected. This was confirmed experimentally using large-area porous alumina fabricated using imprint method [43, 44]. Using alumina with a= 500 nm, a band gap in near-IR was measured (1200 - 1300 nm wavelength). To open the band gap in the visible (at 630 nm as proposed above) we will need an alumina with interpore distance of $\sim$ 300 nm and pore diameter of 240 nm. For porous alumina, the interpore spacing can be varied between 50 nm and 500 nm, leading to theoretical photonic band gaps centered at wavelengths in the range between 100 and 1300 nm, depending on the filling ratio. The electronic band gap of alumina (corundum) is around 7.5 eV, while porous alumina has a lower band gap due to its amorphous nature. Experimentally, however, absorptions for wavelengths above 400 nm is negligible over the size of a photonic crystal. This is valid also for PMMA fabricated structures.

Although, for practical implementation, the realization of such structures in AAO or PMMA is feasible, there are some constrains. Without any pre-patterning procedure, highly ordered AAO films are made of few-μm -size domains in which the ordering is preserved but the orientation of the inter-domain lattice is random. Hence, even if the ordered AAO can be made over squares centimeters, the poly-domain structure prohibit the realization of photonic band gap structures over large ar-

eas. Using PMMA, this problem is eliminated as the lattice is precisely patterned using EBL. Other problem is related to the low refractive index of both materials. We have treated only infinite structure, with no propagation of light in the z-direction. Finite-height structures are more practical, yet they require some special design. As already mentioned, the photonic crystal slab is an excellent option. However, this configuration requires index guiding properties and one of the main requirements is the high index contrast of the dielectric compared to the surrounding media. As for both, n is close to 1.5, it would be relativelly difficult to find materials with lower n (actually, PMMA and alumina are sometimes used as low-refractive substrates). The best option is to use structures completely embedded in air ($\epsilon = 1$). Obviously, it is impossible to do that for all the discussed configurations (try to imagine a suspended rod-type structure). For air-hole like structure this is possible, as the configuration is self-sustained (down to a given filling ratio). The option that is widely used is the definition of the photonic crystal on top of a sacrificial layer (~ 1 μm thick) and then remove it to obtain the suspended structure (of course, all of that on a rigid substrate for handiness). For AAO this seems technologically challenging.

And last, is the ability to define defects in PMMA and AAO photonic structures (applicable in general for all photonic crystals). Up to now we have treated periodic lattices of rods or air-holes and observed that in some conditions we can inhibit the propagation of light through these ordered lattices, which normally are transparent. A question that could arise is why do we need that, what for render a transparent material opaque? We can use them to inhibit spontaneous emission (2D or 3D structures) or to build perfect mirrors (1D multilayered films) but, perhaps, one of the most studied aspect is the light localization and guiding using defects. Basically, by modifying one or an array of lattice elements in a photonic crystal it is possible to confine the light in that region. For examples, in a slab, the index guiding will confine the propagation in z-direction and the in-plane band gap will restrict the propagation in the x-y-direction (valid for the light with the frequency within the band gap). One example of such waveguided mode is shown in Figure 2.5 (right panel). Here, a line-defect is created by removing an array of rods along the Γ - K direction. This can be extended to any of 1D, 2D or 3D systems and obtain an analogous of electrical wiring but this time with photons.

Even if the photonic slabs can be treated as 3D systems they are not truly 3D photonic crystals. In the same way as for 2D photonic crystals, a structure with discrete translational symmetry in three-dimensions is called a 3D photonic crystal. Using these structures it is possible to

achieve full 3D control over the light propagation. They are also largely encountered in the nature, for example in the natural opal formed from close-packed domains of amorphous colloidal spheres of silica. Some insects and butterflies (*Morpho* and *Ancyluris meliboeus* butterflies,) have also micro- and nano-structured photonic crystal domains on their wings responsible for brilliant iridescent colors [45–47]. Some of the representative structures of the class (with full band gap) are the diamond lattice of spheres [48], the Yablonovite [49], the woodpile crystal [50, 51] and inverse opal structures [52]. We will not review all of these structures and will turn our attention to the simple cubic lattice. As it will be shown in Chapter 4, a cubic lattice can be simply fabricated in a single-step EBL process. Moreover, the inversion of a cubic lattice of rectangular rods results as well in a cubic lattice of rectangular rods. For example, in Figure 4.27 (**a**), a polyaniline cubic lattice fabricated by inverting a PMMA cubic lattice is shown (as you can see, it can be roughly approximated to a cubic lattice of rectangular rods). We will focus only on the inverted structure and analyze the two realizable geometries: (i) rectangular rods lattice and (ii) cubic lattice of spheres connected by rectangular rods (closer to the real structure).

First, we will discuss the case of silicon and then will see how things are changed for a lower dielectric lattice, for instance, using PMMA (the case of the original template). The computation result is shown in Figure 2.6. As it can be observed, it is possible to open a complete band gap in a cubic lattice of high-dielectric rectangular rods (see inset). The gap is relatively high (7.62%) and centered at $0.38 \cdot f$. It is obtained for the vein size of $0.3 \cdot a$ (for this geometry only the vein size can be tunned). Direct writing of such a perfect lattice using the procedure described in Section 4.2.3 may be difficult. At the intersection point of high-dose rods with the low-dose lines, the resist will be over-exposed and it will look more like a bump. It can be approximated to a sphere and the new structure is a cubic lattice of spheres connected by rectangular rods. In this configuration the band structure is susceptible to both, the vein size and the sphere radius. We will consider the same structure as in the previous case ($0.3 \cdot a$ vein size) and look how the band gap is modified for different sphere sizes. Sphere radius below $0.15 \cdot a$ has no physical sense as it is englobed by the rectangular rods. Increasing further, no significant change can be detected in the gap size (band gap is situated between band 2 and 3). At $0.225 \cdot a$ it starts to have an influence and the band gap decreases with the increase in sphere radius until it vanishes completely at $0.325 \cdot a$. Yet, we can see that a new band gap appears (between the band 5 and 6) that reaches a maximum size of 9% and then, disapears at $0.5 \cdot a$.

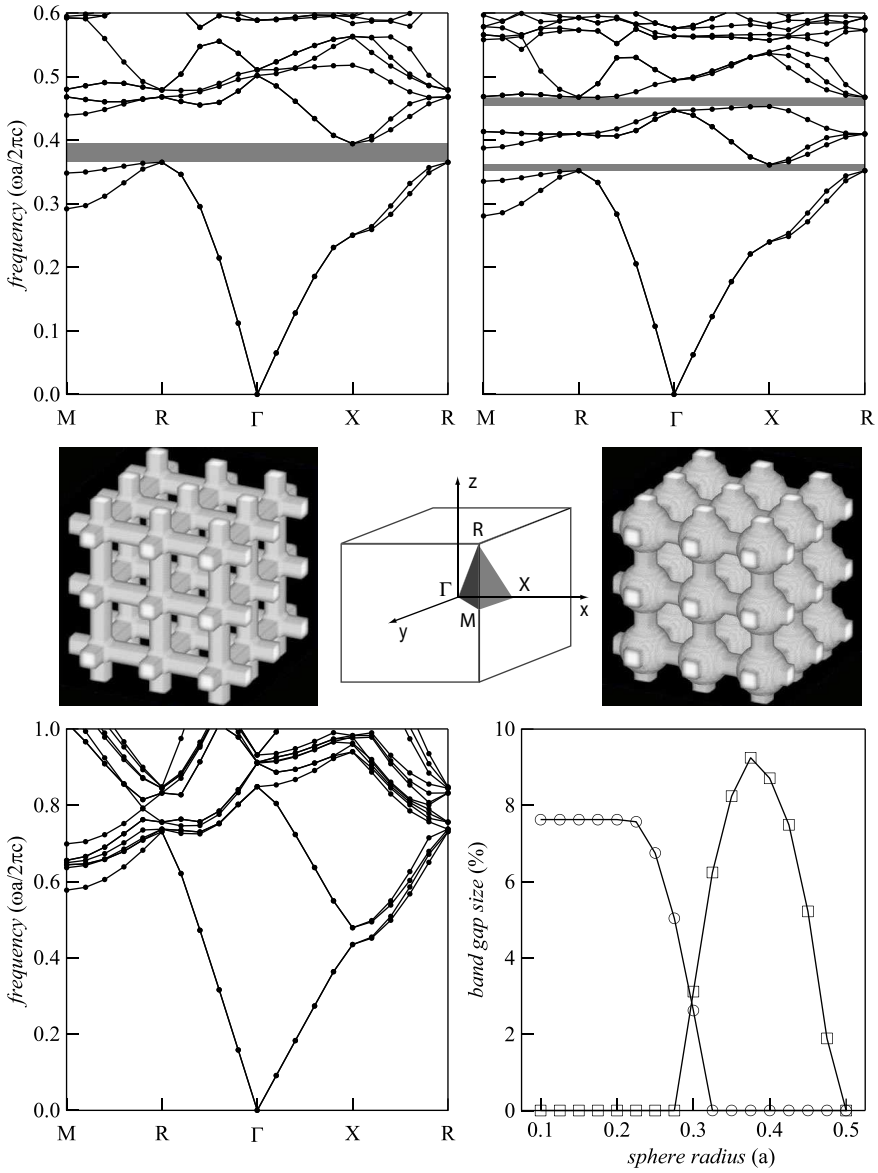

Figure 2.6: Photonic band structure for cubic lattices made of rectangular rods with (top-right) and without (top-left) spheres at the intersection points (ϵ= 13). Middle: corresponding lattice structures and the first Brillouin zone, with high symmetry k-points marked. Bottom-left: band structure for a crystal made out of PMMA. Bottom-right: the influence of the sphere radius on the size of the second (open circles) and the fifth (open squares) band gaps for the cubic lattice of silicon spheres and rectangles.

As such, it is possible to open a complete 3D bang gap using structures fabricated in a single EBL writing step. The only requirement is that a high-dielectric material for fabrication is needed. Calculations show that silicon is a good candidate. The main problem is to reliably fill the template with silicon without compromising the template structure (PMMA template are relatively sensitive to temperature and operating chemistry). Presumably, using CVD or ALD methods this could realized, though experimental verifications are required. How about the band-gap in the as-fabricated PMMA templates? Due to the low dielectric constant, the complete band gap is absent. Yet, as it can be observed from the band diagram, a gap exists in the Γ - X direction or physically, in one of the direction parallel to the rectangular rods. In Figure 4.7 you will see some colored patterns. They were made using the developed RDM-3D-EBL on a multilayered resist stack by varying the exposure doses and lattice spacing from pattern to pattern. Probably, it is premature to attribute those colors to a photonic band gap as the environmental configuration in which they were made does not allow for direct evidence. Nevertheless, it is possible to achieve that and some further work can be done in order to improve that. As a summary to this section, we can say that porous materials can be (and are) used as photonic crystal structures to control the flow of light. The self-organized materials are extremely useful as they allow for the fabrication of photonic structures on very large areas. Their main drawback is the momentary lack of reliable techniques to create various kinds of defects, providing "plenty room" for EBL and micro- and nano-fabrication techniques.

2.2.2 Plasmonics

Plasmonics enables the control of light with sub-wavelength metallic structures. It offers an opportunity to merge photonics and electronics at nanoscale dimensions, and to realize very large scale electronics and photonics integration. Already well known applications are the surface plasmon resonance and surface enhanced Raman spectroscopy. Among emerging applications are: superlenses (or sub-wavelength lithography), cloaking devices, negative refractive index materials, optical antennas and twizzers [53]). We will briefly discuss here only (i) useful materials for plasmonics (ii) periodic structures, preferentially fabricated using porous materials or self-assembling methods.

The interaction of metals with electromagnetic fields can be also understood in a classical framework based on Maxwell's equations (see Section 2.2.1.1). The differences arise from the metallic nature of matter in this case compared to the dielectric medium treated previously. Hence,

J and ρ can no more be neglected. Over a wide frequency range, the optical properties of metals can be explained by a plasma model, where a gas of free electrons moves against a fixed background of positive ion cores. The optical response of metals (including as well other materials) in the far infrared and mid infrared spectral range (or bellow the threshold of transitions between electronic bands) can be described fairly well by the classical oscillator Drude model. However, this model is not adequate for the description at high frequencies. For example, in the cases of gold and silver, the most important metals for plasmonic studies, this validity breaks down at the boundary between the near-infrared and the visible [54]. Above their respective band edge thresholds, photons are very efficient in inducing interband transitions, where electrons from the filled band bellow the Fermi surface are excited to higher bands. The main consequence of these processes concerning surface plasmon polaritons is an increased damping and competition between the excitations at visible frequencies. To overcome the limitations of the Drude model several Lorentzian terms to account for the interband transition have to be added [55]. The dielectric function of the free electron gas will look like:

$$\epsilon(\omega) = \epsilon_\infty - \frac{\omega_p^2}{\omega^2 + i\gamma\omega} + \sum_{j=1}^{n} \frac{A_j}{\omega_j^2 - \omega^2 - i\gamma_j\omega}$$

where the sum term is a Lorentz-oscillator term with A_j, ω_j and γ_j accounts for oscillator's strength, center frequency and damping, $\omega_p^2 = \frac{ne^2}{\epsilon_0 m}$ is the plasma frequency of the free electron gas, ϵ_∞ originates from the residual polarization due to the positive background of the ion cores.

Interesting, a similar equation will be used in Chapter 4 to find the optical constants of polyaniline in the protonated (doped) state. We have not yet reached the high infrared reflection and negative values for the real part of the dielectric constant specific of metallic phase. Nevertheless, metallic transport in polyaniline exists. This was demonstrated by Lee *et al.* in a recent paper by performing temperature dependent resistivity measurements [56]. The metallic nature was also confirmed by reflectance measurements and data modeling using the Drude model. They found that the reflectance dropped throughout the mid-infrared to a minimum at 1.4 eV, indicative of the free-carrier plasma resonance in near-infrared, characteristic of a metal[11]. Then why not to use polyaniline instead of metals for the above mentioned plasmonic applications? Mainly because to produce surface plasmon effects we need to know how to process metals at the nanoscale, a fact that is not valid for polyaniline.

[11]For most metals, the plasma frequency is in the ultraviolet regime, 5 - 15 eV explaining why most of them have the shiny reflection in the visible.

As you will see in Chapter 4 a high structural control over polyaniline nanostructuring can be achieved which may encourage research in this field.

Many of the optical range plasmonic effects arise in nanoscale metallic structures. Control over the propagation of SPP[12] or plasmon waveguides is much alike the photonic crystals waveguides or slabs. Control over the transmission of light through sub-wavelength apertures via plasmon excitations is of great importance as well. Fundamentally, they rely on completely different approaches that can be sometimes easier to transpose experimentally. As we saw in the previous Section, photonic crystals have to be designed in order to bulk confine the light hence, bulk microprocessing is needed. As their name states, the propagation of SPP is a surface confined phenomena and requires only surface processing. Metal surface bumps or gratings are already enough to achieve the SPP confinement. Ordered metallic dot and line arrays, height modulated structures and holes in thin-metal films are only few examples to be cited. A SPP Bragg reflector was demonstrated by Ditlbacher consisting of ordered particle arrays on a metal substrate [57]. This concept can be further extended to create band gaps or subsequently waveguides for SPP [58]. SPP waveguiding is possible to achieve also along metal stripes or Y-splitters though their fabrication is not related to porous materials [59].

Other class of artificial materials with controlled photonic response are metamaterials. Metamaterials are structured photonic media with unit cells smaller than the wavelength of light and unlike natural substances, enable magnetism to be achieved at optical frequencies. As for photonic crystals, these unit cells can be regarded as the elementary building blocks of an artificial material, in analogy to atoms in conventional materials. The ring is the "leitmotif" in plasmonics with large applications for surface enhanced spectroscopies such as surface enhanced Raman spectroscopy, surface enhanced infrared absorption and localized surface plasmon resonance [60]. A structure with reach physics is the SRR[13], which in the simplest form is a ring with a gap. The SRR structure can exhibit negative permeability and combined with wire or rods

[12]Surface plasmon polaritons are electromagnetic excitations propagating at the interface between a dielectric and a conductor, evanescently confined in the perpendicular direction arising via the coupling of the electromagnetic fields to oscillations of the conductor's electron plasma.

[13]A magnetic flux induces a magnetic moment in a SRR via the induction of currents flowing in circular paths. The structure acts as a sub-wavelength LC circuit. The magnetic permeability μ will then exhibit a resonance at $\omega_{LC} = 1/\sqrt{LC}$ and for frequencies above that, μ will be negative.

arrays should exhibit a frequency region where both $\epsilon < 0$ and $\mu < 0$ implying negative refraction index [61–63]. Recently, the group of Giessen have realized new types of three-dimensional photonic metamaterials and stereometamaterials at optical frequencies by stacking multiple layers of SRR arrays [64, 65].

As you will see in Section 4.4.3, there are many ways to fabricate nanostructured gold-polyaniline composites. For instance, shadow metal evaporation parallel to the main axis of diameter modulated nanowires produces stacked self-aligned gold-rings. It is possible to obtain 3D SRR arrays just by tilting slightly the main axis of the sample, where the SRR size and vertical spacing can be easily accessed through adequate RDM-3D-EBL processing. By carefully tuning those parameters it is possible to achieve $\mu < 0$ in these potential metamaterials. Now, if we will dope polyaniline and render it metallic, then ϵ as well can be turned on the negative side and we may obtain a structure that will exhibit negative refractive index. Dedope the polyaniline or chemically modify it and the property will be destroyed. And all of that in a reversible way. For the moment, we are relatively far from observing these phenomena, nevertheless, we propose the methodology for their physical realization.

2.3 Nanowire electronics

Another way to use the porous materials is to exploit their confined media to build 1D electrically active devices. In the following we will review some of the template confined fabrication techniques as well as the characterization techniques with main emphasis on single-nanowire devices. The field is so reach that we will don't have space even to briefly describe it[14].

2.3.1 Template confined fabrication

Electrochemical deposition is probably one of the most used techniques for the template confined fabrication [66]. It consists in electroplating the desired material inside the void channels. The structural parameters are transfered with high fidelity. Due to the rich chemistry and well established electrochemical protocols complex systems with precise composition and structural engineering can be fabricated. Simple metallic, organic, semiconducting or hybrid multi-layered nanosystems

[14] Make a simple comparison with optics. We can electrically characterize the insulators, obtain many parameters (leak currents, capacitance, breaking voltage), make an extended analysis and even write papers. An opaque material basically does not transmit light and that's all.

(wire, rods and dots) have been synthesized and characterized using this technique [25,26,29–31,67–72,72–76]. As for templates, almost all of the materials described in Chapter 1 have been used. This type of processing requires a conductive layer (typically a metal film) on one side of the porous membrane acting as working electrode during the electrodeposition. Relatively large plating areas are required in order to monitor the process and ensure reproducibility[15].

Confined synthesis is another option for the low-dimensional structuring. It includes chemical and physico-chemical synthesis or deposition methods. Non-, poor-conducting (polymers, metal and semiconductor oxides) and materials difficult to realize otherwise (carbon nanotubes, III-V semiconductors) are fabricated using this approach. Direct chemical synthesis (polymerization, precipitation, pyrolysis), ALD, CVD and PECVD growth are only few to be cited [12,13,17,18,74,77–82]. Contrary to the electrodeposition, here are no limitations in size or quantities of fabricated materials. Single as well as a large number of nanostructures can be achieved in the same batch process. The limitation mainly concerns the compatibility between the porous matrix chemical and physical stability and the deposition method. With this respect, AAO templates are the most used as they can withstand temperatures as high as 650°C and have good mechanical and chemical resistance.

Wetting or infiltration of soft materials into the pores allows the nanoscale structuring of materials that are difficult to accomplish using previous methods. Melted polymers and liquid crystals as well as various solutions of small molecules have been tested and provided valuable results [83–89]. Infiltration is based either on pressure injection or capillary induced mass transport. Again, there are no limitation in quantity of fabricated nanostructures. The main restriction is the size of the pore and the capability to fill them entirelly. Also, removal of the residual material on the surface of the template is required.

Physical mask etching and deposition is a very powerful technique to nanofabrication using porous templates [84, 90–92]. It has almost no limitations with respect to the material to be patterned, the processing scale and quantity. In stencil mask deposition, the evaporated material travels (penetrates) through the pores and is deposited on the substrate. Removal of the matrix is required to access the nanofabricates (an inverted morphology is obtained). The main drawback is the clogging of the pores with the incoming material and hence, low aspect ratio (tapered nanoposts are obtained). Etching using porous materials as masks transfers the pattern with the same morphology to the substrate.

[15] Electroless plating can avoid this limitation.

Anisotropical etching (RIE, ion milling) is preferred and the main limitation here is the etch resistance of the mask. These techniques also require good alignment of the pores with respect to the substrate.

2.3.2 Characterization techniques

A major inconsistency in employing porous materials for nanoelectronics is that using present knowledge we are exploiting only a small part of the potential provided, namely, the reduced diameter of the channels, and for some application, the elevated aspect ratio as well. High-patterning density, structural ordering and exceptional mechanical, chemical and optoelectronic properties are simply ignored[16]. A great effort was focused on the mass integration of template fabricated nanowires into operational devices with few reliable proposals for parallel processing at the moment (see Fig. 2.7). We don't want with the following descriptions to convince you that our work is the best in the field. Neither that in the next PC you will buy there will be circuits statistically routing single polyaniline nanowires devices. This Section just gives an idea of the current status and the reader will judge himself where our work is situated.

2.3.2.1 Template-embedded methods

Within this methods we will include not only those approaches that keep the nanowires (or generally, fabricated nanostructures) embedded in the original template but generally, approaches where the as-fabricated structural ordering is preserved (Fig. 2.7 (**a**) - (**d**)). These techniques require either self-sustained or substrate supported porous membranes. One of the most powerful method is the bulk characterization of fabricated nanostructures [25, 93, 103, 104]. It basically reduces to build macro-scale electrodes on both sides of the template and measure large number of nanostructures (typically 10^5 - 10^{10}). The first contact is actually the working electrode for the electrodeposition or the seeding layer for the various types of growth and is made of a thick metal film.

[16] One can found in literature many cases when *high-patterning densities* (exceeding 10^{11} per inch^2) obtained using porous materials with *high potential for applied nanoelectronics* are strongly emphasized and actually only **1** single nanowire is somehow electrically contacted on the substrate, of course, implying the destruction of the template and laborious work to re-position and build electrical connections (the total area including the nanowire and electrodes being of order of few μm^2). Where are the rest of $10^{11} - \mathbf{1}$ it is not clear. Probably after staying some time in a well labeled flask they are thrown away. As for the occupied area of the new "nanodevice", you loose 3 to 4 orders of magnitude in patterning density for each occupied μm^2. Isn't a little bit early to etiquette them as nanomaterials for nanoelectronics?

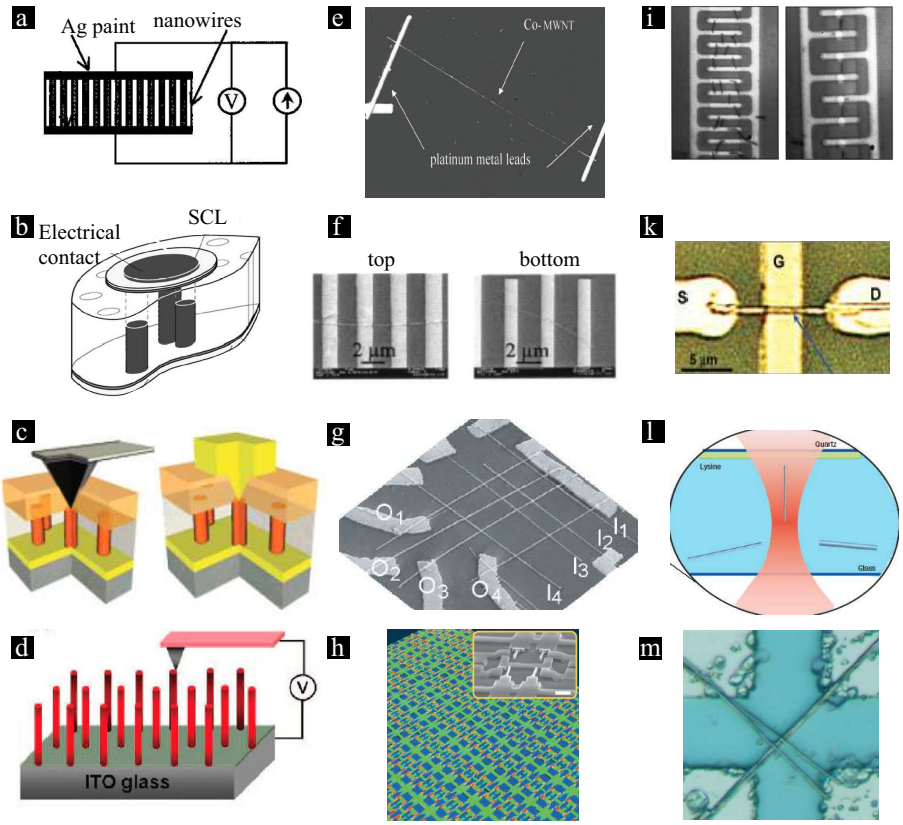

Figure 2.7: (**a**) Bulk electrical connection using conducting silver paint. From [93]. (**b**) Measuring single nanowires using self-contacting techniques. From [94]. (**c**) Contacting AAO embedded single nanowires using nanoindentation. From [67]. (**d**) Current sensing AFM characterization of single polypyrrole nanowires fabricated using block copolymer templates. From [25]. (**e**), (**f**) Top and bottom definition of electrodes using lithography. From [95, 96]. (**g**) SEM image of a 4×4 crossed-nanowires field-effect transistor decoder. From [97]. (**h**) 3D height image collected by confocal scanning laser microscopy on an array of 3D SWNT. The inset shows a SEM image of the 3D structure. From [98] (**i**) SEM images showing arrays of electric field assembled nanowires. From [99]. (**k**) 3-terminal nanowire device obtained combining electric-field assembly and lithography. From [100]. (**l**) Schematic of the optical trapping experiment using single-beam optical-tweezers system. From [101]. (**m**) A junction of crossing nickel nanowires on ferromagnetic electrodes obtained using magnetic field alignment. From [102].

The second electrode is usually made by metal evaporation using shadow masking with relatively large apertures (few tens of μm^2) or simply using a droplet of conductive paste deposited on the sample surface. It is very useful as it allows fast screening of the electrical behavior of novel synthesized systems and, as it requires large number of nanostructures, the synthesis is facilitated as well (mainly for electrochemically prepared samples). The drawbacks are related to the averaging of the measured properties, no advantage from the high-structural density and ordering as well as difficult scale-down implementation.

A slightly modified approach is the use of a self-contacting layer in the above mentioned configuration [94]. This method is restricted to electrochemical processing. First, a metal film is evaporated on the free sides of the porous membrane (the other being already covered with the conductive impermeable film). The metal film should be thin enough to avoid clogging the pores, yet thick enough to be electrically continuous. During the subsequent electroplating, as soon as the first emerging nanowire(s) will contact the self-contacting layer, the growth of the other nanowires is interrupted, by favoring the formation of a film of the deposited material on this contacting layer. This method enables the electrical connection of a single nanowire. If working on large areas, low pore densities are preferred. The process is scalable and we have used a modified version to locally restrict the number of contacted from a statistically grown bunch of nanowires (see Section 3.5).

Single-ion-track etched templates were used for single nanowire synthesis and characterization [105]. This is an ingenious method to control and characterize single nanostructures though, due to the relatively increased experimental protocol, it is difficult to scale-down the technology or to integrate it into mass production. A similar in concept approach is presented in Section 4.5 where single polyaniline nanowires are grown and circuit-integrated in parallel.

More recent techniques are based on the use of SPM probes to isolate and interrogate single nanostructures fabricated using porous materials [25,67,68,84]. Despite the fact that some of them require removal of the template mask for subsequent characterization, the structural integrity is preserved. Basically, after mass template fabrication, a SPM probe is either used to directly characterize or to isolate and build subsequently electrical connection for one single nanostructure. SPM probes have thus been used in nanoindentation, current-sensing or in piezoresponse modes. The process is readily scalable and offers the potential to truly exploit the benefits provided by porous templates. It will be shown in Section 3.4.3 that it is possible to operate in parallel thousands of SPM tips and statistically perform mainly single nanostructures interrogation.

2.3.2.2 Template-free approaches

Within this class, we include techniques where the as-fabricated structural integrity is perturbed (Fig. 2.7 (**e**) - (**m**)). As an intermediate step the removal of the nanowire from the original substrate and dispersion in a carrier media is performed. Probably one of the most employed is the top-contact definition using lithographic methods [95, 96, 103, 106–108]. The nanowires are arbitrarily transfered from the suspension to a desired substrate, their position with respect to some alignment marks is acquired and then, lithography and metal deposition is performed to build the electrical connections. This platform is widely used for single nanowire characterization. It lacks the ability of parallel integration and may require laborious experimental work. Dispersion of nanowires on top of pre-fabricated electrodes can be also used.

Position controlled dispersion can be done using flow alignment techniques [97, 98, 109–114]. Shear forces associated with a rapidly moving fluid, positions the nanoscale objects in the direction corresponding to the flow vector of the fluid. Air or liquid flow alignment have been demonstrated. The technique is very powerful as it allows multi-layered alignment of nanostructures with controlled directionality. The group of Prof. C. M. Lieber advanced significantly the field and by demonstrating rationale logic gates, computation and other circuits including sensing devices made out of fluid assembled nanowires.

Electrical trapping exploits the dipole arrangement (and hence the nanowire axis positioning) in an alternating high-electric field generated between two microelectrodes [99, 100]. Magnetic nanowires have can be positioned using externally applied magnetic fields [102, 115]. Infrared single-beam optical traps were used to individually trap, transfer and assemble high-aspect-ratio semiconductor nanowires (diameters as small as 20 nm and aspect ratios of more than 100) into arbitrary 3D structures in a fluid environment [101]. Mechanical manipulation on a surface of nanowires can be also done using SPM probes [83].

When the parallel processing is possible, the described techniques and procedures are too heavy to handle at large scale. Most of them are designed to operate only at the laboratory level. As well, the occupied area of the new devices is much more larger than the as-synthesized specific area. Even for the techniques using SPM tips for electrical interrogation, thus preserving the patterning density, a preliminary alignment step was performed in order to ascertain for single-object characterization. We will show later that this is not compulsory and a high probability (close to 100%) to land the tip on a single nanostructure can be obtained purely statistically. As for the necessity to fabricate or not large number

of nanostructures and then spend time to "separate" them, we will show that with some systems this can be done by patterning, growing and processing a given set of single nanowires.

2.4 Nanowire-based photonics

Today's ability to manipulate photons is in many ways in its infancy, compared with how we can manipulate electrons. For example, the all-optical switches are still very rudimentary and bulky, and the size of an optical integrated circuit is most often in the millimeter or centimeter range rather than the sub micrometer dimensions common in electronic technology. For the control of the electron flow we don't need a perfect crystal. In fact, we are using everything else but not perfect crystals in modern electronics (amorphous and polycrystalline conductors and semiconductors are at the basis of present technologies). For light, we are still at the point where a perfect lattice is needed.

Nevertheless, we are starting to learn how to exploit light at the nanoscale and out of the nanoscale objects. $III-V$ axial or radial heterostructures, carbon nanotubes as well as many other nanoscale conjugated systems (polymers, liquid crystals) show great promises for the fabrication of nanoscale integrated optoelectronic systems [83,113,116–119]. Many groups have achieved effective coupling between the light emitting nanostructures (nanowires, quantum dots) to photonic structures to study the light emission inhibition or guiding. Photonic crystal and quantum dot technologies for all-optical switches and logic devices are believed to be the future for ultra-fast optical digital processing system [106, 120].

We can grow many types of nanostructures using the void channels of the templates. We can also use the void channels to build photonic crystals. Isn't this a direct way to fulfill the ambitious task of nanowire-based photonics? Imagine future devices where on the different ends of a waveguide (made of a porous material), light-emitting and light-collecting (or sensing) nano-devices are created using the same porous material yet, this time, exploiting only one single nanopore. Place a "tunable" photonic element somewhere in between and you have long years of fruitful research to do. The possibilities are vast. Yet, we have still some work to do in order to achieve and reliably control that. In the following you will see two different design concepts that provide the same result: cross-bar nanowire devices embedded in dielectric matrices with potential for next-generation optoelectronic nanodevices.

Chapter 3

AAO templates

> Pour une passoire, ce n'est pas un défaut d'avoir des trous.
>
> *Proverbe libanais*

3.1 Overview

The drive toward superior materials for nanotechnology applications at the frontier of the knowledge is usually hampered by their stability and the difficulties to preciselly control and manipulate their structural and physical properties. Today, the research spotlights are focused on self-organized nanostructured materials with a periodic arrangement of nanopores. Much interest has been put on the hexagonal densely packed nanoporous structures obtained by anodization. The electrochemical formation of self-organized nanoporous structures produced by the anodic oxidation, besides aluminum, has been reported for only a few materials such as Si [121, 122], InP [123], Ti [124, 125], Nb [126], Hf [127] and Sn [128]. During recent years, the anodization of aluminum, due to its great commercial significance, represented one of the most important and widespread method used for the synthesis of ordered nanostructures consisting of close-packed cells in a hexagonal arrangement with nanopores at their centers. However, full technological benefit from the provided architectures is missing. The major drawback that restricts their pervasive integration is the mismatch between their morphology and today's technological ability.

In this Chapter we will deal with porous anodic aluminum oxide templates. A full processing technology, enabling parallel integration of template synthesized and embedded nanowires, is described. A short

overview of the anodic oxidation of aluminum, fabrication methods and some important applications is intended to introduce the reader to this field. The emphasis is put on the micro- and nano-processing technology elaborated during this thesis allowing for an unprecedent level of integration of nanoporous alumina templates into the microfabrication technology. Alumina structuring, nanowire decorated microelectrodes, single nanowire growth resolution together with other structuring approaches are converged to build up devices. By means of a statistical processing method, we show that ultimate resolution structuring of virtually any type of nanoporous template is possible.

3.2 Anodic oxidation of aluminum

Electrochemical oxidation of aluminum is used since almost a century for protective and/or decorative coating of aluminum products. It has been found that certain electrolytes used for the anodization of the aluminum produce compact oxide layers while others produce porous ones. The first characterization of these oxide layers dates back to the early 50's [129]. A nanoporous structure is formed when a competitive equilibrium is established between electrochemical oxide growth and chemical dissolution of the oxide in certain acidic electrolytes [130, 131]. Although the anodization process has been extensively studied, the involved complex processes are not yet fully elucidated. The simplified view of the anodization mechanism can be represented as described in the following [132, 133]. It is not fully clear which oxygen carrying anion species, O^{2-} or OH^{-}, is involved in the anodic process. The OH^{-} ions are generated in the anodizing electrolyte from water by simple splitting, or by the cathodic reduction of water and dissolved oxygen following reactions 3.1 and 3.2. On the other hand, O^{2-} ions can be formed at the electrolyte/oxide interface from adsorbed OH^{-} ions by oxygen vacancy annihilation, simple splitting of water at the interface, or from water by interaction with adsorbed electrolyte anions. Anodic polarization of aluminum in the acidic electrolyte leads to the amorphous oxide film growth according to reactions 3.3, 3.4 and 3.5. The main contribution to the anodic current is given by the reaction 3.6.

The evolution of oxygen at the metal/oxide interface was reported as well for the aluminum anodization in various electrolytes accounting for reactions 3.7, 3.8 and 3.9. The formation of oxygen bubbles within anodic alumina, according to reaction 3.9 in the vicinity of the metal/film interface, can proceed due to the presence and compositions of impurities or second-phase particles [133, 134]. It was also suggested that oxygen

evolution is directly linked to the growth of the pores in alumina and can be used for testing transition form barrier-type to porous-type coatings [132]. The anodic process is further complicated in the presence of electrolyte anions susceptible to oxidation. Recently, a self-organized process that occurs during the anodization of aluminum in acidic electrolytes has become one of the most frequently employed method for the synthesis of highly ordered nanostructures.

$$H_2O + 2e^- \rightarrow 2OH^- + H_2 \tag{3.1}$$
$$O_2 + 2H_2O + 4e^- \rightarrow 4OH^- \tag{3.2}$$
$$2Al^{3+} + 3H_2O \rightarrow Al_2O_3 + 6H^+ + 6e^- \tag{3.3}$$
$$2Al + 6OH^- \rightarrow Al_2O_3 + 3H_2O + 3e^- \tag{3.4}$$
$$2Al + 3O^{2-} \rightarrow Al_2O_3 + 6e^- \tag{3.5}$$
$$Al \rightarrow Al^{3+} + 3e^- \tag{3.6}$$
$$2H_2O \rightarrow O_2 + 4H^+ + 4e^- \tag{3.7}$$
$$4OH^- \rightarrow 2H_2O + O_2 + 4e^- \tag{3.8}$$
$$2O^{2-} \rightarrow O_2 + 4e^- \tag{3.9}$$

3.2.1 Nonporous anodization

Aluminum forms instantly a barrier oxide layer when in contact with air. This compact barrier layer has a thickness of 1 - 2 nm and withstands electric field as high as 1 V/nm. It also protects the aluminum from further corrosion. A strongly adherent, non-porous oxide layer could be also formed by anodizing aluminium in neutral solutions (pH = 5 - 7) in which the anodic oxide layer is not chemically affected and stays practically insoluble. The group of electrolytes used for this barrier-type film formation includes boric acid, ammonium borate, ammonium tartrate and aqueous phosphate solutions, as well as tetraborate in ethylene glycol, perchloric acid with ethanol and some organic electrolytes such as citric, malic, succinic, and glycolic acids [135]. The main applications of nonporous alumina are restricted to protective, insulating or capacitive coatings.

3.2.2 Porous anodization

For anodic porous alumina, the film growth is associated with localized dissolution of the oxide, as a result of which pores are formed in the oxide film. Although long time it was generally accepted that the nature

of an electrolyte used for anodizing aluminum is a key factor which determines the type of oxide grown on the surface, recent experiments have misconfirmed that. Porous anodic layer formation has been reported for various acidic electrolytes such as malonic [136], tartaric [137], citric [138, 139], malic, glycolic [140] and even chromic acid [141]. Anodic porous oxide films have been also obtained in unpopular electrolytes, including a mixed solution of phosphoric and organic acids with cerium salt [142], or in a mixture of oxalic acid, sodium tungstate, phosphoric and hypophosphorous acids [143]. The porous oxide film was also observed for anodization carried out in a fluoride-containing oxalic acid electrolyte [144]. The formation of nanopores by self-organized anodization has also been studied in a mixture of sulfuric and oxalic acids [145]. In fact, these results show that there is strict rule in the selection of electrolytes for the formation of barrier or porous films during the anodization of aluminum. Moreover, the transition from a barrier-type film to a porous oxide occurs easily; the anodizing time is responsible for the development of a porous oxide structure on a previously formed barrier-type film. Some excellent reviews on barrier-type oxide films have been published [135, 146]. Details of the porous oxide layers were equally reported[1] [135, 150].

It is widely recognized that pore formation is attributed to the thermally assisted, field-accelerated dissolution of oxide at the oxide/electrolyte interface. On the other hand, the growth of oxide occurs mainly at the oxide/metal interface for typical acidic electrolytes including sulfuric, phosphoric, and oxalic acids. The growth of porous alumina involves the inward migration of oxygen-containing ions (O^{2-} or OH^{-}) from the electrolyte through the barrier layer, and the simultaneous outward drift of Al^{3+} ions across the oxide layer.

Pore's growth is accompanied by a phenomenon of self-ordering towards perfectly ordered honeycomb nanoporous structure (Fig. 3.1). Highly-ordered nanostructures are characterized by a set of parameters: pore diameter, wall thickness, barrier layer thickness and interpore distance. The uniform pore diameter, which is easily controllable by altering the anodizing conditions, can range from a few nanometers to hundreds of nanometers. The depth of the fine parallel channels can be

[1]Note that a fiber-like porous oxide morphology has been reported for the anodization of aluminum in chromic [147] and sulfuric acid [148]. A completely different morphology of the oxide layer formed by anodizing aluminum in oxalic or sulfuric acid has been observed by Palibroda et al. [149]. Interestingly, a cross-sectional view of an anodized layer exhibits hemispherical and spherical patterns that appear during anodization as a result of simultaneous gas evolution and the formation of a gel-like, nascent oxide.

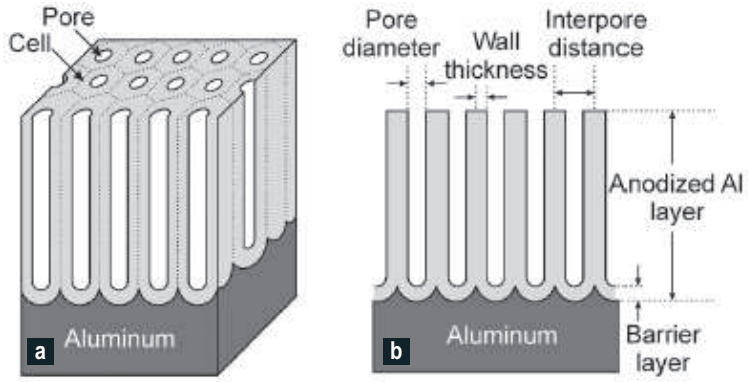

Figure 3.1: Idealized structure of anodic porous alumina (**a**) and a cross-sectional view of the anodized layer (**b**).

as high as 100 μm, a characteristic which makes anodic porous alumina one of the most desired nanostructures with high aspect ratio and high pore density. During the steady state of oxide growth, current density under potentiostatic conditions or anodizing potential under galvanostatic anodization of aluminum remain almost unchanged. Systematic studies have shown that the degree of the pore ordering could be influenced by the preparation conditions, i.e. anodization time, electrolyte type and its pH, applied voltage and temperature [151]. Perfect regularity could be obtained by pre-patterning the aluminum surface before anodization with various techniques like e-beam lithography or nanoindentation [152]. The process of anodization has been extensively described using semi empirical models. For instance, the pore diameter and the interpore distance depend linearly on the anodization voltage: $D_p = \lambda_p \times U$ and $D_{int} = \zeta_{int} \times U$, where D_p and D_{int} are the pore diameter and interpore distance respectively and λ_p and ζ_{int} are the linear regression correlation parameters. ζ_{int} was found to be dependent on the anodization regime and electrolyte chemistry while λ_p less or not at all (see Chapter 1 in [153] for an exhaustive description). For the as-prepared alumina, the obtained pore diameter varies between 15 and 50 nm depending on the anodization conditions. It can be further increased through the so called enlargement or widening step and the achievable diameter is limited by the interpore distance. Contrary to the pore diameter, once anodized, the interpore distance could no more be changed and typical values are ranging from 50 up to 500 nm. The ability to modulate the interpore distance or pore diameter has been used to de-

sign and fabricate novel types of hyperbranched and 3D pore-modulated AAO templates. Meng *et al.* have exploited these properties to build hierarchically branched nanopores, nanotubes and nanowires [74]. They have gradually decreased the anodization voltage and thinned the barrier layer before further anodization and then fabricated a large variety of multibranched architectures. Finally, they functionalized them by CVD with carbon nanotubes or electrochemical deposition of metallic nanowires. A different approach was used by Lee and co-workers. Using pulse-anodization of aluminum they achieved a structural engineering of nanoporous AAO and fabricated diameter modulated nanochannels or delaminated single AAO slabs [84, 154].

Common alumina membranes obtained by anodic oxidation of aluminum foils could be supported on the remaining non oxidized aluminum substrate or self-supported if they are removed from this substrate. The minimal thickness of the self-supported membrane is limited to $\sim$ 20-50 μm due to brittleness. The membrane can be removed, either by selective chemical etching of aluminum, by diminishing stepwise the anodization voltage [131], or by reversing the applied voltages [155]. For supported nanoporous membranes on aluminum, despite the high melting point of Al_2O_3 ($\sim$ 2050°C), the highest working temperature is given by the melting point of aluminum ($\sim$ 658°C). Other limiting factors are the recrystallization temperature of the alumina ($>$ 400°C) and its phase transformations ($>$ 820°C) which can cause mechanical deformation of the self-supported membranes. These drawbacks limit the use of nanoporous alumina as templates for processes such as CVD, where high temperatures are needed. They also restrain thermal treatments of the nanowires arrays which are synthesized by electrochemical methods thus limiting severely the advantages of this low temperature synthesis when these treatments are needed.

To conclude, the main features of alumina templates are: the ordered arrangement of nanopores in a high density structure (10^9 - 10^{12} pores/cm^2) and the ability to control the interpore distances by the anodization voltages. The pore diameter is also related to the anodization voltage but it can be easily increased by etching: the typical ranges is between 5 and 300 nm in function of the preparation conditions.

3.3 AAO microstructuring

Although highly-ordered AAO templates are strongly desirable, their fabrication it is not always compatible with the intended application. For instance, a major problem could be related to the fabrication of sup-

ported AAO templates. Here we refer to the fabrication of supported AAO membranes on substrates other than aluminum. For example, glass, Si, SiO_2 covered with thin metal films or patterned substrates bearing basic metal electrodes or prefabricated circuitry. For this type of systems, the high-ordering is relatively hard to achieve. Perfect ordering in AAO is done using additional aluminum surface preparation procedures. Electrochemical polishing, two-step anodization and aluminum surface pre-patterning are the most used techniques. The first two methods are proceeding through the stripping of a sacrificial, relatively thick (of the order of micrometers), aluminum layer. Applying them to a supported aluminum layer can be quite difficult[2].

This is why throughout this Chapter, partially ordered, 1 - 2 μm thick, supported AAO membranes have been used. They have been fabricated on various substrates with different structural complexity. Pore ordering was not a concern and as it will be shown it barely influenced the reliability of the fabricated devices. However, for the devices requiring a high-ordering degree, this issue has to be solved. Optimization of deposition procedures in order to start with a thick (more than 10 μm) aluminum with a mirror-quality surface is under way and preliminary results are promising. Nevertheless, if the process works in the worst conditions[3] then, there should be no problems in transposing the technology to a highly-ordered structure. The processing philosophy will remain the same even for other active elements than metallic nanowires studied in this work. Only the growth steps and the reliability of electrical contacts (if an electrical device will be built) will need to be adapted accordingly.

[2] Initial aluminum films are typically prepared either by physical vapor deposition or sputtering techniques. Their thickness is limited to few micrometers mostly due to technical constrains (see next Section for details). Surface roughness reduction by electro-polishing or the use of pre-anodization step to induce ordering will consume massively the deposited aluminum, complicating the procedure. Surface pre-patterning could be an alternative and it was reported for already flattened substrates. In this technique either a mold bearing protrusions made out of a hard material (Ni, SiC or diamond) is impinged on the aluminum surface, or argon milling through a lithographically defined mask or focused ion beam milling are used to seed the nucleation points for pores in the desired pattern. The deposited aluminum morphology is affected when deposited on structured substrates (bearing metallic electrodes or various circuitry) and, as it will be detailed in Section 3.3.2, the best option is to have a conformal deposition (*i.e.* aluminum molds and follows the underneath profile). Adapting these techniques to 3D Al profiles will require a laborious work.

[3] Usually, reduced ordering is associated with the low quality AAO and hence, to the "worst" fabrication and operation conditions.

3.3.1 Supported AAO fabrication

The general process starts with a physical vapor deposition on a carefully cleaned substrate of a conducting underlayer. This conducting layer has a double role of serving as an anodization barrier during electrochemical oxidation of the aluminum layer, and as working electrode for further electroplating processes. It should not oxidize under anodization conditions, typically being a layer of gold or platinum. Intermediate adherence layers are used between the substrate and the conducting layer, and between the conducting layer and the subsequent aluminum layer.

Aluminum layer deposition is a critical step in the sense that small thicknesses (up to a few hundred nm) are easy to realize but thicker ones need special deposition conditions. The temperature of the substrate and deposition rate are key factors for compact aluminum layers deposition without hillock and pitting defects [156,157]. At substrate temperatures higher than ∼70°C (Fig. 3.2 (**a**)) and also at low temperatures (Fig. 3.2 (**b**)) such defects are present.

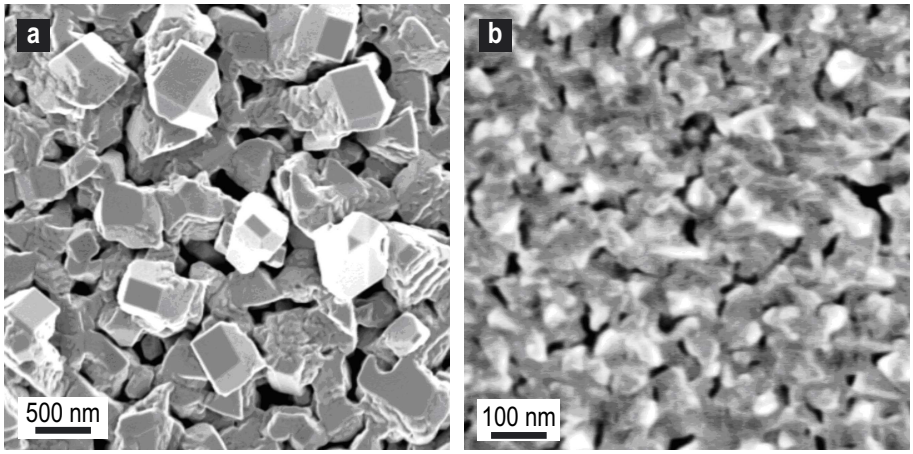

Figure 3.2: SEM micrographs from aluminum thin film surfaces, deposited by e-beam evaporation at a rate of 60 Å/min: (**a**) the substrate temperature was not kept constant but it was allowed to vary naturally from room temperature (300K) to ∼ 400 K during deposition; the total thickness was 2 μm and (**b**) substrate was cooled to ∼ 77 K; the deposited thickness was ∼ 1 μm.

When the temperature of the substrate is kept constant at about 300 K for deposition rates larger than 300 Å/min, e-beam deposited *Al* layers are compact and without defects. The deposit is polycrystalline with grain sizes (and surface roughness) decreasing with increasing de-

position rate. Experimental investigations show that high rates, up to 6000 Å/min at room temperature, permit the realization of e-beam deposited Al layers with thicknesses up to 10 μm. On the other hand, using magnetron sputtering, the Al layer thickness can reach up to 2 μm for deposition rates of $\sim$ 1000 Å/min.

Depending on the final objectives, thermal treatment at 400 - 450°C for 20 min - 4 h in Ar gas and/or electrochemical polishing in perchloric acid ($HClO_4$) containing electrolytes at constant current densities of 100-200 mA/cm^2, can follow the deposition step to increase grain sizes and decrease surface roughness. For anodization, low working temperatures of about 0°C are used. By controlling the anodization current at the end of the process, when no more metallic aluminum remains on the substrate, nanopores down to the conducting underlayer can be obtained. This allows for the subsequent growth of nanowires inside nanopores by DC electrodeposition. Pore widening to desired values follows the anodization step using mainly hydrofluoric, phosphoric or sulfuric acid solutions at temperatures ranging between 30 - 40°C. This step terminates, in principle, the supported nanoporous alumina fabrication. By controlling the preparation conditions, pore diameters can be adjusted between 5 - 350 nm and pore lengths between 150 nm - 10 μm.

3.3.2 Nanowire decorated microelectrodes

The process presented in the previous Section is a general way to produce supported alumina. For the specific realization of nanowire based devices, specific criteria are required and the fabrication is AAO fabrication is slightly modified. A full fabrication process sheet is given in the Appendix A. First, we have to work on insulating substrates: for example glass or oxidized silicon. For the simplicity, thermally oxidized silicon wafers, with a grown 300 nm thick SiO_2 layer have been used as fabrication platforms. A thick oxide layer was choosed to ensure handiness during subsequent processing steps and to avoid shorting with the underlying silicon layer. Second, for the processing and electrical characterization simplicity, patterned rather than full-wafer deposited metallic underlayers were preferred. Photolithography and physical vapor deposition were employed to pattern the metallic tracks. Mainly, they were fabricated in Au with an adhesion Ti layer. A typical lift off structuring was as follows. 1.5 μm thick image reversal photoresist[4] was spin coated on the wafer and used as masking material. An i-line UV source was employed for exposure through a laser generated photolithography mask[5].

[4] AZ 5214E, MicroChemicals GmbH
[5] Photronics Inc.

After development of the resist, a Ti and Au bilayer was deposited using electron-beam evaporation, followed by lift off in acetone. The thickness of metallic stripes was tunned in order to induce a minimal effect on the anodization and electrochemical growth process. They don't have to be too thick as to avoid protruding morphology of the aluminum layer, yet, thick enough to allow for low resistivity of the metallic tracks. A good compromise was found to be: 2 - 4 nm of Ti and 40 - 50 nm of Au. Pads design plays an essential role as well: as electrochemistry is used to grow the active parts, the metallic stripes which will serve as bottom electrodes have to be electrically connected to external wires. Next, Al is deposited covering all the surface. An intermediate 5 nm Ti adhesion layer is used and prior the metalization, a short exposure to an Ar plasma is performed (though not necessary) to remove any residual contaminants. This finalizes the pre-fabrication steps. Up to this point, the processing is classical and apparently not requiring any optimization[6]. All the steps are done on a 3-inch wafer and after AAO precursor deposition the wafer is diced in 10 mm $\times$ 6 mm chips constrained by the anodization procedure. A schematic view of the chips is given in Figure 3.3.

Single step anodic oxidation[7] of the 1 - 2 μm thick Al layer was performed in $H_2C_2O_4$ (0.3 M) at 60 V using a two electrode cell. It is believed that the surface oxide layer provides uniform pore nucleation sites at the early stage of anodization, preventing local catastrophic events such as local flow of high electrical current and defects by surface pitting. As the anodization is accompanied by a large evolution of heat, it has to be effectively removed using an appropriate electrochemical setup, maintaining the electrolyte and the substrate at 2°C during the anodic oxidation process. Eventually, the pores could be enlarged in an orthophosphoric acid solution (0.5 M) at 30°C (typically 45 min for a pore diameter of $\sim$ 90 nm). Initially, the enlargement step was realized prior to the electrodeposition though it was found to induce reliability instabilities (see further discussion about the statistic variations and top electrode issues). Subsequently, it was found that a two step enlargement gives good reproducibility: 80 - 90 % of the nominal values shortly after the anodization, and the rest priot the electroplating.

A full view of a processed chip-supported AAO is given in Figure 3.4 (**a**). The design of chips is simple: an array of stripes with external bonding pads working as BE's and orthogonally to them, an array of

[6]Only during the aluminum anodization it was found that the patterning method of the underlying electrodes is very important and is discussed further.

[7]If otherwise mentioned, these are the typical anodization parameters used in this work.

incomplete tracks for the TE's definition. Overlay alignment marks are very important as further processing needs accurate placement. As it can be observed, the anodization results in a circular supported AAO membrane surrounded by the initial, conducting Al film. To avoid electrical shortening on the BE, the anodization has to be complete, down to the Ti layer. The "good" samples displayed resistance of the order of MΩ between different BE's attributed to the semiconducting TiO_x layer. This implies that the areas which are no more in contact with the remaining Al layer will be no more able to sustain the electrodeposition (referring to the case presented in Fig. 3.4 (**a**)). Electroplating at this stage (by connecting the working electrode to the Al film) will occur only on the electrically conductive areas.

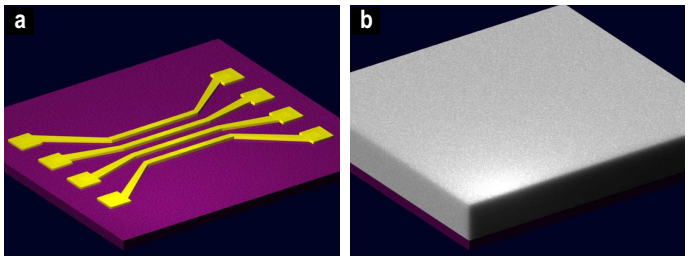

Figure 3.3: Schematized view of the pre-fabrication steps. (**a**) Bottom electrodes definition. Connection pads for top electrodes are also defined during this steps (not shown for the simplicity). (**b**) Deposition of the Al layer.

The anodic oxidation of aluminum (as well as the uniformity of electrochemically grown structures) was found to be very dependent on the quality of the fabricated electrodes. Three different cases were designated: non-patterned, ordinary patterned (in occurrence using metal lift-off) and defect-free patterned (other than lift-off, wet etching being the representative) samples. After the anodization, the quality of AAO is difficult to be visually verified, yet anomalies could be detected in the anodization curves and they will be discussed below. Moreover, to assess the quality of AAO, electroplating was used to fill the pores followed by template removal and SEM inspection. Examples of architectures fabricated on top of lift off patterned microelectrodes are presented in Figure 3.5, while the electrochemical behavior is displayed in Figure 3.4 (**b**). The analysis of non-patterned samples (Fig. 3.5 (**a**)) reveals a high degree of uniformity of the grown structures. The few detectable voids are mostly due to the coalescence of the nanowires after the dissolution of the alumina. A slightly different situation occurs in the case of patterned

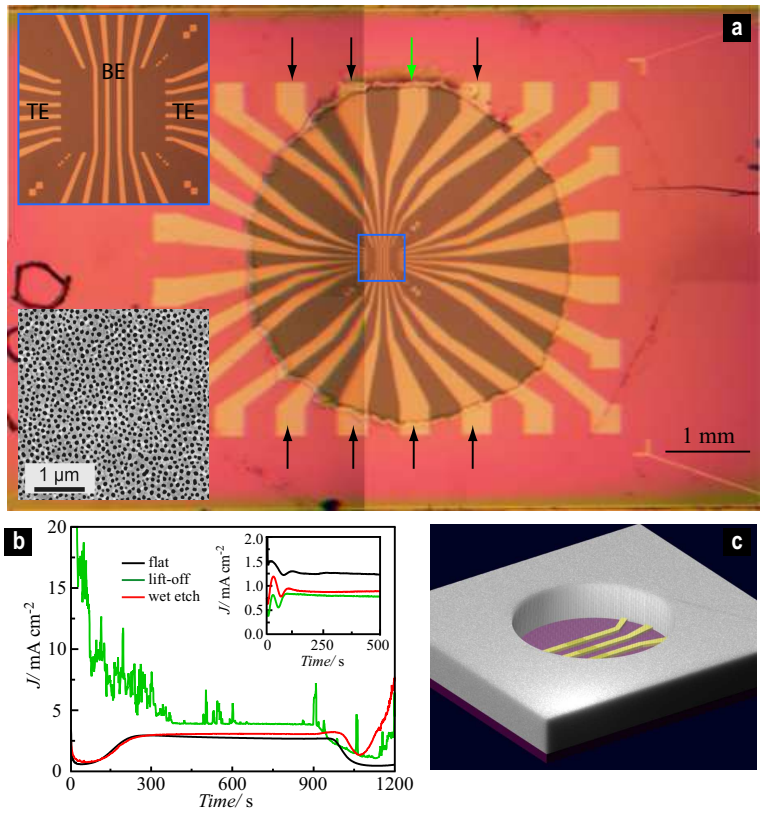

Figure 3.4: (**a**) View of an anodized chip. The middle circular area is AAO while the rest is the remaining aluminum film. Arrows are indicating working BE's. The anodization area has to be chosen in a such a way that the remaining *Al* film overlaps with the BE's. The green arrow indicates a situation to be avoided. For security (as well as for 4 - terminal measurements) each BE has 2 external pads and at least one of them had a good overlap with the aluminum layer. The blue-bordered inset shows the central area with 4 BE's and 6 precursor pads for TE's. A series of alignment marks are defined in the photolithographic step for subsequent processing. SEM inset shows the typical AAO morphology after pore enlargement. (**b**) Typical anodization curves of 1 μm thick aluminum films deposited on non-patterned substrates (black), ordinary (green) and defect-free (red) patterned samples. The anodization conditions are identical. Inset: Corresponding *Ni* electrodeposition curves. (**c**) Schematic representation of the chip after the anodization step.

substrates (Fig. 3.5 (**b**)). An increased number of void-type defects is detected in comparison to the non-patterned samples. Noticeable is the absence of parasitic nanowires outside the microelectrodes areas. The

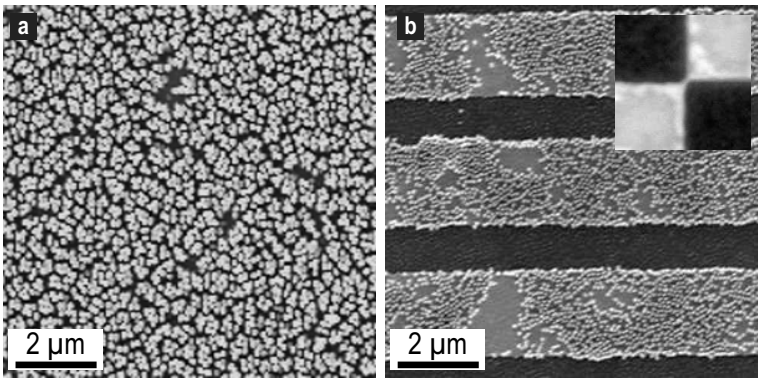

Figure 3.5: Top view SEM micrographs depicting Ni nanowires (diameter 80 nm, length 1.2 μm). The corresponding anodization and electroplating curves are shown in Figure 3.4 (**b**). (**a**) Homogeneous growth on non-patterned substrates. (**b**) Non-uniform growth on lift-off patterned microelectrodes. Inset: optical micrograph showing the aluminum residuals after the anodization.

nanowires coverage varies from 65 to 85 % of the area of metallic pads. The variation in the fabricated structures between the patterned and non-patterned substrates can be interpreted in terms of different behavior during anodization (Fig. 3.4 (**b**)). The high noise level and the modified shape of the anodization curve for ordinary lift-off patterned samples offer direct evidence for a disturbed anodization mechanism. The anodic oxidation is altered by the surface and bulk imperfections present in the aluminum layer [158]. They originate from typical lift off problems (retention, ears and redeposition) which increase the surface roughness of the aluminum. Each of them will induce a non-uniform deposition of the aluminum layer translated into an inhomogeneous anodization. The electrochemical process is stopped once the anodic current starts to increase (using a computer controlled current compliance), originating from contact between the electrolyte and the underlying conductive layer. In other words, the in-depth advancement of the pores will be irregular, some of them reaching faster the underlying conductive layer than others. This will imply that in some areas, non-anodized aluminum will still be present prohibiting subsequent electroplating (or even if taking place, stripped during the template removal step). These areas can be detected using a optical microscope having the appearance of white spots (inset to Fig. 3.5 (**b**)). Initially, we tried to overcome this step by increasing the current compliance during the anodization (from 10 - 15 to 75 mA/cm^{-2}). Although, with relatively good results, the reverse

effect was the destruction of the metallic tracks due to high anodization voltages and currents (and associated thermal effects), especially in the areas where the first pores are reaching the substrate. Eventually, pulsed anodization (anodizing followed by pause intervals), only at the end of the process, was implemented to diminish the thermal effects. The technique was left aside as a simpler solution was found by adequately processing the metallic tracks.

Improved anodization conditions can be achieved using defect-free patterned microelectrodes (red curves in Fig. 3.4 (**b**)). Two approaches have been successfully used: wet etching definition and rigorous cleaning of lift-off patterned metallic electrodes. The cleaning and the defect removal were performed by prolonged ultrasonication (15 - 60 minutes) in hot acetone in a cleanroom environment. The etch patterned samples were prepared as follows. The Ti/Au stack was electron-beam evaporated on the oxidized wafers. The same UV exposure procedure with a positive tone photoresist[8] produces an inversed image of the developed photoresist. The Au film was etched away in a home-made *Aqua Regia* solution (visual inspection was used to detect the complete removal of gold film). After the photoresist removal (in hot acetone), the wafers were shortly dipped (10 - 15 seconds) in a freshly prepared Piranha etch solution to remove the underlying Ti layer. No significant difference in anodization was found between the etched and lift-off decontaminated patterned electrodes. Yet, the later microstructure has the disadvantage of being less reproducible as the prolonged ultrasonication may destroy the metallic strips. This is why all the subsequent work was done using wet etch microstructuring of the bottom underlayer. Referring again to Figure 3.4 (**b**), important is the fact that for all the cases (flat, lift-off and wet etched samples), the electrodeposition curves are smooth and resembling, therefore supporting the supposition that the critical fabrication step is the anodic aluminum oxidation.

The improved quality of fabricated nanowire patterns using wet etch patterned microelectrodes is clearly demonstrated in Figure 3.6, presenting cross-section snapshots acquired at the different stages of the processing. Uniform growth of nanowires inside the alumina template is observed without any significant difference in their height. After the alumina removal, uniformly distributed close-packed nanowire patterns are found on the substrate (more than 95% coverage) demonstrating the overall good nucleation and filling of the pores. There are still some minor "Y-type" defects present only at the edges of the microelectrodes (Fig. 3.6 (**g**) and (**h**)). Their nature is explained by the nonparallel pore

[8] AZ 6612, MicroChemicals GmbH

initiation caused by the 3D profile of the *Al* layer. *Al* deposit follows the substrate morphology and creates a local protrusion at the edges of metallic electrodes. As the pores are nucleated perpendicular to the metallic surface, in the respective areas, they will no more be parallel and will end up with the fabrication of branched nanopores or nanowires. Though following a different structuring mechanism, a large variety of multilevel structures with interesting optoelectronic properties could be obtained exploiting the "Y-type" nanoarchitectures [74, 83].

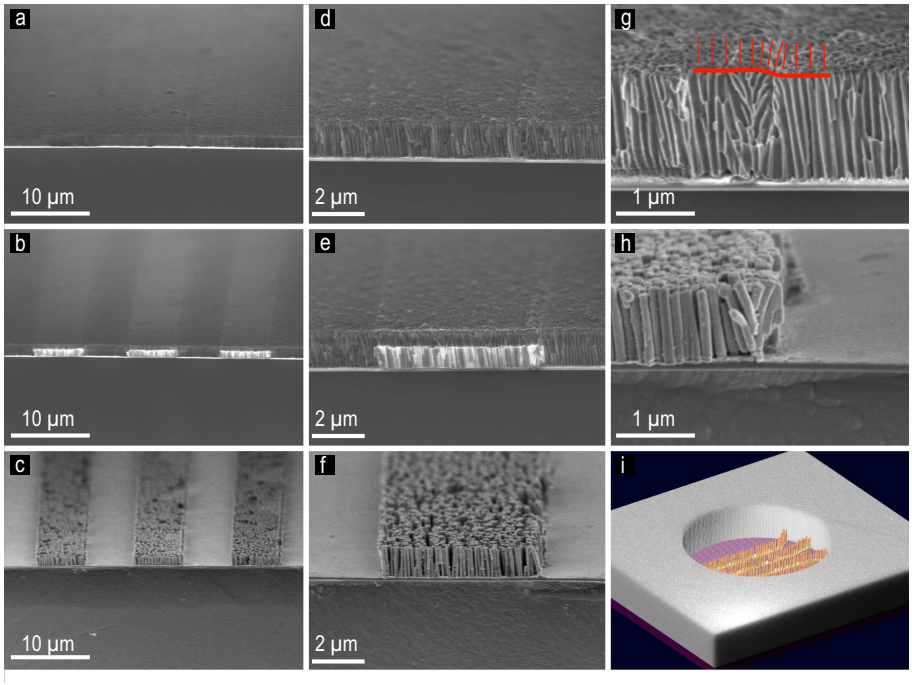

Figure 3.6: Sequential SEM imaging of the fabrication steps ((**a**) - (**c**) enlarged view, (**d**) - (**f**) - one microelectrode close-up). (**a**), (**d**) AAO covering the metallic tracks. (**b**), (**e**) Partial *Ni* electroplated membranes. (**c**), (**f**) Free standing nanowires after the removal of the alumina. Cross-section images of the Y-branched defects after the anodic aluminum oxidation (**g**) and the electroplating (**h**). (**i**) Schematic view of the chip after electroplating.

Important to note is that this process provides a direct bottom-up, self-aligned nanowire patterning protocol. The electroplating will take place only on top of conducting pads and if they are in contact with the external electrode. Equivalently, using CVD-type deposition techniques, growth will take place only on top of catalyst areas. Further, using adapted electrochemical set-up's and adequate circuit design it is

possible to grow separately distinct types of nanowires on closely spaced microelectrodes. This type of architectures could be useful for thermoelectric applications as well as for the fabrication of sensing devices or nanoscale high-performance electrochemical batteries [69, 159]. However, for single nanowire devices, further processing to isolate a reduced number of nanowires (1 is preferred) and structure the AAO and the remaining aluminum film is required and discussed in the sequel.

3.3.3 AAO patterning

At the stage presented in Figure 3.4 (**a**) all of the electrodes (BE's and TE's) are electrically shunted. To build up vertical nanowire crossbar devices we will need to keep AAO in some areas, remove it form others (for example to reveal the TE's viases) and for sure, get rid of the shunting aluminum layer between each electrode. The detailed protocol is discussed in the following.

The process is based on the wet etch chemistry of the AAO and aluminum layer. As the thickness of both is relatively high (> 1 μm) dry etching (RIE, argon milling) is unsuitable, almost impossible, because it will implie the use of thick or extremely hard masks. Wet etching, using strong basic solutions was found to work excellently using thin mask films. Aqueous potassium hydroxide solution (2M KOH or $NaOH$) was used to etch both components. Due to relatively harsh chemistry, PMMA masks were found to be unsuitable. PECVD SiN_x instead resists well with no signs of degradation. After the anodization, the chips were cleaned in acetone with 1 to 2 minutes of ultrasonication to remove any surface residuals[9]. Next, a 300 to 400 nm thick SiN_x film was deposited using a PECVD system (see Section 3.4.1 for the SiN_x deposition and RIE details). 1 μm thick PMMA film was used to pattern and transfer the desired design onto the SiN_x layer using EBL and RIE. Important, yet not critical, is to reveal the alignment marks during the AAO microstructuring step. SE signal from buried marks will be very low (almost absent) if using low emission currents. The first EBL step, requiring exposure of large areas (with relatively low resolution) was done using high working beam currents (15 - 25 nA) to increase the throughput. It also enabled facile visualization of marks and respectively alignment. Subsequent EBL steps require higher resolution (*i.e.* low beam currents) making troublesome visualization of the marks. So, clearing the AAO from the top can facilitate the work. Aluminum plots are also left on each contact pad, helping the reliable bonding. Subsequently, the sam-

[9] As the process it is not performed in a clean room environement, it is better to do so.

ples were immersed in the KOH and leaved until complete removal of aluminum layer was visually detected[10]. Visual instead of timed detection was preferred because of the variation in the etching rates; aging of the hydroxide solution being the influencing factor. Typically, the etch takes 6 - 8 minutes. After this lapse of time, two dippings, each 1 minute long in different KOH baths were used to rinse the surface of Al^{3+} ions which could precipitate during the water rinse step. The remaining Ti and TiO_x layers were removed using a HF 2% solution. The dipping is short (15 - 25 seconds) and again visual detection is used to stop the etch. As soon as the sample surface starts to change in color (evidence of gradual removal of SiO_2 layer) it was left for another 10 seconds for assurance[11]. The remaining SiN_x was subsequently stripped using RIE[12]. Its presence and morphology is embarrassing for further processing (PMMA coating, top contact definition). For example, the self-contacting layer (as it will be discussed in Section 3.5) needs to be defined directly on top of the AAO membrane.

Basically, at this point, only a small AAO slab needs to be defined on top of the BE's (as schematically presented in Fig. 3.7 (**d**)). The rest could be effectively removed. It is the specificity of the present process that forced us to adapt the particular design presented in Figure 3.7 (**a**). The electrochemical growth requires an electrical continuity between the macroscopic electrode and the plating area. This is realized by using the remaining aluminum layer after the anodization. During the EBL step, a macroscopic contact pad is defined in Al, on the edge of the

[10]Similar to the work of Li *et al.*, the wet etch of AAO was found to occur in a highly anisotropic way [160] (Fig. 3.7 (**b**), (**c**)). They have microstructured ordered AAO templates for photonic applications using an evaporated and photolithographically patterned Al layer. As their membranes were supported by Al, selective wet etch chemistries (acid based mixtures compared to the base solution used in our protocols) were used to stepwise remove each of the components and maintain "supported" the AAO slabs. In our case, such restriction is absent, both components being removed using the same chemistry. Interesting is that the etching anisotropy is insensitive to the process chemistry. Since in the opened area the solution can penetrate into the holes and therefore the etching takes place at the whole oxide/solution interface, the actually removed lateral part is only half of the pore wall thickness. Therefore, the etching is quite fast in the parts with open pores. On the other hand, full removal of aluminum requires longer times, explaining the large undercuts obtained (Fig. 3.7 (**b**), (**c**)).

[11]The color change indicates the full removal of the Ti in the SiO_2 areas, presumably, as well from the TE's pads. A slight over etch was used. The removal of Ti/TiO_x from metallic pads is very important as it will dictate the quality of top electrical connections. This is one of the steps were the use of thick SiO_2 film is justified.

[12]Unprotected SiO_2 areas are exposed to plasma etching as well, being thinned down again. This is another argument to use thick SiO_2 film.

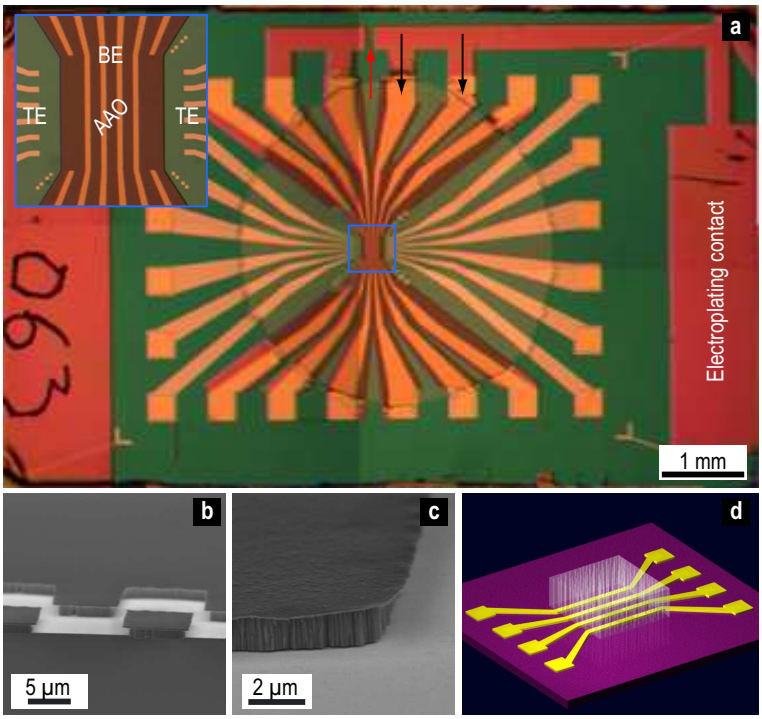

Figure 3.7: (**a**) Optical microscope view of the chip after the AAO and aluminum etching. The PMMA and SiN_x masks are still present. Macroscopic electroplating electrode is connected only to 2 BE's (marked by black arrows). The split area is marked by the red arrow. The need for aluminum film overlap with the working BE's is evident. Square pads of aluminum are left on each connection pad (not visible) to facilitate wire bonding. The AAO is left all along the working BE's (see main text for discussions). The circular area (replica of the original AAO membrane) is the result of non-uniform etching of SiO_2 layer during the Ti/TiO_x wet etch step (HF 2%). Inset: magnified view of the central area. The alignment marks are revealed to facilitate their imaging during subsequent EBL steps. (**b**), (**c**) Crossection view of arbitrarily etched AAO slabs with SiN_x layer on top. Highly anisotropic etching as well as the large undercut are visible. The exposed area is free of any residual material. The remaining SiN_x "umbrella" is stripped and not used subsequently for confined electroplating. (**d**) Simplified view of the achieved step.

chip, to facilitate the interface with the electrochemical set-up (noted as "Electroplating contact" in Fig. 3.7 (**a**)). A stripe is also defined connecting the later to the working BE's. Their number and position (black arrows) can be controlled using splitters (red arrow) defined as well during the EBL step. Due to the nature of active parts (for the moment

only metallic nanowires) the basic cross-bar circuit was employed: $1 \times n$ design. The practical realization was limited to the use of 6 TE's. On the discussed chip, 2 BE's are operational at this step, yet only one of them will be used further (caution taken in case that processing errors will alter the quality of one of them).

As it will be shown further, very reduced areas, or in other words, a countable number of nanowires will be electrodeposited. From the experimental point of view this implies plating currents of the order of few nA. The problem is that there are always some defects, ramping up the current into the hundreds of nA to few μA making the use of preliminary calibrations troublesome. For example, the initial work was done using an AAO slab with a configuration as presented in Figure 3.7 (**d**), requiring a great deal of work to mask the pads of the exposed BE's (as the electrochemical cells working areas are few mm across). This was tested using very thick SiN_x layers (1 - 3 μm) with no satisfactory results. The main problem was the isolation of interface area between the BE's and the AAO slab margins. Straight corners and elevated height profiles of AAO was impossible to conformally coat and completely isolate from the electrolyte, using PECVD technique. This could be accomplished using variable angle deposition as in the case of TE's definition discussed in Section 3.5.2, yet leaving AAO all along the BE's connections was found easier to implement and was further used. During the masking step for confined electroplating, they are protected by the same masking layer and the topography induced defects are minimized. Anyway, defects are still present (though, at lesser extent) and these aspects could be optimized further either through more careful processing or by using controlled large electroplating zones (patterned somewhere outside the active areas) to increase in signal to noise ratio.

3.4 AAO nanostructuring

This Section deals with the reliable fabrication of single (or few) nanowire architectures. This could be done in two ways. In the first method, the nanowires could be grown all over the BE's and then they are contacted preferentially. One approach, based on the use of AFM nanoindentation was proposed by Fusil *et al.* and was used to characterize and to build single nanowire spin-transfer devices [67, 68]. The protocol requires mechanical polishing of the filled templates (because of the non-uniformity in the electrochemically grown structures) and the use of inert metals during the final step of electroplating is preferred. The other method, which was adapted in this work, is to locally con-

fine the growth using a mask and to contact the grown bunch(es). Both of them have advantages and disadvantages and the present choice was based on technical limitations. PECVD SiN_x films were found to be excellent candidates for the masking step. Though, in the final device there are no more traces of SiN_x, during the fabrication it plays a crucial role. The deposition, etching as well as some physico-chemical properties of used SiN_x films are presented.

3.4.1 Silicon nitride deposition and etching

The very first test consisted in depositing (at 50°C) and patterning a SiN_x mask on top of aluminum and then anodizing this stack. The results were catastrophic (non-uniform anodization, SiN_x breakdown) and were left aside. The pre-existing stack is typically made of $Ti/Au/Ti/Al$. Increased temperature may induce interdiffusion between layers, degrading the quality of the alumina when reaching the underlayer and subsequently the quality of electrodeposits. Hence, SiN_x deposits were performed at a substrate temperature of ~ 40°C. The reacting gases composition was selected arbitrarily, based on a pre-existing recipe in the used tool. The unique recipe used is the following[13]: deposition pressure - 0.8 mTorr; RF power density - 60 mW/cm^2; gas flow and composition: SiH_4 5% dilluted in N_2 - 500 sccm, NH_3 - 2 sccm and N_2 - 750 sccm.

In time, it was found that the low temperature deposition is not the best option. First, the reproducibility was poor. The used tool has calibrated working temperature range between 150 - 350°C. Temperature control below 100°C was difficult and the deposition were actually made in between 30 and 60°C, each time being different. Second, residual porosity posed problems for effective masking. Many of samples were partially or completely electroplating even when using 200 nm thick SiN_x. And third problem was the adhesion, especially on the revealed metallic parts. It is well known that the quality of the PECVD films increases with the deposition temperature: higher etch resistance, decrease in the porosity, better adherence, improved dielectric properties. Obviously, we were not in the good regime.

Subsequently, the deposition temperature was raised to 150°C. Porosity as well as adhesion problems were effectively eliminated. To further improve the adhesion, an *in situ* pre-clean step was performed using N_2O as reactive gas (deposition pressure - 1 mTorr; RF power density - 60 mW/cm^2; gas flow - 100 sccm). The glow discharge splits the N_2O molecules following a simple reaction: $N_2O \rightarrow N_2 + O^{\cdot}$ providing reactive oxygen radicals for the cleaning reaction. To have a better view on

[13] Using a Oxford PlasmaLab100 PECVD system.

	50°C	150°C	250°C	350°C
Deposition rate (nm/min)	24	18	18	16
Etch rate (nm/min)	> 50	35	13	4
n (at 632 nm)	1.8	2.4	2.7	2.8
k (at 632 nm)	0.02	0.03	0.07	0.09
Adhesion on Au	poor	good	good	good
Adhesion on Pd	poor	good	excel	excel
Adhesion on Al	poor	good	excel	excel

Table 3.1: Silicon nitride properties function of deposition temperature. Deposition and etch rates were determined using ellipsometry. Etch rate is refereed to the wet buffered HF removal rate. The augmentation of n and k is indicative of an increase in Si content. Adhesion was verified using scotch tape test and 15 minutes ultrasonication in water. Qualificatives were ascribed as follows: poor - scotch test negative; good - scotch test positive while ultrasonication with slight signs of degradation; excel - both tests positive.

the influence of the deposition temperature on the quality of the SiN_x a series of experiments were performed and the results are summarized in Table 3.1. Clearly, the 50°C deposit is the worst. Higher temperatures mainly influences the etch rate and slightly the adhesion. Spectroscopic ellipsometry measurements give us some insight into the nature of deposited films. The fit models were different for different temperatures, indicating different chemical and structural composition. The refractive indexes of films (even for those deposited at 350°C) were found to be increased compared to stoichiometric Si_3N_4 indicating a high content of silicon. In a seminal work, Charavel *et al.* showed that the refractive index of PECVD SiN_x films increases linearly with the Si content [161]. They have correlated the electrical properties of metal-insulator-metal capacitors using SiN_x dielectrics (reliability, breakdown and leakage current) and the physical properties and showed that the behavior of the fabricated devices can be predicted by analysing physical properties of the dielectric. In our case the study was not so profound, being limited to basic mechanical and chemical properties. Presumably, the 25 to 2 mass flow ratios between the SiH_4 and NH_3 in the reaction mixture is at the origin of the elevated Si content [162]. Higher quality films however, brought some complications for the reactive ion etching using PMMA mask (discussed in the next paragraphs).

Other complication was the correlation between the thickness of used of SiN_x and AAO morphology. Initially, the pores were not enlarged, being randomly distributed over the surface and mainly concentrated at

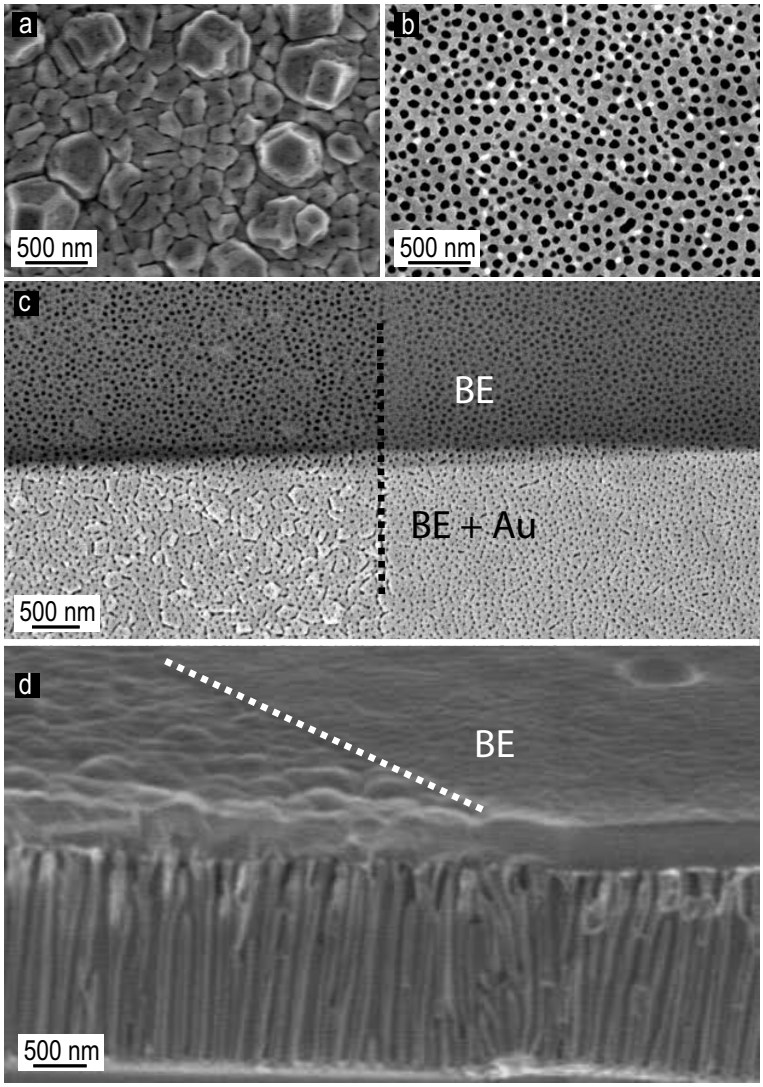

Figure 3.8: AAO surface before (**a**) and after (**b**) pore enlargement. (**c**) Top view of AAO on top of SiO_2 (left) and BE (right). The lower part of the surface is covered with 40 nm of Au. (**d**) Morphology of the SiN_x deposited on enlarged AAO. Underlying layers: left - SiO_2, right - BE.

the initial aluminum grain boundaries. Their diameter is around 10 - 20 nm. Hence, 100 - 150 nm SiN_x was found to be enough to protect effectively the pores. The pore enlargement was realized with the patterned mask on top and obviously occurring only in the exposed area.

The process was found to be instable. A correlation between the mask size and the number of grown nanowires was difficult to establish. As was found later (and detailed bellow) the instability originates from the pore widening step. Thus, increased reproducibility was attained using a pre-enlargement process (about 80 - 90% of nominal value) after the anodization, the rest being done shortly before the electroplating. The dissimilarities are attributed to differences in the morphology of AAO before and after pore enlargement (see for comparison Figure 3.8: (**a**) surface of the pristine anodized sample and (**b**) the same surface after the enlargement). During this step, a part of Al_2O_3 is etched away from the pore sidewalls increasing their diameter. But at the same time, the alumina is etched from the surface, changing completely the porous membrane appearance (take a look again at the panels (**a**) and (**b**)). This occurs also for a masked AAO though it is difficult to predict the etched configuration.

Associated to the increase in the pore size was the use of thicker masking layer to avoid any parasitic growth. In this configuration, 200 to 400 nm of SiN_x were found to clog effectively the porous surface. The drawback was that increased etch times (already enhanced by the use of 150°C deposits) using the same thickness and patterned resolution PMMA masks was required.

Figure 3.8 (**c**) shows the top view of the AAO surface at the BE's boundary. For the reasons explained in Section 3.5.2 the samples is partially coated with Au. Clear differences between the AAO surface present on Au and on SiO_2 surface can be detected. For example, grain boundaries, originating from initial polycrystalline aluminum film could be still observed in the outer-BE's area, the morphology being comparable with the case presented in panel (**a**), although, the pores were enlarged. The alumina grown on BE's is clear of such defects and resembles more to normal case (fortunately, this is the region of interest). The same could be ascribed to the morphology of deposited silicon nitride film (Fig. 3.8 (**d**)). The surface is smoother on AAO grown in BE's area than in outer region. Differences in surface topography of AAO on these two regions could be at the origin of this effect. Most remarkable is the difference in AAO morphology.

In principle, this could be attributed to two distinct steps present in the AAO fabrication: anodic oxidation or deposition of the aluminum film. Let's suppose that the anodization step is at the origin and the aluminum film has the same composition and morphology throughout the volume. As the observed difference is a surface phenomenon, the discrepancy should arise in the very first moments of anodization by dissimilarities in the heat dissipation or current density non-uniformities.

Yet, considering the "bulkiness" of the as-deposited aluminum film, the anodization should be uniform and not influenced by the underlying structure. Only at the end, when the Al film is thinned and the Au pads are responsible for the current uniformity and heat dissipation or generation due to high current densities involved, anomalies should be observed (and they are detected as already described). However, they could not influence the top most surface morphology. Hence, the first supposition can be ruled out and the origin of the discrepancy can be attributed to the aluminum deposition step or, to a different aluminum crystallisation behavior on patterned and non-patterned areas of the substrate.

As mentioned at the beginning, a good thermalization of the substrate is needed to have uniform aluminum films. The difference in thermal conductivity between Au and SiO_2 is almost three orders of magnitude at room temperature (300 and 1 W/mK, respectively). Thus, aluminum crystallization during the deposition step is strongly affected by the difference in thermal dissipation between the two type of substrates. Presumably, this happens only at the beginning, while the thickness is still low, yet, already providing dissimilar morphology seeding layers for subsequent metal crystallization. Subsequently, the film growth will take place non-uniformly and so the anodization. Chemical surface pattern could be also invoked, nevertheless being minimized by the evaporation of the Ti layer prior the Al deposition.

For selective electroplating, SiN_x mask has to be locally removed to allow for the electrolyte to be in contact with the BE's. This was typically done by transferring the pattern from an EBL exposed PMMA mask to the SiN_x layer using RIE. Contrary to the PECVD step, the etching protocol was continuously improved. The initially used, 100 nm thick nitride films were easy to etch. EBL using 100 to 200 nm PMMA allowed for 20 - 30 nm resolution in resist film and 50 - 70 nm in SiN_x. The RIE was based on SF_6 and CHF_3 chemistry achieving etch rates selectivities of 1.5 (PMMA to SiN_x) [1]. Once the thickness was raised to 300 - 400 nm and the PECVD was performed at 150°C it was difficult to attain the same resolution in SiN_x. A new protocol was developed. Pure SF_6 chemistry provided excellent result in therms of selectivity and anisotropy[14]. Etch rates function of operating parameters were determined and results are presented in Figure 3.9. It can be observed that the total chamber pressure has an interesting influence on the components removal rates and especially on the selectivity. By increasing the pressure, a slight acceleration of the removal rate for both components is detected, reaching a maximum and then monotonically decreasing. This

[14]Using a PlasmaLab100 ICP-RIE system.

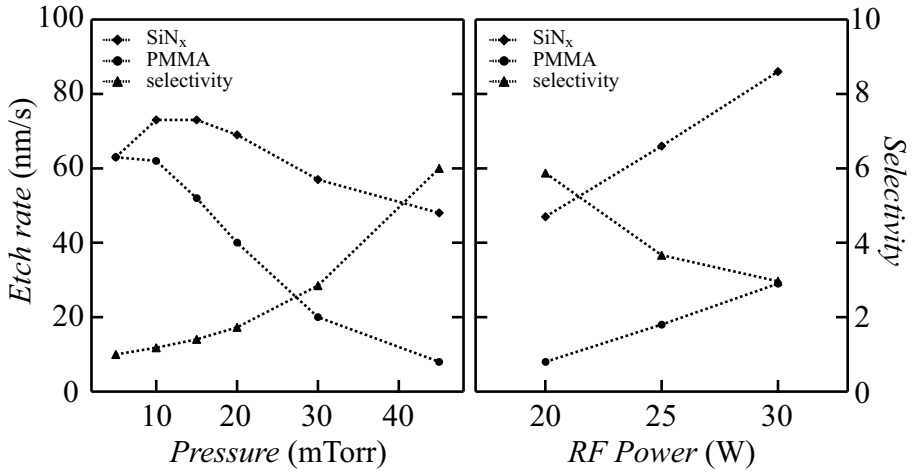

Figure 3.9: Measured SiN_x and PMMA etch rates as well as the calculated selectivity defined as their ratio function of: (left) total chamber pressure (RF power constant - 20 W) and (right) RF power (pressure constant at 45 mTorr). SF_6 flow - 100 sccm; table height - 20 mm; substrate held at RT.

could be explained by 2 factors. First, an increase in pressure while keeping constant the gas flow signifies a low rate arrival of fresh reactant and, as explained in next paragraph, combined with a large amount of organic species generated during the plasma and their subsequent fluorination can result in the precipitation of fluoro-polymers on the sample surface and decrease in the etch rates. The other factor is based on the observation that the DC bias generated during plasma is decreasing with the increase in pressure signifying less mechanical damaging (or removal rate) of both components. Important, however, is the enhancement of the selectivity, reaching values as high as 6 (SiN_x to PMMA etch rates ratio) at 45 mTorr explained by a reactive selective removal rather than ion stripping. Keeping the pressure constant at 45 mTorr, the influence of RF power upon etching dynamics was tested. Both were found to increase linearly (as well as the DC bias) with the increase in RF power, diminishing drastically the selectivity. As higher pressures or lower RF power is difficult to attain and maintain it was decided to work in this conditions: 45 mTorr and 20 W.

Important to note is the sample etch configuration. Several small samples are etched at a time; while the etcher tool is designed to process one wafer (3-inch diameter). This introduces a necessity of using a wafer support, on which the sample is lying during the process. It is impor-

tant to maintain same chemistry in the plasma chamber and as the wafer support is much bigger than the samples of interest, it will influence primarily the enchant composition. As the silicon is known to be etched effectively in SF_6 plasma, it was decided to work with PMMA coated wafers (from where the assumption that many fluorinated organic species are generated in the chamber). The edges of samples can perturb the flow of etching gas and thus affect the etching rate. Differences between the electrical conductivity of a sample substrate and supporting wafer influence locally the homogeneity of the electric field, which in turn influences the etching rate. Despite small differences, the etching characteristic remains linear and the amount of etched material proportional to the RIE period. Examples of etched holes in nitride masks and subsequently grown nanowire architectures are discussed in the following.

3.4.2 Selective electroplating

Once the mask was structured, the samples were electroplated, allowing the growth only in the exposed area. The electrodeposition was carried out using an EG&G PAR 263 potentiostat (Princeton Applied Research) in a conventional three-electrode cell with a Pt counter electrode and $Ag/AgCl$ as reference electrode. In order to ensure a homogeneous growth, the pulse plating method was used to deposit the Ni nanowires from a solution containing $NiSO_4$ (0.5 M) and H_3BO_3 (0.5 M) at RT. The deposition process is stopped as soon as the first nanowires emerge at the surface, as detected by a rapid increase of the plating current. For the following characterization steps, the SiN_x layer was completely removed using the same SF_6 plasma etching recipe followed by wet chemical etching of the alumina with a solution of 2M $NaOH$. This yields freestanding nanowires on the substrate, which could be imaged easily using a SEM.

Examples of fabricated architectures are presented in Figure 3.10. By carefully adjusting the dimensions of the openings in the SiN_x (see next Section) mask and, the interpore distance in the alumina template we were able to grow either single or bunches of nanowires. Panel (**a**) shows an array of 3×3 mask openings fabricated using early protocols (PECVD on non-enlarged pores, EBL, enlargement). Thin SiN_x layer (100 nm) and high-energy electron imaging (5 keV) allows for the visualization of the underlying AAO. Non-uniform, 15 - 20 nm diameter pore organization can be detected. Grown architectures on both, non-patterned and structured substrates are shown in panels (**b**) to (**f**). Bunches of nanowires ((**c**), (**f**)) were easy to achieve by fabricating relatively large openings (few hundreds of nanometers). The number of nanowires in

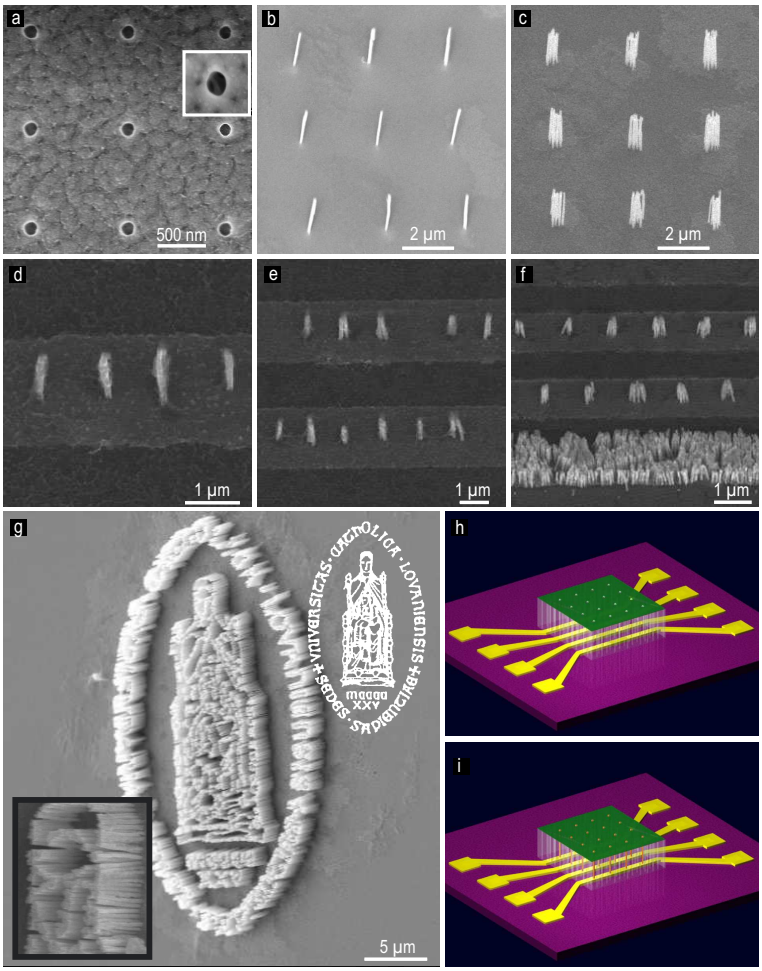

Figure 3.10: (**a**) Top view of a fabricated silicon nitride mask. Inset: zoom revealing the presence of pores in the alumina layer. (**b**) - (**f**) Micrographs of fabricated single- and multi-nanowire architectures on planar substrates and microelectrodes. (**g**) Complex "art-work" made out of nanowires. The original picture (top inset) was converted into an input signal to the EBL pattern generator. Bottom - left inset: magnified view revealing nanowire pixelization. It must be noted the high contrast between patterned and nonpatterned areas. (**h**), (**i**) Schematic representation of the achieved steps.

each group was not uniform (even for equal size opening) and this was attributed to the processing variations. The initial work methodology was mainly based on high-throughput screening of the achieved resolution. A large number (few thousands) of mask openings, with various

diameters (50 - 500 nm), were used for the study. Eventually, single-nanowire resolution regions were obtained. Interesting was that in these area, mainly single, doubled or missing nanowires were observed (panels (**b**), (**d**) and (**e**)). Regions like those presented in (**b**) and (**d**) were extremely rare, yet showing that it is possible to achieve single nanowire resolution. Eventually, this led to the systematic study on the number of accessed nanopores using selective mask processing of AAO templates. More complex architectures composed of distinct nanowires could be obtained by adequately designing the exposure pattern (panel (**g**)).

Going back to the sample fabrication step achieved in Figure 3.7, worth mentioning are some important aspects regarding this type of device processing. First, the AAO has to be left to ensure mechanical and chemical encapsulation. Thus, the determination of grown and subsequently contacted nanowires has to be performed indirectly. Next, due to the $1 \times n$ design (n was typically 6), only 6 openings were to be defined. The extremely low working area or reduced number of nanowires (minimum 6 required and typically around 50 patterned) necessitates plating currents of the order of few nA, sometimes lower than the noise of the system, making the reproducible fabrication of multijunction nanowires difficult. The presence of defects further induced complications. Plating current density function of time plot was usually featureless, close to 0, during the pore plating and only once they emerged from the template, current jumps could be detected, indicative of higher plating area. Another important aspect is the insertion of a "self-contacting layer" in between the AAO and nitride mask before mask structuring and electroplating. It should be thick enough to ensure electrical continuity yet thin enough to avoid clogging the pores (see fabrication details in Section 3.5.2). These two steps could schematically represented as depicted in Figure 3.10 (**h**) and (**i**). Before detailing further, we'll say few words about the selective electroplating statistics.

3.4.3 Statistical interpretation

As already intuitively suggested, if no overlay alignment is used, the number of accessed nanopores depends on the size of the openings in the nitride mask. Some questions regarding these processing aspects have been already raised by the referees during the publication procedure of the above presented results [1]. To cite them: (i) *does the exposure of only a portion of the nanopore opening yield smaller diameter nanowires, or there is any effect on the growth rate associated with the electrodeposition?* and (ii) *it should be very difficult to have patterns like shown in Figure 3.10 (**b**) with single pores exposed for patterning. To grow single*

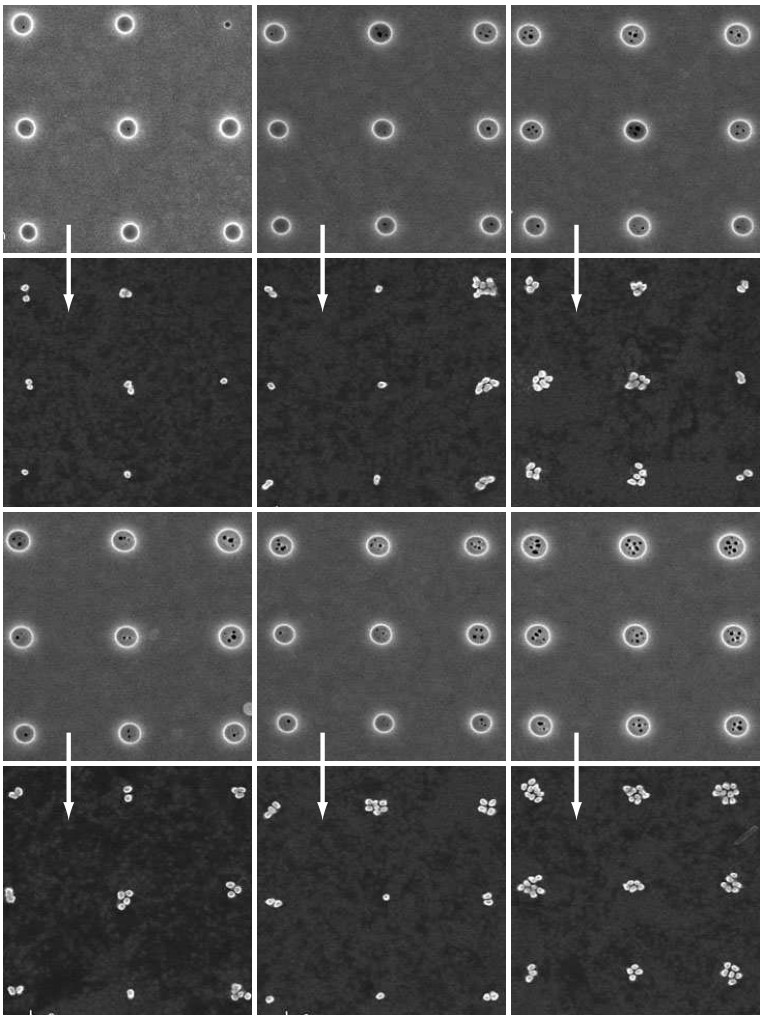

Figure 3.11: Top view SEM micrographs presenting used masks and obtained nanowires architectures for the statistical study. The correspondence between the images is given by the arrows. Scale bar is given by the center-to-center mask distance of 2 μm. Direct imaging of revealed pores is difficult and usually erroneous (low contrast, depending on the electron acceleration energy and magnification) explaining why subsequent electroplating was used for the study.

nanowires, we have to etch holes through PMMA / SiN_x at exact positions where the nanopores are located. How the authors achieve this? Or it was purely by luck? Indeed, at that moment most of the structures were done "purely by luck". However, observations like why only 0, 1 and

2 nanowires were grown in areas where majoritarily a single nanowires was expected, intrigued us as well. The first question, concerning the overlap between the mask openings and the pores and what is the operation threshold which allows electroplating to occur also aroused our curiosity. Hence, at some point of the project, a systematic study was set in place, explaining and revealing many remarkable aspects.

Two directions have been attacked: (i) experimental studies of the number of accessed nanopores function of mask diameter and (ii) developments of a simulation method to enable fast screening of the experimental behavior. Briefly, the experimental part can be described as follows. Selective-site electroplating was realized by patterning a 350-nm thick SiN_x (PECVD 150°C) mask deposited on top of AAO. Circular masks with diameters (D_{exp}) ranging from 30 to 500 nm, defined using EBL and RIE, were used for the statistical study of the selective AAO patterning. The patterning was purely random due to the absence of mask overlay alignment. To study the overlapping occurrence of the mask with the template pores, pre-enlarged AAO was used. Comparing again surface morphologies of AAO before and after enlargement (Fig. 3.8 (**a**) and (**b**)) it is clear that the pore widening step will interfere, yielding the overall processing dispersions rather than the masking statistic dispersions. After Ni electroplating, the size of the masks was determined using SEM inspection (±9 nm measurement error, pixel size in the acquired micrographs) followed by SiN_x and AAO removal. To avoid as much as possible to induce processing errors, the thickness of the electroplated material was limited to 200 nm. Low aspect ratio nanowires are mechanically more stable and their removal during the template release was minimized. The samples were inspected again by SEM to count the number of grown nanowires. A series of SEM snapshots acquired in each step is shown in Figure 3.11. They give just a partial overview as more than 100 of such images were acquired and analyzed. The number of events corresponding to the observation of a fixed number of nanowires for a mask diameter D_{exp} was counted; the D_{exp} bin being set to 18 nm (pixel size in the acquired images). The data accumulated for each bin was divided by the total number of events within the respective bin, to obtain the probability. About 1100 events were included in the histogram shown in Figure 3.12.

The experimental behavior was found to be simply simulated using a common image analysis procedure (see Appendix B for details). The probability of having N nanopores inside a circular mask at various locations on AAO surface was computed using image analysis routines

provided by Igor Pro software[15]. Basically, a circular ROI was generated on top of SEM images and the number of nanopores inside the ROI was counted.

Intuitively, one can reason that the number of revealed nanopores in the lithographic process will depend on the geometry and size of the mask. Indeed, as displayed in Figure 3.12, a definite resolution probability could be achieved for a given circular mask diameter range. Note

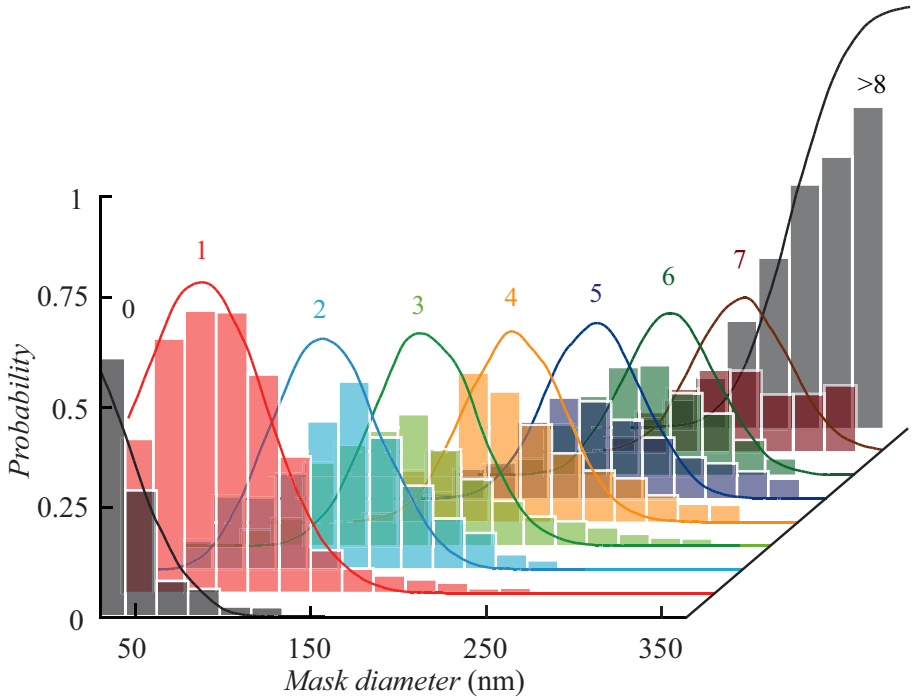

Figure 3.12: Experimental histograms and simulated probability dispersions for selection and processing of a given number of nanopores inside an alumina template with short range pore ordering. For the sake of clarity, the histograms and curves are shifted. The mask size cutoff is 30 nm. The mean pore diameter (d_{mean}) and interpore distance (h_{mean}) are 72 and 132 nm, respectively. For simulation, a counting threshold close to 0 was used. The good agreement with the experiment is explained by the self-repair mechanism of the mask during the etch step through accommodation of the frontier pores (see further).

that the patterning resolution (from 0 to more than 8) is given in our experiments as the number of the subsequent grown nanowires and not the revealed nanopores, hence, processing induced variations are unavoid-

[15]Wave Metrics Inc.

able. The sources of experimental errors (as compared to the simulation approach) can be categorized as follows:

- Defects due to up-ward or down-ward pore branching (a surface revealed nanopore will produce 2 nanowires or reversely and probably counter-balanced if present at the same amount in the template) or insufficient bottom barrier removal (no nanowire will be grown for a revealed nanopore).
- Clogging of the pores with the masking material (again, no nanowire will be grown for a revealed nanopore).
- Processing instabilities during the template removal or drying and sample manipulation. Removal of the nanowires is the error source. For example, even if "correct" number of nanowires was grown for a given mask diameter, 1 or more removed nanowires will imply that the respective mask will be accounted for a wrong pore resolution.
- Measurement and counting. As the diameter determination and especially the nanowire counting was done manually, errors are unavoidable.

Conceptual understanding of this manufacturing path simply resumes to the counting of the number of nanopores inside a region of interest, arbitrary selected from an image that describes the morphology of the template. The good agreement (within the error bars) between the experiment and the simulation of the patterning process proves that, fundamentally, there is no preference to any specific sites of the templates. Remarkably, the single-nanopore resolution is realized with a yield as high as 70% at a mask diameter of ∼70 nm for the considered case (red histogram in Fig. 3.12). Furthermore, it interferes only with (∼9%) null-, (∼18%) double-, and (<3%) triple-pore patterning resolution. Now, the first experimental observations (explained above) are more clear. In the areas where mainly 1 nanowire was observed (or roughly in the maximum probability range), 0 and 2 were also present. The same is of applicability for bunches of nanowires. More we increase the size mask, more we will statistically grow different numbers of nanowires for the same mask size. For example, at the 4-nanowire maximum, there will be as well 2, 3, 5, 6 and 7 grown nanowires (and the spread further increases for bigger masks).

Having set in place and validating the simulation protocol, templates with different morphologies have been studied. Qualitative analysis of the AAO templates (mean pore diameter and interpore distance distribution) is based on a Delaunay tessellation and has been detailed

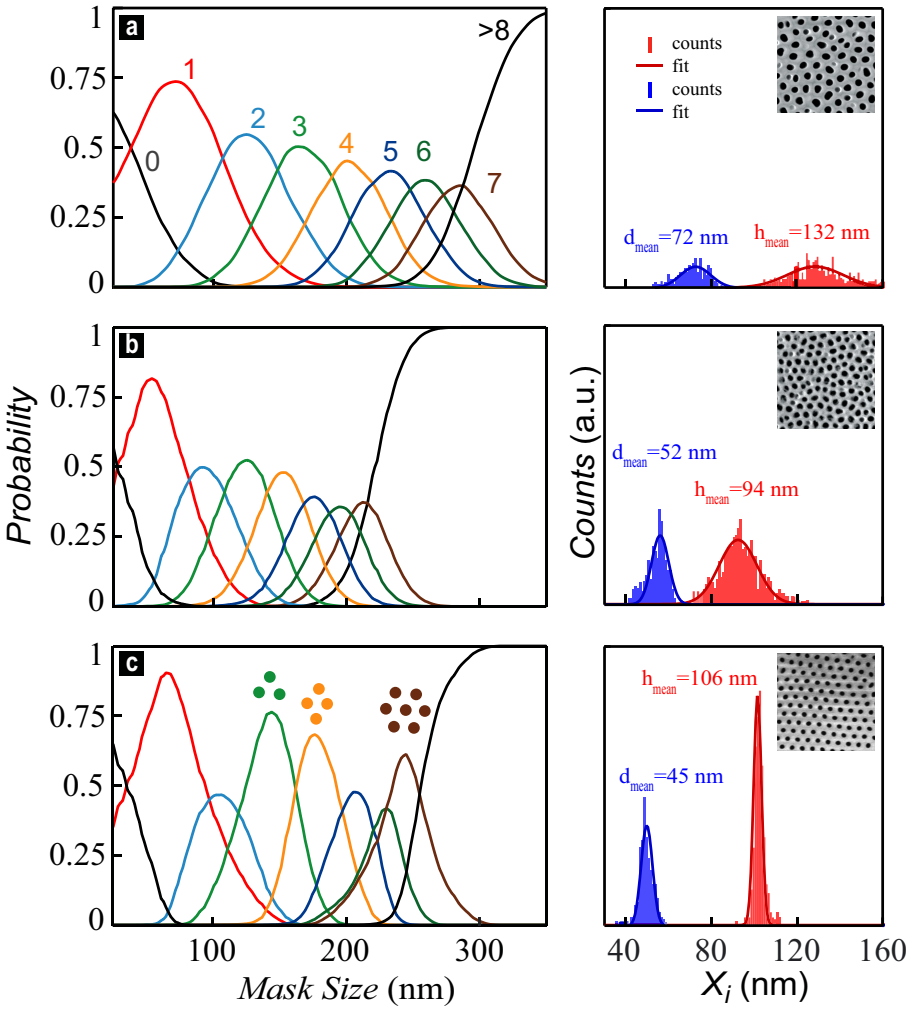

Figure 3.13: Simulated probability distribution using a circular mask for different morphology of AAO (left) and respective pore diameter (d_{mean}) and interpore distance h_{mean} size distribution histograms (right). (**a**) Short range ordered AAO anodized at 60 V (the same as shown in Figure 3.12 without shifting the curves). (**b**) Partially ordered AAO fabricated at 40 V having a lower interpore distance. Increased ordering compared to previous case is quantitatively described by the narrower interpore distribution (or qualitatively detected by inspecting carefully the SEM micrograph). (**c**) Highly-ordered AAO (confirmed by the narrow interpore distance distribution) fabricated in a 2-step anodization process. Insets: 1×1 μm^2 SEM views of analyzed template surfaces.

elsewhere [163]. Short-range, partially and highly-ordered AAO surfaces (prepared using different anodization conditions, for example, by changing the anodization voltage) were tested. It is found that downscaling the template features primarily translates into a left-side shift of the probability peak positions accompanied by a reduction of the full-width at half maximum (compare Fig. 3.13 (**a**) with (**b**)). However, due to a relative pore ordering, some predominant resolutions could be already detected. Higher nanopore ordering degree has a more intriguing influence upon the selection probabilities (Fig. 3.13 (**c**)). A preferential behavior for some nanopore-resolution numbers (3, 4 and 7) together with a detrimental effect on the others (2, 5 and 6) can be observed. This is correlated to the radial symmetry of the circular mask and the hexagonal packing of the nanopores. Noticeably, the single-pore resolution at its maximum expectation overlaps only with null- and double-pore resolution to a lesser extent and it increases up to 90 % compared to the random-nanopore template. Correlation between the mean lattice parameters and the obtained probability plots is difficult to establish. Let's analyze, for example, the highly-ordered case (panel (**c**)). The peak maximum for single-pore resolution is achieved for a mask diameter of 65 nm. The relationship between h_{mean}, d_{mean} and the peak position it is not straightforward. One would be tempted to state that the maximum will be obtained for a mask diameter of $h_{mean} - d_{mean}$, yet, 57 nm obtained is slightly lower than the obtained value (the same applies for the rest of templates). The morphology histograms give us an indication about the degree of uniformity in the template and not about the lattice geometry. However, the probability enhancement for some numbers of nanopores (3, 4 and 7) indicates that the symmetry of the template as well as of the mask could play a role.

Unexpectedly, statistically patterning using a square mask, was found to alter insignificantly the probability dispersion (Fig. 3.14 (**a**)). The single nanopore resolution remains close to 90%. Mainly, a left-side "compression" compared to circular mask is observed and some modification of the higher-number pore resolution (5, 6 and 7). The square mask has to be treated carefully. Overlapping pattern of a 4-fold rotational symmetry shape with a p6m wallpaper symmetry group will be angular rotation dependent. The pattern alignment will be repetitive each 30°. Hence, rotation of the square during the simulation is required. In a different way, this will happen as well in practice. Perfect lattice in highly ordered templates exists over spatially limited domains[16]. Ori-

[16]Typically tens of microns in size without any pre-patterning procedures. This could be increased using pre-structuring techniques. For example, graphoepitaxy for

entation is different from a domain to an adjacent one. Without any preliminary analysis of the lattice orientation, the square mask orientation will take any possible angle with respect to the template symmetry. Or the same as keeping the template pattern orientation fixed and rotating the mask around it's center. Of course, a preliminary analysis to

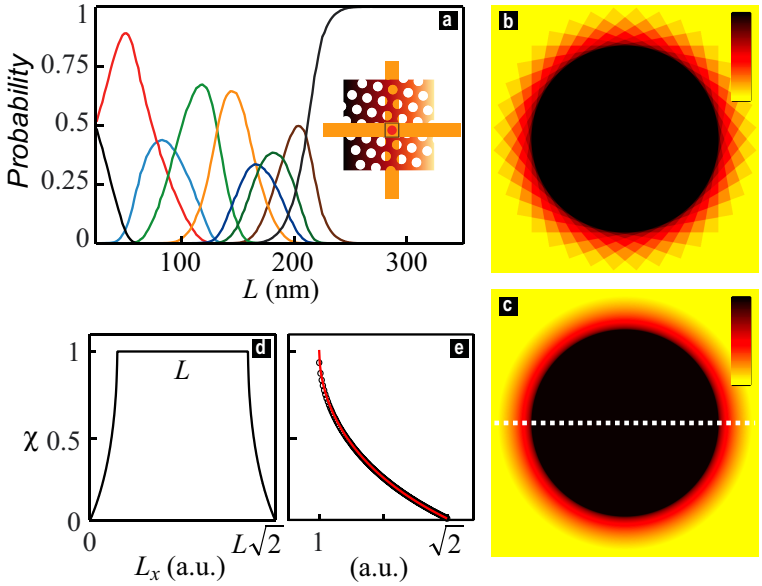

Figure 3.14: Interpretation of probability plots using a square mask. (**a**) Simulated probabilities for a highly ordered AAO template. Color code for the achieved resolution is the same as in previous Figures. (**b**) The actual shape of the used mask. The image is the average of 9 rotated squares. (**c**) The real shape of an arbitrarily positioned square mask revealing the radial symmetry. The plot is the approximation of an infinite number of rotated squares (in reality, is the average of 1000 squares). Color bar scale: 0 (yellow) to 1 (black) intersection probability (χ). (**d**) Crossection plot of (χ) along the diagonal shown in panel (**c**). (**e**) Close-up on the decreasing range (open circles) and the fit to function (red line).

determine the domains orientation could be done. Yet, this will imply a laborious mapping procedure and the subsequent patterning will be no more purely statistic as some degree of alignment is imposed. Moreover, this will be possible only for ordered structures, without any sense for partially or short-range ordered templates. A full, 90° rotation of the square was applied for the simulation presented in Figure 3.14 (**a**). Prac-

block-copolymers, stamping or etching for inorganic templates and so on.

tically, this was done by rotating the square by 10° for each simulation (from initial 0° to 80°) and then averaging the data. The actual shape of the used mask is presented in panel (**b**) (or 9 superposed squares). As it was difficult to define such mask in the simulation procedure (see further) the method using the rotation of the square was used. The circular symmetry is already visible. For a real case, discretization will be transformed into an infinity of rotational positions and the shape of the mask will look as presented in panel (**c**). Now it can be observed that the mask has a perfect circular symmetry, almost identical to the circular mask. The difference is the blurred concentric area. The square has two characteristic lengths: the lateral size L and the diagonal $L\sqrt{2}$. A pore (diameter d) centered at $(\frac{d}{2}+\frac{L}{2}, \frac{d}{2}+\frac{L\sqrt{2}}{2})$ from the center of the mask will intersect or not with the square mask depending on the rotation angle. Hence, an intersection probability (χ), intrinsic to the mask shape has to be defined. $\chi = 1$ if the pore is tangent to the mask and subsequently will decrease function of the distance. Variation of χ along the diameter of the obtained shape is presented in panel (**d**). Intersection probability of 1 is obtained over a range width L (or for the central disc which has actually the diameter equal to the lateral size of the initial square). Outside this range, χ diminishes following a simple relation $\chi = 1 - \frac{4}{\pi}\arccos\frac{1}{x}$. Hence, a square mask used for a statistical patterning can be treated as circular mask, explaining the similarities between the probability dispersion plots. The rationale can be extended to every shape of mask (if they will have any practical signification), each time being approximated to a circle with a "blurred" region. Their size will be however dictated by the initial mask design.

Some aspects need to be further studied. For example, the correlation between the left-side shift and the geometry of masks would be interesting to explore. The peak maximum for single-nanopore resolution is at ∼65 nm circular mask diameter and ∼50 nm lateral size for square masks. This signifies that the shell of the main circle for square masks is very important, contributing substantially to the patterning probability. Presumably, both the mask and the template parameters have to be taken into account to explain the left-side shift. Important, however, is that single-nanopore resolution with a probability as high as 90 % could be obtained using a square mask as well. Though, patterning a mask with squares having 50 nm lateral size may have no practical signification, indirect use of a squared shape is of importance. For instance, it could be regarded as the intersection of 2 orthogonally crisscrossed stripes defined on different parts of the template. Hence, this may enable the integration of the present method within the Hewlett Packard

proposed cross-bar latch technology [164].

3.4.4 Analytical modeling

Despite the simplicity of the analysis there are still some intriguing points. The existence of double pore resolution at the maximum expectation for the single pore is somehow unanticipated. One can reason that for random templates this may be explained by the wide interpore distance and pore diameter distributions and that inevitably there will be an overlap. But, the same behavior is observed for the highly ordered templates (narrower interpore distance and pore diameter distributions), where one would naturally expect that the maximum for the single-pore resolution occurs when the mask diameter is equal to the difference between interpore distance and pore diameter. Furthermore, while the probability dispersion for the short range ordered templates is properly fitted following a Gaussian function, the same approximation failed for the highly ordered templates relying on a different analytical distribution. To get more insight into this aspect, the problem has been mathematically modelized. To simplify the representation, a perfect triangular lattice (d pore diameter and h interpore distance) has been artificially generated and probability distributions for a given pore resolution patterning have been simulated using the presented image analysis protocol (Fig. 3.15 (**d**), open circles). It turns out that the intersection occurrence of a mask having a diameter D with the lattice pores is proportional to the surface areas generated by the "virtual" circles having the diameter equal to $D + d$ concentric with the pore[17]. The intersection area of 2, 3, or more circles is subsequently proportional to the probability of 2, 3 or more pore resolution. The probability thus, will be the fraction of surface area for each type of intersection. The issue takes into a surface optimization problem.

Due to the triangular symmetry, the surface area calculation can be limited to the triangular elementary cell. For the case I (Fig. 3.15 (**a**)), only null- and single-pore resolution is expected and the analytical functions describing the patterning probabilities are: $P_0^I = 1 - P_1^I$ (1) and $P_1^I = \pi\frac{\sqrt{3}}{6}(\frac{D+d}{h})^2$ (2), respectively. Obviously, the square power law distribution described by the equation (2) has no local maxima and hence neither does the single-pore resolution. Actually, the first maximum occurs for the case II (Fig. 3.15 (**b**)), when the overlapping of two virtual circles marks the onset for the double-pore patterning resolution[18]. The

[17]This representation is nothing else than the 2D projection of the efficient cross-sections as described by the collision theory.

[18]The upper limit of case I is actually the Thue theorem.

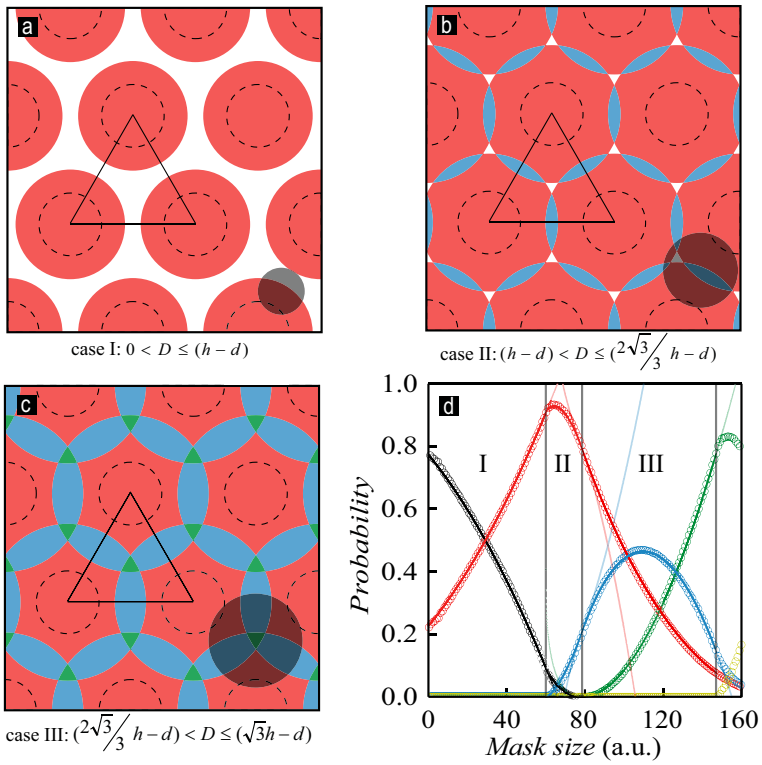

Figure 3.15: Analytical representation of the statistical structuring methodology. (**a**) - (**c**) The dashed curves are delimiting the pores (60 a.u. and 120 a.u.), the gray circle represents the circular mask, and the areas enclosed by the virtual circles are the probability surface plots. The colors white, red, blue and green correspond to the probabilities for null-, single-, double- and triple-pore resolution, respectively. The geometrical boundary conditions for each case are also given. (**d**) Image analysis simulated (open circles) and analytically-computed (solid curves) probabilities. The functions describing the probabilities have values also outside the boundary condition, although with no physical signification (shallow curves). The color code has a double signification: it delimits (i) the surface area fraction for each finite-pore resolution and (ii) the loci of the mask center to achieve it.

probability functions write as:

$$P_0^{II} = 1 - P_1^{II} - P_2^{II} \tag{3}$$

$$P_1^{II} = \pi \frac{\sqrt{3}}{6} \left(\frac{D+d}{h} \right)^2 - 2P_2^{II} \tag{4}$$

$$P_2^{II} = \sqrt{3} h^{-2} \left[(D+d)^2 \arccos\left(\frac{h}{D+d} \right) - h\sqrt{(D+d)^2 - h^2} \right] \tag{5}$$

where P_0^{II}, P_1^{II} and P_2^{II} represent, respectively, null-, single- and double-pore resolution. Indeed, P_1^{II} reaches a maximum and then monotonically decreases. Continuing further to the case III (Fig. 3.15 (**c**)), marked by the overlapping between three virtual circles, we observe the onset for P_3^{III}, while P_0^{III} completely vanishes. Concomitantly, P_1^{III} continues to decrease whereas P_2^{III} passes through a maximum. The elaborated analytical equations describing case III are skipped, yet, following the same principle, the calculation can be extended to any diameter D of interest.

As it can be observed, no fundamental length-scale is intervening in the probability equation description. Thus, this approach is scale invariant. The same selection statistics will apply when considering a STM probe approaching surface lattice atoms or when walking on brick pavements (how many atoms or bricks and how often will be accessed with the STM tip or foot, respectively)[19].

Let's take another example. Make an origami lattice and watch through a tube and check how many and how often lattice features one will detect. Scale down the origami and the tube and you are in the nanoscale statistical patterning regime. For an appropriate tube size and a hexagonal origami lattice one will detect very often only one feature. Increase a little bit the tube size and you will no more see only one, but more features, with finite probability. Further, whenever one will see more than one feature, they will not be arbitrarily placed with respect to each other; they will obey precise symmetry selection criteria. For examples, 3 features will be selected always in the C3v symmetry group as can be seen in Figure 3.15 (**d**). No other geometrical combination of 3 features will possible using a circular mask. Change the mask diameter as you want, the "green loci" will always be the result of the intersection of 3 virtual circles centered at the corners of the triangular unit cell.

For realistic statistical nanostructuring, the pores and the mask will no more be described by perfect circles and the regular arrangement will be disturbed. Interpretation will rely on a Gaussian distribution rather than on precise geometrical functions. However, important is that the analytical approach remains the same: by "expanding" the pores linearly with the mask size there will be always a finite probability for null- and double-nanopore patterning resolution at the maximum expectation of single-pore resolution. One of the key issues is to find the optimal in-

[19] This scale invariance is ubiquitous in science. Designing the photonic crystals (as decribed in Chapter 2) is very much similar in scaling conception with the present statistical protocol: one conceives the device at centimeter scale (microwave regime) and then transposes the design at the nanometer scale (optical frequencies) and it will work.

terplay between the lattice parameters and the geometry of the mask to minimize this effect and to maximize the single-pore resolution probability. Making a parallel to the honeycomb perfection, the hexagonal packing of the pores in a template seems to provide the highest probability to achieve the single-nanopore resolution using the statistical approach. For example, a perfect square lattice will have a maximum probability of $2\tan\frac{\pi}{8} = 0.828$ compared to $2\sqrt{3}\tan\frac{\pi}{12} = 0.928$ for the hexagonal lattice, provided that both of them are bearing circular pores (values obtained by solving the equation (4) at maximum: $d(P_1^{II})/d(D) = 0$). Interesting is that the probability of 0.904 obtained for single-pore resolution, calculated through simulation on the fabricated ordered templates (Fig. 3.13 (**c**)), is very close to the ideal value. This corroborates the high ordering degree of the template and highlights the robustness of the statistical procedure against the structural inhomogeneities of the template via smearing and averaging effects. Also, experimentally achieved resolution (using a short-range ordered template) is only 24% lower than the ideal value. Other important observation is the relationship between the peak position and the template structural parameters. For the perfect hexagonal packing, the single-pore resolution maximum is achieved at a mask diameter of $\frac{h}{\cos\pi/12} - d$. This indicates that aside the characteristic dimensions of the template h and d, lattice pattern infers and has a contribution as well (*i.e.* the $\cos\pi/12$ denominator originating from the hexagonal symmetry).

Though, it could be conjectured that the hexagonal lattice will provide the highest yield using the statistical patterning or selection approach, some exceptions may arise. For example, following the analytical protocol, if a combination of mask pattern, template features geometry and ordering will result in a hexagonal tiling (p6m wallpaper symmetry group) then, probability of 1 could be reached. Though in practice, this would be almost impossible to realize, systems approaching this perfection exists. For example, Masuda *et al.* fabricated AAO templates having hexagonal pores arranged in a hexagonal lattice [165]. Using a circular mask it is possible to achieve single-pore resolution as high as 0.96. Technologically, this translates into an increase in the processing complexity with a little gain in processing resolution reliability. Furthermore, downscaling AAO features while still preserving their geometry seems difficult. Recent progress in block-copolymer self-assembly showed that organization could be induced in patterns other than hexagonal using advanced engineering of polymer structure and composition. In the same manner as square arrays were possible to construct through supramolecular assembly of hydrogen-bonding units with controlled phase separation of di-block copolymers [91], it could be possible to obtain hexagonal

pores in the tens of nanometer size regime. Related to the Thue's theorem and the honeycomb perfection, the hexagonal lattice offers the most optimal template features arrangement for the statistical approach. So, even if it is possible to increase the probability by engineering the pore geometry or the masking design, the aspect of increasing the single-pore resolution to values higher than 0.928 will be an interplay between the process complexity and the application defect tolerance.

3.4.5 Counting threshold and process reliability

Up to this point we have detailed only one concern raised by the referee's report (see the first paragraph in Section 3.4.3). The second is detailed in the following. *Does the exposure of only a portion of the nanopore opening yield smaller diameter nanowires, or do we see an effect on the growth rate associated with the electrodeposition?* The answer to the first part of the question was no, because the diameter of the grown nanowires is set by the pore size. However, the second part was more intriguing. Indeed, what would happen if the overlapping of the mask with the pore will be only few nanometer across? Will the liquid penetrate and allow the electroplating in the respective pore and what will be the operation threshold in our case and in general? For example, for the situation schematically shown in Figure 3.16 (**a**) it is difficult predict the number of grown nanowires: 1, 4 or 6. One can be certain that a fully revealed nanopore will yield one nanowire. Partially revealed pores will more probably result as well in grown nanowires, hence there is a chance to access 4 sites. Accordingly, the probability plots will be affected as for the same mask size, the number of valid nanopores (or grown nanowires) will be different. We have analyzed these aspects and the obtained result was remarkable.

Careful SEM inspection of the fabricated masks revealed that the etching step is correcting the pattern shape and accomodates the frontier pores. As can be visualized in panels (**b**) to (**d**), the pores which in principle should remain covered by the nitride, are completely revealed. Moreover, sometimes, some of them were also exposed outside the masking area. This is attributed to the surface corrugation in the PECVD masking material and bowl-shaped profile resulting from the isotropic RIE step (panels (**e**) and (**f**)). The surface roughness will induce a non-uniform etching profile while bowl-shape will imply the SiN_x thinning at the bottom of the mask. Mechanical stability of the presumably created thin masking layer could play also a role in the process. Reacting gas penetration in the partially masked nanopores and subsequent "bottom" removal could explain also the complete removal as well as the presence

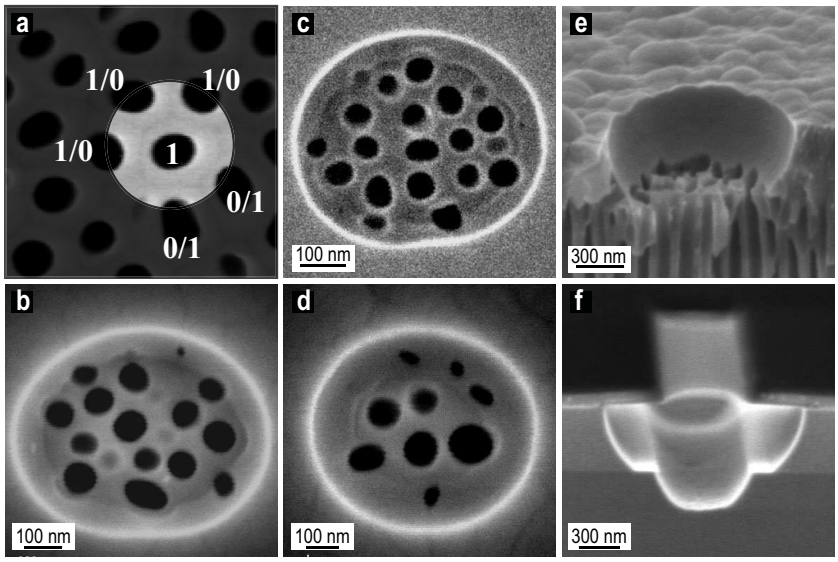

Figure 3.16: (**a**) Schematic representation of masking uncertainty. While the growth is clearly possible in the central pore, an incertitude for top (likely the grow will occur) and bottom (presumably no growth will occur) pores exists. (**b**) - (**d**) Top SEM views of self-repaired masks. The inclusion of frontier pores is visible. Sometimes, even outside mask area pores were revealed (**d**). (**e**) Crossection view of the same type of masks outlining the bowl-shaped profile. (**f**) Etched PMMA/SiN_x/Si stack using the same recipe. Uniform etching profile is visible.

of exposed pores outside the masked region (remember that the etch step is majoritarily reactive: high-pressure, low applied RF power and measured DC bias). A bottom-up Y-branched nanopore having only one branch exposed will allow the gas circulation also in the second branch (etching for the underneath) and hence, give the appearance of an outside mask revealed pore. For comparison, the etching profile on a flat Si substrate is given in panel (**f**). The PECVD layer is flat, the bowl-shape is present as well and the bottom profile is more uniform. Interesting is that the etching trench in the underlying Si reproduces well the PMMA mask shape, giving the impression that Si is etched anisotropically in SF_6 plasma, despite that it is generally known that the process proceeds in a highly isotropic way. Exception are known, for example, using SF_6/Ar microwave multipolar plasma operated at low pressures [166]. As it was not the main concern of this work, an in depth analysis was not performed; however it would be interesting to study this etching process

in detail.

Let's consider the computational approach and how see these parameters could be integrated. In the simulation, a counting threshold, ζ, was introduced. If the intersection of ROI with a pore displayed by the SEM image is less than the threshold value, defined as $\zeta \times A_{mean}$, the pore is accounted as 0, otherwise it is accounted as 1. The influence of ζ on the probability plots was calculated. For the simulation, SEM images describing the surface morphology of AAO used for the experimental statistic study were employed. This also allowed to determine the experimental value of ζ for the selective electroplating process.

The patterning probability distribution dependence is shown in Figure 3.17 (**a**). ζ was varied from 0 to 0.429 in steps of 0.039. Interesting to observe is that it has almost no influence upon the achieved resolution and the probability plots are resembling quite well. A quantitative analysis was done by fitting each plot using a Gaussian equation and comparing the fit coefficients. The obtained coefficients are shown in Table 3.2. It is clear that W_1 and W_3 remain constant (within the error range) and only W_2 increases. This signifies that the maximum value and FWHM of the distribution (closely related to W_3) are maintained constant for various ζ values and only the peak center position changes. In other words, the same probability could be obtained for various threshold values just by adjusting the mask size. Up to a certain value (depending on the pore size uniformity), ζ mainly induces a right-shift of the probability plots without altering the overall shape and the maxima values. Only once the area of pores are becoming comparable in size with the $\zeta \times A_{mean}$ value and hence, excluded from the simulation, the probability plots are affected and no more reflect the reality. This is schematically shown in Figure 3.17 (**b**), showing the distribution of the pore surface area on a typical short-range ordered AAO surface. The plot can be regarded as a replica of pore diameter distribution (see Fig. 3.13 (**a**)). The wide spread in the pore surface area, ranging from 1500 to 5800 nm^2 can be observed. The mean value[20], corresponding to the Gaussian fit peak is at $\sim$ 4000 nm^2. The minimum detected value for pore surface area is around 1100 nm^2. Hence, for $\zeta < 0.276$ (or $\zeta \times A_{mean} < 1100$ nm^2), all of the pores will be included in the simulation. As the simulation protocol is based on surface area comparisons and not on the shape recognition, for higher values, some of the pores will no more be included

[20] A careful interpretation is required for the short-range ordered templates. Due to a large spread in pore diameter, multiple images have to be analyzed and averaged to apply a Gaussian fit properly. Even so, discrepancies could arise. For example, in panel (**b**), we obtain $A_{mean} = 3650$ nm^2 using an arithmetical averaging method yet, the fit indicates a maximum at 4000 nm^2.

ζ	W_1	W_2	W_3
0	0.71	65.5±0.4	51.7±0.7
0.039	0.72	75.8±0.5	49.3±0.8
0.078	0.72	82.4±0.5	48.9±0.7
0.117	0.72	87.7±0.4	49.6±0.8
0.156	0.72	93.0±0.4	49.2±0.6
0.195	0.72	97.5±0.3	49.4±0.5
0.234	0.72	101.7±0.2	49.6±0.4
0.273	0.72	105.8±0.3	49.4±0.4
0.312	0.72	109.8±0.3	49.5±0.4
0.351	0.72	113.9±0.3	50.4±0.4
0.390	0.71	118.1±0.2	51.4±0.3
0.429	0.71	122.0±0.2	52.2±0.3

Table 3.2: Gaussian fit coefficients for the simulated probability plots presented in Figure 3.17 as a function of ζ. The fit function is $P = W_0 + W_1 \exp \frac{-(D-W_2)}{W_3}$, where $W_0 = 0$ and P, D are the probability and mask diameter, respectively. W_1 indicates the achieved probability and W_2 peak position.

in the simulation[21]. This signifies that fewer pores will be included in the simulation and the shape of probability plots will start to change. In Figure 3.17 (**a**), ζ values as high as 0.429 have been used, indicated in panel (**b**) by the vertical arrow. The pores having the surface area lower than this value have been not simulated. However, as only 5% of pores have been excluded, the probability plots are only slightly affected.

Giving the fact that small variations in ζ induce a horizontal shift in the probability distribution, it would be difficult to ascertain the experimental ζ value during the selective electroplating process (see Fig. 3.12). The MSE between the experimental and simulated distributions for each patterning resolution, function of ζ was calculated and is represented in Figure 3.17 (**c**) (following the same color code). Each plot is characterized by a minimum centered at a different ζ value. Negative values have no physical signification. The fact that in some cases MSE minimizes for $\zeta < 0$ is due to the experimental errors (as already detailed). As the simulated curves are shifted uniformly with ζ, the sum of all errors gives

[21] Suppose that you use $\zeta = 0.33$, signifying that surface area for the intersection of the mask with the pore has to be larger than 1320 nm^2 to account, by definition, the pore as 1. However, if some pores are smaller in surface than the respective value, even if they are completely encircled by the ROI, they will be counted as 0 (surface area pondering instead of shape recognition).

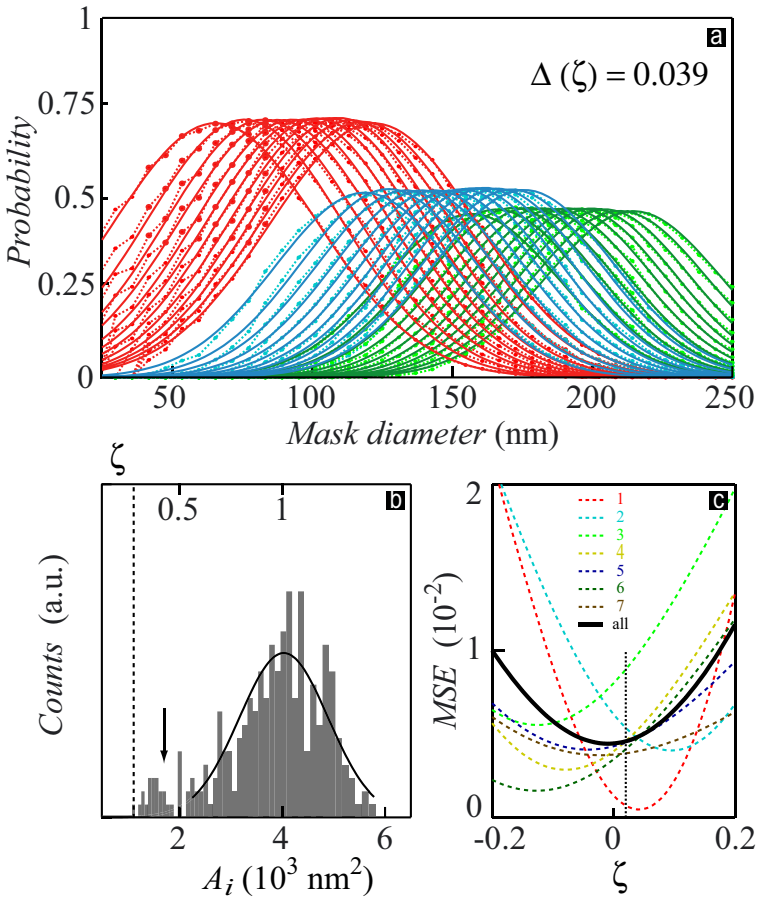

Figure 3.17: (**a**) Probability plots function of ζ. The short-range ordered AAO template was simulated. The morphology is the same as for the statistical experiment (Figs. 3.12 and 3.13 (**a**)). Only, 1-, 2- and 3-nanopore resolution are represented. (**b**) Distribution of the nanopores surface area (bars) and the Gaussian fit (line). By definition, $\zeta = 1$ corresponds to the peak maximum in the Gaussian fit or A_{mean}. The dashed vertical line shows the ζ value for which all of the pores are included in the simulation. Arrow indicates the maximum value used for simulations presented in panel (**a**). (**c**) Calculated MSE function of ζ for the experimental statistical histograms and respective simulated data.

the overall MSE dependence (black line). In correlation with the SEM observations of self-repaired masks, ζ value for the selective electroplating process using the described protocol is found to be 0 (or at least close to 0 for 1- to 7-nanopore resolution). To calculate the absolute value, more parameters need to be taken into account: mask size uncertainty,

fraction of branched nanopores in the analyzed templates as well as the probability of nanowire removal during the subsequent processing steps. What is important, is the minimal influence of ζ on the achieved probability. For an increased ζ value the same probability could be revoked by increasing the mask size. This behavior can be simply explained using the analytical representation (Fig. 3.15). Increasing the threshold value translates into a decrease of the apparent pore diameter and, accordingly, a decrease of the size of the virtual circles defining the probability surface plots. Obviously, this can be recalled by increasing the mask size[22].

3.4.6 Statistical processing

The presented statistical approach is very important for the AAO structuring process and single-nanowire device fabrication adopted in this work. Primarily, this analysis provides a simple protocol to determine the mask size to be used and the number of grown nanowires. As the electroplated nanowire(s) remain embedded in AAO, it is difficult to determine their precise number. However, the size of the patterned mask can be measured without deteriorating the architecture integrity[23] and the probability to grow a given number of nanowires can be inferred. Using electrical measurements it is possible to ascertain precisely the number of contacted nanowires and not of grown nanowires.

Many developed nanotechnologies are using the templates to grow advanced low-dimensional systems and then, "destroy" them and finish with a disordered system requiring further processing. Further processing means dispersion on a new substrate and contacts realization. There are however methods (aside the presented selective AAO electroplating protocol) which are statistical by their nature. Scanning probe interrogation on single nanostructures fabricated and embedded or not in the original template is one approach. For example, Piraux *et al.* have used AFM tip indentation to create nano-sized holes in a insulating polymer film with the prospect of electrically connecting single nanowires fabricated and embedded inside AAO (Figure 3.18 (**a**)) [67]. Lee *et al.* have used a slightly different approach. They employed block copolymers templates as confined media for electrochemical growth of various

[22]The x-axis shift (or the increase in mask diameter value to achieve the same probability) function of ζ value is related to the surface area of circle-circle intersection.

[23]It is worth mentioning here that while the EBL can provide a precise control over the pattern size and shape, the employed RIE step proceeds in a non-uniform way, hence a direct correlation between the designed pattern and final mask size is difficult, SEM inspection of the etched hole being preferred.

conducting polymers and after matrix removal, used a current sensing AFM probe to measure single polymer nanorods (Figure 3.18 (**b**)) [25]. Both approaches could operate the SPM in conducting and morphology imaging mode, to ascertain for single objects. Interesting, in both papers, some approximations correlating the probe diameter with the template morphology were done. Based on them, the authors considered their measurements as representative for single objects yet, without any in-depth statistic analysis. But their methodology, fundamentally, is identical to the presented statistical selective AAO structuring: arbitrary placing a probe on a template surface is the same as the described AAO masking process. Using more tips, large areas could be scanned

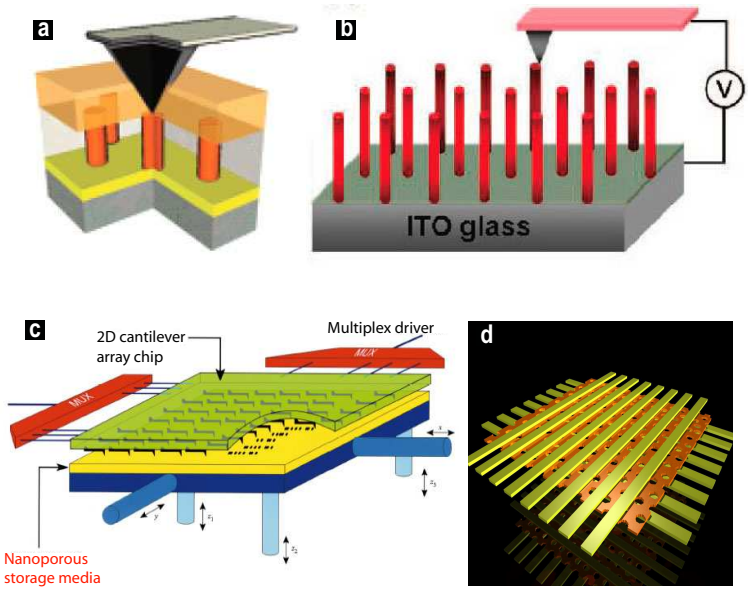

Figure 3.18: (**a**) SPM nano-indentation approach (reproduced from [67]). (**b**) conducting - AFM interrogation of template free, supported polypyrrole nanorods (reproduced from [25]). (**c**) Schematic view of the Millipede concept (reproduced form [167]). (**d**) The envisioned cross-bar latch integrating porous membranes.

and parallel interrogation of single nanowires could be possible. Parallel actuation of thousand of AFM tips is not new, as the concept, called "Millipede", proposed by IBM, is in its prototype version since 2000 [167]. It was presented as a new data storage vision having a potentially ultrahigh density, terabit capacity, small form factor and high data rate. Its potential for ultrahigh storage density has been demon-

strated by a new thermomechanical local-probe technique to store and read back data in very thin polymer films. In addition to data storage in polymers or other media Millipede may open up new perspectives and opportunities in many areas in nanotechnology as envisioned by its fathers. Why not using nanoporous materials? Confining the material of interest in the template nano-channels and then statistically probing them with thousand of tips operated in parallel seems feasible. Moreover, a plethora of active materials (metals, semiconductors, polymers, organic molecular assemblies and so on) and effects (electric, magnetic or optic) could be exploited without any evident impediment for the characterization and easily adaptable to any desired specific application[24]. Increasing the ordering, the single-element resolution could be increased up to 92%, though short-range ordered templates are good as well by providing 70% reliability to achieve the same resolution.

Furthermore, as already nuanced, a square mask provides very strict selection rules as well. This geometry can be regarded as the product of intersection of 2 orthogonal stripes. Structuring both on the same side of the template may have no technological relevance. Patterning them on different sides of the template completely changes the architecture significance. In this configuration, it can be regarded as a cross-bar latch node. Multiple lines could be criss-crossed and if their size adjusted accordingly to the template structural parameters, a high prospect of contacting primarily single nanostructures could be achieved. Many materials could be integrated and the high throughput nano-fabrication is complemented by the parallel characterization. Extending further the concept, as relatively high probabilities to address single nano-structures in high-density matrices is possible, the method could be an alternative for TERAMAC defect tolerant computing architectures [168–173].

One final interesting aspect is the mentioned counting threshold or ζ. While for the selective electroplating it was found to be close to 0 due to the shape correction of the mask during the etch step, we may not be so lucky with other applications. Using the SPM's approaches or filled porous templates the self-repairing is no more possible. For example, a reliable electrical connection will require some contact area and ζ will have a finite value to account for that. Certainly, ζ will be process dependent. Nevertheless, as already explained and shown in Figure 3.17, it influences only the peak position and not the patterning probability. Technologically, this implies that the same single-pore selection reliability can be achieved for different threshold values just by adjusting the

[24]For example, the thermomechanical local-probe technique used has still unresolved technical issues, the irreversible polymer degradation being the main concern.

mask size.

3.5 Single nanowire crossbar devices

Now, I switch from the task of growing single nanowires to the task to electrically connecting them at the both extremities. Basically, the type of active material deposited inside the nanopores will dictate the employed strategy for the subsequent contacting method and it would be difficult to establish a general approach. This work was initially focused on the fabrication of various magnetic devices in cross-bar latch architectures[25]. To build such devices, metals such as Ni, Co, Cu or $Ni_{20}Fe_{80}$ alloy are usually employed. The bottom contact with the Au pads is formed during the electroplating and remains protected from the corrosion or oxidation by the subsequently deposited metal. It is the top part of the nanowires that poses problems. The cited metals are known to form and oxide layer on their surface once in contact with air and moisture. The oxide barrier layer has to be removed, otherwise it will deteriorate the electrical characteristics of the devices. Terminating the electroplating with a noble metal is an alternative, yet it complicates the electrochemical processing by requiring the use of different electrolyte baths.

Two approaches have been envisioned at the beginning. The first is based on the oxide layer removal prior the top contact metal deposition. *In situ* etch and metal deposition could be performed only in

[25] A primary problem in cross-bar latch architectures is the crosstalking. The term crosstalk refers to any phenomenon by which a signal transmitted on one circuit or channel of a transmission system creates an undesired effect in another circuit or channel. In the cross-bar latch architectures this phenomenon is imminent. Applied signal to one cross-point propagates all over the circuit being susceptible of influencing other cross-points (destroying the bits during the write erase steps). There are few methods to avoid such undesirable effects. The simplest is the construction of $1 \times n$ architectures which are very useful to characterize the electrical properties (Here, 1 row $\times$ 6 columns). For example, a specific location can be written by applying a programming voltage or current to the selected row, while maintaining all the unselected rows and columns at one-half of the voltage of the selected row [174–176]. That specific location is further read by applying a read-voltage to the selected row with all unselected rows and columns at 0 V, and reading the current in the associated column. Current rectification in such devices is an attractive property, because it can minimize cross talk between individual elements in arrays. The rectifying element can be intrinsic to the device or additional processing can be done to add diodes at each cross-point [177, 178]. As preliminary experiments were performed on metallic nanowires (with no rectifying behavior) and that building additional rectifying elements on the fabricated devices will require further work, the first option was adopted.

a sputtering system, implying an *Ar* strip step. As the electrodes are lithography defined, the processing necessitates thick, over-exposed bi-layer resist stacks to whitstand the etching step and the conformal metal deposition for a good lift-off. The second, which was finally the working option is based on the use of a self-contacting layer. As it is detailed in the following, this approach allows for statistical control of the number of grown nanowires and concomitantly for a precise control on the number of connected nanowires.

The design of the top electrical connection is based on 2 important steps: (i) realization of the self contacting layer and (ii) top electrode definition. Both are based on the same fabrication principle. EBL over-exposure of thick double layer resist stack to obtain a pronounced resist undercut and variable angle metal deposition.

3.5.1 Self-contacting layer definition

A thin metal film was patterned in the areas where the selective electroplating will take place. The SCL should be thin enough to avoid clogging the pores, yet thick enough to remain electrically continuous. During the electroplating, the first emerged nanowire will contact this layer and further electrodeposition will take place as well on the SCL. This has several implications: (i) the plating current density in the rest of the pores diminishes reducing the growth rate for the remained nanowires, (ii) at the same time, the pores are rapidly clogged with the new electrodeposited material and (iii) the electrical contact is "naturally" formed and remains protected by the re-deposited metal. Subsequently, it is enough to contact this layer to have access to the nanowire.

In principle, EBL and metal evaporation could be enough to realize that. Yet, due to the specific morphology of the AAO it was decided to use double-angled evaporation through a large undercut in the resist layer. This step was done in order to confine the SCL only on top of the AAO membrane. As already mentioned, AAO templates can be also used as physical vapor deposition mask if pores are aligned parallel to the incoming beam [84, 179]. The successful use of AAO stencil masks as thick as 500 nm have been reported. This means that the metal could penetrate to that depth along the pores. The difficulty comes from the fact the penetration is expected to occur in a non-uniform way and the pores sidewalls to be "contaminated" by metal to different extents (depending on their diameter and orientation)[26]. Using angled

[26]The first tests were done using normal metal deposition and lift-off. During the electrodeposition, large anomalies were detected from sample to sample. The estimated thickness (or the height of nanowires) for the deposited metal before reaching

evaporation, the thickness of the SCL could be confined only to the top of the pores with very few variations mainly depending on the pores diameter. Thus, a better reproducibility was possible.

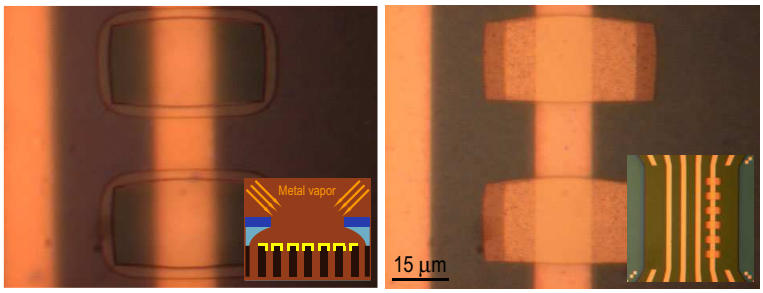

Figure 3.19: Top-view optical micrographs of the overexposed resist (left) and patterned SCL's (right). Insets: schematic view of the angled evaporation technique (left) and close-up on the central part of the chip after the SCL definition.

Angled evaporation implies a special design of the used resist mask. Normal profile will fail in a correct processing as the deposited metal in the patterned area will not be interrupted from the metal deposited on the rest of the resist. This will result in a difficult lift-off with many defects, especially in the formation of the retention years. For that, a highly overexposed, double layer resist stack was used (2 μm PMMA(8.5)MAA and 1 μm PMMA). Even when evaporating metal at 45° tilt, there is no continuity between the metal deposited in patterned area and on the resist. Subsequent lift-off is performed without any difficulty and no special treatments.

Examples of the used masks and obtained SCL's are shown in Figure 3.19. The large undercut is clearly visible and it extends in the PMMA(8.5)MAA for 3 - 5 μm with respect to the top PMMA layer. For a 3 μm resist stack, a 3 μm undercut is already enough to evaporate metal at 45° tilt. The sample tilting was performed *in situ* and 2 + 2 nm of Ti followed by 20 + 20 nm of Au[27] were evaporated successively at ± 45° with respect to the sample normal. The sample was placed such that the beam arrival direction was perpendicular to the BE's axis. From geometrical considerations, the maximum penetration depth of metal along

the SCL (observed by sudden jumps in the electroplating plots) varied from 200 to 800 nm making impossible a reproducible processing.

[27]Treating the film thickness as the height perpendicular to the substrate plane. Physically, due to the 45° tilt, $2\sqrt{2} + 2\sqrt{2}$ nm of Ti followed by $20\sqrt{2} + 20\sqrt{2}$ nm of Au were evaporated.

the pores is equal to the pore's diameter (here, $\sim$ 80 nm).

After lift-off removal of the remained resist, the samples were processed for the selective growth of nanowires only on top of the SCL[28]. PECVD was used to protect the AAO surface by 300 nm thick SiN_x deposited at 150°C. EBL was subsequently used to define 100 nm holes in a 200 nm thick PMMA layer and then the pattern was transfered to the SiN_x layer using RIE as already described. The samples were over-etched: 9 minutes instead of expected 6 minutes. At this stage, 6 selective electroplating masks with a nominal diameter of $\sim$ 300 nm are present only at the center of the SCL's on the working BE.

After a short soak in H_3PO_4 0.5 M at 30°C for 5 min (the post-enlargement step), Ni was selectively electrodeposited. This brief enlargement step is mainly done to "rehydrate" and "clean" the AAO pores sidewalls after being so long exposed to air and to various process chemicals. As an extremely reduced number of nanowires are plated on each sample ($\sim$ 50 as expected by the processing statistics) caution is required. The plating current is of the order of few nA (if no parasitic growth sites are present). To increase the signal to noise ratio the electrochemical cell is placed in a Faraday cage. Once the nanowires are contacting the SCL's, small jumps in the plating current could be observed (not shown here). Typically, all of the 6 SCL's are connected. A Ni "mushroom cap" is also formed on each plated area. At this stage, the samples are ready for final processing namely, the top contact definition.

3.5.2 Top contact definition and SCL statistics

As the Ni is known to oxidize slowly in air, direct patterning of TE's will fail in the realization of a good electrical connection as it has to be realized through the oxide layer. Hence, the SiN_x film protecting the SCL slabs was removed (using the same recipe as for its etching). This exposes the underlying gold film which is electrically connected to the nanowire(s). Thus, the nanowires are actually connected through the SCL.

Due to the sharp bent profile of the patterned AAO film (see Figure 3.7 (**b**) and (**c**)) angled metal deposition was again required. The preparation and exposure protocol is identical to that for the SCL patterning with the exception of the pattern design (lines connecting the opposite TE's precursor pads and covering the SCL area). A $\pm 45°$ tilt angle was used to deposit 1 μm of Al[29]. An example of conformally coated AAO

[28] Which, obviously, were defined on top of the operational BE's for further processing (see Figure 3.7 (**a**)).

[29] To avoid any metal accumulation at the AAO slab edges, the sample tilt was

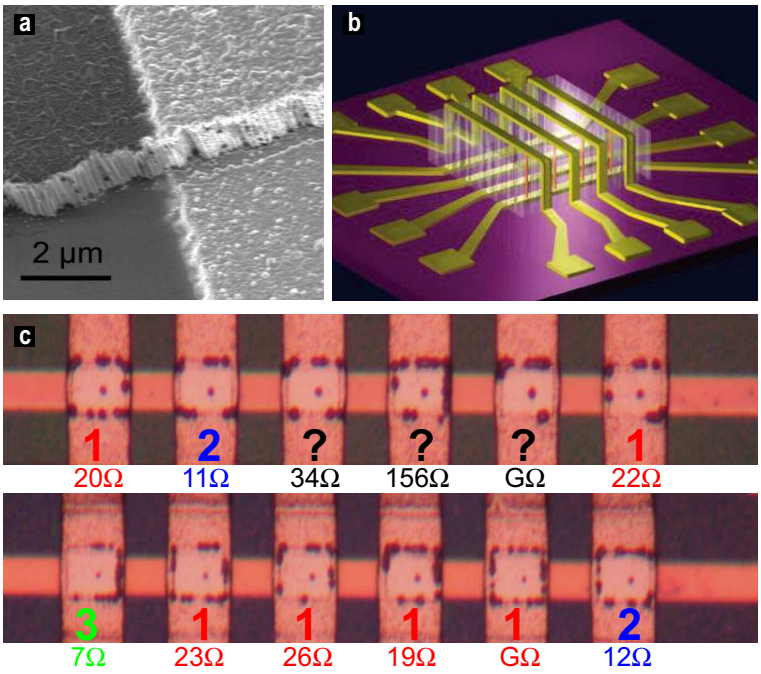

Figure 3.20: (**a**) Tilted SEM view of a TE surmounting the AAO edge. Shadowed area during angled metal deposition is visible. (**b**) Schematic view of the final device. (**c**) Optical micrographs of two fabricated 1×6 crossbar devices. The central black spots are the cap of flooded nanowires. Due to a defectuous processing, the growth can be observed as well on some parts of the SCL. A 50% yield to connect a single nanowire is achieved.

step edge is shown in Figure 3.20 (**a**). Thick metal coating was used because of the relatively non-uniform profile of the AAO slab sidewalls. This step in principle finishes the processing and a crossbar devices with single nanowires connected at each cross point is obtained (panel (**b**)).

Even if an increased number of defects in the contact area was detected, the preliminary results are promising[30]. The resistance of each cross point was measured in a pseudo-4-contact configuration in DC

switched after each deposited 20 nm. Again, the film thickness is measured normal to the substrate and physically 1.414 μm of aluminum was evaporated.

[30]For the respective samples the SCL patterning step was problematic. Metal particles originated during the lift off protocol sedimented on the SCL area and their removal was unsuccessful. Hence, the SiN_x deposit didn't conformally coated them and in the following processing steps parts of the metal were exposed. Probably, the growth on those area occurred once the SCL was electrically contacted by the growing nanowires.

mode. The expected resistance for 1 single Ni nanowire (bulk resistivity 7×10^{-8} Ωm, 80 nm diameter and 1.5 μm) is 21 Ω. On 6 crosspoints, approximately the same resistance was measured (as noted in the Figure 3.20 (**c**)). The small variations could be attributed to differences in contact resistance as well as variations in the nanowire diameter. Deficient sites have been also detected as well as double or triple connected nanowires sites. It seems that the SCL has a "cheating" effect on the growth "gambling": it reduces the contacting statistics to 1 nanowire. Thus, it is possible to statistically control the number of grown nanowires and contact only 1. This can be important for applications were the environment of the analyzed nanowires is important (thermalization, mutual influence or coupling). Further work will be required to in depth analyze the self-contacting statistics.

3.6 Conclusion

In this Chapter we have primarily presented a full processing path for single nanowire devices using AAO templates. Various approaches for the AAO micro- and nanostructuring have been developed to ensure a facile fabrication. The processing demands are fairly well compatible with the present CMOS requirements and a future co-integration is not to be excluded. The AAO morphology is fully exploited by keeping the nanowires embedded, offering physico-chemical stability and enabling vertical structuring. We developed a statistical approach to structure porous materials with high potential for nanotechnology. The exemplification is done using a porous alumina membrane but as the theoretical model is dimensionless the concept is of applicability at any scale. We stress that this line-of-thought is not limited only to the porous materials but could be generalized to any lattices. Interrogation of single - elements from various arrays of particles, wires, pores, tubes or of any desired objects, sizing from nano- to, let's say, origami-scales, could be performed easily using a single unified approach as described in this Chapter. For sure, at the nanoscale this is of great interest.

Chapter 4

Polymer templates

> Simplicity is the ultimate sophistication.
>
> *Leonardo da Vinci*

4.1 Why EBL templates?

The previous Chapter presented techniques and approaches to structure AAO nanotemplates. Although such self-assembled porous materials can be finely tuned, there is still a limited range over which the modifications can be made. For example, we will not always strive for a hexagonal pattern, which represents the typical arrangement in self organized systems. Square or mixed-pattern lattices could be very useful, yet difficult to realize through self-assembly. The things may get worse if we would like to design defects in a photonic crystal structure. Coupling a quantum wire or a cavity to a photonic crystal will require a great deal of work and accuracy; yet, all of them are made using regular arrangements of dielectric material. The experimental approaches described in the previous chapter (patterning and single nanopore-resolution structuring) could solve these issues. However, the complexity of the process increases and simpler solutions are welcome. A final, practical aspect of the problem is that the fabrication of the self-assembled structures requires extended materials knowledge or advanced experimental setups.

Let's consider lithographic approaches summarized in Table 4.1. If one would consider a relatively thick resist film, irradiate small-diameter dots and reveal the exposed areas he will end-up with a material bearing void channels (air) in a dielectric matrix (the remaining resist film). Much more alike a porous material. Interestingly, we can fill-up the voids with a given material and fabricate an inverse replica of the template or

transfer the pattern from the resist film to the substrate resulting in a porous material. Obviously, with this approach the pattern design can be readily changed to satisfy the application demands. Characteristic dimensions can be easily down-scaled to sub-10 nm region and pattern densities as high as 1 Teradot/inch^2 [180, 181] could be obtained. Also, patterning single- or a specific number of nanowires at predefined positions becomes more easier. However, there are some technical and material related limitations to this approach:

- **Achievable resolution.** For example, high-resolution, sub-50 nm patterning can be achieved either using EBL, nanoimprinting, or electron projection lithography.

- **Aspect ratio of the template channels.** This is typically bellow 100 and it is mostly dependent on the penetration depth of the used irradiation.

- **Pattern transfer and stability.** Due to the chemical nature of this type of templates (usually organic materials) this aspect is troublesome. Typically, mild processing conditions are of applicability: reduced temperatures and resist specific chemistry. Moreover, intermediate steps are sometimes required (e.g. transitional masking layers) and subsequent processing and stability of the resist encapsulated devices is delicate.

In the following Chapter we will deal with EBL nanofabricated templates and their subsequent utilization for the ultimate resolution structuring of the polyaniline. After few general considerations, challenges in the ultra-high resolution lithography will be presented. As throughout this thesis the *e-beam* structuring of PMMA-based resists has been extensively used and improved, an emphasis on their state of the art is given. The operation principle and the implications of the novel resist- and dose-modulated 3D EBL technique are presented. Subsequently, we will detail the electroless polymerization of aniline: the growth mechanism, the engaging implications and the optoelectronic properties of the synthesized material are discussed. Finally, we will show that by converging EBL nanostructuring with the electroless polymerization polyaniline, nanoarchitecturing with an unprecedent structural control can be achieved. This enables the design and the realization of a series of devices and circuit elements based on single polyaniline nanowires.

	Tool	Application	Resolution	Cost
Optical Lithography	Mask Aligner	Small batch R&D	500 nm	0.5 M$
	Laser Direct Write	Production Small batch	500 nm	0.3-2 M$
	Stepper	Production	100 nm	5-10 M$
Next generation methods	EUV, XRL, SCALPEL	Production	<50 nm	>10 M$
Printing techniques	Nanoimprinting, MIMIC, μCP	Small batch R&D	<10 nm	<0.5 M$
EBL	Mask fabrication	Production	50 nm	>5 M$
	Direct Write	Small batch R&D	< 10 nm	<0.1-5 M$
Scanning probe techniques	STM, AFM, Dip Pen	R&D	<10 nm	<0.5 M$

Table 4.1: Overview of modern lithographic techniques. It is almost evident that a direct write EBL offer the most balanced lithography equilibrium between the price (including the maintenance and overall processing costs) and the patterning resolution. Although it is a serial method and sometimes it is regarded as a low throughput and costly technique it clearly presents many advantages: (i) very high resolution, almost to the atomic level for R&D applications and small batch production; (ii) established top-down technology; (iii) simple change of design rules; (iv) easiness for next generation device process development. A careful analysis reveals that all the rest of techniques (excluding the scanning probe approaches) are at some point dependent on the EBL as they will require the master or the mask fabrication.

4.2 Electron beam lithography

Electron beam lithography is a specialized technique for creating extremely fine patterns. It has its origins from early scanning electron microscopes; adequate, highly specialized tools have been developed since[1]. The technique consists in scanning a beam of electrons across a surface covered with a resist film sensitive to those electrons, thus depositing energy in the desired pattern into the resist film. The first electron beam lithography machines were developed in the late 1960's. Shortly thereafter came the discovery of PMMA as an excellent electron beam resist [182] and the EBL became one of the most powerful tools for micro- and nanoscale processing.

[1]Though, even nowadays, much work continues to be done on converted SEMs.

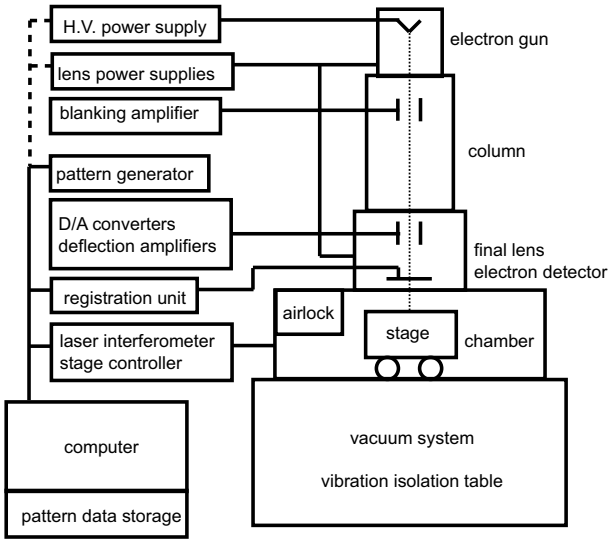

Figure 4.1: Schematic diagram showing the main components of an EBL system. Reprinted from [183].

Fig. 4.1 shows the block diagram of a typical electron beam lithography tool. The column is responsible for generating, accelerating and scanning the electron beam. In a SEM, the beam is scanned uniformly all over the surface. Underneath the column is a chamber containing a stage for moving the sample around and facilities for loading and unloading it. The stage is controlled by piezo-DC motor hybrid technologies using a set of laser interferometers to achieve sub-10 nm positioning control by software and visual inspection. Associated with the chamber is a vacuum system needed to maintain an appropriate vacuum level throughout the machine and also during the load and unload cycles. A set of control electronics supplies power and signals to the various parts of the machine. Finally, the system is controlled by a computer, which may be anything from a personal computer to a mainframe. The computer handles diverse functions such as setting up an exposure job, loading and unloading the sample, aligning and focusing the electron beam, and sending pattern data to the pattern generator. Throughout this work two systems have been used for EBL structuring:

- A modified FEI XL30 SEM (PHILIPS) with ELPHY Plus package and compact laser interferometer controlled stage (RAITH). The maximum acceleration energy is 30 keV. The system is semiautomatic: manual load-unload, semiautomatic exposure and align-

ment protocols. Electron optics does not allow high electron beam currents for small beam sizes. Typical high-resolution lithography uses 50 pA beam current. It accommodates maximum 3-inch samples.

- A high resolution electron beam lithography system JBX-9300FS (JEOL). The maximum acceleration energy is 100 keV. The system is fully automatic. Electron optics allows higher electron beam currents for small beam sizes. For example, higher resolution (than the previous case) lithography is possible using a beam current of 1 nA (20 times faster)! It accommodates up to 8-inch wafers with an autoloader capacity of 2 cassettes.

4.2.1 General considerations

In the following we will analyse the fabrication of nanometer sized porous templates using EBL. The considered example is based on PMMA as the electron sensitive material, deposited on a 10 nm thick platinum film. In a first approximation, we will use Si as the substrate. The usage of the platinum film will be justified in the following sections. *Suppose that we would like to fabricate 50 nm diameter channels, having a spacing of 200 nm in a 1 μm thick resist.* Even if the modern EBL tools are guaranteed to provide sub-50 nm resolution, would it be possible to realize the envisioned structure in every type of machine? The first thing to check is the penetration depth of the electrons and related to that, the spatial profile of the forward and backward scattered electrons. Intuitively, this is correlated to the acceleration energy. The incident electron penetrates into the resist on a substrate and undergoes complicated scattering processes, in which the incident electron loses its energy due to inelastic collisions. For practical application to EBL, the spatial distribution of energy dissipation is the most important quantity.

The theoretical prediction of electron trajectories in the defined multilayer sample is realized using a Monte Carlo simulation using the CASINO software[2]. Monte-Carlo simulations have become basic methods for theoretical studies of EBL, such as proximity effects [184], spatial ultimate resolution and the optimum of exposure conditions. The complex single scattering Monte Carlo program is specifically designed for low energy beam interaction and can be used to generate many of the recorded signals (X-rays and backscattered electrons) in a SEM. The main idea is

[2]The CASINO acronym is been derived from the word "monte CArlo SImulation of electroN trajectory in sOlids". It is a free ware software developed by the research team of Raynald Gauvin (Ph.D., Full professor at Université de Sherbrooke, Québec, Canada). http://www.gel.usherbrooke.ca/casino/

to simulate enough electron trajectories to represent the realistic conditions used to image structures by SEM. The described stack has been subjected to the virtual exposure and the result is depicted in Figure 4.2. Applying a step-function cutoff filter to the computed distribution provides a simple way to approximate the resist decomposition and developing processes. With such a filter, it is possible to achieve quantitative agreement between the predicted and observed profile in the resist film. In a simple representation, the "dense blue" areas can be regarded as the completely removed areas after the exposure and the development. Only 500 electrons per exposed area have been used in the simulation for the simplicity. This is the equivalent of an exposure dose of approximately 3 μC/cm^2. In practice, 100-300 μC/cm^2 is the working window at 30 keV acceleration energy. Even so, the data can be considered valid.

4.2.1.1 High vs. low electron energy

As can be visualized in the Fig. 4.2, the electron beam energy has a drastic influence upon the penetration depth and the scattering profile. At 5 keV acceleration energy, the electrons barely penetrate down to the half-thickness of the resist stack. The simulation does not include the charging effect, which is very significative at low beam energies and the real profile will be more blurred. One thing is clear: at this energy, it is impossible to fabricate the envisioned structure (PMMA-based porous membrane with 50 nm diameter void channels in a 1 μm thick resist and pitch of 200 nm). By using thinner resist it is possible to fabricate distinct structures, though, with lower aspect ratio. Nevertheless, the low energy exposure has some intrinsic advantages. For example, it is an excellent option for high-sensitivity resists as it requires very low exposing times and thus ensures a high throughput. The proximity effect is negligible and has a very low damaging effect on the resist and substrate. The reverse side is that, as it requires very thin resist films, it complicates the pattern transfer. One interesting aspect is the ability of 3D resist shaping using low-energy beams. Let's take a look again at the upper panel of the Fig. 4.2. Removing the exposed area in a developer will result in a local resist thinning. Varying the energy (or the penetration depth) along a horizontal line will provide a 3D resist profile after subsequent processing [189]. The approach is not straightforward as changing the acceleration energy implies readjustments of the column optics and the overlay alignment can be loosed. Other, more easier to use, 3D EBL approaches will be discussed further.

At 30 keV the picture changes. The electrons have now sufficient energy to penetrate completely the resist. However, forward and back-

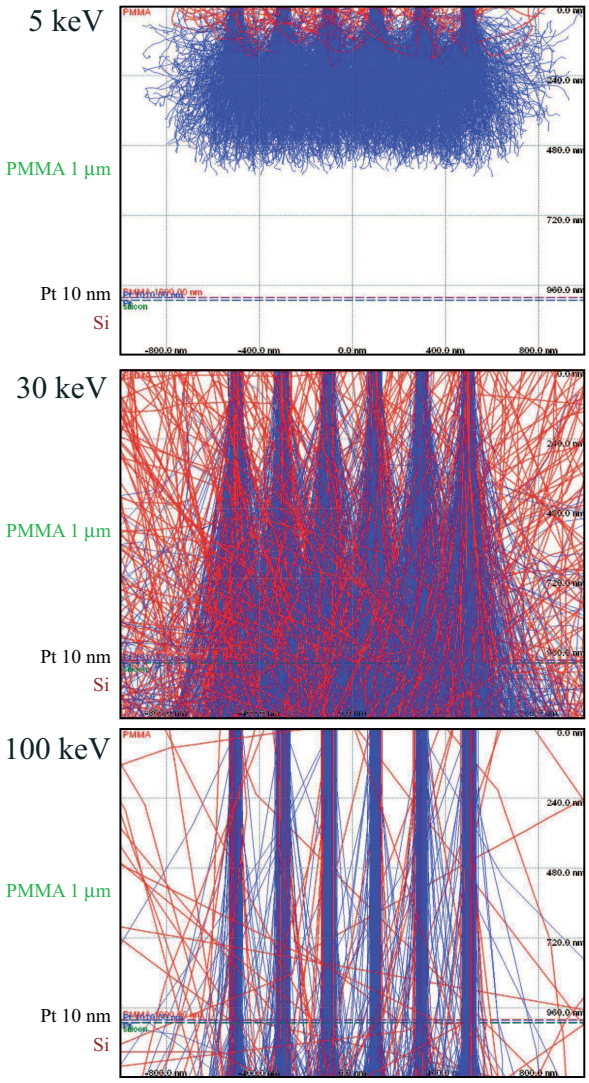

Figure 4.2: CASINO simulation of the PMMA (1 μm) / Pt (10 nm) / Si (substrate) stack exposed to different energy electron beams. The beam radius is 50 nm and the spacing is 200 nm. 500 electrons have been used for the simulation. The program uses different models to simulate the interaction of electrons with a solid [185]. The following physical model was used here: total cross section and partial cross section - Mott by interpolation; effective section ionisation - Casnati [186]; ionisation potential and dE/dS calculation - Joy and Luo [187]; random number generator - Press *et al.* [188]. Blue and red lines are the trajectories of forward and backward scattered electrons. The collision points are omitted for the simplicity. Plot scale: X axis = 2200 nm and Y axis = 1200 nm.

ward scattering and associated proximity effects are important making impossible to fabricate closely spaced channels. The range of 15 - 30 keV beam energy is one of the most used in the EBL systems. Therefore, physical models are continuously developed and improved to correct these complex and unwanted phenomena.

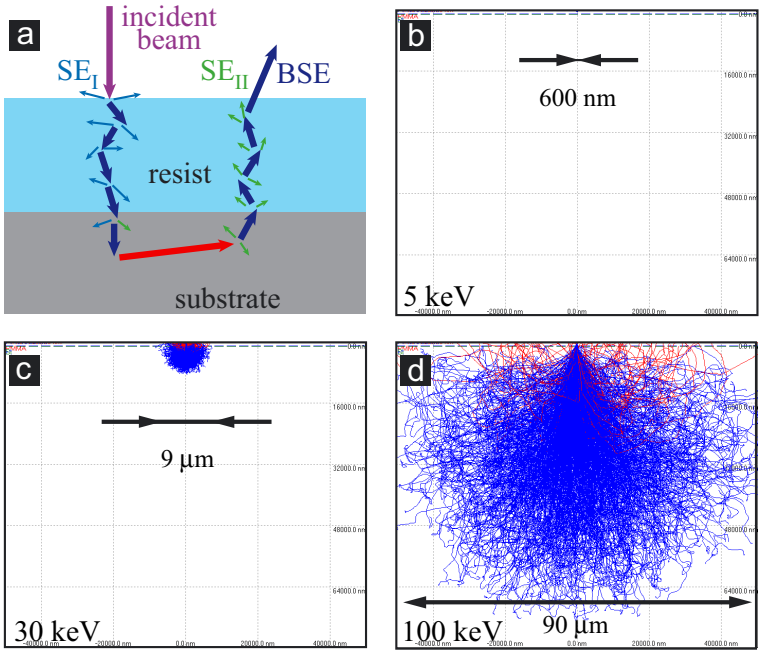

Figure 4.3: (**a**) Schematic representation of the electron-material interactions. Big and small arrows are the high- and low-energy electrons, respectively. The spatial distribution is very dependent on the beam energy. (**b - d**) Wide view (X axis = 100 μm, Y axis = 80 μm) of the impact generated by different electron energies. Electron beam size is 50 nm. Scale bars on each image are representing the area affected by the proximity effect. Back scattering coefficients are: 0.046, 0.157 and 0.11 for 5, 30 and 100 keV, respectively.

At this stage is worth mentioning few words about the resist and substrate interactions with the electron beam. Primary, as already mentioned, the incident beam suffers from forward and backward scattering. The first (blue trajectories in Figs. 4.2 and 4.3), occurs very often, is an inelastic process and generates secondary electrons with a few-eV kinetic energy. The few-eV electrons are very important as they are actually responsible for most of the resist exposure. An empirical formula can be used to calculate the increase in the effective beam diameter due to forward scattering. If R_t is the resist thickness in nanometers and

V_b is the beam voltage in kilovolts then the widening of the beam in nanometers can be approximated as $d_f = 0.9(R_t/V_b)^{0.9}$. Important to note that this is only the widening of the beam and not the profile of the final shape after the subsequent processing. The second type of scattering (red trajectories in Figs. 4.2 and 4.3), takes place occasionally, is an elastic process and generates high kinetic energy electrons (in the range of primary electrons). These electrons will further produce few-eV electrons through forward scattering but far from the incident beam region (the origin of the proximity effect). The distribution of the resist exposure can be estimated using the energy deposition function $F(r) = k\{\exp[-(r/\sigma_f)^2] + \eta(\sigma_f/\sigma_b)^2 \exp[-(r/\sigma_b)^2]\}$. The distributions of scattered electrons can be approximated as Gaussians with σ_f and σ_b being the characteristic widths for the forward-scattered and backscattered electrons, respectively [190]. Here r is the radial distance from the exposure center, η is the ratio between the energy dissipation of backscattered and incident electrons along the beam axis, and k is a constant used to normalize $F(r)$ to 1 at r=0.

At 100 keV the simulation profile looks more like the desired structure (Fig. 4.2). Each exposed zone is distinct and "heavily" affected by the electrons while the "in-between" area not. The backscattering in the resist films is also less important. This originates from the high-penetration depth of the electrons and the fact that all the discussed events are taking place deep in the substrate. The simulation shows that PMMA thickness as high as 10 μm could be used to create the desired structure. In practice, this is difficult. The fragility of the template, which is the result of the poor mechanical stability, as well as the large residual stress in the thick spin-coated polymers films (in occurrence PMMA) are among the reasons. Dark erosion of the unexposed or partially exposed areas plays also a key role. The development implies the selective removal of the exposed areas using a specific chemistry. Those chemicals are optimized to ensure a good contrast if reacted short times but they also have a detrimental effect on the remaining resist film. Swelling induces degradation and undesirable deformations in the resist pattern and dark erosion - the dissolution of the partially or unexposed areas. Trying to fabricate channels having 50 nm in diameter and 2 - 4 μm in length will require long developing times. Arrival of the fresh developer and the removal of the dissolved components (without any external driving force such as ultrasonication) are the limiting steps in this process. Nevertheless, high energy EBL, remains the only option for high-resolution processing of thick resist films.

To end-up, Table 4.2 summarizes the discussed aspects. Each energy range will be more appropriate for a given application. The main part

1-5 keV		5-30 keV		30-100 keV	
high resist sensitivity	+	very well understood	+	very thick resists	+
high throughput	+	acceptable throughput	+	process latitude	+
no proximity effect	+	"economic" equipment	+	substrate damage	?
pattern transfer	±	forward scattering	±	low resist sensitivity	±
3D resist shaping	+	proximity effect	±	resist heating	±
thin resists	±			costly equipment	±
sub 30 nm resolution		sub 10 nm resolution		sub 10 nm resolution	

Table 4.2: Influence of electron energy on resist-type, porous templates manufacturing.

of the work presented in this Chapter was done using a 100 keV electron beam.

4.2.1.2 Resist types

Electron beam resists are the recording and transfer media for EBL. The usual resists are polymers dissolved in a liquid solvent [183]. Electron-beam resists are classified upon the type of the induced modification following exposure:

- Positive resists: average molecular weight is reduced by exposure. Exposed area is solved much faster in the developer and thus removed. Examples: PMMA, EBR-9[3], ZEP[4], PBS, PMGI as well as some photoresists from AZ series in different formulations.

- Negative resists (chemically amplified): average molecular weight is increased by exposure (cross-linking of molecules). Unexposed area is removed in the developer. Examples: COP[5], Shipley SAL-601[6], P(SI-CMS)[7], EPTR[8], FOX12[9] and NEB - 22[10].

If we will expose a positive resist to a range of doses and then develop the pattern and plot the average film thickness versus dose we will obtain

[3]Acrylate-based resist, poly(2,2,2-trifluoroethyl–chloroacrylate).
[4]Copolymer of -chloromethacrylate and -methylstyrene.
[5]Epoxy copolymer of glycidyl methacrylate and ethyl acrylate.
[6]A mix of a base polymer, an acid generator and a crosslinking agent.
[7]Poly trimethylsilylmethyl-methacrylate chloromethylstyrene.
[8]A combination of o-cresol novolac glycidyl ether and triphenylsulfonium hexafluoroantimonate photoinitiator.
[9]Hydrogen SilsesQuioxane.
[10]A mix of propylene glycol monomethyl ether acetate, poly vinyl phenol derivatives, photoactive compound and crosslinking agent.

what is called a gradation curve. The sensitivity of the resist is defined as the point at which all of the film is removed *i.e.* at the clearing dose. Ideally, the film thickness would drop abruptly to zero at the critical dose. In practice, the thickness line drops with a finite slope. Schematic representation of gradation curves for a positive and a negative resist is given in Fig. 4.4.

The resist contrast is defined as $\gamma = [\log D_0/D_1]^{-1}$, where D_1 is the largest dose at which nothing is removed (the extrapolation of the linear portion in Fig. 4.4 (**a**) to 1) and D_0 is the dose at which all of the film is lost (the extrapolation of the linear portion in Fig. 4.4 (**a**) to 0). The same expression defines the contrast of a negative resist (the film is retained where irradiated) by inverting the therms in the logarithmic fraction. Briefly, high-resolution as well as high-aspect ratio nanostructuring is easier to be done using high γ resists. In order to minimize bias and proximity effects, positive resists should usually be exposed and/or developed as lightly as possible while still adequately clearing the resist down to the substrate.

The low contrast resists, even if longtime considered as not suitable for EBL, have been found to be excellent candidates for the 3D EBL applications. Operating above the D_0 (for the case of positive resists) is considered as conventional lithography while in between D_1 and D_0 as 3D lithography. By using different exposure dose in this region (dotted vertical lines in Fig. 4.4 (**a**)) we can modify the remaining resist thickness to two different values (dotted horizontal lines). The resists with low contrast (γ close to 1) will be much easier to 3D process. Exposing more complex patterns with various doses will yield various 3D topological profiles in the resist. This technology is also known as gray-scale 3D EBL [191]. This kind of structures have already found utility in MEMS applications [192], microlenses, phase holograms and optical mirrors [193]. This is an example of 3D transcription of a 2D digital pattern. Nevertheless, it is not really a 3D patterning technique. It provides only a controlled topographical profile and not an internal resist structuring. Detailed description of truly 3D lithographic approaches as well as an exhaustive description of a novel 3D EBL approach will be given in the Section 4.2.3.

At the first sight, the approach can be compared with the 3D resist shaping using variable energy beam as discussed in the previous Section, Fig. 4.3. Nevertheless, there are several technological and fundamental differences between them. From the practical point of view, it is easier to modulate the exposure dose than the beam energy. The exposure mechanism is different as well. The energy modulation technique is based on different penetration depth of the beam. In the dose modulation

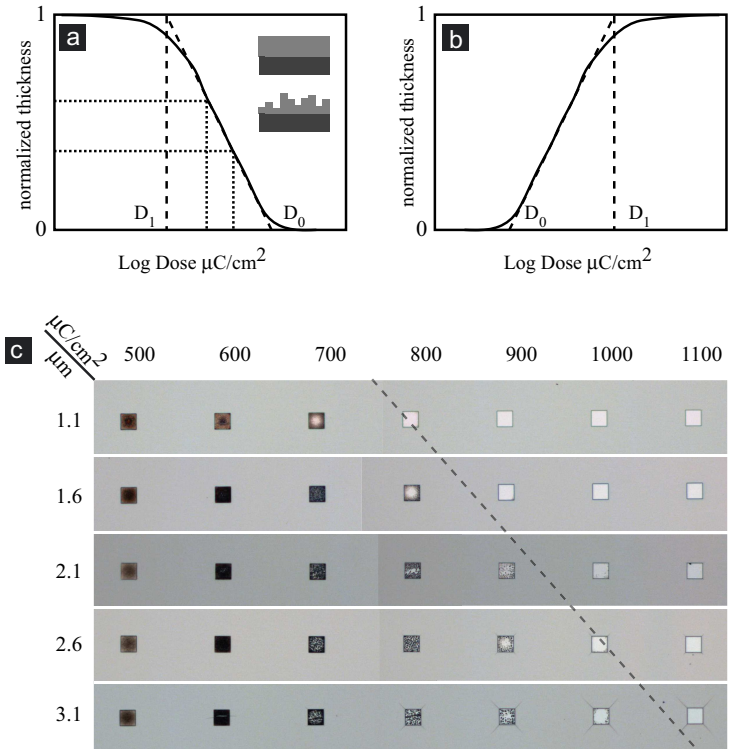

Figure 4.4: Remaining thickness versus exposure dose for a positive (**a**) and a negative (**b**) resist. These are the typical shapes for the resist gradation curves. Absolute dose values are very much dependent on the acceleration energy, pattern design, density and developing procedure. The clearing dose is typically linearly depended on the beam energy and the resist thickness. Inset: Schematized view of the gray-scale 3D lithography. Each segment is exposed at a different dose in between D_1 and D_0. (**c**) Example of clearance dose dependence on the PMMA resist thickness. White squares are the cleared zones and the gray or the "dirty" areas are significative of the remaining resist. The dotted is an eye-guide for the linear extrapolation. Calibration was performed using a 100 keV beam on Si/SiO_2 [400 nm] / Pt [130 nm] substrates for each case. The exposed areas ($50 \times 50\ \mu m^2$) were developed (3 min) in a MIBK/IPA mixture (1/3 v/v), rinsed with IPA (2 min) and DI water (5 min) and dried in N_2.

approach (the beam is completely penetrating the substrate) the shaping is provided by a combination of the deposited energy profile and the subsequent developing procedure [194, 195]. As described in previous Section, the resist is primarily exposed by the few-eV energy electrons

generated through the collisions with the resist atoms. Increasing the dose (or the number of electrons), statistically, will increase the number of collisions deep in the resist and thus will permit its removal. This is a simplified picture as the influence of the beam energy, chemistry of the developing procedure and other phenomena have to be taken in consideration for a complete description.

PMMA is one of the first materials developed for e-beam lithography [182, 196]. It is a positive resist based on a special grade of polymethyl methacrylate designed to provide high contrast and high resolution for e-beam, deep UV (220-250 nm) and X-ray lithographic processes. Standard products include 495k and 950k molecular weight polymer in a wide range of concentrations formulated in chlorobenzene or anisole[11]. Upon electron irradiation, the polymer chains are broken into small fragments that preferentially dissolved in a solvent. The common solvent is the MIBK, yet it is too strong (increased dark erosion, poor contrast) and it is usually mixed with a weaker developer such as IPA[12]. A mixture of 1 volume MIBK and 3 volumes IPA enables very high contrast but low sensitivity [197]. The sensitivity of PMMA scales linearly with electron acceleration voltage. Interestingly, it can be used also as negative resist: if exposed to more than 15-20 times the clearance dose, crosslinking will occur[13]. In its positive mode, PMMA has an intrinsic resolution of less than 10 nm as first shown by Van der Gaag and Sherer using a system having a lower resolution [198][14]. In the negative mode, the resolution is at least 50 nm, the processing is complicated and with the invention of ultra-high resolution negative resists, it has not found large applicability. Finally, we note that, by exposing PMMA (or any other resist) on a thin membrane (as will it be discussed in the next section), the exposure due to secondary electrons can be greatly reduced and the process latitude thereby significantly increased.

[11] The resists used in our laboratory are purchased from Microchem Corp, www.microchem.com

[12] Which is also a developer and not an inert dilution media or an antisolvent as typically considered.

[13] This is typically observed during alignments on the chip such as the "contamination dot" - exposure of one spot for extended times. The center of the spot will be crosslinked, leaving resist on the substrate, while the surrounding area is exposed positively (proximity effect) and washed away.

[14] As at that time the typical beam size was of the order of 40-50 nm, they had the ingenious idea of overlapping several low-voltage electron beams and only developing their intersecting areas in a high-contrast bilayer resist (100k and 950k PMMA). Nowadays, the electron optics are focusing the electron beam down to 1 nm allowing for direct writing of sub-10 nm structures.

4.2.1.3 Substrate influence

In this part we will discuss the influence of the substrate on the EBL. As already discussed, while the electrons continue to penetrate through the resist into the substrate, many of them will experience large angle scattering events. They may return back through the resist at a significant distance from the incident beam (see for example Fig. 4.3 for the influence of the beam energy on the characteristic length), causing additional resist exposure (or the electron beam proximity effect). The backscattering is also very sensitive to the substrate. Low-atomic number materials gives less backscattering. An illustrative example is given in Fig. 4.5. Only 30 and 100 keV beams have been simulated. High- (Pt) and low- (Teflon) atomic number materials as well as vacuum were used as substrates. One can clearly observe that the Pt has an enhanced electron-blocking effect and the backscattering is enormous (the backscattering coefficient is approximately 0.47 for both 30 and 100 keV). A teflon sheet (or any other polymeric material) reduces almost by half the backscattering events compared to the Si substrate (0.074 and 0.046 compared to 0.157 and 0.11 for 30 and 100 keV, respectively; see also Fig. 4.3 (**b**) and (**d**)). This is explained by the fact that the constituent elements (C, H, O and N) have lower atomic weights. The situation will be similar for other substrates: glass, SiO_2, Si_3N_4, polysilicon and porous silicon as well as thin metal films. To get rid of this annoying effect, the best option is to work with suspended resist films or deposited on electron transparent substrates. Practically, working with a suspended 1 μm thick PMMA film will be extremely delicate. An excellent solution is to work on suspended (yet, mechanically stable) Si_3N_4 membranes. The approach is not new and has been extensively used for ultra-high resolution EBL [199] and TEM structuring [200].

4.2.2 High-resolution lithography

The primary goal of e-beam lithography is the high resolution and high speed (implying a trademark between the resist sensitivity and the operation beam current) processing. The problem is that the highest resolution resists are usually the least sensitive. We can see a reason for this trend when we consider the limit of resist sensitivity. For example, NEB-22 or FOX12 negative resists have a sensitivity of 10 - 20 μC/cm^2 at 30 keV. Exposing a 10 $\times$ 10 nm^2 pixel will require 60 - 120 electrons. At this sensitivity, every small changes in the number of electrons will cause variations in the dose delivered to each pixel. If the sensitivity is increased further, then the number of electrons in each pixel becomes

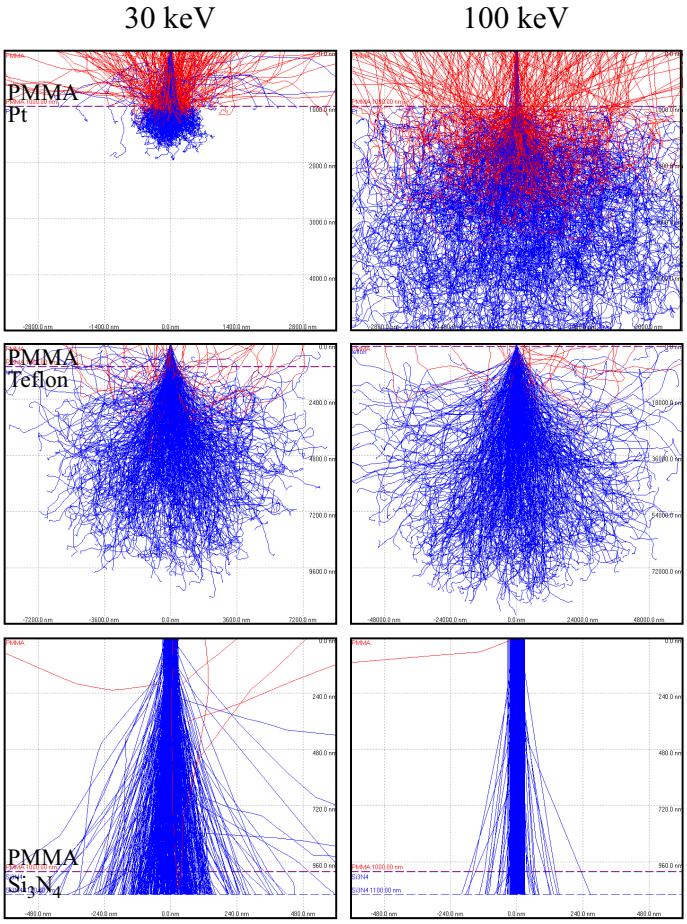

Figure 4.5: Substrate influence on the EBL parameters. Platinum, teflon and vacuum substrates have been simulated at 30 and 100 keV. The resist thickness is 1 μm. Plot scaling: X = 6 μm × Y = 5 μm for Pt; 18 μm × 12 μm for teflon at 30 keV and 120 μm × 90 μm at 100 keV; and 1 μm × 1.2 μm for vacuum.

too small to allow an even exposure of the pattern. There are also tool limiting factors[15]. Although there is room for improving the sensitivity of both high and low resolution resists, the statistics of resist exposure will eventually limit the resist sensitivity and exposure rate.

The PMMA is a good candidate for the high-resolution processing.

[15]For example, the tool in our laboratory (FEI XL30 - RAITH Elphy Plus) has a minimum recommended writing speed of 1 μs. This will require beam currents of 10-20 pA, slightly bellow the used values (25 - 50 pA). The current can be diminished by reducing the size of the strip apertures but still remains in a very critical range.

Simple and reproducible processing conditions, low sensitivity, sub-10 nm lithography and very well established and documented protocols provide the best option for an EBL beginner. Nevertheless, pattern transfer to another materials is difficult as it has poor dry etch resistance. For example, fabrication of high-aspect ratio using PMMA as masking material will imply thick resist films, which in turn will have a detrimental effect on the achievable resolution and pattern density and even if this can be achieved, isotropic removal of the PMMA mask during the etch will heavily affect the pattern transfer. Intermediate processing steps (thin sacrificial mask etching or Cr liftoff metalization) have been found to fulfill these tasks. In subsequent sections we will show that the PMMA is a good candidate for the nanoscale patterning of polyaniline.

4.2.3 Resist and dose modulated 3D EBL

In the following we will present a novel 3D EBL approach developed in our lab. Before detailing the mechanism and the advantages of the technique, we drop few words about general approaches for 3D nanoscale structuring. Ordered 3D nanostructures are very important for many areas of nanotechnology: NEMS and MEMS [98], photonic [201] and plasmonic [64] devices, biomimetics [202] and surface functionalization [203], microfluidics [204] and biomedical applications [205]. Typical 3D manufacturing rely on multi-step processing, progressive planar lithography and layering of materials. This require accurate registration and overlay alignment between the layers. In theory, this layer-by-layer approach can be extended to fabricate all major types of 3D structures. But exponential increase in production costs and the accumulation of defects as the number of layers increases retains their practical implementation. Alternative, non-trivial techniques, have been developed to provide access to certain types of 3D structures in a more effective fashion. They can be primarily divided into 2 main sections: (i) advanced lithography and (ii) structural engineering of bottom-up approaches. They are briefly described below.

- Focused beam writing - serial processing. The principle relies on the weak interaction of the out of focus beam with the substrate or resist (ideally also transparent) and strong in the focal point. Laser beam ablation [206] or induced deposition [207] and two-photon absorption polymerization (also called Direct Laser Writing) [208] are the most important techniques. The pattern is generated by essentially varying the exposure dose during scanning.

- Holographic lithography - parallel processing. It relies on the in-

terference between intersecting laser beams [209]. The technique is widely used in the photonic industry for the fabrication of holographic diffraction gratings and anti-reflection coatings. Single or double (orthogonal) interference exposure will generate mainly 2D patterns in the imaging resist. Four coherent laser beam focused onto the same spot were used to generate a 3D photonic crystal, the lattice parameters being determined by the configuration of laser beams.

- Phase mask lithography - parallel processing. Here, light passing through a phase mask having relief features comparable in size to the wavelength generates a 3D distribution of intensity that exposes the resist film throughout its thickness [210].

- Gray-scale lithography - parallel processing. This is a conventional lithography which works on the principle of "all-or-no" illumination. The gray-scale lithography encodes the final shape of a structure on the mask in the form of an optical density contour map that determines the illumination density during the exposure of the resist. Two types of gray-scale masks are in use: half-tone masks (produces gray-scale levels through variation in the thickness of absorbing mask material) [211] and high-energy beam-sensitive glass masks (the gray scale level is determined by the density of metal atoms, such as Ag, contained in a glass matrix) [212]. The gray scale 3D EBL method presented above can be assigned to this class.

- Angled processing - serial and parallel processing. This extends to various approaches: lithography with exposing beams obliques to the resist film, two-axis-of-rotation systems in EBL [213] or variable angle XRL [214]. Another interesting approach uses standard lithography 2D mask definition and subsequent angled etching [215]. Glancing angle deposition is used to engineer thin films with feature sizes in the nano-scale regime using large deposition tilit angles (more than 80°). Slanted posts, chevrons, helices and vertical posts architectures can be fabricated [87] with an enormous potential for large-scale microfabrication on the optical scale of 3D photonic crystals [216].

- Add-on layer-by-layer fabrication - parallel and serial processing. Here, 2D patterns are first created using standard techniques and are subsequently assembled either by micromanipulation or wafer fusion bonding techniques [217].

- Self-assembly and self-organization - parallel processing. This is a very broad field including various approaches based on the self-organization of mater. Colloidal lithography is a very powerful technique for opal and inverse-opal geometry structuring [52, 79, 218]. Selective pattern induced crystallization [219,220], 3D defect engineering [221], masked etching or deposition [222] as well as mechanically [86] and electrically [85] actuated optoelectronic architectures can be accessed. Self-assembled block-copolymers are promising platforms for low dimensional structuring for various applications due to their ability to aggregate into 1D, 2D and 3D periodic structures scaling from few nanometers up to micrometer scale [223]. Structural engineering of porous templates belong to this class as well, including hierarchical branching and controlled fabrication in AAO templates [74] and pore diameter modulation in AAO [224] or porous silicon [121].

- Polytypic growth - parallel processing. This methods is based on controlled production of branched or hyper-branched nanostructures by engineering the co-existence of two or more crystal structures in different domains of the same crystal. Inorganic III-V nanowires are the typical materials [225, 226].

4.2.3.1 Resist composition modulation

Our approach, uses both, EBL and bottom-up engineering to generate 3D structures. The method fully exploits the different interactions - in terms of exposure parameters or clearance doses - of the electron beam with the PMMA and copolymer PMMA(8.5)MAA positive resists. The later is a copolymer resists based on a mixture of PMMA and 8.5% methacrylic acid and has an increased electron sensitivity. The double or triple layers based on both components have been extensively used for thick metal liftoff and mainly in the fabrication of T-gate structures for high electron mobility transistors [227]. All of the mentioned components are imaging resists and the less sensitive of them sets the patterning resolution. Combination of non-imaging (LOR or LOL) and imaging resists can be also used, yet requiring different developing procedures for each layer. In this configuration, the imaging component will set the resolution while the other one is used only to create the undercut. The use of a non-imaging layer implies also loosing the full pattern control as it erodes isotropically in the developer. Chen and collaborators have used double- or multiple-layer resist structuring for various photonic applications. They have fabricated ordered 2D arrays of CdSe pillars using

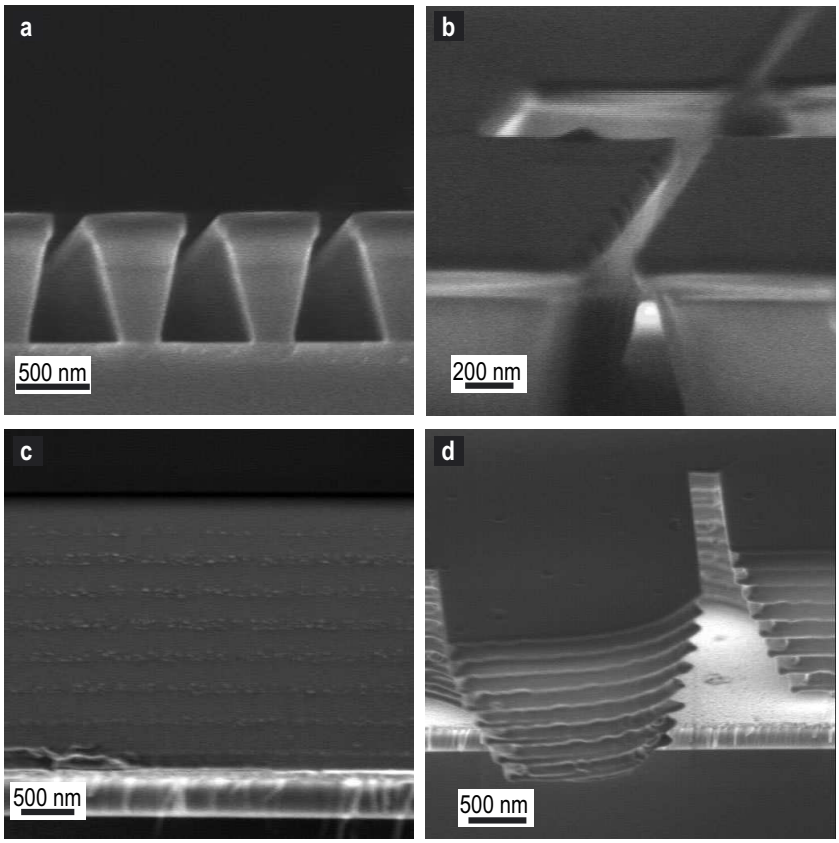

Figure 4.6: (**a**) and (**b**) Negative resist profiles in bilayer PMMA(8.5)MAA/PMMA stacks. (**c**) SEM view of a cleaved multilayered stack. The horizontal "bubbled" lines correspond to the PMMA(8.5)MAA layers. The components contrast under SEM inspection is not permanent. Prolongated exposure blurs out the image due to the charging effect and the contrast disappears. (**d**) Cleaved view of the same stack but after EBL exposure (at 30 keV) and development. The pattern was overexposed (1500 μC/cm^2) to ensure handiness during the subsequent processing.

EBL and electrochemical deposition [75] and recently shown an approach for single-step EBL fabrication of polymer-based photonic crystals [228]. Single-step exposure, yet multi-step processing as each layer stack needed separate development requiring careful timing (and probably a complicate resist backing procedure as LOR-type resists' development rates are extremely sensitive to the baking time and temperature). They also did not succeeded to further inverse or functionalize their templates.

Typical double or multilayered structures used in this work are de-

tailed in the following. Examples of high-undercut resist profiles are presented in Fig. 4.6 (**a**) and (**b**). Larger undercuts, very helpful for oblique angle thick-metal evaporation have been already discussed in Section 3.5.2. It is evident that by using this kind of profiles, very thick (eventually, thicker than the resist stack) metal liftoff is possible. The process latitude is set by the resolution in the PMMA top-most layer. One important aspect is the polar/non-polar combination that avoids the intermixing of the layers and hence, preserves the composition modulation. The incompatibility of the carrier solvent with the already deposited film for both components (chlorobenzene or anisole for PMMA and ethyl lactate for PMMA(8.5)MAA) enables a simple composition engineering. Example of a multilayer stack precursor is shown in Fig. 4.6 (**c**). A single component resist film will result in nanopores with uniform diameters after EBL processing, while composition-modulated resist stacks will yield diameter-modulated nanochannels (Fig. 4.6 (**d**)). As already explained, this is caused by increased electron sensitivity of PMMA(8.5)MAA layers and thus higher dissolution rate in a developer. SEM inspection of the fabricated structures is quite difficult. The structures have to be cleaved along the exposed patterns to reveal their internal structure which is not straightforward. Indirect imaging of the fabricated templates can be done by inspecting the architectures grown inside this templates (inverted replica) and will be detailed in Section 4.4.2.

The resist modulation is implemented by sequentially coating each stack component. The axial control with nanometer-precision is effectively achieved by controlling the thickness and the sequence of the coated layers. A typical procedure consists in spin coating each stack component on the substrate from the respective resist solution followed by a soft-bake for 15 min to remove the remaining solvent. Although, often regarded as a very simple and basic approach for application of thin-films, the underlying mechanisms and associated phenomena in spin coating are very complex. Even nowadays there are unexpected findings using "standard spin-coating" of "simple polymers". Kern and collaborators have found that nanoscale fibers with a diameter down to 25 nm (centimeter scale length) can emerge from a polymer solution (PMMA) during spin-coating [229]. The explanation relied upon Raleigh-Taylor instability of the spin-coated liquid film that arises due to a competition between the centrifugal force and the Laplace force induced by the surface curvature. Well, this is a quite intricate interpretation for a "simple" procedure. While the authors have exploited this phenomenon to show that a large variety of nanostructures can be easily accessed through spin-coating, in our case this turned out to be a nightmare during the

multilayer coating. The fibers are generated after each coating, especially when using concentrated solutions, contaminating the spin-coater environment and the sample surface. If not removed from the surface (by strong N_2 blown) before the layer soft-bake (130°C, above the T_g of PMMA and PMMA(8.5)MAA hence enabling their adhesion) or the next layer coating, they will compromise the uniformity of the next layer creating non uniform resist coatings and striations. If this happens, the sample has to be cleaned and the process restarts from the beginning. Caution is of applicability for the spin coater environment too. It is good to clean it after maximum 4 - 6 coatings to avoid any surprises.

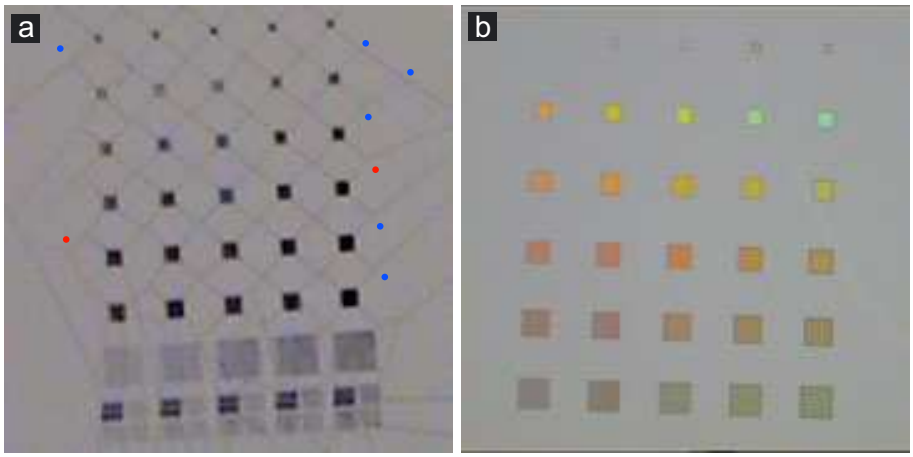

Figure 4.7: (**a**) Example of stress induced fracturing in the multilayer resist stack. The exposed patterns are composed of square arrays of dots. The cracks nucleate at the weakest points (straight corners of the square arrays) and propagate along the diagonal. The propagation length could be as high as 150 μm. Whenever they meet, the propagating direction is perturbed either following only one of the directions (blue dots) or following a new direction (red dots). (**b**) Examples of stress-released resist stacks. The uniform colorization (due to the light diffraction) is an indicative of structural integrity, and of a photonic band gap for the incident light (Γ - X direction, see Chapter 2 for details). Pattern center-to-center distance on both images is 50 μm.

Another important aspect is the residual stress in the resist stack [230]. If not treated correctly, the exerted forces will shear and destroy the template. No signs of degradation could be visualized on the samples after the coating sequence or after the bake procedure. Only after removing the exposed areas the cracks are formed and the structural integrity of the templates is altered. The resist swelling during the de-

veloper action may also contribute to this effect, though it is not clear at which extent. The stress can be effectively released by prolongate (24 - 48 hours) thermal annealing at 130°C followed by a slow cooling down to room temperature. Nevertheless, even doing so, the cracking in the resist was not completely eliminated. For very thick stacks this was almost impossible and was always accompanied by formation of cracks along specific directions. An example is given in Fig. 4.7 (**a**) where a 6 μm thick resist was used. The gray areas are the remaining of exposed dots arrays (arranged in a square lattice) after the development. The designed template is completely destroyed. In turn, a new "template" is generated. A series of few-nanometer width and micrometer long aligned lines can be observed (see Section 4.4.1 for the achievable resolution). They preferentially nucleate at the sharp edges of the square patterns and are aligned along their diagonal. Presumably, under further optimization and proper design this type of fracture induced structuring could be exploited for the high-throughput, large area nanoscale patterning [231]. If properly processed, the exposed patterns remained intact and showed no signs of degradation. Typically the combination of (i) thin resist film, (ii) high spin coating speed, (iii) minimal use of ultrasonication bath during the development and (iv) adequate drying of the templates (no N_2 blow drying after water rinsing)[16] can ensure a good mechanical stability of the templates.

4.2.3.2 Dose modulation

Additional structural features can be added by exposing side-patterns at a lower dose on the above mentioned stacks. The contrast curves for used components is presented in Fig. 4.8. As it can be observed, there is a dose range for which the PMMA layer is almost unaffected and the PMMA(8.5)MAA layer can be fully removed. The process window of interest in this case is located between 30 and 50 μC/cm^2. For example, exposing a stack comprising both components at a dose of 40 μC/cm^2 will expose only the copolymer layer. By designing openings to allow for the developer to remove those areas, buried channels or void spaces can be fabricated. Patterning, following the same principle, a multilayer stack, will create self-aligned voids. Their height is set by the thickness of the copolymer layer and width and length primarily by the exposing pattern. The use of an imaging resist component is imperative. Otherwise, it will be removed isotropically and will not allow for internal

[16] As it will be detailed further, CPD is an excellent technique for drying fragile nanostructures. For the hydrophobic PMMA templates, drying out IPA tends to collapse the brittle structures, while using water this can be partially avoided

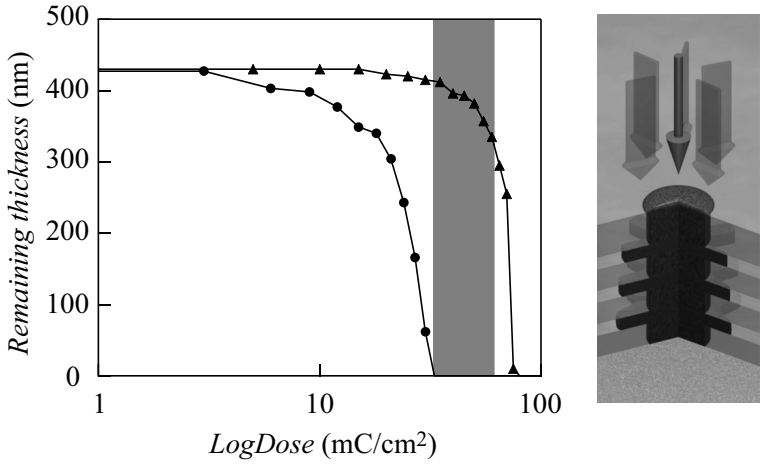

Figure 4.8: (left) Contrast curves for 440 nm thick PMMA (closed triangles) and PMMA(8.5)MAA (closed diamonds) single layer resists. The exposure was performed using a 30 keV electron beam. The calibration was performed on Si/SiO_2 [400 nm] / Pt [130 nm] substrates for both cases. The exposed areas (10×50 μm^2) were developed (2 min) in a MIBK/IPA mixture (1/3 v/v), rinsed with IPA (1 min) and DI water (5 min) and dried in N_2. The gray area represents the dose region where PMMA(8.5)MAA can be fully removed while PMMA partially or not. (right) Schematic view of resist and modulated 3D EBL. The central part is written above the clearance dose of the stack while the side lines at a lower dose, only to expose the copolymer component.

structural engineering. For example, exposing a central pillar at a high dose and side-lines at a lower dose (each of them being calibrated accordingly) will result in a diameter modulated template bearing in-plane protrusions. As it will be shown in Section 4.4.2 filling-up the voids with polyaniline followed by subsequent removal of the template will result in the fabrication of the branched, hyper-branched and other complex 3D structures. More complex will be the internal structure of the template, more time will be needed for the complete removal of the exposed areas in the developer because all the solvent exchange will take place only through the top most opening. For example, the hyper-branched nanopillars that will be described in Section 4.4.2 required up to 18 minutes of developer soaking with short bursts of ultrasonication.

A higher difference in sensitivities between the two components can apparently increase the process latitude. However, if the difference is to high, the less sensitive component will be heavily affected during the exposure of the central pillar and the side-branching can be embodied

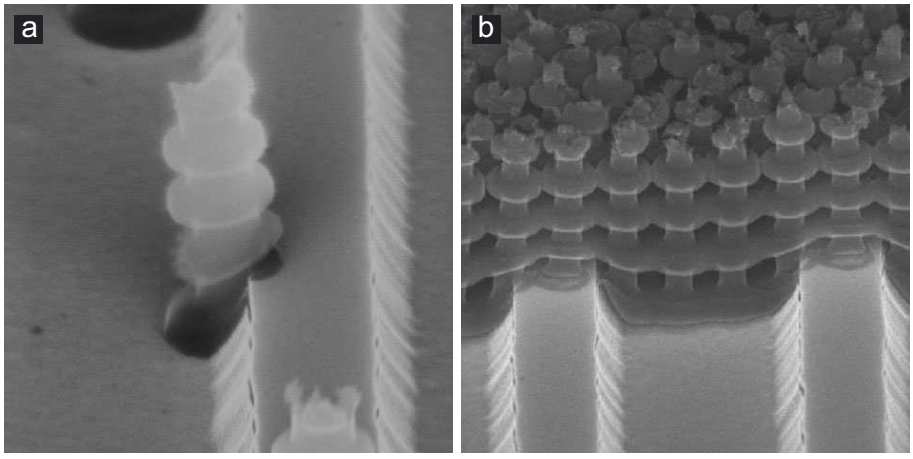

Figure 4.9: Examples showing the first test on substrate induced resist modulation structuring. Only the bottom three layers are affected by the surface topology.

in the diameter modulation provided by the forward and backward scattered electron cone. A lower contrast instead can be useful allowing for the larger operation-dose window. Three different components can be used to create even more complex 3D shapes. The use of a non-planar substrate was tested and is under optimization Fig. 4.9. The topography was created using dry etching of the silicon substrate. Less pronounced protrusions as well as lower spin coating speeds are the two directions to be studied in order to minimize the surface planarization. Another envisioned option is the use of alternating positive and negative resist components. In the exposed regions, the positive component will be removed while the negative not, and vice versa. This may allow for the fabrication of f.c.c. lattice.

4.2.3.3 When 1+2=3

As intuitively presented in the previous section, 1D design of the resist template combined with 2D digital exposure patterns enable the fabrication of complex 3D architectures. The method proceeds in one step as the structures are generated in a single- exposure and development protocol. The geometric parameters can be tuned through the thicknesses of the coated layers, the design of the exposing 2D pattern and dose modulation. One simple example is given in Fig. 4.10. The snapshots are the inverted replica of the template obtained using polyaniline

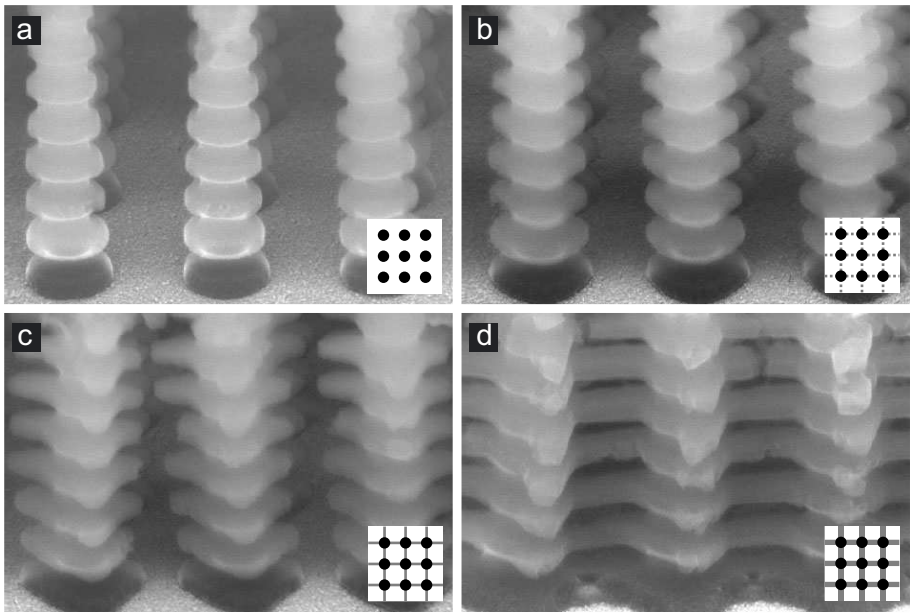

Figure 4.10: Exemplification of the potential provided by the resist and dose modulated 3D EBL. Only one parameter changes (the side-branching dose) between the structures. The resist stack accommodates a total of 16 alternating 100 nm thick PMMA and PMMA(8.5)MAA layers. The substrate is Pt [130 nm] / SiO_2 [400 nm] / Si [bulk]. Central pillars have been exposed at a dose of 500 $\mu C/cm^2$ using an acceleration energy of 100 keV. The samples were developed for 12 minutes (comprising 1 minute under ultrasonication) in a MIBK/IPA mixture (1/3 v/v), rinsed with IPA (3 min) and DI water (6 min) and let to dry in air. From (**a**) to (**d**) the side-branching dose is 0, 75, 150 and 225 $\mu C/cm^2$. Inset: schematic view of the pattern design. Pillar pitch = 800 nm.

electroless deposition. Using the same resist stack, pattern design and identical central pillar dose, a series of distinct and ordered 3D lattices can be accessed only by changing the side-branching dose. When only the central pillar is exposed, diameter modulated pillars with perfect circular symmetry are obtained. As already mentioned, this is the result of the conical profile of the forward and backscattered electron exposure. At 75 $\mu C/cm^2$ the disks corresponding to the copolymer layer are 4-side sharpened and transformed into squares. The structure now can be described as a series of squares suspended by a central circular pillar. A better visualization of this type of suspended chess-board structures can be seen in Fig. 4.27. By increasing further the side-lines dose to

150 μC/cm^2, the branches continue to "grow" yielding 4-sided star-like structures. Eventually, in between 150 and 225 μC/cm^2, the star arms merge materializing into a simple cubic lattice, in a first approximation. The initial templates can be regarded as the inverted replicas of the presented structures. It is straightforward that the pattern transfer from those templates is impossible to be done using etching or physical deposition methods. Only approaches like electrochemical or chemical growth or ALD can fulfill these tasks. The electroless polymerization of aniline is more than suited for this type of processing. Other types of fabricated architectures, functionalized composites and smart nanoassemblies will be given in Section 4.4.2.

4.3 Polyaniline

Conducting polymers form a class of materials relatively far from their origins, if we consider 1977 as being the historical moment when Nobel Prize laureates Alan Heeger, Hideki Shirakawa and Alan MacDiarmid proved the possibility of chemically tuning the electrical properties of some emblematic polymers. Ever since, outstanding innovations have been achieved on the road towards polymer-based electronic devices, such as organic thin film transistors (OTFTs), photovoltaic cells (PCs), organic emitting devices (OLEDs), etc. Some key attributes of the organic-based technology (flexibility, low-temperature processing, large-area, low costs) allow its compatibility with very different substrates (Si, glass, plastic, paper) leading to impressive applications, some of which are already in commercial production. Amongst the family of conducting polymers, also known as synthetic metals, the polyaniline is unique due to its ease of synthesis, environmental stability, controllable electrical conductivity and interesting redox properties associated with the chain nitrogens. The aniline polymers are also known to exhibit crystallinity and solution or counterion-induced processability. Furthermore, the secondary doping can substantially improve the electrical properties. The excellent processability, together with the presence of a number of intrinsic redox states, have substantially enhanced the potential applications of aniline polymers for use in practical devices.

4.3.1 Historical background

Although it was discovered 150 years ago, only recently the polyaniline has attracted the attention of the scientific community due to the discovery of its high electrical conductivity. The monomer aniline was obtained for the first time by a medical doctor Letheby from the pyrolytic

distillation of indigo and was called "Krystallin" because it produced well formed crystalline salts with sulfuric and phosphoric acid [232]. In 1840, Fritzsche also obtained a colorless oil from indigo, called it aniline ostensibly from the Spanish a*ñ*il (indigo), and oxidized it to polyaniline (PANI). The electrical properties of such powders as well as the relation of their π-conjugation with the semiconducting and conducting properties were not investigated and scientifically unknown. Some believe this to be the first report of polyaniline, although the first definitive report of polyaniline did not occur until 1862.

Since, occasional reports about the structure of PANI appeared in the literature and would continue periodically until the 1960s. In 1963, D. E. Weiss and coworkers reported high conductivity in oxidized iodine-doped polypyrrole, a polyacetylene derivative [233]. They achieved a quite low resistivity of 1 $\Omega\times$cm. In a series of detailed papers, they also described the effects of doping with iodine on conductivity, the conductivity type (n or p), and electron spin resonance of polypyrrole. They also submitted a patent application (5246/61, June 5, 1961) for conducting polypyrrole. In 1965, the group reached resistances as low as 0.03 $\Omega\times$cm with other conductive polymers [234, 235]. This is roughly equivalent to present-day efforts. This extensive work was "lost" until recently. In 1974, as a "proof of concept" for their version of the now-accepted model of conduction in such materials, John McGinness and his coworkers built and reported a voltage-controlled organic-polymer switch [236]. Their device used melanin, a self-doped mixed copolymer of oxidized polyacetylene, polypyrrole and polyaniline. It is now in the Smithsonian's collection of early electronic devices. In the "ON" state, this material has almost metallic conductivity. The device also exhibited negative differential resistance, now a well-characterized hallmark of electronically-active organic materials. Though published in a major journal Science and reflected in a news article in the journal Nature, this work was also "lost" until similar devices emerged decades later [237].

In 1977 Alan J. Heeger, Alan MacDiarmid and Hideki Shirakawa reported metallic conductivity in iodine-doped polyacetylene, similar to that reported a decade earlier by D. E. Weiss and coworkers for iodine-doped polypyrrole. Unfortunately, they did not cited the earlier papers. Extensive research and development in the semiconducting and conducting properties of a large family of conjugated, sp^2 hybridized polymers followed. This large international effort resulted in development of organic polymeric light emitting diodes, solar cells, transistors and so forth. Though their priority is questioned, Heeger, MacDiarmid and Shirakawa eventually received the 2000 Nobel prize in Chemistry "For the discovery and development of conductive polymers". In subsequent years, the

study of polyaniline exploded and currently a vast literature on the synthesis, properties, and applications of polyaniline exists.

4.3.2 Redox states and associated applications

Although the synthetic methods to produce polyaniline are quite simple, its mechanism of polymerization and the exact nature of its oxidation chemistry are quite complex. The aniline polymers have the general formula $[(-B-NH-B-NH-)_x(-B-N=Q=N-)_{1-x}]_y$ in which B and Q denote the C_6H_4 rings in the benzenoid and quinonoid forms respectivelly. Thus, aniline polymers are basically poly(p-phenyleneimineamine)s, in which the neutral intrinsic redox states can vary from that of the fully oxidized pernigraniline (PNA, x=0), to that of the fully reduced leucoemeraldine (LM, x=1). The intrinsically half-oxidized polymer has been termed emeraldine (EM, x=0.5), and the 75% intrinsically oxidized polymer, is termed nigraniline (NA, x=0.75). A more clear view of these structures is given in Figure 4.11.

The intrinsic redox states associated with the nitrogen atoms are unique to PANI and play a governing role on the doping behavior and physicochemical properties of this polymer. While in many other conducting polymers, the conductivity is a function only of the oxidation state, i.e., the number of electrons added to or removed from the π-system of the neutral polymer backbone, polyaniline was the first case where the conductivity was found to depend on two variables - the oxidation state of the polymer and the extent of protonation of the nitrogen atoms in the backbone [238]. It has been shown that protonation of polyaniline believed to be in the emeraldine oxidation state led to a dramatic change in conductivity, from 10^{-10} S/cm for the unprotonated polymer to 5 S/cm when "doped" by equilibration with aqueous acids at pH$\sim$0 [238].

Though, EM is by far the most studied oxidation state of polyaniline other oxidation states have been also studied, especially the reversible interconversion between them:

- Leucoemeraldine. This is the completely reduced form of polyaniline. Colorless solid material. In powder form, less than 25% of the amine nitrogens can be protonated in the absence of oxygen. The degree of protonation in leucoemeraldine can be increased to about 50% with 3 M $HClO_4$, similar to that achievable with emeraldine base in powder form. In solution, leucoemeraldine is easily oxidized by dissolved oxygen. It remains a poor electrical conductor even when doped with acids. It can be obtained by reacting emeraldine

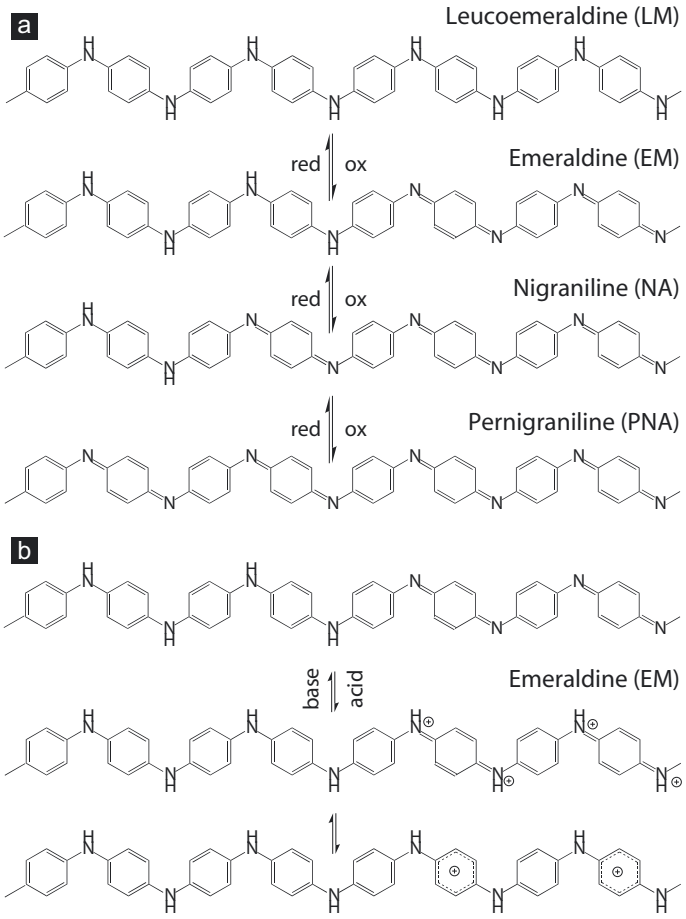

Figure 4.11: (**a**) Octameric structures of the most common polyaniline redox states. (**b**) Structures of emeraldine oxidation state in basified (dedoped) and acidified (doped) form and the imine - enamine tautomerism of doped emeraldine.

with a reducing agent (hydrazine or sodium borohydride). Due to its limited air stability it has not found any direct utility.

- Emeraldine. It is the most stable and studied polyaniline oxidation state. Generally, aniline polymerization leads to an oxidation state close to emeraldine, which color is blue or green depending on the doping degree. It has found a pleiade of applications due to its exceptional properties: metal-to-insulator transition upon simple chemical fonctionalization [56], bistable electrical conductivity [239], various optoelectronic devices [240], intelligent sur-

faces [241], sensing and biosensing [242, 243], electrochemical and chemical activity [244] are only few to be mentioned. A vast literature exists and the more interested reader is called to check for these reviews [245–248].

- Nigraniline. It is also known as aniline black. Nigraniline is probably the oldest synthetic organic pigment, discovered around 1860. It is mostly used in specialty coatings where very deep blacks are required. It poses a strong tinting strength, a low scattering power and a very strong light absorption capability. Other properties are moderate and the material was rather poorly studied.

- Pernigraniline. This is the highest oxidation state of polyaniline. Similarly to NA, it has a moderate electrical conductivity. It is the only known polymer besides polyacetylene that is known to exhibit a two-fold degenerate ground state. It undergoes hydrolisys in acidic media. Again, due to its not very attractive properties and quite reduced stability, it was poorly studied.

4.3.3 Synthesis and nanoscale structuring

Aniline polymers are usually prepared by direct oxidative polymerization of aniline in the presence of an acid and a chemical oxidant or by electrochemical polymerization on different electrode materials. As usual, chemical polymerization of aniline is provided by the use of some of the known oxidants, which are able to generate radical cations and other highly reactive species upon interaction with aniline. Once generated, these reactive species react with aniline molecules, leading to the growing polymer chains. A number of known oxidants were investigated in polymerization of aniline: $(NH_4)_2S_2O_8$, $K_2Cr_2O_7$, $FeCl_3$, $SnCl_4$, H_2O_2. The properties and the morphology of the resulting polymer are known to be depend strongly on the nature of oxidant used, as well as on the reaction conditions (concentration, temperature, type of acid).

The work of Jozefowicz in the 1970s provided a good understanding of the polyaniline oxidation states and their interconversion [255]. In the 1980s, the work of MacDiarmid [256], Genies [257] and Ohsaka [258] continued to provide better physicochemical insights into this family of electroactive polymers. The structure of the oxidized insulating form of PANI prepared via oxidative polymerization is approximately a 50% copolymer of diamine and diimine units, corresponding to the EM base structure. The synthesis and characterization of the EM and LM oxidation states of polyaniline are the most documented. While typically synthesis and subsequent characterization and processing was carried

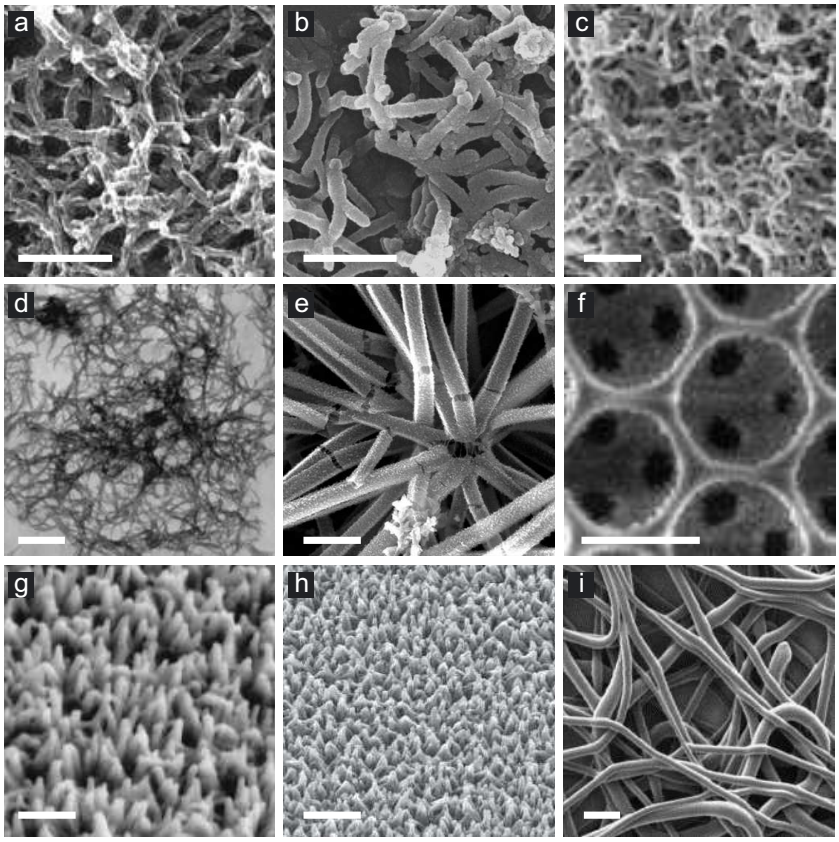

Figure 4.12: Overview of the polyaniline nanostructuring methods. Polyaniline nanofibers obtained using (**a**) interfacial (reproduced from [249]), (**b**) surfactant assisted (reproduced from [78]), (**c**) seeding (reproduced from [250]) and (**d**) oligomer assisted (reproduced from [251]) polymerizations. (**e**) Use of reactive manganese templates provided a route for polyaniline nanotube fabrication (reproduced from [77]), while (**f**) polyaniline inverse opals have been obtained by inverting colloidal silica templates (reproduced from [73]). Aligned nanofibers have been obtained using (**g**) stepwise electrochemical deposition (reproduced from [252]) or (**h**) by diluted polymerization (reproduced from [253]). (**i**) Macro- and nanoscale polyaniline nanofibers obtained using electrospinning of 2-acrylamido-2-methyl-1-propanesulfonic acid doped polyaniline (reproduced from [254]). Scale bars: (**a**) to (**h**) 500 nm and (**i**) 5 μm.

with bulk quantities of polyaniline, in recent years, a lot of effort was focused on the nanoscale structuring of this material. Yet, the very poor solubility in organic solvents (hence, difficult solution based processing) and the high glass transition temperatures (therefore, difficult printing)

have restricted direct nanoscale patterning.

To overcome this major technological inconvenience, direct synthesis methods have been proposed. Using these methods, polyaniline nanostructures (typically nanofibers and nanowires) are directly synthesized by properly choosing the polymerization conditions and environment. They can be subsequently used as synthesized, dispersed in a different polymer matrix or processed to select and characterize single polyaniline nanoelements. Depending on the patterning mechanism and fabrication approach they can be classified as follows.

- Interfacial polymerization (Fig. 4.12 **a**). One of the easiest and less-expensive means of obtaining nanofibers in one step (Fig. 4.12 **a**). It is based on an aqueous/organic biphasic system. One component, typically the organic solvent, is used to disolve the aniline and the second (the aqueous acid solution) is used to dissolve the oxidant. A great variety of organic solvents can be used, including benzene, hexane, toluene, carbon tetrachloride, chloroform, methylene chloride, diethyl ether, carbon disulfide, or o-dichlorobenzene, the shape and size of the nanofibers being not affected by the solvent. Bringing them in contact, allows for the polymerization to occur only at the interface between the two media (from which the term of interfacial polymerization) [249]. The syntheses can be accomplished in one pot with a wide choice of solvent pairs, acid dopants, and reagent concentrations over a broad range of temperatures.

- Surfactant assisted polymerization (Fig. 4.12 **b**). It is based on the ability of some surfactants to form micelles or tubules that act as templates for the synthesis [78]. β-naphthalene sulfonic acid, naphtalene-1,5-disulfonic acid, D-10-camphorsulfonic acid or hexadecyltrimethylammonium chloride are some representative examples. They also can act as a doping acid and can remain incorporated in the polyaniline matrix. Submicrometer-sized polyaniline tubular or fibrilar morphologies are typically obtained.

- Seeding polymerization (Fig. 4.12 **c**). Seeding a conventional chemical oxidative polymerization of aniline with very small amounts of biological, inorganic, or organic nanofibers (usually $<1\%$). This induces changes in the morphology of the resulting doped polyaniline powder from nonfibrillar (particulate) to almost exclusively nanofibers. Seed nanofibers were fabricated from: as prepared polyaniline nanofibers, single-wall carbon nanotube bundles, nanofibrous hexapeptide (Ac-VQIVYK-amide) and V_2O_5 nanofibers [250].

- Oligomer assisted polymerization (Fig. 4.12 **d**). Aniline oligomers are used to accelerate the reaction by assisting monomer oxidation (autocatalytic effect). The oxidant is incrementally added to the reaction vessel. The aniline oligomers serve not only to accelerate the polymerization reaction, but also to act as seeds for the growth. This is due to the lower redox potential as compared to that of aniline monomer and the initiation of chain growth will likely be dominated by these oligomers [251].

- Template assisted chemical and electrochemical growth (Fig. 4.12 **e** and **f**) make use of hard templates to assist and confine the polymerization. Alumina, block-copolymers, zeolites, colloidal crystals have been successfully applied to nanostructure the polyaniline. Both, chemical and electrochemical methods have been used, though, electrochemistry is preferred because it avoids the undesirable bulk reaction and subsequent decontamination and rigorous washing. Depending on the nature of the template, the release can be damaging for the structural and chemical integrity of the polyaniline nanostructures. A slightly different approach was used by Pan *et al.* in producing polyaniline nanotubes [77]. They have used reactive templates of manganese oxide (MnO_2) acting also as chemical oxidative initiator for aniline polymerization. This effect causes the template to be spontaneously removed after the reaction, because the manganese oxide is reduced into soluble Mn^{2+} ions, whereas the aniline monomer is oxidatively polymerized.

- Stepwise deposition (Fig. 4.12 **g**). Templateless electrochemical polymerization. A typical procedure involves electrochemical deposition in an aniline-containing electrolyte solution, by using the substrate as the working electrode [252]. In a first step, high-density currents are used for the polymerization which are producing polyaniline nanoparticles (nucleation sites), rather than continuous films. The initial stage is followed by continuing the reaction with reduced current density. The electropolymerization takes place preferentially on the already formed nucleation sites and produces aligned nanofibers.

- Diluted polymerization (Fig. 4.12 **h**). Recently developed technique resulting in aligned polyaniline nanowires grafted on various substrates. Very low concentration of monomer and oxidants are used which favors the heterogeneous nucleation to occur first on the solid substrates. The proposed mechanism is very much similar to the stepwise electrochemical polymerization [253].

- Electro spinning (Fig. 4.12 **i**). Nanofibers are prepared using the electro spinning technique. Electro spinning uses electrical forces to produce polymer fibers with nanometer-scale diameters [259]. Electro spinning occurs when the electrical forces at the surface of a polymer solution or melt overcome the surface tension and cause an electrically charged jet to be ejected. For the aniline polymers, due to their low solubility, only low molecular weight polymers or mixtures with other, more soluble polymers are possible to be electro spinned.

Thus, nanoscale structuring of polyaniline down to 30 nm feature size using different methods is possible and each of them has its own advantages and drawbacks. Interesting is the resemblance of the morphologies between different polymerization approaches. For example, no clear difference could be attributed to structures fabricated by interfacial, seeding and surfactant or oligomer assisted polymerization (Figs. 4.12 **a** - **d**). The same can be ascribed to the stepwise electrochemical and diluted polymerization (Figs. 4.12 **g**, **h**). This originates from fundamental similarities in the reaction mechanism or the imprinted growth history on the final morphology. It is clear that the solution based synthesis penalties any alignment resulting in disordered aggregates, from which is hard to separate and isolate single objects, explaining why only bulk quantities of nanostructures have been used and characterized so far. Substrate synthesis increases the alignment. Using hard templates ordering can be achieved. Nevertheless, without addressing a criticism, it is quite difficult to imagine how to isolate and characterize a single distinct nanowire or how to integrate these techniques into a device fabrication line. In the following, an approach will be presented which not only allows for a higher-resolution patterning of polyaniline but also for single - nano object growth and processing with an unprecedent accuracy level. By elegantly co-integrating EBL templates with the electroless polymerization of aniline we show that the polyaniline can be structured with an unprecedent areal patterning density and 3D structural control.

4.3.4 Aniline electroless polymerization

Different from electropolymerization and chemical polymerization, electroless polymerization of aniline is a relatively novel method for synthesizing polyaniline films or nanostructures. In electroless polymerization, aniline molecules are oxidized to polyaniline by soluble oxygen on a platinum or palladium substrate (in a first approximation; as it will be shown further the polymerization is not limited only to these sub-

strates). The reaction is initiated by catalysis of the substrate and proceeds continuously with presumably the autocatalysis of the polyaniline film being deposited. The principle of autocatalytic polymerization of aniline is similar to that of autocatalytic plating. Autocatalytic plating is also called electroless plating.

4.3.4.1 Intrinsic advantages

Electroless plating proceeds along an electrochemical mechanism that involves anodic and cathodic half-reactions, both occurring at a single substrate without applying electrolytic current. In contrast, electroplating involves anodic reactions at the anode and cathodic reactions at the cathode, and is initiated by an electrolytic current. The key for the feasibility of electroless plating is that the overall reaction, although thermodynamically feasible, cannot proceed to any great extent without the catalytic initiation of some substrate and autocatalysis of the metallic film being deposited. By electroless plating, a uniform metallic film can form onto a substrate of any shape that is not available to carry uniform electric current as an electrode, or even onto a dielectric substrate after being catalyst-activated. In the case of aniline electroless polymerization, the presence of platinum coatings for the initiation and the propagation of the reaction is imperative. Palladium coatings have been found also to promote the reaction. Nevertheless, due to its reduced activity and hence, lower polymerization rates compared to platinum, Pd is less attractive and its applicability was not studied in detail. The process is similar to the surface initiated polymerization, where an initiator is selectively grafted on a surface to induce the polymerization [260]. However, there are some fundamental differences. For example, the platinum not only initiates but also maintains the reaction. The reaction is not only surface initiated but also surface confined as no polymer could be found in the reaction media even after prolongated times[17]. This is very useful for the subsequent processing and for nanoscale patterning. No rigorous procedures for the removal of eventually formed unbound polymer are needed implying only washing of nonreacted monomer and formed salts. Nanoscale patterning is facilitated as well. Templates can be filled easily if created on top of platinum coatings and as the reaction occurs in a "bottom-up" way, the risks of template clogging or the formation of a undesired polymer film on top of nanostructures, compromising structural integrity is eliminated. Using other methods, this can be troublesome.

[17] Eventually, if the reaction vessel was Piranha cleaned prior the polymerization and not adequately treated to remove the oxidative nucleation points created by the Piranha cleaning, the reaction media turned into slightly reddish after some time.

Other advantages are originating form the electroless nature of this type of growth. Compared to electrochemical deposition where the electrolytic current is a measure of the deposited quantity, no such control is needed in the present method. Thus, nanoscale growth is possible here, while it is unfeasible by using electrochemistry as the nanoscale quantities to be deposited will imply extremely (seen as impossible to attain) low plating currents. As well, electrochemistry requires continuous electrical connection to the area of interest. No such condition is required for the electroless deposition case. The growth was successfully conducted on nanoscale catalyst elements deposited on an insulator substrate without any external electrical connection. Very important, it was found that other conductive substrates can initiated the growth, provided that they are in contact with some platinum elements. This extends the processing methodology to virtually any type of substrate combining variate metallic and even semiconducting coatings.

4.3.4.2 Growth mechanism

The most generalized mechanism of aniline polymerization can be described as follows (Fig. 4.13). The aniline monomer first undergoes a protonation reaction in acidic reaction media. Subsequent oxidation leads to the formation of dimeric species (p-aminodiphenylamine, N-N'-diphenylhydrazine and benzidine). It is considered as the rate-determining step because the oxidation potential of aniline is higher than those of dimers and subsequently formed oligomers and polymer [261]. This effect is exploited in oligomer assisted polymerization as already discussed above. Upon formation, the dimers are immediately oxidized and then react with an aniline monomer via an electrophilic aromatic substitution, followed by further oxidation and deprotonation to afford the trimers. This process is repeated, leading eventually to the formation of polyaniline. Though the actual mechanism of polymerization is more complex and the debate is still open, this picture represents quite well the polymerization process. Questions like what forces the oligo- and polyaniline chains to grow or how the emeraldine oxidation state of polyaniline is reached are still continuing to be raised by the researchers. In the simplified mechanism presented in Fig. 4.13 the polyaniline is synthesized in its fully reduced form (Leucoemeraldine) though it has been fully documented that the most common phase in which polyaniline is produced is emeraldine oxidation state. Are some steps missing or there are subsequent protonation induced oxidation/reduction reactions (as depicted in lower panel of the Fig. 4.13)? These points are quite far from the context of this work and will not be further discussed.

In the electroless polymerization, the aniline undergoes probably the same reactions to obtain the polyaniline. It is the cathodic reaction and the catalytic effect of the platinum that changes everything. The electroless deposition of polyaniline is supposed to proceed through the same equations involving two half-cell reactions simultaneously occurring at a single substrate. At a certain moment, some areas of the substrate act as anodes for the anodic half-reaction, while others as cathodes for the cathodic one. As has been showed by XPS analysis, the product of electroless polymerization was found to be chemically similar to the chemical and electrochemical obtained polymers but different in morphology [262, 263].

The polymerization kinetics has been studied in order to calibrate the growth rate and decript the influence of various parameters. Typical reaction mixture consisted in 0.4 M H_2SO_4 and 0.32 M $C_6H_5NH_2$ aqueous solution. Aniline (technical grade) was distilled twice at room temperature under vacuum before usage. 2 mL of H_2SO_4 (98%, reagent grade) were first mixed with 100 mL of DI water followed by stepwise addition of 3 mL aniline under agitation. Oxygen was continuously bubbled through the solution during the polymerization. This ensures a constant concentration for the dissolved oxygen. Typically, the reaction was thermostated at 50°C. It was found that no reaction occurs when oxygen was depleted from the solution or when not in presence of platinum. The presence of platinum seems to be crucial for the reaction. In fact it is well known that the aniline is oxidized if exposed to air with the formation of red-colored oligomers. An acidic solution, for example aniline sulphate, is stable and remains colorless for months, even when exposed to air or oxygen. Thus, the reaction is not feasible without the catalytic action of platinum. When catalyst coated samples were added to the reaction vessel, gradually a green color could be visualized on the metallized parts. The green color is characteristic of the acidified emeraldine oxidation state.

The polymerization rate was found to be sensitive to the reaction temperature but constant in time. Oxidized silicon chips were metalized with 100 nm Pt (2 nm of Ti layer was used to promote the adhesion, both e-beam deposited at 1 Å/s evaporation rate) and put into the reactor at different temperature. At equal intervals of time, samples were removed, washed with copious amount of DI water, re-acidified with 1M HCl and dried in vacuum. The thickness of the grown polyaniline was measured using surface profilometry. The temperature influence is shown in Fig. 4.14. A linear dependence of the polyaniline thickness in time was found. This signifies that the polymerization rate is constant. These data are in contradiction with pioneering work of Liao *et al.* and Chen *et al.*

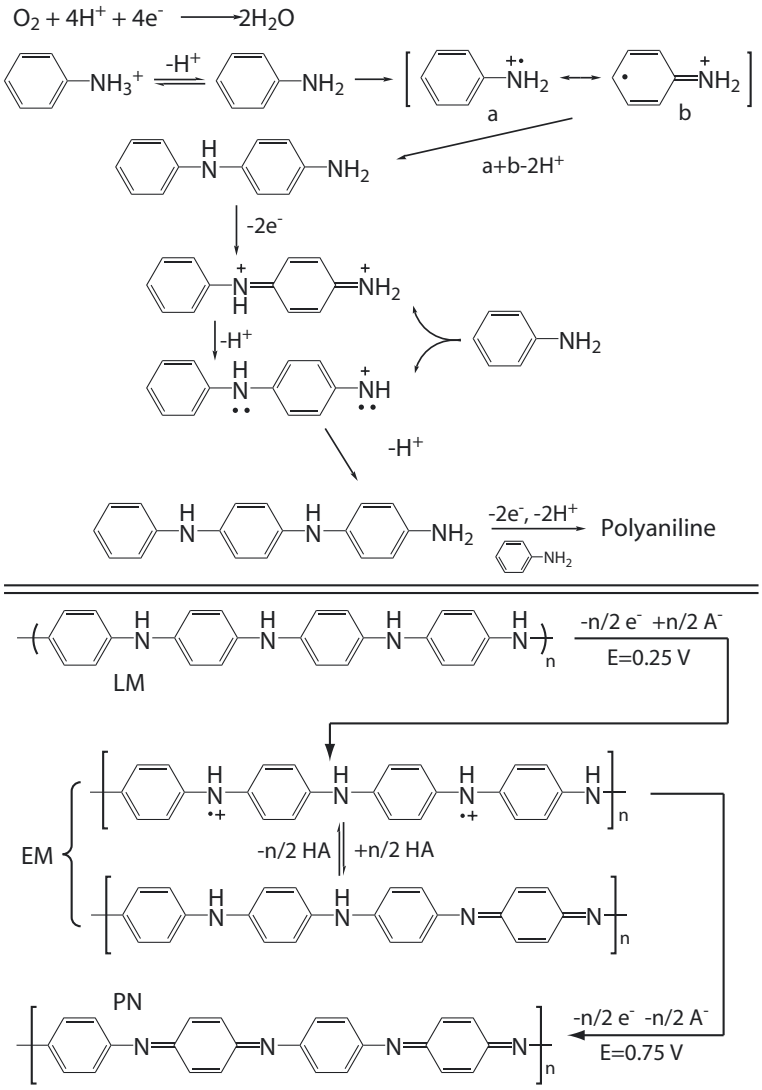

Figure 4.13: Reaction pathways for the polymerization of aniline. Upper scheme: cathodic half-reaction occurring during the electroless polymerization and possible reaction mechanism for the anodic half-reaction. This is one of the general pictures describing the oxidative or electrochemical polymerization of aniline. The net reaction summarizes to the oxidation of aniline by the dissolved oxygen with the formation of polyaniline. Lower scheme: Generalized scheme of the oxidative and non-oxidative (protonic acid) doping of polyaniline.

[263, 264]. They have observed very slow polymerization rates (1 μm of polyaniline after 7 days of polymerization) compared to extremely high

rates observed in this work. For example, at 70°C, the growth occurs at a rate of 400 nm/hour.

In a recent work, Attout *et al.* presented even higher polymerization rates: 500 nm/hour at 80°C [262]. They have also studied the influence of the reaction temperature on the polymerization rate. The polymerization rate was found to increase with the temperature in an exponential way, reaching a maximum at ∼80°C and then followed by a decrease at higher temperatures. The same behavior was found also in this work and almost no polymerization occurred when reacting at 95°C. Deactivation of the reaction with the temperature is unusual as typically all the chemical reactions are following the classical Arrhenius exponential temperature rate coefficient activation. This behavior is explained by the dissolution of the oxygen from the aqueous media upon heating and hence, the reaction slow down. Another discordance with the initial work of Liao *et al.* is the absence of the autocatalytic effect. They have stated that the formed polyaniline has an autocatalytic effect on the subsequent polymerization[18]. No such effect was observed in our experiments and typically the polymer thickness was linear in time. Some discordances from the linearity, however, have been sometimes observed. Especially, when using oxidized highly doped silicon wafers coated with platinum. During the dicing, the metal was spread from the surface of sample and created a metallic contact with the underlying silicon. As it will be shown further, this induced the polyaniline growth on silicon as well and hence, disturbed the growth on platinum. For a better reproducibility and to avoid this instabilities, isolating substrates have been subsequently used for the growth calibrations. Worth mentioning also that for these experiments, the sample were cleaned in fresh Piranha solution and afterwards rinsed with water prior to the immersion in the reactant solution.

It was also observed that the thickness of platinum has an influence upon the polymerization rate. This was again in discordance with the work of Liao and co-workers as they stated that the platinum plays only the role of initiation and subsequent growth is dictated by the already grown polyaniline. If this is true, then the thickness of the metal had to influence only the beginning of the polymerization and once the polyaniline film covers the entire surface it should no more be of importance. This was not observed in our work. Both, the influence of the thickness of the metal deposited on different substrates and the surface treatment condition have been studied. Glass slides were used as catalyst supports and $Ar/H_2(5\%)$ plasma cleaning at room temperature (1 min, 50 sccm,

[18]Though, even in their work it is not clear the presence of the autocatalytic effect of the polyaniline. For example, Figure 2 in their paper shows a decrease in the polymerization rate.

2.5 mW/cm^2 power density, 15 mTorr) was performed prior to the polymerization. The metalization was carried out in a e-beam evaporator with a base pressure of 2×10^{-7} mbar and metal evaporation rate of 1 Å/s. The reaction was carried on at 50°C. After the PANI growth, the samples were washed with copious amounts of DI water, acidified with a 1M HCl solution, blown dry in a N_2 stream and vacuum dried for 12 hours. The thickness measurements were realized using surface profilometry. The platinum topography was examined with atomic force microscopy (AFM) in tapping mode. The surface roughness R over a 2×2 μm^2 area was estimated using the functions provided by SPIP v.4.6.1 Scanning Probe Image Processor.

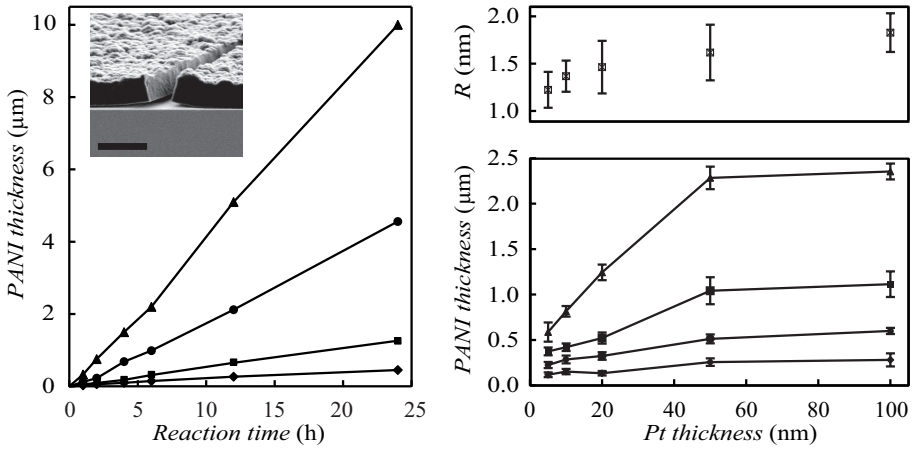

Figure 4.14: Left: Polyaniline thickness function of the reaction temperature. Closed diamonds, squares, circles and triangles are corresponding to 10, 30, 50 and 70°C, respectively. Inset: SEM side-view showing the compact bulk and rough surface morphology of the electroless deposited polyaniline. Right: Polyaniline thickness for different reaction times (lower graph chart) and the evolution of the platinum surface roughness (upper graph chart) as a function of the evaporated platinum film thickness. Closed diamonds, circles, squares and triangles are corresponding to 3, 6, 12 and 24 hours reaction time, respectively.

As shown in Fig. 4.14, the polymerization rate increases with the platinum film thickness (up to cca. 50 nm) and then saturates. The evolution of the platinum surface roughness is mimicking this dependence. Alike evolution has been found to occur for the platinum films grown on Si(100) [265]. This is further translated into an increase in the effective electroactive surface, i.e., in the number of active sites available for the electrochemical reactions [266]. It is well known that the platinum

group metals, such as platinum or palladium, are excellent catalysts for many electrochemical and chemical reactions (especially for the cathodic half-reaction as shown in Fig. 4.13). Their morphology and poisoning are also known factors influencing the outcome of the catalytic reaction. In this case is the platinum film thickness that controls the morphology (dictated by the dynamics of the metal crystallization upon evaporation on the substrate) and hence, polymerization rate. The kinetics of the aniline electro polymerization on platinum surfaces seems rather morphology than thickness dependent. In favor of this is the enhancement of the polymerization rate on catalyst coated Teflon®FEP sheets (approximately 3 μm thick polyaniline film was grown in 24 hours on a 10 nm thick platinum film displaying a surface roughness of about 3 nm) since the roughness of the metal coating on this substrate is larger than on glass. Presumably, using rougher catalysts coatings (either using rough substrates or changing the metal deposition parameters), higher polymerization rates can be achieved. This aspect may also contribute again to the discordances between different reports. Different metal coatings, prepared in different conditions (Liao *et al.* and Chen *et al.* have used metal plates compared to thin films deposits) may give rise to differences in the polymerization rates.

Other key parameters in the aniline electroless polymerization are the catalyst surface cleanliness and reactivity. For example, a 10 μm thick PANI layer grows on freshly evaporated 100 nm thick platinum films in similar conditions. In turn, aging of the samples has been found to have a detrimental effect on the polymerization rates. This is related to the adsorption of different contaminants and subsequent inhibition and reduction of the number of reactive sites necessary for the polymerization. Interestingly, Piranha cleaning reactivated the surfaces almost at the same degree as for the as-evaporated case. Surface reactivation through plasma was found to be dependent on the dry etch chemistry. Pure O_2 cleaning (using RF-inductively coupled plasma and ozone cleaner) strongly altered the catalytic activity, while pure Ar or mixed Ar/H_2 restored the catalytic properties of the substrates. The latter was preferred due to its mild operation conditions and its effectiveness observed even for short plasma exposure times. As it will be shown further, these protocols are degrading also the PMMA templates and depending on the desired processing scale they were adjusted accordingly. This behavior is explained by the formation of an inhibiting platinum oxide film on the surface upon the oxygen plasma treatment, which can be further stripped out using energetic Ar^+ ions bombardment or through H_2 reductive plasma [267]. A simple way to qualitatively check the catalyst activity is to dip the samples in 10 - 30 % aqueous solution of H_2O_2

(hydrogene peroxide). It is known that H_2O_2 undergoes in time a decomposition reaction with the formation of water and oxygen following a simple reaction: $2H_2O_2 \rightarrow 2H_2O + O_2(gas)$. Platinum catalysis this reaction. The samples with good catalytic activity have been found to react energetically with H_2O_2 with violent evolution of oxygen form the platinum surface while inhibited ones (O_2 plasma treated or aged) reacted less or very slow. Equivalently, when dipped in the polymerization media, the active samples displayed the green colorization on the surface much faster than the inhibited ones. Thus dipping the samples in a hydrogen peroxide solution enabled fast screening of the catalytic activity of platinum coatings. Quantitative description of the catalytic activity can be performed using gas sorption-desorption experiments or electrochemical studies (for example using classical chronoamperometric oxidation of hexacyanoferrate). Palladium was found to behave in a very special way. Though the polymerization of aniline occurs as well, no more than 200 - 300 nm of polyaniline per day have been grown on palladium, even after vigorous Piranha cleaning. Plasma or thermal treatment have been found to have a minimal effect on the growth rates. Only on freshly evaporated palladium, a record thickness of 3 μm of polyaniline in 1 day was achieved. It is not clear for the moment what is the inhibition mechanism for the case of palladium and why its catalytic activity is difficult to be restored.

4.3.4.3 Optoelectronic properties

As it will be shown in Sections 4.4.1 and 4.4.2 it is possible to pattern the polyaniline at various scales and in many complex architectural configurations. For example, 3D photonic crystal structures and lattices were fabricated. Polyaniline turns out to be a good candidate for the fabrication of chemically tunable photonic devices[19]. Doping/dedoping of polyaniline by using acid/base chemistry induces profound changes in its electronic structure (for example, metal-insulator transitions). Important is the reversibility and hence tunability of these transformations. Monkman *et al.* have studied the doping dependence of the optical properties of polyaniline films using infrared reflectivity measurements on a series of samples with different dopant acids and various doping levels. They have observed typical fingerprints of a disordered metal such as a very high reflectivity in the far-infrared and a plasma resonance [268]. The later could be exploited in plasmonic devices if one could build

[19]Moreover, due to the presence of the third-order nonlinear susceptibility in polyaniline (or nonlinear optical response) this material could be very useful for the fabrication of next generation flexible, tunable, all-optical devices.

ordered polyaniline nanostructures. Other groups, have fabricated photonic crystals using polyaniline and have tested the modification of the optical stop bands upon exposure to different chemicals. Their fabrication was based on the use of ordered silica colloidal crystals and subsequent electroplating and inversion with polyaniline [40, 269]. Despite the fact that the polyaniline has strong absorption bands in the visible range of spectrum and an extended tail in the infrared it was possible to build photonic crystals and to chemically modify their photonic band gap.

The optoelectronic properties of electroless synthesized polyaniline have been studied as well. Absorption spectra were acquired on 150 nm thick polyaniline films grown on a semitransparent 10 nm thick Pt film on glass. After the growth, the samples were washed with water to remove any unreacted aniline sulfate and then either reacidified with 1M HCl for measurement on the emeraldine salt phase or rinsed with 1M NH_4OH to characterize the emeraldine base. The samples were vacuum dried. The specific absorption peaks for the emeraldine salt are present. The 3.6 eV peak corresponds to the π - π^* band gap transition, while the 1.5 and 3 eV maxima are due to the presence of the polaron band [270, 271]. These absorption peaks disappear in the base form and the maximum centered at 2 eV is indicative of the formation of excitons [272].

For the variable angle spectroscopic ellipsometry the samples were prepared in a different way. Transparent or semitransparent substrates are to be avoided as they induce to many incertitudes in the measurements and especially in the data interpretation. For that, optically thick Pt films (130 nm) were used as seeding layer. First, the optical constants of platinum have been modeled based on variable angle spectroscopic ellipsometry. The characterization of optically thick samples (either bulk substrates of optically absorbing materials with no coatings or thick films of optically absorbing materials) is in some ways both the simplest and the most difficult of ellipsometric analyses. It is the simplest in that fitting the data merely requires "inverting" the measured Ψ and Δ values to obtain n and k values for the substrate. It is very complicated in that such systems do not often occur in nature, and nearly all "bulk" samples actually have some sort of surface overlayer on them (native oxide or surface roughness usually). The neglect of this overlayer will yield optical constants which are not correct for the substrate. If these constants are then used for a coated substrate from which the oxide or overlayer was removed prior to film deposition, difficulties may be encountered in the subsequent analysis of the coating. Typically, a film is considered optically thick if it not back-reflects the light-beam from the bottom side of the film. For platinum, coatings thicker than 60 nm have been found to behave as optically thick, or treated as a bulk substrate. Surface

roughness ($\sim$ 1 nm for 130 nm platinum deposited on thermally grown silicon oxide) has been not taken into account. The surface was cleaned in the same way as before polymerization. The acquired Ψ and Δ values were direct inverted to obtain the optical constants of the substrate using "point by point" fit procedure provided by WVASE software. They were found to vary from batch to batch (because the roughness and surface contaminants are not taken into account) and, typically, the samples used to determine the optical constants of platinum were used also to characterize the optical constants of polyaniline.

Similar to the work of Monkman *et al.*, an anisotropic model was found to give the best fit [273, 274] to the experimental data (Fig. 4.15 (**b**), (**f**) and (**c**), (**g**)). A Drude-Lorentz model with three oscillators and a free carrier contribution was used for the emeraldine salt and a Lorentz model with two oscillators for the emeraldine base. The surface roughness was modeled using an effective medium approximation. The data analysis was performed using the WVASE software (version 3.610)[20].

Clearly, the optical properties (absorption and refractive indexes) can be effectively modulated upon acid or base treatments. This is already visible from the acquired Ψ and Δ. Quantitative analysis can be done form the extracted n and k dispersions. Although the ellipsometry is not the most suited method for the optical index determination (0.01 - 0.05 accuracy) it is a simple and a rapid method for its evaluation. For example, at 2 eV photon energy (or 620 nm wavelength) the estimated refractive index is 1.3 in the doped state and 2 in the dedoped state. This is a huge variation for an optical index and could be used to tune the optic properties of a polyaniline photonic crystal. However, the high-absorption (and hence attenuation of the propagating waves) of polyaniline in the visible range of spectrum could limit its applicability. There are some techniques to avoid these undesirable effects (see Chapter 2 for details).

[20]The Lorentz oscillator parametric model for the dispersion of the optical constants of materials is derived based on the assumption that the response of electrons in a material to a driving electric field (in this case due to the light beam) is similar to the response of a harmonically driven mass on a spring subject to a dissipative force. Within this analogy, the mass corresponds to the electron, the spring represents the electrostatic force on the electron due to all of the other electrons and nuclei in the solid, and the dissipative force (friction, for the mass on a spring) represents the electron energy loss due to emission of a photon. The Lorentz model can accurately describe the optical constants of many materials, and is particularly useful for resonant absorptive processes (dye absorption lines, vibrational bands in FTIR data, etc.). It also has the useful property of reducing to the Drude model for free electron absorption in the limit of an oscillator centered at zero energy, which is very useful for transparent conducting oxides and heavily doped semiconductors. See also Chapter 2.

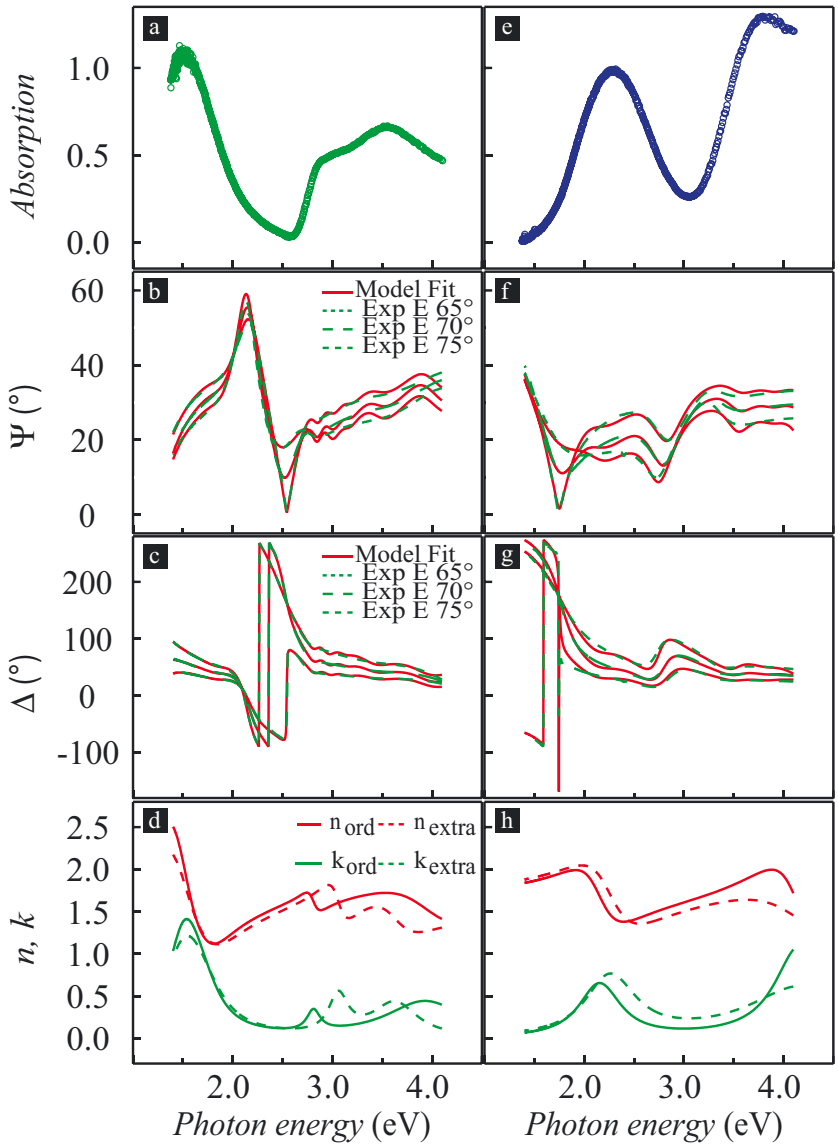

Figure 4.15: Chemical tunability of optical properties of the as-synthesized polyaniline films in the 1M HCl doped emeraldine salt (**a-d**) and 1M NH_4OH dedoped emeraldine base (**e-h**) forms. Absorption spectra (**a**, **e**). Measured ellipsometric angles Ψ (**b**, **f**) and Δ (**c**, **g**) as well as the best fits to the acquired data using a variable angle ellipsometer (VASE, J. A. Woollam). Extracted ordinary (in-plane) and extraordinary (out-of-plane) refraction index and extinction coefficient (**d**, **h**).

A 7% change in the thickness was also observed between the two forms of the emeraldine (172 nm for the base and 185 nm for the salt). This is due to the unique chemistry of the polyaniline. The incorporation of dopant ions is accompanied by charge repulsions and hence, volume expansion, property that has been extensively exploited to build mechanical actuators using the polyaniline [275] or other conjugated polymers [276]. Volume variation is known also to occur between the dry and wet states of polyaniline, again due to the incorporation of solvent molecules in the polymer matrix. As it will be shown in Sections 4.4.1 and 4.4.2 this actuation is rather annoying when building large interconnected polyaniline assemblies.

4.3.5 Nanoscale chemistry

As has been highlighted in previous sections, one of the big advantage of the electroless polymerization is that it proceeds without any electrolytic current supply and external control. Thus, the growth can be conducted on isolated catalyst elements only by controlling the temperature and the morphology. In a series of experiments, the growth was studied on platinum islands defined onto thermally oxidized silicon. The square catalyst islands have been defined using EBL and metal physical vapor deposition via a lift-off protocol (1 nm Ti to promote the adhesion followed by 40 nm of Pt, both evaporated at a rate of 1 Å/s). The samples were subsequently cleaned in hot acetone under sonication and prior to the polymerization reaction they were plasma cleaned and activated. The growth was characterized using AFM, SEM and optical microscopy. Figure 4.16 (**a**) shows a series of 750×750 nm^2 platinum slabs covered with 200 nm of polyaniline. Each of them operates independently and can be treated as a nanoscale polymerization reactor. As it can be observed, all nanoreactors behave identically and each of them produces approximately 0.15 pg of polyaniline (assuming a density of 1 g/cm^3 for the polymer). Thus, the present approach allows to control the positioning of single nanoscale polymer structures.

Subsequently, individual platinum nanoreactors have been used to induce self-aligned 2D growth. As it can be visualised in Figure 4.16 (**b**), the incipient stages of growth (for a 200 nm film thickness) show that the polyaniline pattern clearly preserves the initial shape of the platinum islands; the white square delimits the size and the orientation of one initial catalyst slab and it is here guide to the eye. These polymer elements grown on each Pt pad do not seem to merge with each other. Doubling the thickness of the polymer film strongly alters the obtained structure by mutual hindrance (Fig. 4.16 **c**). In this stage, the

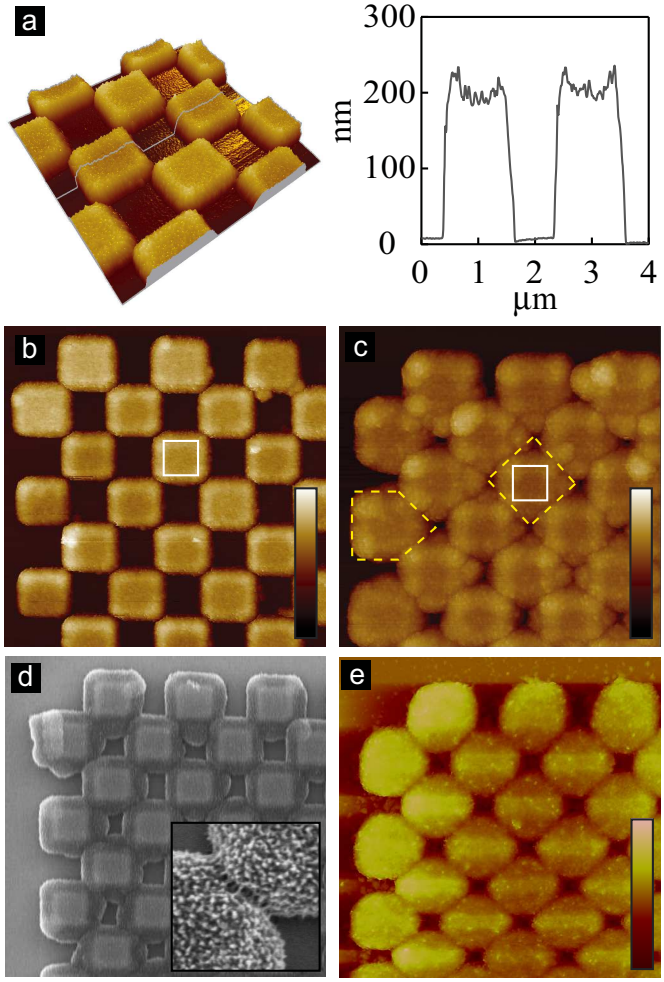

Figure 4.16: Micro- and nano-scale chemistry using platinum miniaturized reactors on an insulating substrate (Si/SiO_2). (**a**) 4×4 μm^2 AFM topography image and height profile plot of polyaniline slabs grown on top of platinum islands. 7×7 μm^2 AFM surface plots (**b**, **c** and (**e**)) and SEM top view (**d**) evidencing 2D self-aligned growth for different polymer coverage and growth configurations. See text for details. Color scale bars: (**b**, **e**) 0-500 nm and (**c**) 0-1000 nm.

central PANI squares are rotated by 90° while the frontier ones are best described by a pentagonal shape (delimited here by the dashed lines). During the reaction, the formed polyaniline is in its doped state due to the protonation at the imine nitrogen by the acidic medium to yield a polysemiquinone radical cation. This induces a surface charge on the

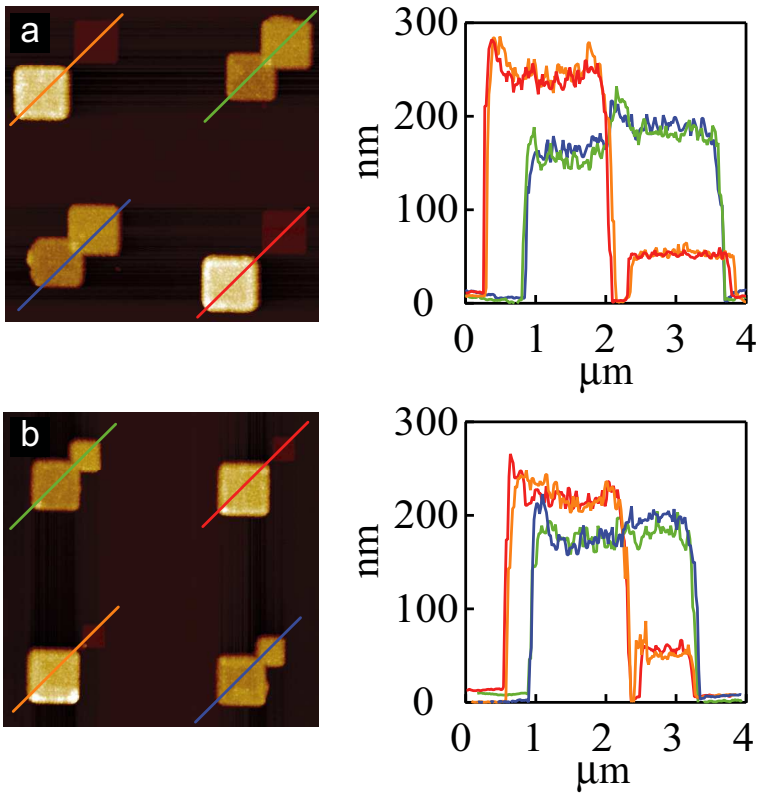

Figure 4.17: Micro- and nano-scale chemistry using platinum and gold miniaturized reactors on an insulating substrate (Si/SiO_2). 4×4 μm^2 AFM surface plots with the respective height profiles for (**a**) 1.2×1.2 μm^2 Pt - Au and (**b**) 1.1×1.1 μm^2 Pt - 0.66×0.66 μm^2 Au alternatively connected pads. The thickness of both metals is 50 nm.

polyaniline which probably is at the origin of the electrostatic repulsion between the growing polymer blocks. However, other parameters, such as the interface with the substrate, might interfere and contribute to the pattern reorganization. Intermediary shapes could be visualized together with the fact that the joining occurs through the formation of polyaniline nanofibrils [277]. For example, Figure 4.16 (**d**) shows a SEM image[21], in which a series of polyaniline octagons originated from square platinum elements are visible. Zooming in the joining area indeed illustrated the presence of PANI nanofibrils. It has been suggested that

[21] A 15 keV electron beam was used to enable transparency of the polyaniline layer and vizualisation of the platinum elements.

the metallic surface is endowed with a common electrode potential for both the electrochemical half-reactions, the open-circuit potential [264]. As the nanoreactors are lying on an insulating substrate, each of them is endowed with this potential and the tiny electrical potential differences that arise between them materialize into the polyaniline nanowires. While the open-circuit potential could also contribute to the electrostatic repulsion between growing elements and the self-arranged pattern formation our experiments rule out this supposition. A fully evaporated (*i.e.* a *Pt* thin film, to ensure electrical shorting between the "catalyst elements") sample was used. Using EBL, squared masks (having the same size as the platinum elements in previous experiment) have been opened in a PMMA mask and the sample was reacted in the same manner. The same surface pattern reorganization behavior of polyaniline was observed though, this time, the "platinum elements" are interconnected and the possible charge differences should be nulled. Following the same rationale, one can reason that once the polyaniline elements are joined (somewhere in between (**b**) and (**c**)), due to the electrical conductivity of polyaniline, the same charging effect should equal on all elements and no more charge differences should arise. Thus, the electrostatic repulsion of charged polyaniline surfaces during the growth remains one of the most plausible explanation for the observed behavior. However, a flagrant consequence of the open circuit-potential charging is that the growth can be extended to virtually any type of conducting material in contact with platinum, thus further increasing the applicability of the method.

The same type of growth was achieved on *Au* islands provided that they are electrically connected to *Pt* catalyst pads. To study that, EBL and lift-off metal deposition was used to define a series of platinum and gold nano- and micro-scale catalyst elements. First, a series of *Au* slabs with various sizes (1 nm *Ti* adhesion layer and 50 nm *Au* deposited both at 1 Å/s) were defined on a thermally oxidized silicon wafer. At the same time, two sets of alignment marks were also defined. In a second step, EBL and metal lift-off was used to define the platinum component of the catalyst elements (1 nm *Ti* adhesion layer and 50 nm *Pt* deposited both at 1 Å/s). The first set of marks ensured a good overlay alignment with the existing gold pads. The design was chosen in a such a way that some dual platinum and gold elements were interconnected whereas some of them not. The second set of marks was used further to define the nanochannels in the PMMA layer for subsequent template confined polymerization. This will be detailed in Section 4.4.1. At this stage, the structure of samples was sufficient to study the mechanism of the growth on dual catalyst elements. Prior the polymerization, the samples were

cleaned in acetone under sonication and plasma treated and activated.

There are several interesting characteristics of the induced growth on *Au*. First, no polymerization occurs on isolated Au islands (Fig. 4.17). Obviously, this was expected, as the gold is known to have no catalytic activity and no growth was detected when gold metallized samples were dipped in the polymerization media during several days. Second, when the *Pt* and *Au* components are in contact, polyaniline grows on gold affecting at the same time the polymerization on platinum. The PANI thickness grown on *Au* is typically larger than the thickness of the PANI block grown on the connected *Pt* nanoreactor. This is probably related to the differences in the surface roughness for the respective metals (0.73 nm for *Pt* and 0.87 nm for *Au* on thermally oxidized silicon), corroborating the data presented in Fig. 4.14. Third, a simple scaling rule can be used to estimate the thickness of the polyaniline grown on each metallic element. The quantity produced on an interconnected *Pt* - *Au* reactor is equal to the quantity produced by a single isolated *Pt* reactor, provided that both *Pt* sites are identical in size. This is exemplified in Fig. 4.17. By calculating the volume of produced PANI, we found that the single *Pt* and the interconnected *Pt* - *Au* reactors approximately produced 0.45 μm^3 and 0.42 μm^3 (panel (**c**)) and 0.32 μm^3 and 0.30 μm^3 (panel (**e**)) of PANI, respectively. This data provides insight into the polymerization mechanism. The oxygen is reduced on the platinum surface (consuming the electrons through the cathodic half-reaction), while the aniline is oxidized on both platinum and gold surface if they are connected (providing the electrons through the anodic half reaction). Consequently, whether in contact or not, the total charge balance has to be the same, meaning that the quantity of polyaniline (i.e. the thickness) will be mainly governed by the platinum catalyst. This scaling rule has been verified multiple times and on different samples[22].

The growth was induced on silicon and porous silicon as well. First, this was observed during the growth calibration on platinum coated silicon wafers. As mentioned earlier, during dicing, the platinum was spread and created an electrical contact with the underlying silicon layer (especially when highly-doped silicon wafers were used). During the polymerization, polyaniline was present on the metal surface and on the edges of

[22]However, due to different degree of catalyst contaminations (insufficient plasma activation, resist residuals) on some samples differences in growth between apparently similar platinum slabs was observed. As well, when big gold pads were in contact with small platinum areas, no growth was detected on both if they were in contact with the solution. Upon suitable masking of gold, the growth occurred in a normal way on the platinum. Thus, this could be used either to induce the growth on gold or other metals or to partially block the polymerization on platinum.

samples as well. Sometimes, when scribing the back-side of the wafers (using a diamond scriber and thus removing the silicon oxide layer) the growth occurred on the scratched areas. See for example Figure 4.18 (**a**).

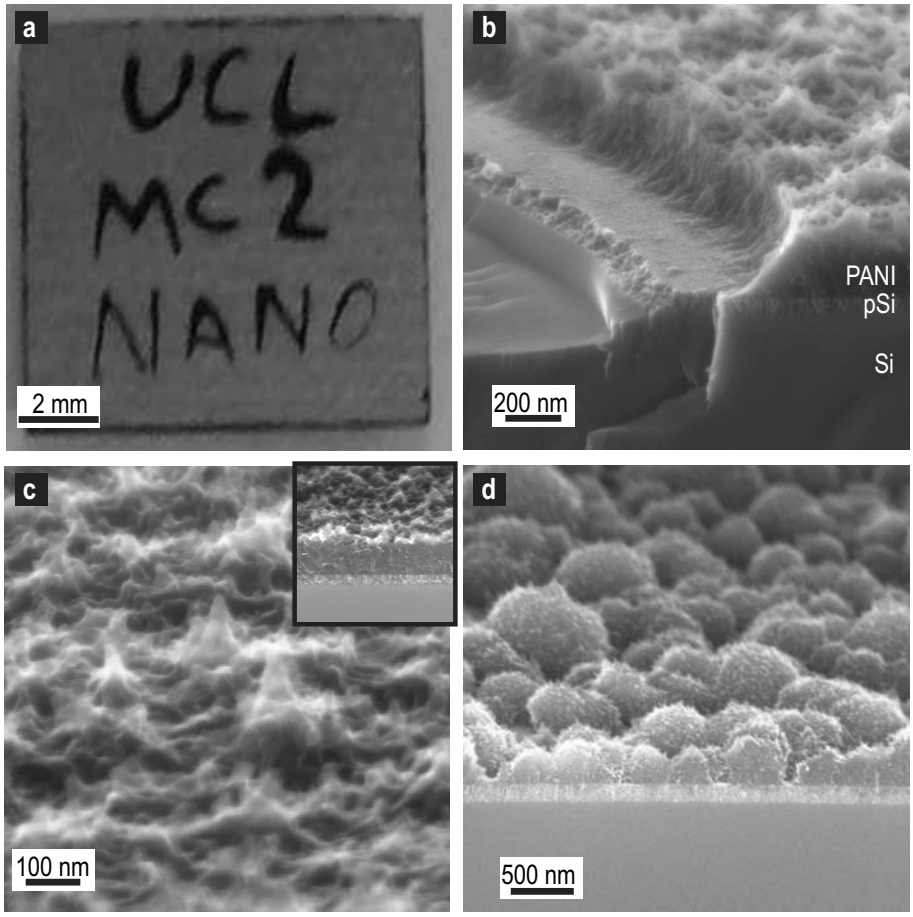

Figure 4.18: (**a**) Back-side of a metalized sample showing the polyaniline growth on the edges of sample and on the scratched areas. The inscription was done using a diamond coated tip. (**b**) Cleaved SEM view of a polyaniline - porous silicon - silicon multilayer. (**c**) Side view of the polyaniline surface morphology grown on oxidant decontaminated porous silicon. Inset: 1×1 μm^2 view of the cleaved sample showing the uniformity of the growth layer. (**d**) Irregular structures obtained when not sufficiently rinsing with water the samples prior to the polymerization.

Interestingly, the polymerization was difficult to achieve on the polished side of the silicon wafers. Some experiments were conducted with-

out any successful results. Highly-doped silicon wafers[23] were first cleaned and subsequently immersed in HF 2% to remove the native oxide and to allow for good electrical connection between the metal and the platinum. Shortly after, the wafers were mounted in a high-vaccum chamber and 100 nm of platinum were deposited on the back-side (unpolished) of the wafer. The electrical connection between the metalized part and the polished side of the wafer was tested using a multimeter. Next, the wafer was diced in small 1×1 cm^2 chips and tested for the polymerization. Cleaning of the front silicon side and platinum activation was performed using a freshly prepared Piranha solution. Unexpectedly, no growth was detected on the silicon whereas on platinum it occurred in a classical way. This may be attributed to the flat surface of silicon and hence, very low number of active sites for the electrochemical reaction. Even if the platinum is in contact with the silicon and the charge transfer can occur, the polymerization rate on polished silicon is low. Probably, scribing with a diamond tip induces nucleation sites and accelerates the polymerization. A different situation was observed when using nanoporous silicon. The porosity was induced using metal assisted chemical etching via the catalytic effect of the same back-side metalized platinum. Thus, platinum plays a dual-catalytic role. First, it is used to assist the chemical etching of the silicon and subsequently to induce the aniline polymerization. More details on the fabrication and mechanism of the catalytic wet etching will be given in Section 5.1. In these conditions, the polymerization occurred on both, catalyst metalized back-side of the wafer and porous silicon film on front side of the wafer (Fig. 4.18 **b**). The nanoscale confined growth on porous silicon is possible as well (see Section 4.4.1) offering the possibility to fabricate various nanoscale organic optoelectronic devices, for examples a hybrid organic-inorganic nano light-emitting device [278]. Accidentally, different morphologies have been found to occur depending on the cleaning and treatment conditions prior the polymerization. For example, when using Piranha to clean (both surfaces) and activate (only the platinum layer) different morphologies of polyaniline grown on top of porous silicon were observed (Fig. 4.18 (**c**) and (**d**)). If the samples were rinsed thoroughly with water (eventually left in water) a uniform coating was detected (**c**), while if rinsed insufficiently, a nonuniform, bump-like coating was detected (**d**). This was attributed to the remaining oxidant (unreacted H_2O_2, known to react with the aniline) in the porous matrix of the silicon inducing an irregular nucleation and polymerization on the

[23] NEYCO s.a.; Silicon wafer, 3AC, elaboration CZ, Orientation [111], dopant : type N, dopant As, resistivity 0.001-0.005 Ωcm, thickness 380 μm, single side polished.

surface. Interesting, yet unexplained for the moment, is the presence of protruding polyaniline fibrils on the surface of uniform coated samples.

4.4 Template confined polymerization

Taking in consideration the mild polymerization conditions and the compatibility of the synthesis with the EBL fabricated PMMA templates, we have succeeded to pattern the polyaniline with an unprecedent resolution, areal pattern density and 3D structural complexity. In the following Sections we will treat the main aspects, achievements and encountered problems. First, 2D template confined polymerization and structuring is discussed. 3D systems offers additional possibilities and are presented next. Finally, the high 3D structural control offers subsequent hierarchical functionalization and guided assembly.

An hierarchical approach was used to multiscale pattern the polyaniline. A schematic representation is given in Fig. 4.19. Various possibilities are offered by this methodology, each of them depending on the final application. The first step is the choice of substrate. Rigid opaque silicon, transparent glass or flexible substrates such as teflon (Teflon®FEP) or polyester (Mylar®A) have been successfully used to obtain polyaniline films or nanostructures. Step 2 representing the catalyst coating, could be also divided in multiple choices. Patterned or not, with additional dual-metal sites, again either in contact or not. Polyaniline growth (step 3) could be also divided into multiple configurations. Film coatings as well as and 2D or 3D nanoscale structuring on uniformly catalyst coated samples can be realized. Nanostructured growth is possible EBL fabricated templates or not, by using miniaturized polymerization reactors either in single or dual metal catalyst configuration, the latest being subsequently divided into interconnected type or not. As it can be observed, there are many possibilities to grow and structure the polyaniline. Further steps in the hierarchy could be added upon subsequent functionalization or assembly of the fabricated structures. Another important aspect is the scalability of the process. From the Fig. 4.19 (and from the data presented in Section 4.3.4) it can be deduced that no restrictions are imposed to the patterning scale or design. Moreover, as it was shown in Section 4.2.3, high precision 3D structuring is possible using engineered templates. It will be shown further that this precise 3D shaping is very useful for subsequent functionalization and geometry driven (and locked) assembly.

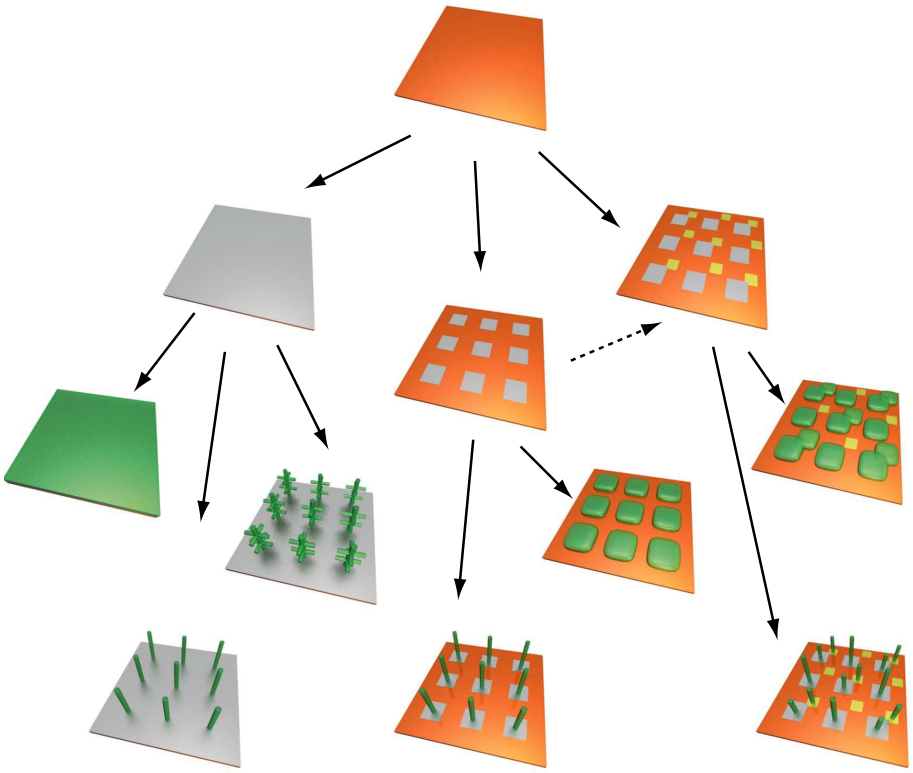

Figure 4.19: Simplified view of the hierarchical approach followed in this work to structure polyaniline.

4.4.1 2D structuring

In this Section, 2D structuring of polyaniline is presented. The spatially confined aniline polymerization is performed using nanofabricated templates generated by EBL. Given this mild polymerization chemistry, standard PMMA positive resist has been employed as template precursor. While resolution as high as 10 nm can be routinely achieved in PMMA, its poor mechanical and chemical resistances do not straightforwardly ensure further high-fidelity pattern transfers. Reactive ion etching is prohibited due to the low etch selectivities that can be achieved. Typically, PMMA is used to pattern an intermediated sacrificial (Cr, SiO_2) layer which is subsequently employed to define the desired layer. This adds additional processing steps and hence stepwise increase in the defects numbers and gradual loose of the initial resolution (implying laborious designing). Unfortunately, this holds for other type of resists as

well. This is technologically important since high-aspect ratio and high-density pattern transfer from the resist template to a desired material is typically troublesome, and so far, has been limited to very few materials.

Some materials are even impossible or not recommended to be patterned in a such a way. Conjugated polymers is one example. Spin on resist and thermal treatment, lithography (EBL or high-energy photon) and RIE or other pattern transfer protocols can irreversibly damage the electronic properties and the chemical structure and hinder their further utility. Moreover, similarities in chemical structure with the standard resist formulations compromise high selectivity in etching rates and thus high-aspect ratio patterning. Our protocol proceeds in a non-destructive way by using the resist patterns as polymerization templates and not as pattern transfer masks.

A typical procedure consists in a 3 steps processing protocol. First, the catalyst is applied on the substrate, either full sample evaporated or structured. Next, the desired PMMA thickness is deposited by spin coating and the pattern is irradiated using EBL. The thickness of the resist will set the processing scale and the maximum thickness of the fabricated nanostructures. High molecular weight (950k) PMMA was used for the EBL in order to achieve the best resolution and contrast necessary for the fabrication of high-aspect ratio nanochannels. PMMA with various formulations (2%, 4%, 7%, 9% and 11%) in chlorobenzene or anisole were used for the template precursor preparation. The PMMA films were made either by coating one thick layer from a concentrated solution at low spin speeds or by multiple coatings from diluted solutions at higher spin speeds. After coating, the samples were baked at 130°C for 24 hours to remove the residual solvent and release the residual stress (especially for thick films).

The exposure was performed either at 30 keV using a modified Scanning Electron Microscope (FEI XL30) with the help of Elphy Plus (Raith) pattern generator, or at 100 keV using a high resolution electron beam lithography system JBX-9300FS (JEOL). The resist thickness and the typical exposure doses for high-resolution and up-scaled polyaniline patterning are 65 - 260 nm, 2 - 7 fC/dot (single shot or dot exposure type was used) and 500 - 4000 nm, 0.2 - 3 mC/cm^2, respectively. The development of the exposed areas was performed in a MIBK/IPA mixture (1/3 v/v) with ultrasonication (1 - 15 min, depending on the processing conditions and targeted resolution) followed by rinsing with IPA (1 - 2 min) and DI water (2 min) and eventually gently blown dry with N_2 or simply let to dry in air. Prior to polymerization, the bottom surface of the nanostructured templates was cleaned and activated as presented in Section 4.3.4.2. The etching times were adjusted in order to minimize

the enlargement of the exposed areas. Typically, we used the shortest times for the thin and the high resolution templates. The filling fraction of the nanochannels accommodated within the templates was set by the polymerization time (Fig. 4.14). The growth can be stopped and inspected at any time by removing the samples from the reaction media and then continuing the polymerization by reintroducing them into the reactor.

After the polymerization, the samples were washed with DI water and then re-acidified with 1M HCl. The template release was performed in hot acetone followed by rinsing with IPA or acetone. To avoid the destructive effects of surface tension during solvent removal, critical point drying was applied. The technique relies on exchanging the initial solvent (IPA or acetone) with liquid CO_2 in a cooled, high-pressure chamber (10 - 12°C, 4.1 - 4.8 MPa). Upon complete solvent exchange, the temperature is raised to bring the liquid CO_2 to its critical point (31.1°C, 7.38 MPa) which is then subsequently evacuated as a gas.

High-areal density patterning is presented in Figure 4.20. The dots are uniform in diameter (22±0.7 nm) with no parasitic growth being detected in between. The height is $\simeq$ 30 nm as measured in SEM cross-section analysis. The EBL pattern was written in a 65 nm thick PMMA resist deposited on 130 nm platinum films (the fine structure of the seeding layer is also visible). No difficulties were found for structuring up to pattern densities of 0.28 teradot/inch^2 (in occurrence, Fig. 4.20 (**c**)). This represents an unprecedent areal pattern density for functional conjugated polymers[24]. Preliminary tests shows that even higher structuring density is possible: 40 nm pitch, equivalent of 0.44 teradot/inch^2 (Fig. 4.20 (**d**)). Direct imaging in a SEM of sub 15 nm dots is quite difficult as the charging effect and the fast degradation of polyaniline occur. Only the presence of dots is detectable without the clear visualization of the spots morphology. This effect is also visible on the rest of the panels in Figure 4.20: blackened and whitened spots are clearly visible[25]. As the electrical bistability was already demonstrated in polyaniline nanos-

[24]In literature, reports on higher structural densities are not so abundant. For example, the process for fabricating NIL molds with high-density patterns and then pattern transfer by NIL has barely improved during the last decade since the demonstration of a 400-gigabit/inch^2 storage density in 1997 [279]. Only recently, challenges related to the fabrication and pattern transfer of 1 teradot/inch^2 patterns using EBL have been treated [180, 181]. Even if the desired patterning density was achieved (by using thin layers of HSQ resist), pattern transfer is not convincing and again was limited to the silicon (material for which the etching protocols well documented).

[25]In the first moments of the visualization, all of the spots appear as white dots. Upon continuous electron exposure, they are turning into blackened, hardly visible spots.

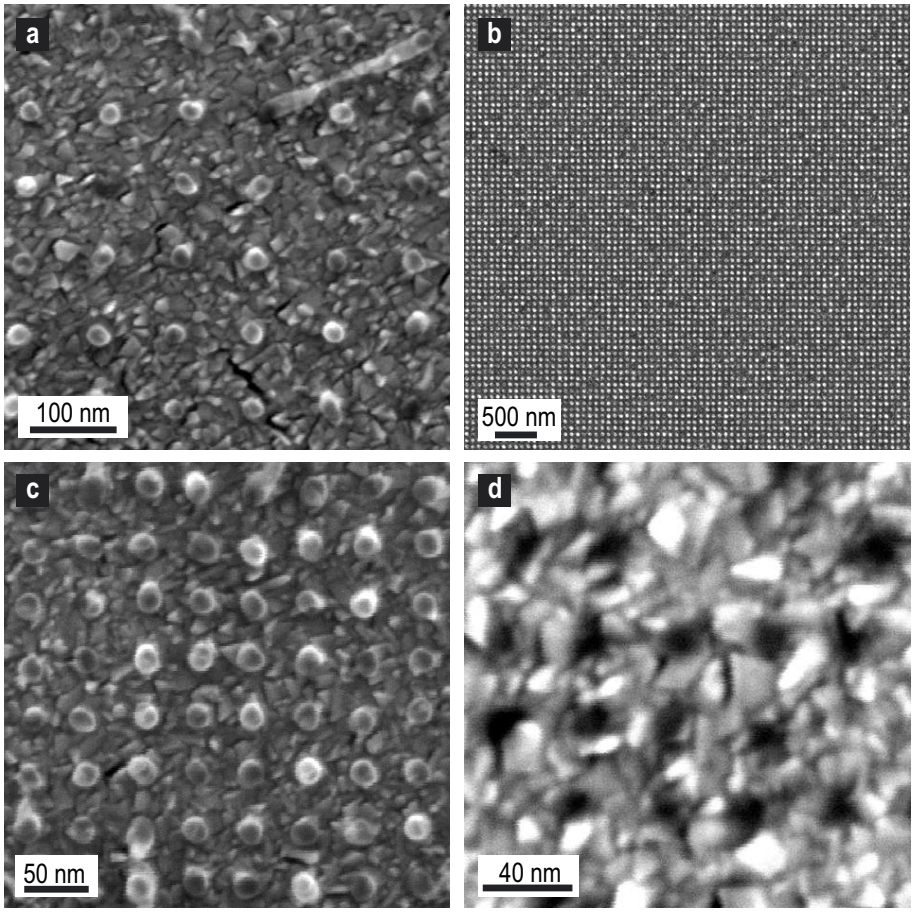

Figure 4.20: High-areal density patterning of polyaniline. (**a**) Polyaniline dots patterned at 100 nm pitch. (**b**) Wide-field view of 75 nm spaced polyaniline dots. (**c**) Close-up on 50 nm pitch square arranged polyaniline dots. (**d**) Evidence for 40 nm pitch patterning. The patterns were generated using a 100 keV beam in a 65 nm thick PMMA resist film. Aniline polymerization was induced by a 130 nm platinum film. The fine structure of the seeding layer is visible cleaned by 3 to 5 s plasma exposure.

tructures and in gold-polyaniline nanocomposites, the applicability of the fabricated nanodots for the high-density data storage systems can be envisioned. The use of a conductive AFM tip to probe their electrical properties is one interesting experiment to be performed and it is currently under study.

Different is the situation if one desires to fabricate higher aspect ratio nanostructures. Obviously, this implies the use of thicker resists while

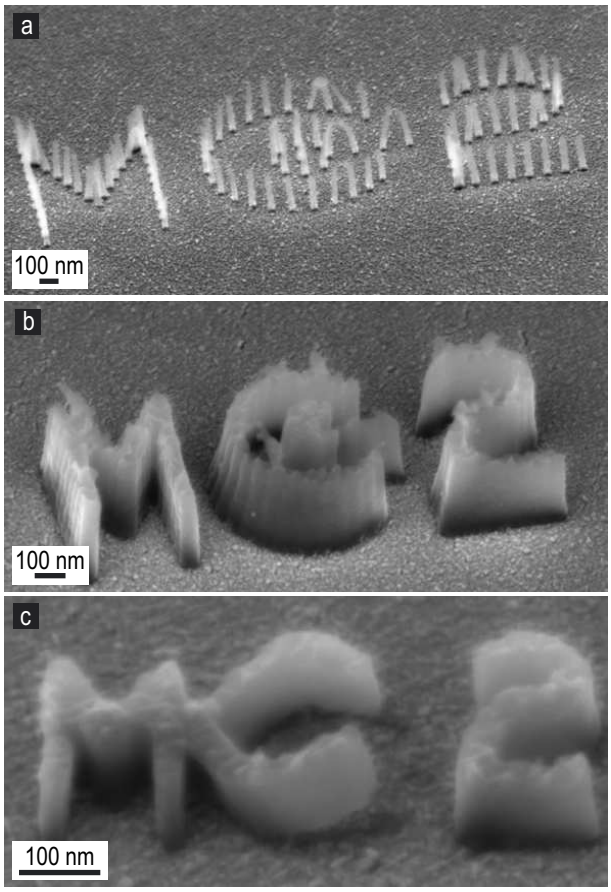

Figure 4.21: MC2 nanoscale inscriptions written out of individual nanowires. The thickness of the PMMA and the developing protocol were the same for all cases. From (**a**) to (**c**) the overall size of letters and exposed spots was gradually decreased. Individual pixelization is present in (**a**). Joined yet still detectable traces of the exposed pillars are visible in (**b**). Complete pixels merging for 100 nm wide letters (**c**).

keeping the same resolution. As was discussed in Section 4.2.1.1 only high-energy electron beams are suited for high aspect ratio patterning. However, there are some limitations. Especially concerning the patterning density. Structures presented in Figure 4.20 show that it is possible to fabricate very dense structures. One should take into account that for the fabrication, 65 nm PMMA films were used. Respectively, filling up to the top of templates will result in something like 65 nm high, 10 - 20 nm in diameter pillars (quite low aspect ratios). Increasing the thickness of

the PMMA precursor can improve that, yet, with the expense of loosing the areal density. On example is given in Figure 4.21. Though, it may look as an artwork or a waste of time to expose "useless" patterns, this example gives a good view of the achievable patterning density using the same resist thickness. The patterns represent the inscription MC2 initially designed to appear as made out of individual nanowires. The thickness of PMMA was 250 nm for all the cases. Clearly, for 100 nm spacing and 50 nm pillars diameter, "pixelization" is possible (Fig. 4.21 (**a**)). Making the letters smaller and smaller diminishes the possibility to realize the pattern from distinct nanowires. However, the pattern design remains imprinted in the obtained structure. As discussed in Section 4.2.1.1 forward scattering widens the size of the beam and combined with the backward scattering (in this case quite important as 130 nm of platinum was used) enlarges the exposed pattern. Other influencing factors are the dark erosion of the partially exposed parts in the developer, enlarging of the revealed areas during the plasma activation (5 to 10 nm of stripped PMMA) and the mechanical stability of the template during the manipulation. Thus, high-aspect ratio combined with high-areal density patterning has some limitations.

By decreasing the spatial density, high-aspect ratio patterning was possible. Structuring resolution as high as 15 nm is demonstrated by fabricating vertically standing, 15 nm in diameter, polyaniline nanowires (Fig. 4.22 (**a**) to (**c**)). This was the minimum size of the nanowires that preserved their structural and alignment integrity throughout the template release, drying and sample manipulation. Nevertheless, ultra-high resolution pattern transfer down to 6-nm is demonstrated (Fig. 4.23). Worth mentioning is the importance of the critical point drying techniques during the template release. Of course, depending on the applications, the template encapsulation can be preserved. In preliminary studies, the template was removed to enable the characterization of the obtained structures. The samples were actually dipped in boiling acetone[26]. When the PMMA was considered as completely removed the samples needed to be dried out.

[26] It was found that dipping them in cold acetone altered the ordering of the polyaniline structures. It is well known that the dissolution of many polymers (PMMA included) occurs by solvent swelling of the polymer matrix and subsequent dissolution. Swelling is accompanied by a volume expansion and hence, may affect the order in the fabricated architectures. In our experiments it was observed that when dipping the samples in boiling acetone, the PMMA was removed in few seconds (nicely detected by the appearance of thin-film interference colors on the surface of the samples indicative of the PMMA gradual removal), while by dipping in cold acetone, PMMA removal required minutes. Moreover, dipping in cold acetone was accompanied by the appearance of cracks all over the surface, signs of stress induced cracking events.

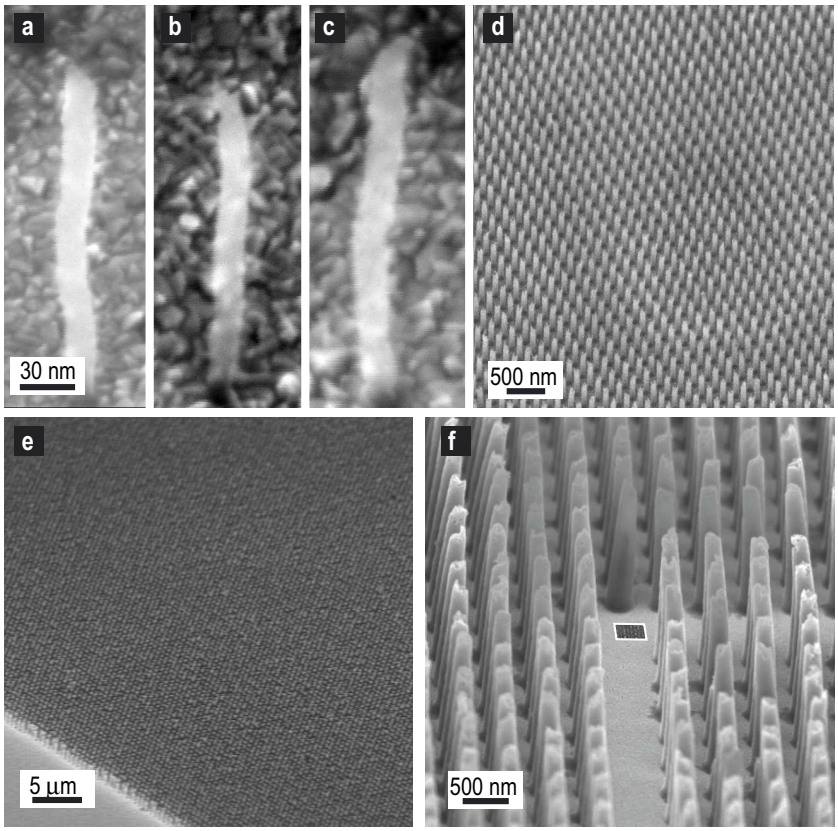

Figure 4.22: (**a**) - (**c**) Examples of fabricated polyaniline nanowires. The diameter is $\simeq$ 15 nm and the height is more than 200 nm. The same scale bar applies for (**a**), (**b**) and (**c**). (**d**) Square lattice having a period of 200 nm, nanowire height of 400 nm and diameter of 65 nm. (**e**) Wide-field view of a defect-free triangular lattice and (**f**) linear defect in a 2D post-type photonic crystal structure having periods of 500 nm. For insight into the scalability of the method, the small area highlighted in the middle of the panel (**f**) has the same size as the area presented in panel Figure 4.20 (**c**).

First experiments were realized just by removing the samples from acetone and let dry in air. This was found to be a very unsuited way to preserve the vertical alignment of the fabricated pillars. Subsequently, fast removal out of boiling dichloromethane (CH_2Cl_2) was used. Since it posses a very low surface tension and a very high volatility it had a less damaging effect on the pillars integrity than acetone. However, it was sufficiently good to apply this technique for relatively big structures (more than 100 nm in diameter). Smaller nanowires were still affected

by the solvent capillarity effects[27]. Only by using CPD, it was possible to retain the vertical alignment. However, the first "unsuccessful" drying experiments have led to the observation of interesting nanoassemblies, which were subsequently improved. They will be discussed in detail in Section 4.4.3.

By carefully removing the template with CPD, large area nanostructuring was achieved. Square and triangular lattice arrangements, composed of polyaniline nanopillars, patterned over various scales, were fabricated. High-density, high-aspect ratio patterning was easier to achieve using a 100 keV electron beam. The long-range proximity effect avoids non-uniform exposure of central and edge structures in dense lattices and no proximity corrections were needed to pattern the polyaniline nanowires over large areas. Panels (**d**) and (**e**) in Figure 4.22 provide some examples: 200 nm pitch lattices with 400 nm height nanowires are easily achieved. Large ($100\times100\mu m^2$) areas with no defects and uniformly distributed polyaniline nanowires were patterned as well. The EBL pattern design are easy to change and point or linear defects could be effectively patterned. Panel (**f**) in Figure 4.22 presents a line defect in a 2D post-type photonic crystal structure.

Eventually, sub-15 nm nanowires demonstrated the ultra high-resolution capability of the method. Their structural stability was found to be very diminished due to the high-aspect ratio combined with a very low base diameter. Ordered arrays were not detected. Single or bunches of nanowires were sometimes visualized on the samples. Presumably, the nanowires are detached during the template release and removed away by the solvent. The fabrication of even narrower nanowires required some special tricks and the reproducibility was quite low (Fig. 4.23 (**c**) and (**d**)). Nevertheless, the ultimate intrinsic resolution in PMMA (which is considered to be in the range of 7 nm) is demonstrated. Not the achievement of this ultimate resolution in PMMA is the most important, but the ability to transfer the pattern at this scale to an active material. It is possible that, at this scale, the polyaniline nanowires are in their crystalline phase. TEM inspections are required to verify this hypothesis. Nanowire transfer from the original substrate to a TEM grid and their subsequent characterization is currently under development.

It was found that the polymerization occurs slower (by a factor of 0.85 - 0.95) in template confined media than in open systems (see Fig. 4.14).

[27] Until the CPD was installed in the new laboratory it was the only good working recipe for the samples drying. Other methods could be used as well, though, due to limited technical capability, they were not optimized. For example, exchanging the working solvent with tert-butanol and subsequent freezing and vacuum drying is one option.

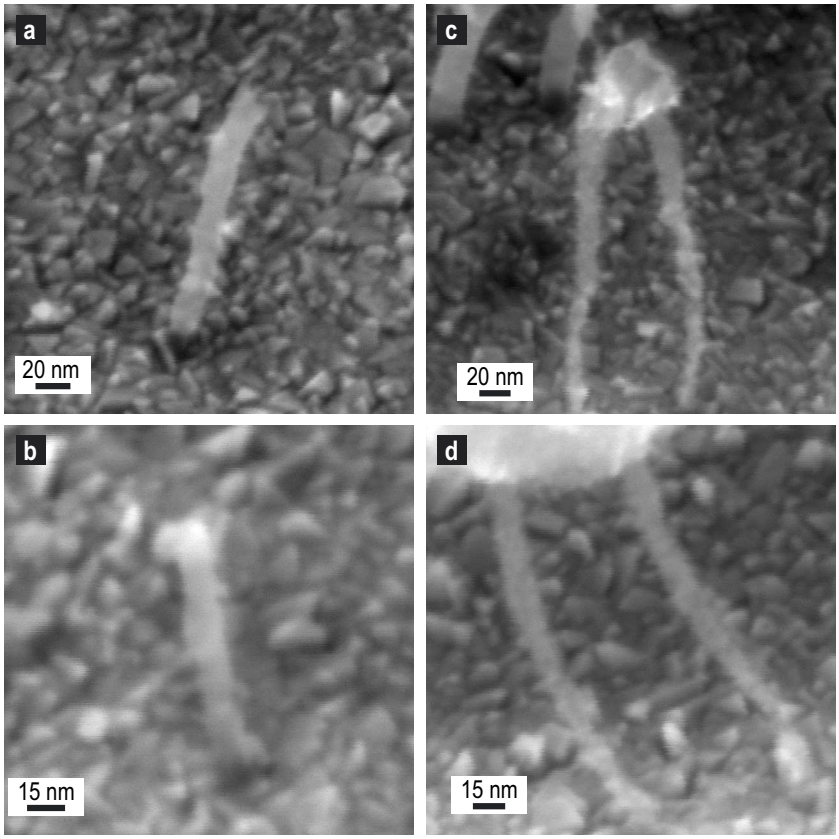

Figure 4.23: (**a**), (**b**) 15 and 10 nm diameter polyaniline nanowires, respectively. (**c**), (**d**) Sub 10 nm diameter polyaniline nanowires. The structural integrity is slightly altered. The exposure was performed using a 100 keV beam. Single shot (or spot) exposure was used. Thus, the resolution is dictated by the intrinsic achievable resolution in PMMA. The development was special as well. Compared to other samples were the development was performed using short exposure to ultrasonication, in this case whole development was performed under sonication. This enhances the solvent exchange, reduces the developing time and minimizes the dark erosion. It can be also observed that the nanowires are not uniform along their axis with a rather negative taper angle. Presumably, at this scale, a crystalline phase in polyaniline could be expected.

This could be explained by the slow diffusion rates of the fresh reactants along the template channels[28]. Another factor could be insufficient cat-

[28]Although, given the relatively slow polymerization rates, and the diffusion time scale compared to the polymerization time it may be that other factors are influencing

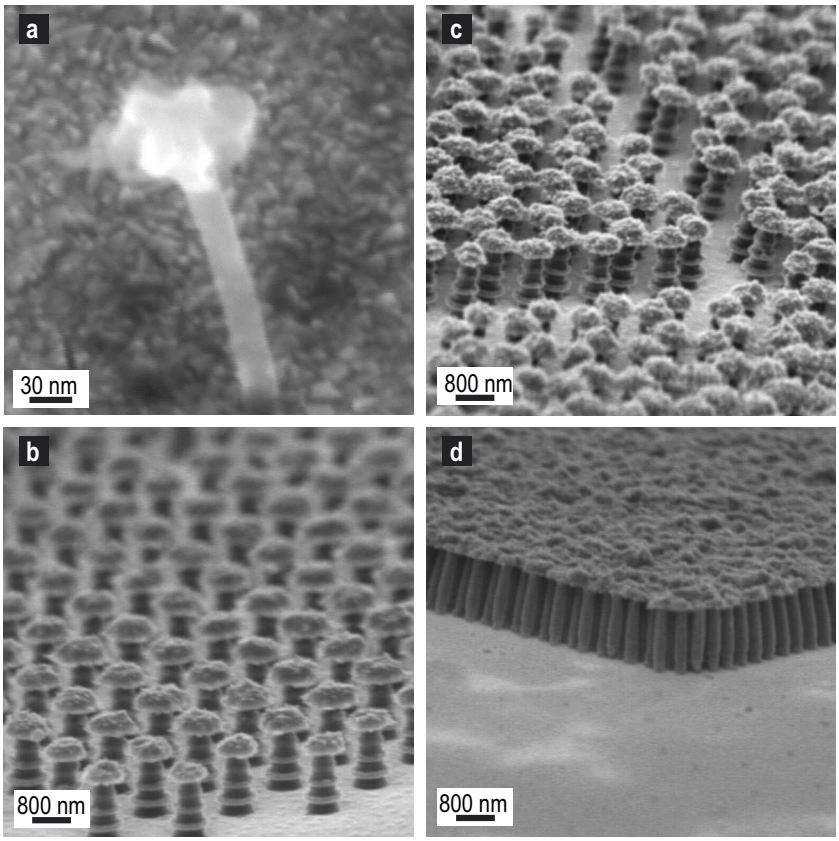

Figure 4.24: If the polyaniline thickness is greater than the thickness of the template, mushroom-like structures are obtained (**a** and **b**). Partial or complete joining of the polyaniline caps resulted in a hexagonal mesh pattern (**c**) or a continuous film (**d**) on top of the pillars. The flooded polyaniline parts may play useful roles, for example, when realizing a top electrical contact or as a counter-plate for two-dimensional confinement of propagating waves. It has as well a negative effect on the structural integrity of the underlying pillars. As it can be observed in panel (**d**) the pillars are bent. Drying induces a shrinkage in the polyaniline overlayer while the bottom part of the pillars is still attached to the surface provoking the deformation of the lattice. The samples were exposed at 100 keV (**a**) and at 30 keV (**b**) - (**d**).

alyst activation. Very short plasma exposure times were used in the case of high-resolution patterning. Presumably, due to the high-aspect ratio of the channels and flash exposure to plasma, the bottom of the template was not activated to the same degree as for the case of open systems and

this reaction slow down.

hence, the polymerization rate was lower. However, the reproducibility from sample to sample was good and when new patterns were studied a preliminary growth calibration was performed. The maximum height of the nanopillars was determined by the thickness of the resist layer. If the growth was allowed to continue above this point, progressively distinct or interconnected mushroom-like caps and continuous polymer films on top of the nanowires were obtained (Fig. 4.25).

Interesting to observe is also the effect of the exposure energy on the taper degree of structures. Patterns presented in panels (**b**) to (**d**) in Fig. 4.24 as well as those presented in Fig. 4.25 were exposed at 30 keV. One can notice easily either the strong positive taper (making abstraction of the diameter modulations) in the fabricated nanostructures or a bump-like morphology. This is the combined effect of the forward and backward scattering effect and obviously, the exposing dose. High doses will always yield positive taper while lower doses, either negative or mainly bump-like pillars. At this energy the proximity effect is very important and large variations in the nanowires diameter were observed depending on their position, within the same pattern. In the case of 100 keV exposure, the dose range to fabricate 0 taper pillars was quite large (either the spots were not exposed for small doses or positive taper was obtained for very high doses), for 30 keV this was more complicated. Fine dose tunning, strongly dependent on the resist thickness and pattern density was required and was not always easy to achieve.

Figure 4.25 show some examples of ultimate resolution patterning and processing. We call it *ultimate* not because of the reduced dimension (which is not so small in this case) but because of the ability to define and grow a precise number of nanowires at a desired position and configuration without any invasive external control. The same type of "chess" structures as discussed in Section 4.3.5 were used for the confined growth. On the pre-existent pattern (platinum and gold slabs, either in contact or not) various exposure configurations were used. A series of single or double nanochannels on each metallic element, only on platinum or on gold were defined. After a standard catalyst cleaning and activation, the samples were dipped in the polymerization reactor and the growth was allowed to occur above the flooding point. Compared to the open system growth, additional polymerization configurations could be studied. For example, the absence of the polymerization on a gold slab connected to a platinum slab with only the first one being exposed to the polymerization media (by defining the channel only on top of the gold island) was possible to detect. This clearly shows the importance of the platinum layer being in contact with the solution. When the elements were electrically connected and both in contact with the solution,

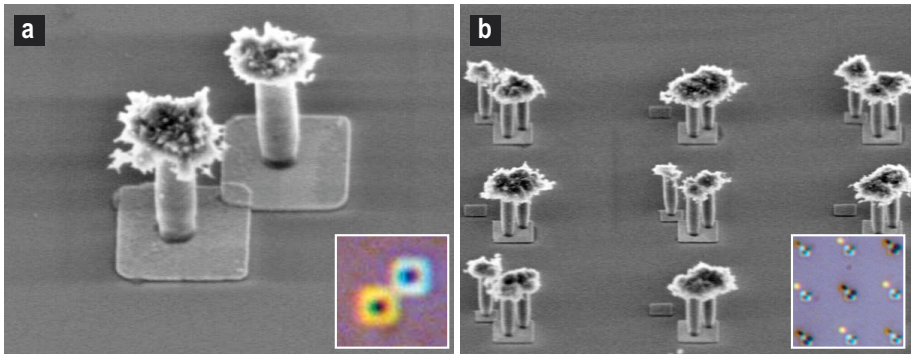

Figure 4.25: (**a**) Single polyaniline pillars grown on 1×1 μm^2 interconnected gold (lower left) and platinum (upper right) islands. (**b**) Extended 3×3 arrays of alternately connected 0.5×0.5 μm^2 gold and 1×1 μm^2 platinum catalyst sites. One and two nanopores have been patterned in the resist, respectively. No signs of polyaniline growth can be detected on the gold pads that are not in contact with the platinum, although a nanopore has been patterned at their center. The miniaturized reactors are patterned on an insulating SiO_2/Si substrate. Insets: bright-field optical micrographs evidencing the nanoreactors dual nature. The scale bar is set by the size of reactors.

the polymerization occurred on Pt and Au (Fig. 4.25 (**a**)). One can notice that the "mushroom" cap is bigger for the structure grown on gold (both of pillars having the same diameter and height) corroborating with the data presented in Figure 4.17. Obviously, no pillars were detected on single, isolated gold slabs and the quantity of polyaniline was divided between the platinum and gold pads whenever they were in contact (Fig. 4.25 (**b**)). Square slabs were used in this experiment to study and exemplify the possibilities of this method. However, the growth is expected to occur in the same manner on micro- and nanoelectrodes opening the possibilities for single polyaniline nanowire device fabrication.

4.4.2 3D structuring

The same approach was applied for 3D structuring of polyaniline. Instead of using single layer resist precursors, multilayered resist stacks were used to define the polymerization templates. The rationale behind this advanced 3D structuring was presented in Section 4.2.3. Multiple-layer stacks were obtained by sequentially coating PMMA and PMMA / MAA. Each layer deposition was followed by 10 min baking at 130°C. At the end, all substrates were kept at 130°C at least 24 hours and slowly cooled down (20°C per hour) to reduce the residual stress in the resist

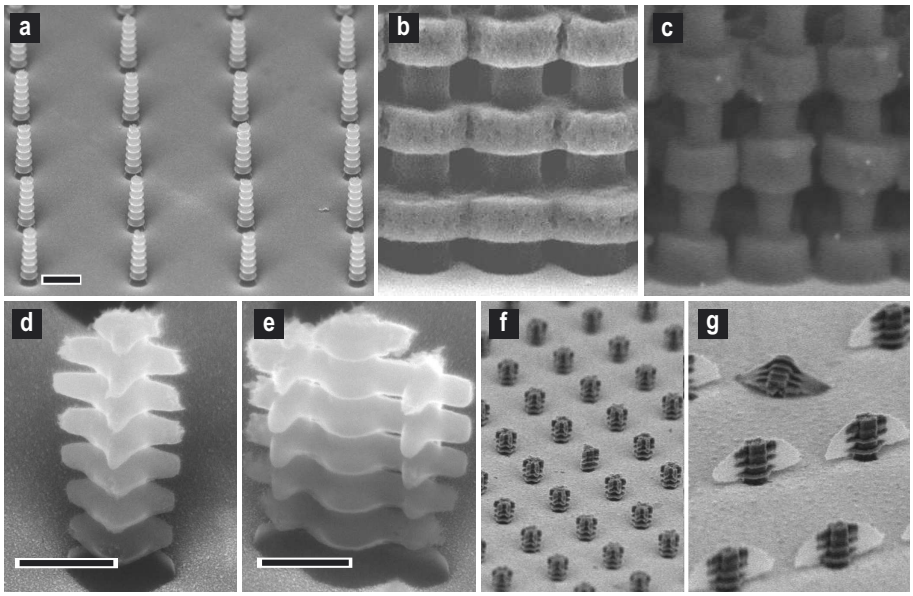

Figure 4.26: Examples of fabricated structures using resist and dose modulated 3D EBL. (**a**) Arrays of diameter modulated polyaniline nanowires. (**b**), (**c**) Complementary structured modulations obtained by inverting the coating sequence. Each modulation is 300 nm thick. (**d**) Branched polyaniline nanopillars. (**e**) Hyper-branched nanopillars obtained by adding additional criss-crossed lines to the branched pattern. (**f**) Array of six-branched nanopillars with a central three-sided structure (pillars pitch 3 μm). (**g**) Array of two-branched pillars with a "bee-like" morphology (pillars pitch 3 μm). The "bee wing" is the outcome of the stress induced cracking in the resist film nucleated by the aligned side-branches. The thickness of the crack is 10 - 15 nm. See Figure 4.7 for the possible propagation length of the cracks. Scale bars: 1 μm (**a**); 500 nm (**d**) and (**e**).

films. Typical exposure parameters for resist- and dose-modulated 3D EBL were: 300 - 1500 μC/cm^2 and 30 - 200 μC/cm^2 exposure dose for central pillars and side branching, respectively with 6 - 15 min developing time at 100 keV. Lower doses (200 - 600 μC/cm^2 and 20 - 60 μC/cm^2) have been used at 30 keV. The absolute values for the EBL processing are strongly dependent on the exposure energy, substrate type and pattern density and were calibrated accordingly. Due to the thick resist films used and complex geometry of the templates the plasma cleaning and activation times were larger than in the case of 2D high-resolution patterning (typically in the order of tens of seconds). After the growth, the samples were treated in the standard way and the template was removed

(with the same precaution as for 2D structures). Examples are given in Figure 4.26.

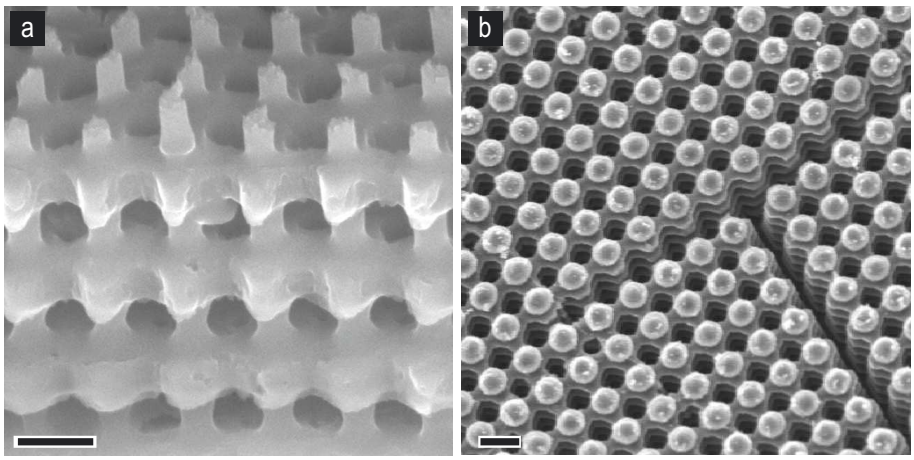

Figure 4.27: (**a**) Polyaniline cubic lattice having the elemental cell of 500 nm. (**b**) Tetragonal (or square cuboid) lattice. The structure could be also visualized as a series of suspended chess-boards planes suspended by central pillars. The middle crack originates from the shrinkage of polyaniline during drying process. Scale bars: 500 nm.

Arrays of diameter modulated nanopillars were obtained by exposing only the central spots at a high-dose (Fig. 4.26 (**a**)). Complementary disposed modulated structures were simply obtained by inverting the coating sequence using the same resist formulations and coating conditions (Fig. 4.26 (**b**) and (**c**)). As detailed in Section 4.2.3, exposure of side lines at a lower dose creates internal protrusions in the resist layer, which after template inversion provides branched nanopillars. The branched structure presented in Figure 4.26 (**d**) was obtained by exposing a central pillar and 4 side lines. Due to this type of exposure, the branches are produced in a self-aligned way. Hyper-branching was achieved by exposing additional criss-crossed lines, orthogonal to the first-order branches (Fig. 4.26 (**e**)). For this kind of structures, two taper degrees have to be defined: for the central pillars and for the modulations. The first one was typically chosen (and relatively simple to adjust) to be close to 0. The taper degree for the modulations was more difficult to control. The PMMA(8.5)MAA being more sensitive, it was not easy to adjust its exposure degree by the forward and backward scattering effects. More important, however, was the development of the exposed area. For the post-type structures, the development (ar-

rival of fresh developer and removal of the dissolved components) occurs through the hole defined in the top-most layer. More the internal structuring is complex (large exposed volumes) more time will take to clear adequately the respective amount. In turn, this will imply more pronounced dark erosion, resist swelling (accompanied by resist cracking) and more prolonged use of ultrasonications, degrading the template and hence the final structure. Exposing less the samples to the developing media will result in non-uniform removal of the exposed parts along the depth of the templates. For example, it can be observed in panels (**d**) and (**e**) in Figure 4.25 that while the central post has a 0 taper degree, side structuring has a negative tapering. This is more pronounced in the case of hyper-branched structures. While the top-most shapes are clearly-defined , lower parts are less pronounced, eventually appearing as simple branches for the lowest levels. It is straightforward that the first levels will be more exposed to the developer and reproduce with high-fidelity the exposed pattern design. However, this was only the case of complex post-type structures. Simple, only modulated pillars have been systematically fabricated having a 0 taper degree for the central post and positive for the axial modulations. Their progressively increased size was extensively exploited for subsequent functionalization and assembly.

When the side-branches were designed to be close enough to join them selfs, complex lattices have been obtained. By adjusting the thickness of each layer (250 nm) with the exposed pillars pitch (500 nm) and adding side-lines in between them, cubic lattices were fabricated (Fig. 4.27 (**a**)). The initial templates have as well a cubic lattice symmetry. Though they were composed of chemically different constituents, the difference in their refractive indexes is extremely small, and from the optical point of view, the structures could be considered as made out of a single component, the PMMA[29]. Subsequent modification of the pillars pitch, resist stack components thickness and exposure dose extends the variety of fabricated structures. For examples, suspended square shapes were fabricated (Fig. 4.27 (**b**)). The ability to sculpt desired shapes with a high geometrical control could be very useful for subsequent processing applications. For example, the squared shapes of the holes as well as their progressively diminished size could be exploited to build up stacked split ring resonators

[29]The Cauchy coefficients (A, B and C) for PMMA and PMMA(8.5)MAA are: 1.488, 2.898 10^{-3}, 1.579 10^{-4} and 1.478, 7.204 10^{-3}, -3.478 10^{-4}. Cauchy's equation is an empirical relationship between the refractive index and wavelength of light used for transparent materials: $n(\lambda) = A + \frac{B}{\lambda^2} + \frac{C}{\lambda^4} + ...$ where n is the refractive index, λ is the wavelength in μm and A, B, C are the empirical coefficients. Substituting, we can see that at 636 nm the refractive index for PMMA is 1.496 and for PMMA(8.5)MAA is 1.494.

(for instance, by evaporating gold under an angle with respect to the sample surface). The self-alignment induced by the fabrication protocol could render the realization in just one step of photonic metamaterials in contrast to actually used, layer-by-layer techniques [64]. In the subsequent, some other fabrication aspects regarding the functionalization and the assembly of fabricated polyaniline structures are presented.

4.4.3 Nanocomposites and macroassemblies

The wide diversity of states in which the polyaniline can exist together with their tunable and reversible optoelectronic, mechanical and surface properties through simple chemical and electrochemical processes, are now elegantly complemented by the ability to ultimately nanostructure and manipulate them. In occurrence, the composition of present 2D and 3D polyaniline architectures can be easily modified by molecular functionalization without affecting their geometry. Acid-base doping-dedoping, various redox modifications, electrophilic and nucleophilic aromatic additions or amine and imine groups modification clearly could enlarge the functionality of the fabricated structures. First, different types of nanostructured gold-polyaniline composites were prepared through simple chemical or physical modifications. Polyaniline - gold nanoparticles composites, with enhanced characteristics as compared to parent constituents, yet exploiting the physical properties of the host as well as the guest, are interesting for a wide range of possible applications [280]. For example, we have found out that the fabricated polyaniline architectures preserve their electrochemical activity by enabling electroless reduction of $[AuCl_4]^-$ (Fig. 4.28 (**a**)). The process has been extensively studied for the recovery of precious metals from the industrial wastes. Electroless recovery of gold ions by the polyaniline has been found to occur through the increase in the initial oxidation state of the polymer followed by subsequent reprotonation and reduction to restore the primary polymer composition. Note that degradation of the polyaniline matrix due to the susceptibility to hydrolysis when existing in superior oxidation states was reported [281]. The reduction rate and the gold cluster morphology are controlled by a complex interplay between solid-liquid interface, pH of the solution and the initial oxidation state of polyaniline [282] and may require some further experiments in order to establish the influencing parameters.

As synthesized gold particles were found to assemble as well on the surface of the polyaniline (Fig. 4.28 (**b**)). This again proves that the polyaniline retain its useful properties throughout the processing and may serve as a subsequent template for various functionalizations. The

electrostatic assembly was performed in acidic media (pH 2 - 3) using mercaptosuccinic acid (MSA) capped gold nanoparticles (40 nm in diameter, BBInternational). The choice for the assembling conditions is two-fold. First, the electrochemical activity of as prepared polyaniline in its emeraldine oxidation state is typically preserved at a pH < 4. At higher values the polymer will simply deprotonate and become neutrally charged (although, self-doping enables the operability even at pH $\simeq 7$). Inversely, the colloidal nanoparticles are instable in acidic media, being susceptible to agglomeration and precipitation. The mercaptosuccinic acid stabilizes the gold colloid in acidic solution down to pH $\simeq 2$ - 3 and also charges negatively the nanoparticle surface. Thus, thermodynamically, the grafting of MSA-capped gold nanoparticles on the positively charged surface of PANI is possible. However, it is not clear how the smooth surface of template confined polyaniline influences the adhesion of nanoparticles and the optimum grafting conditions are still under development.

Another option is to exploit the peculiar 3D morphology, for example the axial modulation of the constructs, to fabricate self-aligned 3D arrays of stacked metallic nano-rings (Fig. 4.28 (**c**)). Gradual increase of the modulations diameter provides an excellent option for the nanoscale stencil mask physical metal deposition. Let's consider a perfect evaporation source that yields a directed and uniform evaporation beam parallel to the pillars axes. The first diameter modulation will act as an "umbrella" protecting protecting the underneath structure from metal vapors. As, in principle, the protrusions are progressively enlarged (from top to bottom), each of them will act in the same way yet receiving small quantities of metal due to those variations. For circular shaped modulations, the metallic structure will resemble a series of concentric circles or, for square shaped modulations concentric square elements. The outer size of a such element will be equal to the inner size of the inferior element. Self-alignment is controlled by the pillar geometry. Evaporating the metal under an angle compared to the pillars axis will provide additional shadowing and hence structuring. For example, tilting such that the inferior modulation is completely hidden by the consecutive superior (and so on) will disrupt the continuity of the metallic elements resulting in the obtention of multiple, self-aligned split ring resonator structures. We expect that, following further optimization, the present method can assist the controlled assembly of nanoparticles (not only metallic, for optical applications) by focusing them either at the sharp edges or at the "armpits" of the diameter-modulated or branched PANI nanostructures to yield vertically stacked, self-aligned nanoring structures [283, 284].

The liquid capillary force induced self-assembly has been studied as

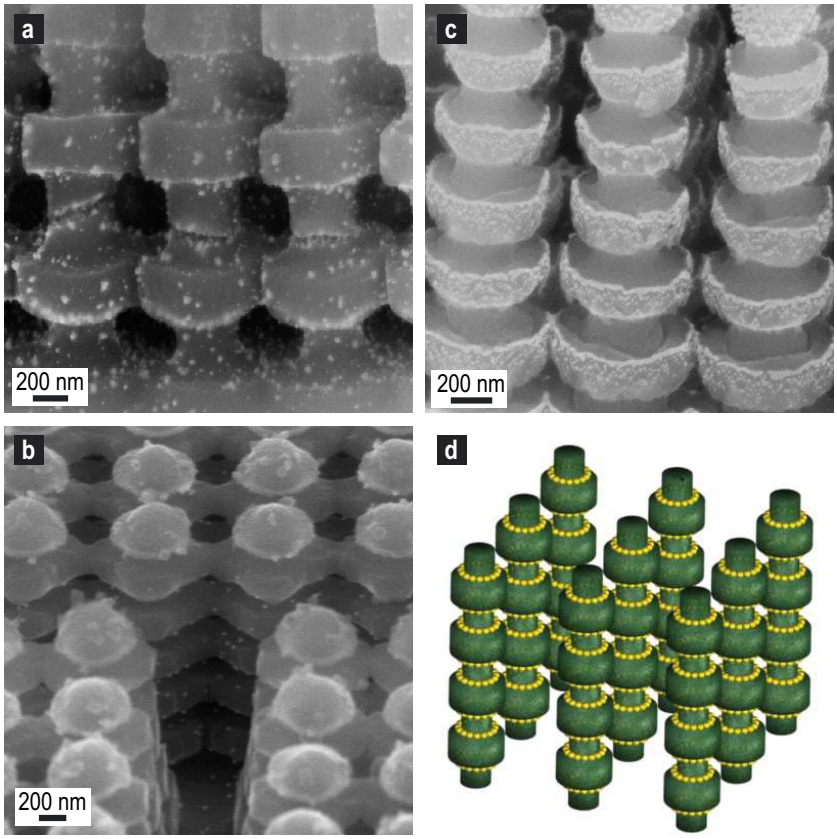

Figure 4.28: (**a**) Cross-section view of a nanocluster-decorated structure fabricated by electroless reduction of gold anions by polyaniline. Particles, despite their size dispersion, are uniformly distributed all over the surface. (**b**) Grafting of prefabricated 40-nm Au nanoparticles. The structure is the same as in Figure 4.27 (**b**). (**c**) Gold nanorings obtained by physical evaporation through self-aligned shadow masking provided by the axial diameter modulations. 10 nm of metal was evaporated parallel to the pillars axis. Metal free zone in between the modulations is clearly visible. (**d**) Schematic view of an envisioned 3D functional PANI architecture obtained by directing the nanoparticle grafting at the structural protrusions of the diameter modulated pillars.

well. First, this effect was observed when drying improperly (without using CPD) the nanowire decorated surfaces and considered as an undesirable effect as the structural integrity was altered. The nanowires are detaching from the substrate, either by agglomerating in a disordered way on the sample surface or by being completely washed away by the solvent. Differences in using or not CPD can be clearly detected by compar-

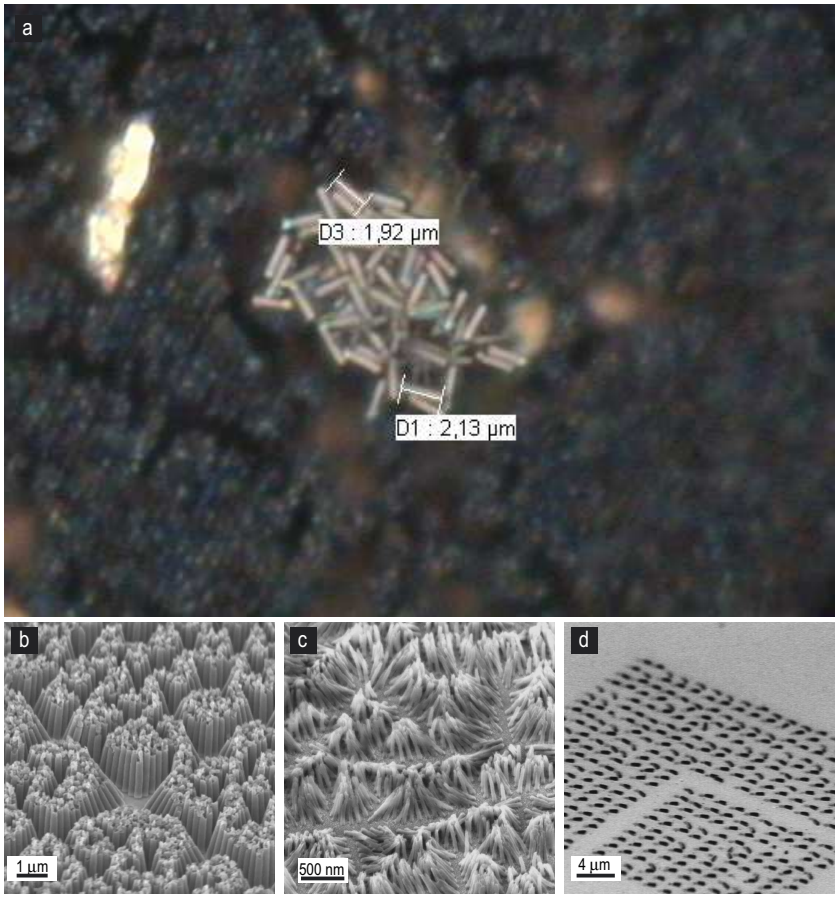

Figure 4.29: (**a**) Bright-field optical micrograph showing disturbed nanowire lattice, result of unsuitable drying. Possibly, a drying liquid droplet has detached the nanowires from the substrate (empty areas nearby are visible) creating the agglomerate. (**b**) Typically, bunches of preferentially detached nanopillars have been observed for closely spaced nanowires. (**c**) Bristle-like morphologies observed for lower diameter pillars and increased pitch. (**d**) Unidirectional in-plane alignment achieved by anisotropically orienting the evaporation front.

ing Figures 4.22 and 4.29. Subsequently, the influence of the nanowires structural parameters and the drying conditions upon the morphology of the assembled structures was studied. First, the nanopillars with uniform diameter were found to commonly aggregate and organize in partially ordered structures, result of exerted capillary forces under isotropic action of the evaporating liquid. Depending on the diameter (Young's modulus, bending stiffness and adhesive energy per unit area) they were found to

assemble differently (Fig. 4.29 (**b**) and (**c**)). The anisotropic orientation of the evaporation front (for example, tilting the samples) enabled slow, almost unidirectional retrieval of the liquid from the sample surface and provided localized positioning of single nanowires. Height, spacing and initial pattern could be further optimized to ensure easy processing for subsequent interrogation and device fabrication [106, 109, 112].

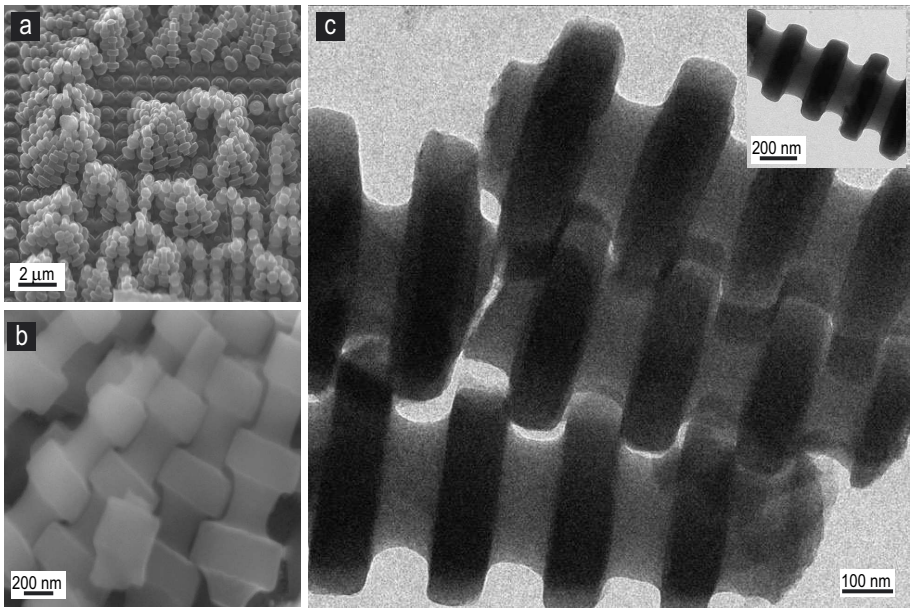

Figure 4.30: (**a**) Wide-field view of assembled diameter-modulated nanopillars obtained by drying out isopropanol. (**b**) Close-up on a self-assembled stack. The length of each diameter modulation is 300 nm. (**c**) Transmission electron micrograph evidencing the high-fidelity packing of the alternating features. Inset: TEM image of a single nanowire showing the uniform diameter of the main pillar and the gradual widening of the modulations.

The 3D modulated architectures have been found to assemble in an orchestrated way, following a different rationale. Specifically, the re-entrant topography of the fabricated nanostructures (disc- or square-shaped, axially-modulated nanowires as well as branched and hyper-branched nanopillars) can induce the pinning of the receding contact line of the liquid menisci in the case of an evaporating liquid. This is expected to increase the capillary forces exerted between the pillars, especially in the geometry modulated segments in order to maximize the contact surface[30]. This will have two major influences on the assembled

[30]Squared modulated structures were found to assemble along the longest protru-

morphology: first, the nanowires could be detached from the substrate (as a result of the competition between the adhesion force per unit area and the liquid interfacial tension) and second, if detached, they will be assembled via a geometry driven key-lock type self-assembly (Fig. 4.30 (**a**) and (**b**)). The structural matching of the alternated modulations not only induces, but also favors a compact stacking with very few interstices. The presented morphologies were obtained by drying anisotropically a droplet of IPA gently deposited on the grown polyaniline structures. The same behavior was observed when transferring the initially ordered pillars from the original substrate to a different sample holder (in occurrence a transmission electron microscopy grid). This holds true as well as for smaller modulation sizes: 100 nm for the structures presented Fig. 4.30 (**c**)). The transfer was performed by "scratching" the sample with a pipette tip. Simultaneously, a droplet of water ($\sim$ 1 ml) was held in between the pipette tip and the surface (hydrophobic platinum blocked droplet spreading over the sample surface) to recover the polyaniline structures. Subsequently, the droplet was let dry in air on the TEM grid. It is not clear for the moment when the pillars assemble: either when they are detached by the moving water droplet or when drying out on the grid.

Interesting is the tendency of the nanostructures to assemble in a radial way. This is the result of the nanopillar disimetry along the axis. The diameter of the main axis remains constant and only the diameter of the modulations gradually increases as already explained (inset to Fig. 4.30 (**c**)). Hence, parallel stacking becomes sterically unfavorable. The high-control over the nanopillars' tapering degree and on the 3D structural features offers the possibility of rationale design for novel spherical, helical or tubular functional macroassemblies [72, 285–287]. Combined with the modulated permeability and mechanical actuation of the polyaniline, these macroassemblies could play a role in the realization of stimuli-activated smart materials [71, 288].

4.5 Single PANI nanowire electronics

I aimed at the fabrication of cross-bar devices having the polyaniline as the active element. Given the fact that the factors influencing the growth are well known and that minute amounts (either template confined or not) of polyaniline can be grown, the task seemed relatively easy. Yet, for the single nanowire based devices, the task was not so simple and new findings concerning the polyaniline growth kinetics have

sions, *i.e.* along the square diagonal (not shown here).

been revealed. Nevertheless, from the technological point of view, the fabrication is straightforward consisting of 3 or 4 processing steps for polyaniline "bulk" or nanowire devices (the blue path and the red path in Figure 4.31, respectively). First, we will discuss the 3-steps protocol and then we will present the cautions required for the reliable template confined growth of single nanowires.

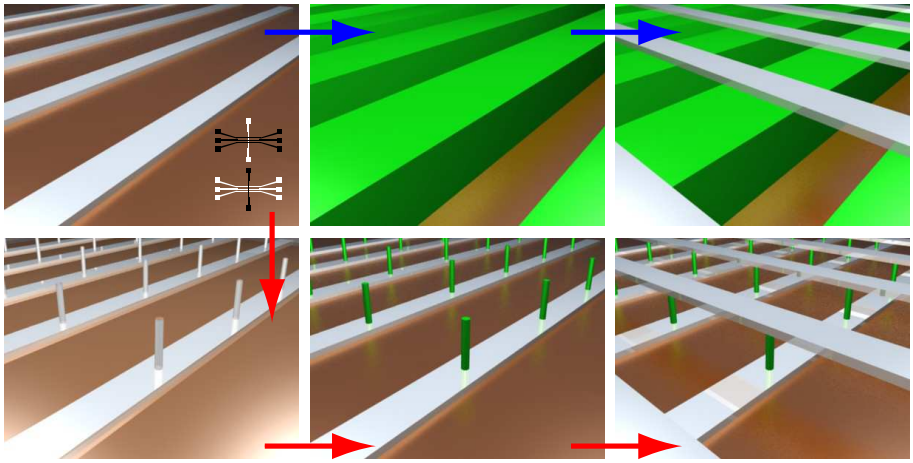

Figure 4.31: Schematic view of the fabrication pathways for the polyaniline circuits. Blue path: patterning the BE's, self-aligned polyaniline growth on structured substrates and definition of TE's. Inset: schematic representation of the used pattern. The same mask was used to defined both, BE's (white pattern) and TE's (black pattern) by simply rotating it by 180°. Red path: patterning the BE's, EBL to define the template channels, template confined polyaniline growth and TE's definition.

Following "the blue path" is a relatively simple task. First, the working substrate has to be chosen. Next, the BE's are defined. Here, this was performed using physical vapor deposition of platinum (2 nm of Ti and 10 - 100 nm of Pt) through a stencil mask. After a proper activation of the catalyst surface, the polyaniline was electroless deposited in a self-aligned way only on top of the BE's. The grown polyaniline can be doped or dedoped in a classical way by simply dipping the samples in 1 M HCl or 1 M NH_4OH solutions. Finally, crisscrossed TE's were defined by evaporating Pd (without any adhesion layer) using the same stencil mask in a rotated configuration (see inset in Fig. 4.31). For the preliminary characterization, BE's and TE's criss-crossed architecture was $1 \times n$ to avoid cross-talking ambiguities.

Figure 4.32 presents the electrical characterization of polyaniline thin

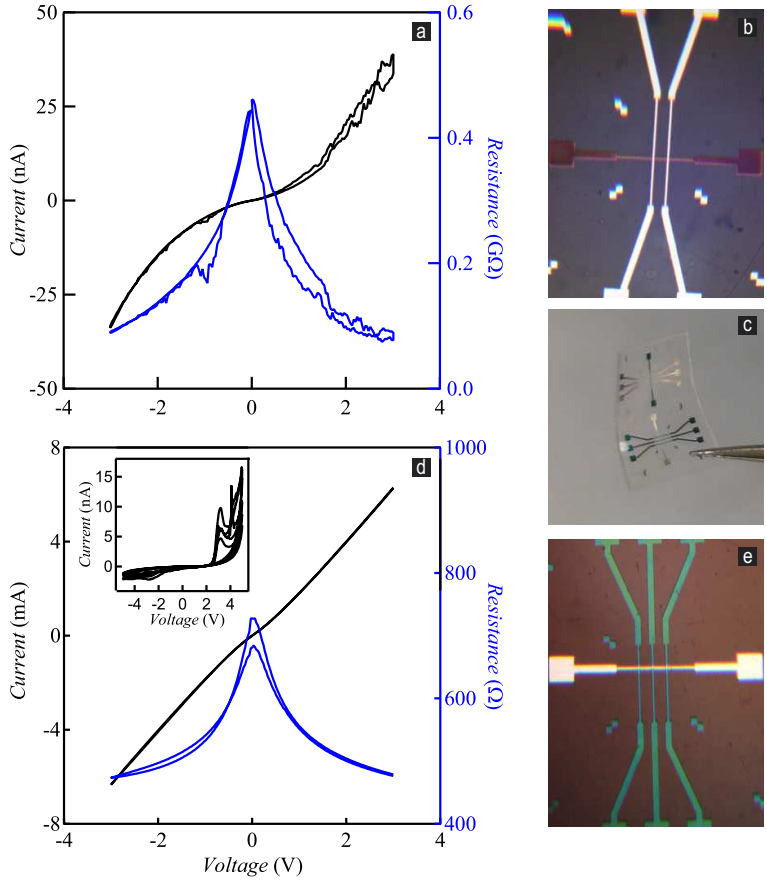

Figure 4.32: (**a**) Measured $I-V$ and calculated 2-terminal resistance curves for the dedoped polyaniline phase with Pd TE. (**b**) Optical micrograph of the measured dedoped device. The active area is 50 × 50 μm^2. (**c**) An example of a prototype device fabricated on Teflon substrate. (**d**) Measured $I-V$ and 4-terminal resistance curves for the doped polyaniline phase with Pd TE. Inset: 5 consecutive $I-V$ traces of a Pt - doped PANI - Al sandwiched structure. (**e**) Optical micrograph of the measured doped device. The active area is 20 × 20 μm^2. For each case, the voltage was applied on the BE's while the TE's were kept grounded.

film crossbar devices in both, doped and dedoped states. The BE's are made of 50 nm Pt and the TE's of Pd. The thickness of polyaniline is 200 nm. A clear enhancement of the conductivity (about 6 orders of magnitude) between the de-protonated and protonated states was detected. For the emeraldine base the non-linear $I-V$ characteristic is more pronounced than for the emeraldine salt. Current instabilities were also

detected for voltage values above 2 V in the case of deprotonated phase. For higher voltages, the current instabilities were more pronounced with irreproducible behavior (not shown here). For the doped phase, no such anomalies were detected (even when biasing up to ± 7 V). A slight rectifying effect can be also detected, probably due to the differences between the nature of BE's and TE's[31].

A promising behavior was found for the samples with *Al* fabricated BE's. The measured currents for both doped and dedoped states were unlikely low. For example, few nA at 5 V bias for the doped state (inset in Fig. 4.32 (**d**)). Yet, a large negative differential resistance feature (at ∼ 3 V) was detected in the positive bias regime. This may be indicative of the polyaniline being switched into a new conductive state. The switch back, with a lower amplitude, was also detected in the reverse bias (at ∼ -3 V). This property could be further studied and exploited for non-volatile memory devices. Reversible electrical bistability was already observed in various aniline derivatives (subjected also to physico-chemical functionalization) [289–291]. However, their protocol does not allow for a reliable patterning of the organic layer and down-scaling may be troublesome in contrast to our method, where it is possible to scale down and reliably pattern nanoscale amounts of polyaniline at precise positions. Interesting as well, in this configuration, a rectifying effect (by a factor of 20 at +/- 5 V) was observed. This effect could be used to effectively avoid the cross-talking effects in this type of devices. Their origin is not well understood for the moment and will require further studies to control them. One possible explanation could rely on the oxidation of the aluminum film when exposed to air and hence, formation of a thin aluminum oxide film at the interface between the polyaniline and aluminum. The good air and liquid permeability of polyaniline favors further the oxide formation at the contact interface. The formation of an insulating barrier explains the low amplitude of the measured signals. Negative differential resistance can be also attributed to the barrier penetration (metal filament formation) when biasing the junction. Further studies will be required to clearly interpret the data and to reliably control, reproduce and exploit this behavior. Moreover, the fabrication process can be readily transposed to any substrate of interest or by using other *Pt* electrodes patterning techniques [292].

[31] The vacuum work functions for *Pt*, *Pd*, *Au* and *Al* are 5.65, 5.12, 5.1 and 4.28 eV, respectively.

4.5.1 Fabrication approach in 4-steps

Following the red path shown in Figure 4.31 requires the additional EBL step to define the template channels. The BE's were defined using the same mask as for the previously described pathway. A 500 to 1000 nm thick PMMA layer was subsequently spin-coated on top. EBL (30 keV beam) was used to defined single template channels with defined position and size ($\sim$ 50 nm). As the TE's definition is performed using coarse visual inspection alignment, the EBL design was adapted accordingly[32]. For instance, an array of dots, all along the BE's was patterned. The pitch was chosen accordingly to the size of the BE to be defined. If one single polyaniline nanowire was intended to be connected, then the pitch was equal to the size of the BE[33]. If multiple nanowires are to be connected, than it is sufficient to decrease the patterning pitch with respect to the size of TE's. Subsequently, the TE's were defined in a similar way as in the previous case.

At this point worth to mention are some interesting findings regarding the growth of reduced amounts of polyaniline using the electroless process. As already shown, the polymerization or the growth rate can be effectively controlled by realizing preliminary calibration tests. Also, the growth kinetics is mainly governed by the catalyst morphology and activity and the reaction temperature (assuming that the other parameters are kept constant). Despite that some deviation were sometimes observed, the fluctuations amplitudes were low ($\sim$ 15 % compared to the calibration tests) and attributed to various factors originating from processing limitations. Yet, large anomalies were observed, especially when using nanostructured catalyst slabs. For example, the structures shown in Figure 4.25 were grown for 3 days[34]. According to the growth calibration shown in Figure 4.14, 7 μm of polyaniline was expected to grow in 3 days. Even by taking into account the mushroom cap, it was still hard to find the reason for a deceleration of the growth rate by a

[32] It is relatively difficult to manually align the sample with the mask pattern when only one single nanowire is patterned. Though it is possible, it requires alignment under a microscope possible mainly for transparent substrate and a good anchoring during further manipulation to avoid any overlay displacement.

[33] Theoretically, there is 0 probability to overlap the TE with 0 or 2 nanowires and probability of 1 to overlap only one nanowire. In practice however, due to the size variation of the TE, the probability to connect one single nanowire is slightly bellow 1.

[34] The samples were periodically removed after 12 hours of growth, inspected and then returned in the reactor. After all of the growth calibrations, this was very unexpected and at that moment, quite discouraging as it signified that either the calibrations were wrong or other unknown yet, very important parameters were to be found.

factor of 4. These aspects were relatively well clarified when fabrication of polyaniline nanowire circuits was initiated.

Figure 4.33 shows an example where on 2 BE's a series of polyaniline nanowires was intended to grow and characterize. It can be observed (though not so easily) that on the lower electrode the polyaniline flooded over the template while on the top-one not. The same patterns with the same exposure dose were defined on both BE's. The single difference (that is making all the differentiation) is the presence of the squares on lower electrode. The presence of squares was found to "accelerate the polymerization rate in the nanochannels" yielding reproducible results as compared to the callibrations. The explanation that we propose relies again on a statistical interpretation of the process[35].

The surface roughness (or the corresponding number of active sites for the electrochemical reaction) estimation is usually performed on large areas, intended to average local non-uniformities and to have an ensemble macroscopic view (for example, the roughness was measured on 4 μm^2 area in Fig. 4.14). The surface roughness estimated on 0.002 μm^2 (the area occupied by a 50 nm diameter pore; for instance, the used size of the channels defined by EBL in PMMA) area can vary strongly from site to site. Overlapping pattern of the pore with the surface features, such as metal grains or grain boundaries (grain sizes of the evaporated platinum can vary from 10 to 50 nm, a mean value will be erroneous to use here) will be different from site to site corresponding also to different local surface roughnesses (more suitable to talk in terms of number of active sites). Of course, the local values can be lower or higher than the mean value. The polymerization kinetics will be thus dictated by the averaged value of active sites. This is valid only for continuous metal surfaces since the implied redox charges are spread uniformly all over the metal. In the case of only few patterned holes, large variations are expected and hence non-reproducible polymerization rates[36]. Making more and more holes will eventually lead to an averaged value close to the measured one and hence, more reproducible behavior. Working with a reduced number of nanochannels (typically, 10 to 50 pores are patterned on a single electrodes), will not provide this luxury. Thus, the addition of the

[35]Experimentally, this was found accidentally. As the nanowires have to be left embedded, the PMMA matrix was kept intact all over the sample. This was quite annoying when trying to make electrical connections requiring manual scratching with lots of complications. At some point, it was decided to open contact holes on top of the bonding pads. The grown polyaniline in those areas was much easier to remove. Yet, this approach exposed as well big Pt areas to the polymerization media during the growth.

[36]Suspiciously, for the moment only reduced polymerization rates were observed.

"sacrificial" areas (big squares in Fig. 4.33), having a "smearing" effect, enables a reproducible working environment[37]. Further understanding of the polymerization process at nanoscale is required to better control the growth[38].

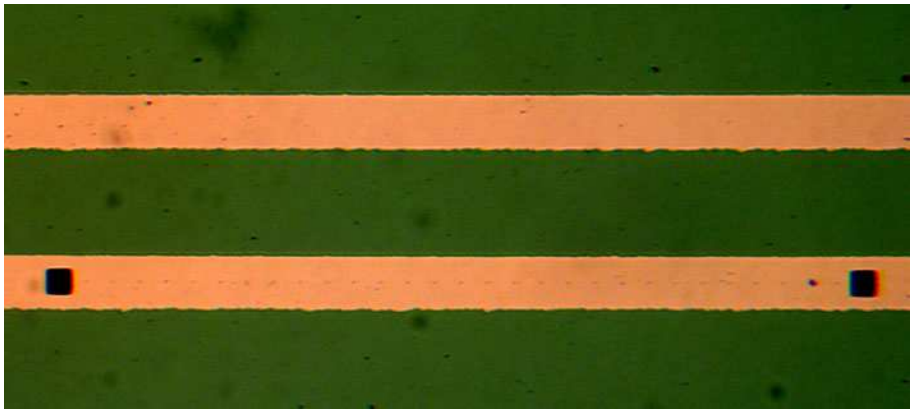

Figure 4.33: Optical microscope wide-filed view of 2 microelectrodes (100 μm width) decorated with polyaniline nanowires. On the lower electrode the polyaniline flooded over the template creating mushroom caps.

Not to neglect is the catalyst activation in the nanoscale confined environments. Relatively high aspect ratio channels (10 to 20 in the respective case) may inhibit good plasma reactivity at the bottom of the nanosized channels, while having a normal action in the larger areas. The platinum surface activity influences mostly the cathodic half-reaction (see Fig. 4.13). *Having lots of active sites for the cathodic, implies that more aniline will be oxidized through the anodic half reaction hence, an increase in the polymerization rate.* This is actually seen when the big squares and the template channels are patterned on the same electrode: the oxygen reduction is primarily taking place in the

[37] This is somehow similar to approaches used in electrochemistry to grow nanoscale quantities. Large plating areas (defined nearby the nanoscale region of interest) are are used to permit reliable monitoring of the process. Nevertheless, fundamentally, the approaches are very different.

[38] For example, using various size nanoscale catalysts elements different polymerization rates were detected (not presented here). Similar to the experiments shown in Section 4.3.5, a series of platinum square slabs with varying sizes from 1.5 μm to 50 nm were used to test the growth. Though they were defined on the same sample (separated by few μm from each other, implying similar processing, cleaning, catalyst activation and growth conditions) the polymerization rates were found to be size-dependent, for catalyst dimensions below 150 nm. One explanation could rely on the platinum surface morphology percolation in reduced size systems.

large activated areas and the aniline oxidation everywhere the solution is in contact with the metal (probably, even if not sufficiently activated), including the channels[39]. While for channels below 100 nm in diameter this may be approved, the same explanation could fail for larger channels. Probably, aside these 2 possibilities there are also other explanations for the observed behavior and further work is required to clarify that. Important at this point, is that by using sacrificial growth areas, template confined growth can be accelerated and reproducibly controlled.

4.5.2 Polyaniline nanowire crossbar devices

Having grown the nanowires, the TE's were defined using the same procedure as for the non-nanostructured polyaniline devices. Preliminary experiments were performed using 500 nm thick PMMA resist and single-shot EBL exposure (using 30 keV electron beam). The estimated diameter for nanowires is less than 50 nm. Two types of morphologies have been characterized with apparently no significant differences in the electrical performance: flooded, mushroom-type, and normal nanowires. Though flooded structures may look as easier to characterize as the top contact is for sure created. Nevertheless, it may be that the nanowires have a dual morphology and composition. Due to the template confinement, the polyaniline comprising the base of the nanowire and the mushroom cap could be different in morphology and hence, may have different electronic transport properties inducing ambiguities in the data interpretation. One simple example is the difference in the transport properties that can be easily detected between the thin-film (Figure 4.32) and single-nanowire crossbar devices (see Figures 4.34, 4.35 and 4.36). For instance, the thin-film polyaniline samples displayed no rectifying effect nor hysteresis in contrast to the nanowire based devices. One explanation could be based on the different molecular structures of the polyaniline for the both types of devices. It was already reported that during the template confined growth, the polyaniline (and other polymers) chains may grow aligned along the template axis. This defect free molecular structure enhances the inter-chain charge transport explaining why the conductive polymer low dimensional structures have lower resistance than the bulk polymer. Further studies using various nanopore diameter templates have shown that decreasing the nanowire diameter leads to an increase in the conductivity corroborating with the theory based on the increased molecular ordering. The mushroom type

[39]There are several facts that are *pro* and *contra*: the growth on gold elements in contact with platinum corroborates; while extremely low polymerization rates on the polished side of silicon contradicts this hypothesis.

nanowires used so far in this work are comprised of both, template confined and bulk like parts. Thus, the measured characteristics are an average of both electronic properties. So even if the mushroom types are somehow easier to contact and characterize the data interpretation requires a strict knowledge of the morphology (for instance, the size of the flooded cap) and careful analysis. The same rationale could be applied for the diameter modulated nanopillars where different electronic properties are expected for the protruded parts. More experiments will be required to get full insight into the size and morphology dependent charge transport of the fabricated nanostructures (see at the end of this Section a detailed description of the perspectives).

Inset in Figure 4.34 (**a**) shows an example of a 100 μm $\times$ 100 μm crossbar point where 2 mushroom-type nanowires are connected[40]. After the polymerization, the respective samples were dipped in DI water for 24 hours to dedope the polyaniline. Ammonia solution is to be avoided as the PMMA is unstable when exposed to basic solutions (mostly the adhesion is degraded). After that time, without drying the sample, they were dipped in HCl 1M for 20 minutes, blown dry in a N_2 stream and loaded in the metallisation chamber, where they were left for 12 hours in a vacuum better than 10^{-4} mbar and afterward, 100 nm of Pd was evaporated at an evaporation rate of 1 Å/s and base pressure 5×10^{-7} mbar.

Figure 4.34 show the current voltage characteristics of the respective sample. The characterization was performed in ambient conditions at a DC voltage sweep rate of 5 mV/sec. The Pt electrode was biased while keeping the Pd electrode grounded. A "hysteresis" in the current is observed upon changing the bias sweep direction. Interestingly, the hysteresis was found to be permanent: once "switched", the devices remained in the respective conductivity state upon repeating the measurement and only after reverse biasing, the "switch-back" is done. Trace-retrace sweeps were recorded starting from 0 V to $\pm$ 1 V. Initially, the voltage was swept to + 1V with no hysteresis observed ($\vec{1}$ - $\vec{2}$). Next, to - 1 V where an increase in the conductivity was observed for the reverse trace ($\vec{3}$ - $\vec{4}$). The voltage was swept again to +1 V, this time with the observation of hysteresis, high and low conductances for the trace and retrace sweep ($\vec{5}$ - $\vec{6}$). Performing again the same mea-

[40]For caution, 2 nanowires with a mushroom-type morphology have been targeted for the moment as inevitable defects may arise during the patterning, growth and processing. Of course, this induces a sort of incertitude in the characterization regarding the electronic properties and the number of contacted nanowires. For the latter aspect, the possibilities are however limited: either none, one or two nanowires can be measured at a time ...

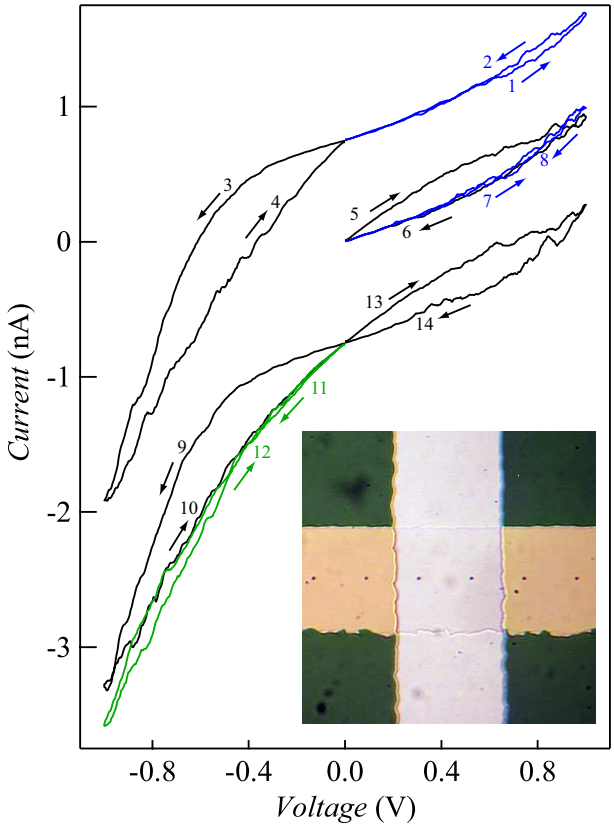

Figure 4.34: $I-V$ characteristics of single polyaniline nanowires. The sequence and the direction of voltage sweeps are marked by numbers. The curves are shifted by 0.75 nA for clarity Insets: micrograph of a crossbar latch and schematic view of the PANI nanowire composition profile upon voltage driven doping/dedoping.

surement followed the low-conductive path in both, trace and retrace ($\vec{7}$ - $\vec{8}$). Going to -1 V, switched the sample to the higher-conductive state ($\vec{9}$ - $\vec{10}$) while, repeating the measurement followed this time only the high-conductive state ($\vec{11}$ - $\vec{12}$). And this could be repeated for several times ($\vec{13}$ - $\vec{14}$). Eventually, the signal was found to degrade, lowering in amplitude yet, preserving the overall shape (not shown here). Thus, the hysteresis is activated only once the nanowire is electrically stressed in the reverse bias.

A similar behavior was found in the $I-V$ characteristic of another sample (Figure 4.35). This time a different measurement approach was used. The trace-retrace hysteresis loops were measured for different ap-

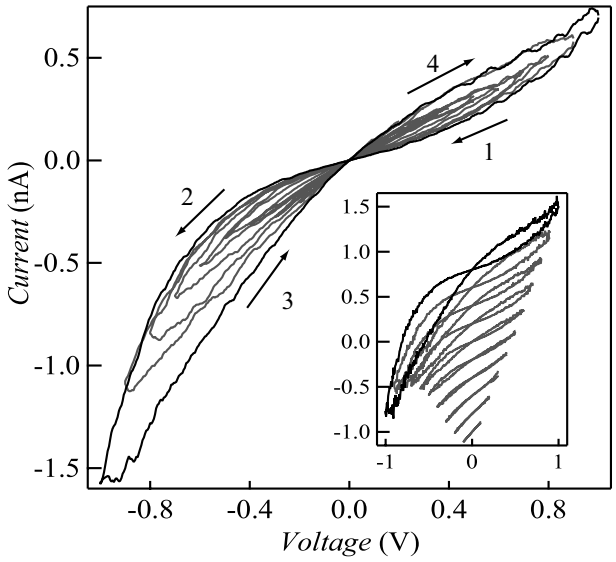

Figure 4.35: Similar hysteresis loop were observed on another mushroom type sample. The signal amplitude is lower than for the sample depicted in Figure 4.34 probably due to a different dopant diffusion depth. Insets: a perspective view with curves shifted by 0.2 nA for clarity.

plied biases, always starting form the positive value. Before measurement, the sample was stressed with -1 V (for 10 sec) to switch it in the higher conductive state. From ± 0.1 V to ± 0.3 V no evident signs of hysteresis are detected. The $I-V$ characteristic is mainly linear with no evident rectifying behavior. The hysteresis starts to be noticeable at ± 0.4 V and the amplitude of the hysteresis loop gradually increases with the applied voltage. Thus, it seems that this effect is bias driven, with an increased intensity for higher voltages and an onset around ± 0.4 V. Also, at high bias values, the rectification becomes more pronounced.

For the moment we don't have a clear explanation for the measured data. Nevertheless, this behavior was observed several times meaning that there may be a potential for building polyaniline nanowires based memory devices. Initially, a explanation was proposed which was rather a speculation than a scientific fact. As mentioned earlier after the growth, the nanowires were left in water for 24 hours. Then they were "shortly" dipped in HCl. It was believed that due to the confined dimensions and specific morphology (500 nm in length and less than 50 nm in diameter polyaniline nanowires, embedded in hydrophobic PMMA which may

limit the diffusion) a complete doping was not achieved[41]. The structure was regarded as a doped top part (including the mushroom cap) connected to a partially (probably through a gradient) doped segment at the bottom. The polyaniline is also known to be ionically (and especially proton) conducting. The proton conduction can be assigned to loosely bound protons and is possible along the polymer backbone because of the presence of amine / imine groups. Thus, the observed behavior was attributed to the bias induced dopant drift along the nanowires. Many of the observed characteristics supported this picture. Applying a negative voltage on the Pt BE will drift toward the positively charged protons, doping more the lower nanowire segment explaining the conductivity increase upon negative bias stressing. The backward drift could be then induced by reversing the bias, or applying a positive voltage on the BE. Hence, the bottom polyaniline segment will be again dedoped and the nanowire will switch OFF in the lower conductivity state. This picture explained fairly well all of the observed phenomena. A threshold voltage could be required to activate the proton mobility and as observed, no hysteresis is present for biases bellow 0.3 V. The current drift for constant applied voltages was also consistent with the model. A negative bias slowly "moves down" the protons and increases the nanowire conductivity while reversing the sign diminishes the conductivity. The drifted protons can remain permanently bounded in some sites and hence, an irreversible "damaging" was observed after prolongated electrical stressing.

Nevertheless, subsequent experiments didn't supported the respective explanation and further studies will be required to better understand and control the hysteretic behavior. The nanowires having a uniform doping profile as well as those in which the "doped" and "dedoped" sequences were inverted[42] displayed the same current-voltage characteristic as previously mentioned. Though the rectifying and hysteretic behavior were still detected, they could no more be interpreted using the bias driven dopant drift picture. For example, panel (**a**) of Figure 4.36 displays the $I - V$ curve of a uniformly doped single nanowire. To realize that, the sample was dipped for 3 hours in DI water (under agitation) after the

[41] This was also observed when working with polyaniline films on transparent substrates and inspecting visually the color. Of course this is a rough estimation. For example, when initially dry, a 200 nm thick film, can be doped or dedoped in less than 2 min. If waterlogged, then it may take up to several minutes to dope and even more to dedope. In such open systems the only restriction for the diffusion is the porosity or the permeability of polyaniline. In confined channels, nanofluidic effects have to be also taken into account. Further work will also imply the use of COMSOL MicroFluidics pack to simulate the dopant diffusion dynamics.

[42] For that, the sample were first doped in HCl and then shortly rinsed with water.

growth and then, re-doped in HCl 1 M for 3 hours. As can be observed, the rectifying behavior is present with the higher conductive part in the negative bias regime. A small hysteresis can be also detected. The same characteristic was found for an as-synthesized nanowire. This time, the sample was only shortly rinsed with HCl 1 M to avoid any surface aniline sulphate crystallization or sulphuric acid residuals. Again, rectification in the positive bias and hysteresis was observed. These data suggested that the doping profile, as initially proposed, is invalid and the rectification and the hysteresis have different origins. Another uniformly doped (using HCl 1 M) nanowire was subjected to different measurement configurations were the source and drain have been flipped. The data are shown in the inset of Figure 4.36 (**b**). Though the measured signal was relatively lower as compared to the previously described completely doped nanowire (shown in panel (**a**)) the data gave some insight into the charge transport mechanism. The Pt has a higher (vacuum) working function than Pd (5.65 and 5.12 eV respectively) and hence, a negatively biased Pt electrode will inject better holes into the p-type polyaniline nanowire than Pd and the current will be higher. Reversely, Pd will inject better electrons and hence, will display a higher current in the positive bias range.

Other phenomena that are at the origin of the memory effects in such type of devices could be at the origin as well. Metal filament formation, very often observed in metal sandwiched thin film devices is difficult to imagine in this configuration. This effect is either current (electromigration) or voltage (field assisted metal evaporation) assisted, requiring high driving forces, and being characterized by abrupt jumps in conductivity. Moreover, typically the filaments are protruding through the active layer shorting the electrodes and enabling the high conductivity state. Here, this can be definitely excluded as the eventual protruding thickness is more than 400 nm, physically not being feasible at such low energies. Intra-molecular proton transfer has been also found to induce electrical bistability in small molecule devices through bias driven keto-enol tautomerism of N,N'-bis (salicylidene)-1,6-hexanaphthenediamine [293]. Here, due to an extended conjugation in the emeraldine salt form, the intra-molecular proton transfer is expected to play an insignificant role as compared to intra-molecular transfer. Bias driven redox changes are not to be neglected. This type of processes are known to proceed through sharp changes in conductivity and at higher voltages, as also observed for other organic memory devices [294], and could seem rather unappropriate to account for the same type of effects in the measured systems (lower threshold voltages, smoother transition). Yet, we are dealing with polyaniline. As mentioned in the beginning, the term polyaniline

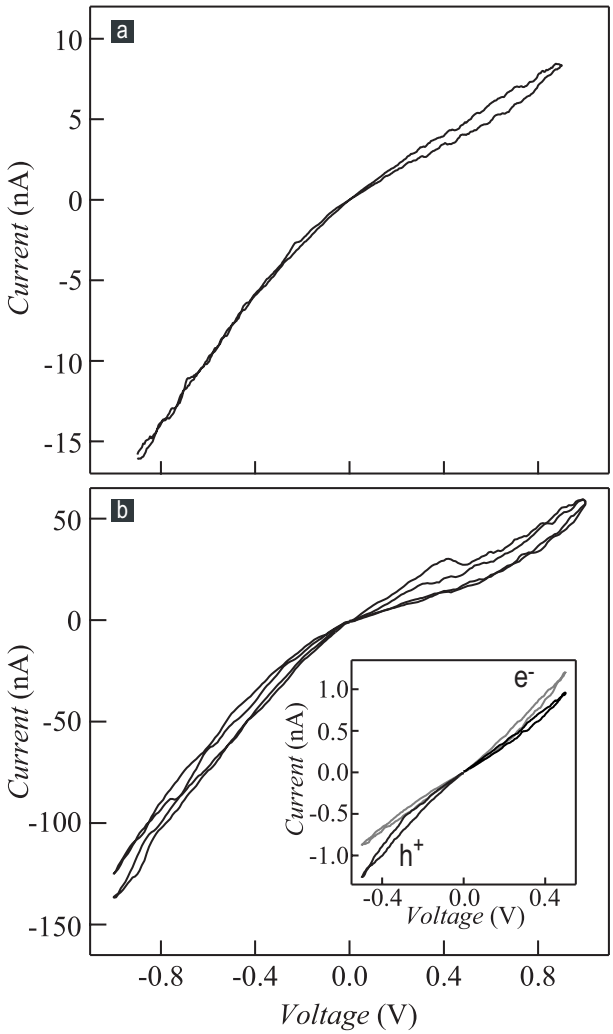

Figure 4.36: Current voltage characteristics of a HCl 1 M doped single nanowire (**a**) and of an as synthesized single nanowire (**b**). Inset: $I - V$ characteristics of a "fully" doped single nanowire by flipping the source-drain configuration. For instance, the Pt was biased while keeping the Pd electrode grounded (black curve) and reversely for the gray curve. All 3 samples are of the mushroom-type.

defines a class of poly-amines and -imines and interconversion between them can be easily achieved using redox and acid/base treatments (see Figure 4.12). In a simple approximation, the redox potential necessary to transform leucoemeraldine into emeraldine is $\sim$ 0.25 V and further

to pernigraniline at 0.75 V (the potentials are measured in solution respective to the saturated $Ag/AgCl$ electrode for the electropolymerized aniline). The interconversion potentials are relatively small and close to the "threshold" value observed for the hysteresis onset (see Figure 4.34). Thus, one possibility may be that initially the nanowire is not made of pure emeraldine and small amounts of leucoemeraldine are present. Hence, bias driven redox changes may occur and modify the conductivity of the entire system. Though the data are corroborating ($\sim$ 0.25 V for the LM to EM conversion and 0.3 V threshold for the hysteresis onset) it is probably premature to attribute the so called "memory effect" to redox changes in the polymer matrix. And finally, the voltage induced drift is not to be excluded and may require some further studies to ascertain for its significance.

A more detailed analysis and characterization of various configuration samples will be required to have a clear vision on the charge transport mechanism. Knowing precisely the composition and the oxidation state of the as-synthesized and of the post-processed polyaniline in both, bulk and template confined configurations may provide a better understanding and interpretation of the electrical data. For instance, though very high conductivities are achieved for the as-prepared sample (C = 0.35 S/cm[43]) it is not clear why such big differences are observed between the pristine and HCl doped sample. Intriguing is the fact that the doping media for the pristine sample is much less "protonated" (0.4 M H_2SO_4) than the subsequent doping agent (1 M HCl). Thus, either the polyaniline undergoes redox transformation during the dedoping/doping protocol or, the counter-ion infers strongly in the transport characteristics. The later explanation is the most plausible though the chemical changes are also expected in the dedoped emeraldine state when exposed to air. The "doping" effect of counter-ion in polyaniline's is relatively well known fact though the mechanism is less understood. For instance the higher conductivity in polyaniline (the metallic phase was demonstrated in the emeraldine oxidation phase) was achieved using camphorsulphonic acid, a relatively weak (as compared to HCl and H_2SO_4) acid [56]. This was attributed to the counter-ion insertion in the polymer matrix and subsequent molecular re-organization resulting in a enhanced charge transport [56]. One direction of study could be finding the optimal growth and/or post-processing condition to achieve even higher conductivities than observed for the moment. The polymerization temperature (and hence the polymerization rate and the mobility of small

[43] One of the highest to date reported conductivity in nanoscale polyaniline structures.

species) could be one influencing factor to study. Some preliminary results show that the electroless polymerization on the surface of platinum can be conducted as well in presence of camphorsulfonic acid. Hence, we expect that by growing the nanowires in such conditions, some record conductivities could be reached.

Other direction to explore is the study of the interdependence between the molecular structure, electrical contact nature and the electrical performance. For instance, by changing the nanowire length (just by adjusting the thickness of the initial PMMA layer) while keeping the diameter constant, the contact resistance could be estimated. The same type of experiment could be applied for mushroom-type nanowires to estimate the resistance of the flooded part and this test could give an idea of the electric properties (and hence, of the molecular structure) for both parts in a flooded nanowire. Yet, to really get insight into the molecular structure (and reversely, correlate that to the electronic properties) structural studies will be required. The preliminary work didn't succeeded primarily because of the incapacity to transfer the nanostructures from the synthesis substrate to the TEM grid, this step requiring further optimization. Future work may imply some experiments were the nanowires could be directly grown on a TEM grid. Other alternative is the use of Raman spectroscopy. This technique has proved to be a useful method for studying conducting polymers and can indicate, with a substantial sensitivity level, the structural and compositional variations in polyaniline derivatives [295]. These studies could be eventually complemented by variable temperature charge transport experiments. At the same time, thermal, mechanical and chemical stability of synthesized polyaniline as well as of fabricated nanostructures and devices could be studied. For instance, the PMMA embedded single polyaniline nanowire devices have a relatively poor stability as the PMMA is easily degraded when thermally or chemically stressed. The stability issues of the TE's need also to be solved. The deposited Pd electrodes are very fragile being readily delaminated when mechanically or thermally stressed. The use of adhesion metal layer is to be avoided as the electrical contact to the polyaniline nanowire will be realized by the respective layer and no more by the metal of interest, this step requiring further design and material optimization.

As for the more applied studies (memory applications or rectifying effect) all of the above mentioned studies could be only of great benefit. Controlling and understanding the polyaniline structure, morphology and electronic properties could enable further rationale molecular and device design. As already mentioned, for the electrical bistability two types of mechanism could be targeted: bias induced redox mod-

ifications and dopants drift. The rectification could be initiated in a first step by changing the chemical nature of the BE and/or TE. And subsequently, the study could be extended to other types of applications and/or devices. Novel material chemistry and nanoscale approaches for electrochemical energy storage applications could be developed and implemented in applications such as lithium batteries and supercapacitors [296]. By growing the polyaniline on n-type porous silicon, high rectification ratio and more important, nanoscale hybrid (organic - semiconductor) light emitting devices fabrication could be envisioned [297]. Fabrication and device integration scalability is to be investigated as well. For example, polyaniline nanodots structured with higher areal pattern densities than presented (0.28 Teradot/inch^2) could be interesting further to study in both perspectives. And finally, template confined electroless polymerization of aniline within other types templates than EBL structured PMMA resist films (for example using block copolymers) or the co-integration of the presented crossbar latch fabrication technology within modern computing design architectures could provide years of fruitful research and exciting results.

4.6 Conclusion

In conclusion, we have shown that one of the most studied conjugated polymers can be now structured with an unprecedent resolution, areal density and 3D morphology. The large variety of working substrates and "grow-on" active materials used to reliably control the electroless polymerization protocol enhances further the applicability of the method. Though the nanoscale structuring was done using EBL defined templates or nanoscale reactors, there is virtually no restriction in using other types porous materials or growth confining systems. In every envisioned case, the reliable growth control of minute quantities of polyaniline will be possible. As for the EBL, we provided a novel protocol for complex 3D structuring using simple methodologies and realizable using basic research tools and capabilities. Finally, we provide simple fabrication schemes for the realization of single polyaniline nanowire based crossbar devices.

Chapter 5

Porous silicon and colloidal mask lithography

I Want to Believe ...

Fox Mulder

Working with porous AAO and 3D structured PMMA templates can be fancy and there is a lot of potential to exploit. However, silicon still remains the material with the most studied properties and the acquired know-how allows to fashion it in unimaginable ways. In the following we will discuss some alternatives to the porous PMMA and AAO templates mainly using silicon as a building block. The first part is dedicated to inducing porosity (macro, micro, nano, meso and nanofibrilar) into bulk monocrystalline silicon. Three different ways based on metal assisted chemical etching are discussed. The second part exploit spontaneous 2D and 3D assembly of polystyrene micro-spheres that could be further used to micromachine silicon as well as other substrates. This work is very recent and only methodologies, some results and possible applications are provided.

5.1 Metal assisted chemical etching of silicon

Porous silicon is of great interest because of its potential for optoelectronic, nanoelectronic and biomedical applications, allowing the production of next generation devices, compatible with microelectronics industry requirements. Basically, porous silicon is silicon with lots of holes in it. It has properties that are very different than that of bulk crystalline or polycrystalline silicon. One of the most used method to

produce it is based on electrochemical oxidation, much more alike the fabrication of AAO [298–300]. The electrolyte is HF; the application of a sufficient anodizitation voltage produces porous silicon[1]. The process was found to be sensitive to the light and different characteristics were observed for anodized samples either illuminated or not. Photoirradiation (most efficiency gained from short wavelength photons) excites the electrons to the conductions bands, creating a hole and activating the $Si-H$ bonds making them susceptible to be attacked by the fluoride ions. Photolithographic electrochemical etching was also used for luminescent color image generation in porous silicon [301]. The most common solution for stain etching is a mixture of HNO_3 and HF.

A very exploited alternative is the metal assisted chemical etching of silicon. In this method, noble metals (Au, Ag, Pt or Pd) are used as silicon oxidation catalysts. A typical etching solution is composed of HF and H_2O_2 without the need for external electrical power. Silicon is inert in a such solution. Only when in presence of metals the silicon is etched. The loading of silicon surface with metal can be done in various ways. Thin metal films, evaporated without any adhesion layer (eventually dewetted using an annealing step to form nanoparticles) and then dipped in the etch solution was the first proposed method [302]. Subsequently, many other techniques have been proposed and tested. In the following we will discuss only as-prepared metal nanoparticle assisted etching (and the influence of their size upon the morphology of porous silicon), "metal free" etching and $AgNO_3$ etch induced formation of silicon nanowires and nanoribbons.

The nanoparticles were drop casted (100 μl) on the surface of the samples and then dipped in a 2.6 M HF and 8.1 M H_2O_2 solution and etched for 30 minutes. The drop-cast deposition results in the formation of particle aggregates as well as in single particles (mainly for bigger sizes). Whenever the aggregates were formed, they sinked together in the silicon bulk with the formation of large pores. Afterward, the samples were washed with water and blown dry with N_2. SEM inspection was used to characterize the surface and the bulk morphology. Figure 5.1 show the results obtained using as-prepared gold nanoparticles[2] assisted etching. A preferential etch of the <100> planes was detected independent of the particle size. When using <100> silicon wafers, perpendicular to the surface pores were mainly detected. Nevertheless, due to the equivalence of the <100>, <010> and <001> direction, parallel

[1] HF is un-reactive with a silicon surface because once it removes the oxide layers, it leaves the surface hydrogen terminated. The obtained $Si-H$ layer acts as a passivating layer.

[2] Used as received in various sizes from BBInternational.

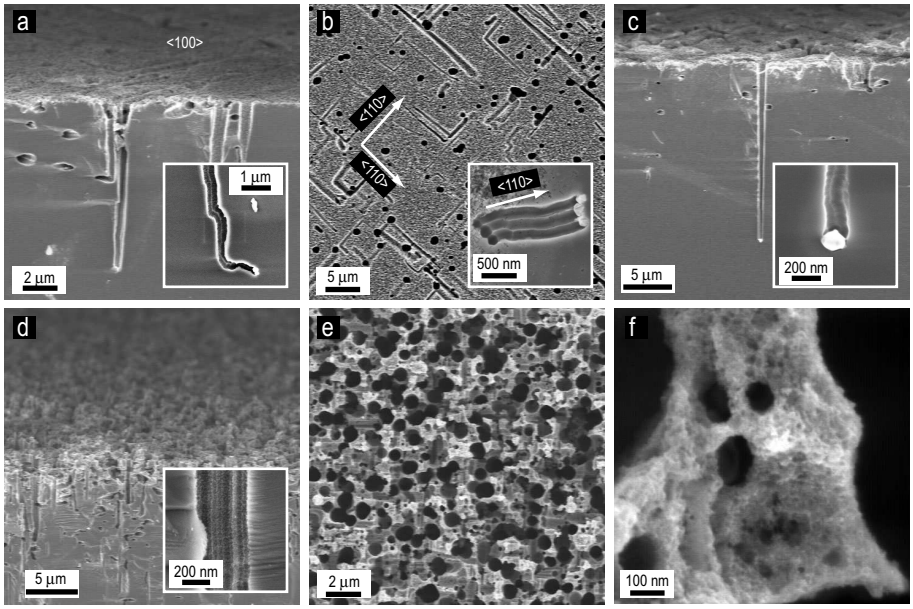

Figure 5.1: (**a**) Pores in <100> *Si* using 200 nm gold particles. Preferential etch of <100> planes is observed. In depth pore propagation along <010> and <001> directions is also detected. Inset: step-like pore. The change in the etch direction is probably dictated by the non-spherical shape of the used particles (not shown here). (**b**) <100> silicon surface carved by 150 nm gold particles. Inset: "3 nanoparticle lithography" defined along <110> direction. (**c**) Crossectional view of the sample from (**a**) showing a 15 μm long pore. Inset: single nanoparticle pore formation. (**d**) Cleaved view of a silicon samples etched using 40 nm gold nanoparticles. Inset: close-up on a multi particle etched pore. The bulk structure of silicon remains intact. (**e**) To view of the sample from (**d**). A complex hierarchical porous matrix is formed. (**f**) Enlarged view from (**e**) showing the "mesoporous" nature of the remaining walls.

as well as step-like propagation could be detected (panel (**a**)). Using <111> wafers, the pores propagation was slanted by 55° with respect to the surface normal. Inspection of the sample surface revealed that the <110> are also preferentially etched (panel (**b**)). Occasionally, groups of nanoparticles were found to propagate in-plane nanostructuring the surface. The overall bulk morphology was affected only for the first 100 - 200 nm. Nanoparticles with diameter of 150 nm were found to behave identically (panel (**c**)). Smaller particles altered significantly the top-most part of the silicon wafers. Asides the etched pores, the surface was found to be rougher with a complex hierarchical morphology (panel (**d**)). The porous film has a dual morphology: large pores (50 - 500 nm) due

do the direct penetration of particles "drilled" into a mesoporous matrix with pore size bellow 15 nm (panels (**e**) and (**f**)).

The pore formation is initiated by the reduction of H_2O_2 following the reaction $H_2O_2 + 2H^+ + 2e^- \rightarrow 2H_2O$ and the oxidation and removal of silicon $Si + 6HF \rightarrow SiF_6^{2-} + 6H^+ + 4e^-$. The metal particle acts as an electron donor-acceptor from silicon to water peroxide catalyzing the reaction. Hence, the etching takes place in the near vicinity of the nanoparticles. Nevertheless, as the generated electrons could also propagate into the bulk silicon, the etching is expected to take place everywhere silicon is in contact with the solution. This explains (i) why the surface of the samples and the sidewalls of the pores were found to be roughened and (ii) the widening of the top most part of the pores (Fig. 5.1 (**c**))[3].

Using the nanoparticles as etch catalyst implies that the porous matrix will remain heavily doped with gold. For some technologies (for examples CMOS), this can be annoying. Hence, a catalyst free process could be more interesting. As already mentioned, the silicon etching can take place far from the metal site. This was exploited to produce porous silicon using a metal-free etching procedure[4]. The protocol was already mentioned in Section 4.3.5 an simply reduces to coat with catalyst (2 nm Ti and 100 nm Pt) one side of a wafer and etch the opposite side. The reactant solution was a mixture of 2.8 M HF and 0.9 M H_2O_2 in water. Upon immersion of the samples, a rapid change in their colorization could be observed indicative of thin-film interference effects (Fig. 5.2 (**b**)). The etch rate was found to be very high (more than 1 μm/min). The obtained porous matrix was comprised of branched sub - 30 nm pores with relatively good size-dispersion (Fig. 5.2 (**a**)). The branching dendritic structure is attributed to the competitive events while preferentially etching <100> planes (see further).

A recently proposed method uses a statistical electrodeposition metal deposition technique to assist the etching and result mainly in the fabrication of nanowires and nanoribbons [303, 304]. Compared with other silicon nanowire growth methods, this approach possesses the further advantages of being a catalyst free, having no saturated dopant contamination and room-temperature process applicable for any type of sub-

[3]The differences in the sample morphologies between the samples etched using 200 or 15 nm particles and those etched using 40 nm particles could be attributed to the different particle concentration in the used suspensions (0.7, 1.66 and 90 $\times$ 10^9 per ml). This implies a higher exposed surface for gold and hence, an enhanced electrochemical reaction.

[4]By metal-free we mean that no metal is used and remains on the useful porous side.

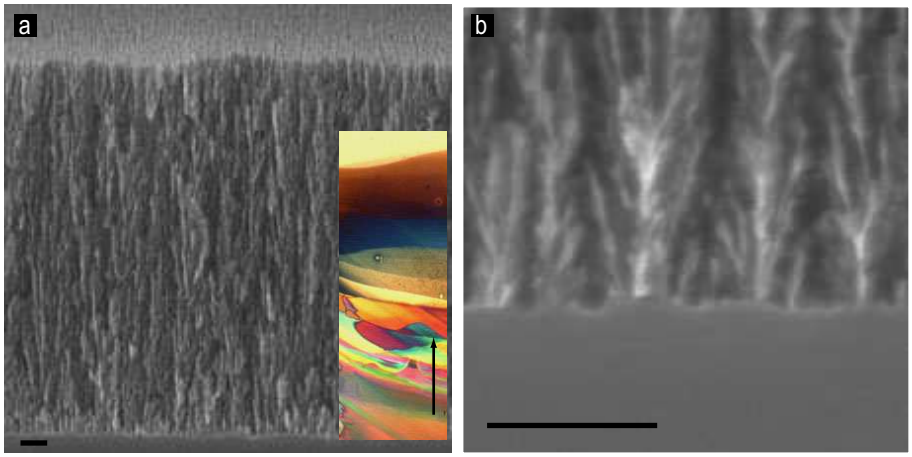

Figure 5.2: (**a**) Cleaved view of the porous matrix obtained using <111> oriented silicon wafers. Inset: Bright field optical micrograph of a etched sample (7 × 20 mm) gradually removed (in about 15 sec) from the solution. The removal direction was upwards (marked by the arrow). The colors are the result of thin-film interference effects under white-light illumination. (**b**) Close-up of the bottom part of the template. Scale bars: 100 nm.

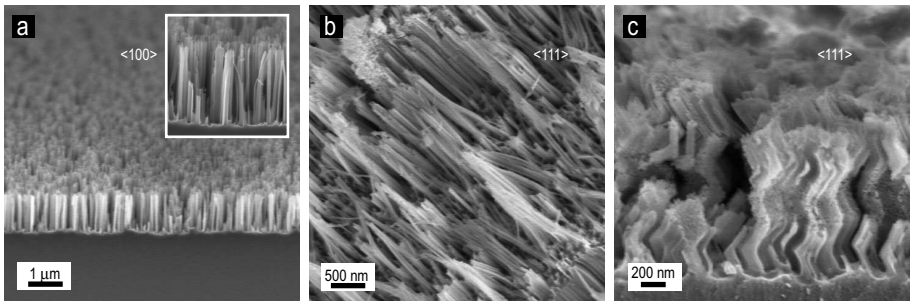

Figure 5.3: (**a**) Uniformly distributed nanostructures obtained by etching silicon <100> wafers in 0.01 M $AgNO_3$ and 2.5 M HF solution. Inset: close-up on the fabricated silicon nanowires. Diameters bellow 15 nm have been detected. (**b**) and (**c**) Nanostructures carved in <111> silicon using 0.34 M $AgNO_3$ and 5 M HF mixture. The etch direction is 55° tilted compared to the surface normal. In (**b**) a uniform etch direction can be visualized while in (**c**) changes in the etch direction (yet, still preserving the 55° tilt) are present.

strate [305]. In this method, a mixture of $AgNO_3$ and HF for the etch is used. The etching process is initiated by the reduction of silver

ions on the silicon surface exposed to the $AgNO_3/HF$ solution. The formation of nano-scaled silver nuclei oxidizes the beneath silicon and sequentially the HF dissolves the formed silicon oxide. Again, the preferentially etched planes are <100>. Reacting a <100> wafer results in vertically standing silicon nanowires uniformly distributed all over the surface (Fig. 5.3 (**a**)). When <111> wafers were employed, the nanowire axis was tilted by 55° with respect to the surface normal (Fig. 5.3 (**b**)). As there is no preference for any of 3 possible <100> planes on a <111> wafer, the nanowires orientation was not uniform all over the surface. In some places, competitive etching of these planes was observed resulting in a chevron-like structure much more alike the architectures obtained using glancing angle deposition technique. These structures may be useful for photonic crystal applications. Though we know why they are obtained we don't know how to control them reliably on large scale.

These three examples show only the "Tip of the Iceberg" of the possibilities enabled by this powerful technique. Many other approaches could be envisioned to further precisely control the etch configuration, the morphology of the obtained architectures with desired optoelectronic properties. For example, using nanoparticle assisted etching it could be envisioned the precise positioning of single nanoparticles resulting in the fabrication of high-aspect ratio single nanopores at predefined positions. A gradient of pore sizes or depths imparts a rainbow of colors to a porous silicon chip, one of a variety of new biosensor technologies in development around the world. The different colors correspond to different sized pores (ranging from a few to hundreds of nanometers) or pore depths (few nanometers to tens or even hundred of micrometers). Because the effective refractive index of porous silicon depends on its porosity (typically, a linear dependence is observed), different optical response could be achieved. Further, changes in the environment (surface functionalization, sorption-desorption or infiltration) translates into a modified optical response very useful for sensing. As porous silicon is known to be bio-compatible it has been extensively used in biosensing applications [306]. The hierarchized porous structures shown in Figure 5.1 (**d** - **f**) could help the device discriminate and detect proteins and other molecules based on their size.

5.2 Colloidal mask lithography

A very powerful nanoscale bottom-up structuring technique is offered by the colloidal lithography. The strategy behind is to exploit the tendency of monodisperse submicrometer spheres to spontaneously organize on a hexagonal or a f.c.c. lattice when assembled in 2D or 3D, respectively. The resulting materials, a hexagonal arrangement of spheres and a synthetic opal respectively, can act as: templates into which a material can be infiltrated, shadow elements for physical deposition or etch masks. Due to the parallel nature of the microsphere assembly, colloidal lithography is capable of making a large-area mask (order of square centimeters) in a relatively short time (2 - 5 hours). Various techniques have been developed for the reliable fabrication of large area ordered colloidal crystals assemblies. The most important are: evaporation methods [307, 308], electrostatic deposition [309, 310], dip-coating [311], Langmuir-Blodget coating [312], interfacial self-assembly [313–315], electrophoretic deposition [316, 317], self-assembly on pre-patterned substrates [220, 318], drop-casting [222] and spin-coating [319, 320]. We have adopted the dip-coating, evaporation and interfacial deposition directions.

Figure 5.4 shows an example of a monocrystaline domain formed by a monolayer of polystyrene spheres (980 nm in diameter) deposited on a glass substrate. A perfect stacking in a hexagonal lattice[5] is also detected in the diffraction pattern. The usefulness of light diffraction is two-fold. First it clearly shows the monocrystalline nature of the pattern. Second, it enables fast determination of the lattice orientation. Subsequent modification may require knowledge of the precise orientation of the lattice to be able to align the "processing beams" along the desired directions (shadow physical evaporation to fabricate lines, circles or SRR's, angled etching or exposure). This can be done using SEM or optical microscope inspection yet, light diffraction is somehow more elegant and gives an idea of the lattice orientation over several square millimeters. Moreover, here the light diffraction (using a millimeter scale laser beam) shows that large area monocrystalline domains can be easily achieved. When scanning the beam over polycrystalline or amorphous area the diffraction pattern was circular indicative of structural non-uniformity.

The peculiar properties of colloidal assemblies can be exploited for various functionalized surfaces or optoelectronic devices. Treating the

[5]The main way to assemble the spheres in 2D is the hexagonal arrangement. Though it can be regarded as a singular option, as we saw in Chapter 2 the hexagonal lattice is the best option for building photonic structures. Moreover, the peculiar geometry of these masks provides the playground for further structural modification or defect engineering.

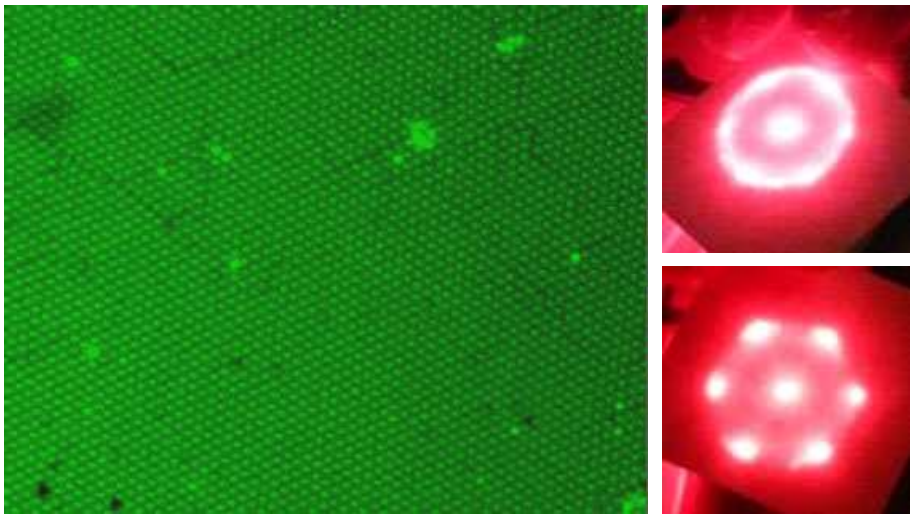

Figure 5.4: Left: optical snapshot of a monocrystalline domain composed of 980 nm latex sphere. Few dislocation defects as well as some parasitic particles are visible. Right: light diffraction patterns on a polycrystalline/amorphous (top) and monocrystalline (bottom) region. The beam ($\sim$ 2 mm in diameter) of a laser pointer was transmitted through the particles assembly on glass and projected on a paper sheet. The diffraction was registered on a similar area (having also the same direction) as shown in the optical micrograph at left. The diffraction pattern is actually the reciprocal lattice of the original lattice (*i.e.* a hexagonal arrangement rotated by 30°, see Chapter 2 for details).

system from a geometrical perspective provides a lot of possibilities for subsequent micro-structuring (see Figure 5.5 for few examples). Hexagonal packing of spheres leaves a honeycomb lattice of "triangular" voids (if projecting the shapes along the surface normal). This lattice is situated at half-sphere-diameter above the substrate. Thus, the system can be treated as a "resist" mask with a large undercut profile providing opportunities for angled physical depositions. For example, orthogonal metal evaporation perfectly reproduces the honeycomb lattice (Fig. 5.5 (**d**)). Subsequent physico-chemical modification can be induced to modify the respective profile. The annealing of the samples merges the spheres by swelling the polystyrene and reduces the void space in-between (not shown here; for illustrative examples see [313, 314]). Oxygen plasma exposure diminishes the size of the spheres while preserving the original lattice parameters providing further place for fine tunning of the structuring mask. Examples of various shapes obtained by gradually exposing the self-assembled masks to the O_2 ashing are shown in

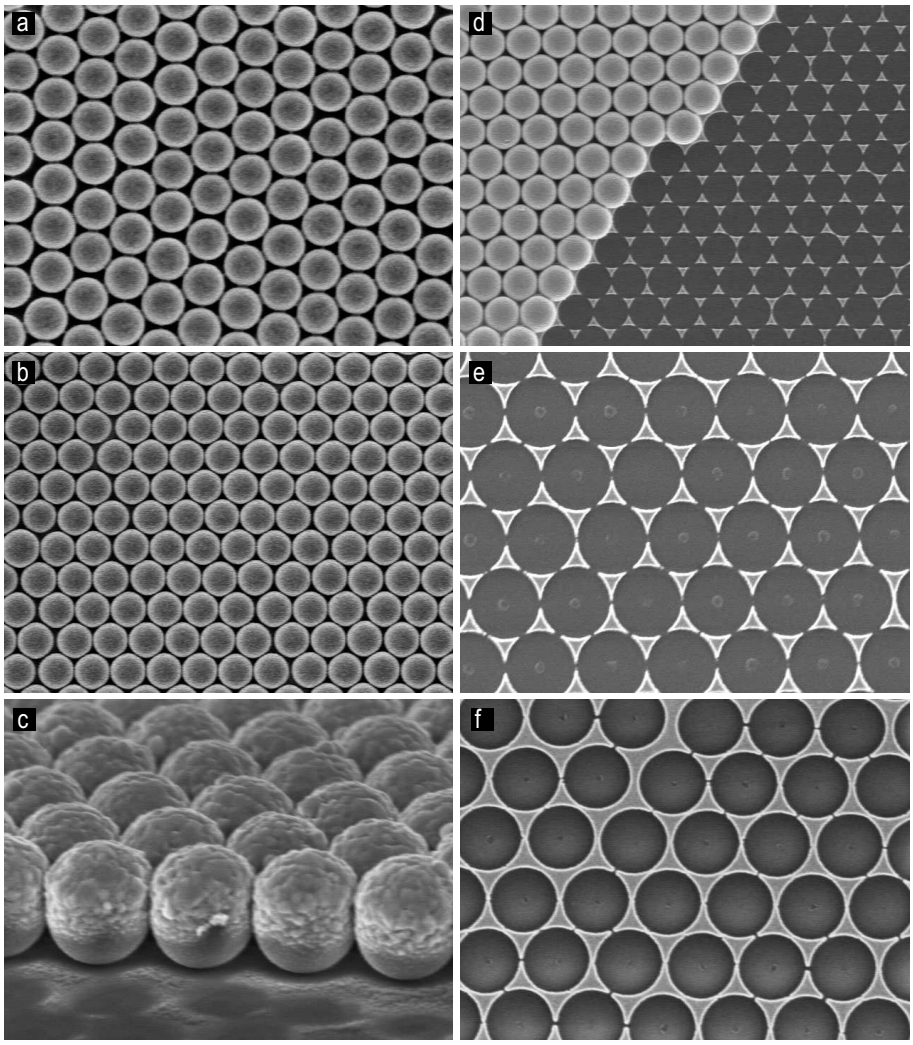

Figure 5.5: Examples of assembled 2D colloidal masks composed of 620 and 980 nm spheres on silicon and glass ((**a**) and (**b**), respectively). (**c**) "Egg-shaped" profiles obtained by conformally coating 980 nm close-packed spheres. 200 nm of aluminum was deposited using a planetary-rotating sample holder on an as-prepared film. When exposing the assemblies to O_2 plasma, the spheres diameter is gradually decreased while preserving the lattice constant. Subsequent orthogonal metal deposition (here 50 nm of Au) and lift-off removal of spheres (using adhesive tape) results in a honeycomb array of various shapes depending on the plasma exposure time ((**d**) - pristine, (**e**) - 5 min. and (**e**) - 15 min.).

panels (**d**) to (**f**) in Figure 5.5. A sort of "glancing deposition" is also shown in panel (**c**) where 200 nm of Al were conformally deposited on the self-assembled spheres. The shapes are elongated (appearing as "kinder-egg") and distinct (the metal layer does not form a continuous film). This results from the combination of both, metal deposition protocol and close-packed arrangement of spheres[6].

Assembling the colloids in a multilayer configuration provides a natural way for 3D lithography. The preferential arrangement will be a f.c.c. lattice of polystyrene spheres. The obtained architecture is porous and the spheres can occupy maximum 0.7405 of the volume available[7]. The void volume can be filled with a desired material and obtain an inverted structure after removal of initial spheres (a f.c.c. lattice of air-holes). The as prepared "meta"-material has already interesting features. It displays a photonic crystal behaviour. This structure is encountered also in nature and well known as opal. In natural opal, the brilliant regions of pure spectral color result form from close-packed domains of colloidal spheres of silica (SiO_2) [322]. In this case, they are formed of polystyrene spheres (having similar ϵ). Although, there is no complete band-gap in opal-like structures (even for structures made of high-dielectric materials) they've become of great interest mainly due to the facile synthesis over large scale using colloidal assembly. Moreover, inverse-opals are known to open complete band-gaps for high-ϵ materials.

Even if there is no complete band-gap, there are prohibited bands in these structures along some of the crystal directions. Specifically, the light propagation is perturbed along the Γ - L direction, or physically, normal to the $<111>$ surface. Figure 5.6 shows some examples of fabricated structures along with the transmission spectra of obtained crystals. The assembly takes in a such way that the $<111>$ planes are parallel to the sample surface hence, normal incidence spectroscopy probes specifically the Γ - L direction. As can be observed, using the same material (here polystyrene), "novel" properties are obtained by changing the microstructure of the material. Different sizes of colloids yield different optical properties. The scale invariance (see Chapter 2) is nicely visualised using these systems: peak-center position ratio is 1.72 with the

[6]The planetary-rotating sample holder enables arrival of evaporated material from any angle on the substrate. For example, a single sphere would be coated almost entirely. Yet, in a self-assembled colloidal film, they are masking each other and the metal is deposited solely on each sphere. A similar approach is used in Glancing Angle Deposition technique.

[7]As stated by the Kepler's conjecture: no packing of spheres can be denser than a face-centered cubic lattice [321]. This holds true for the as-prepared crystal. Subsequent modifications, such as sintering or annealing and hence, deforming the objects, will result in an increase of the filling fraction.

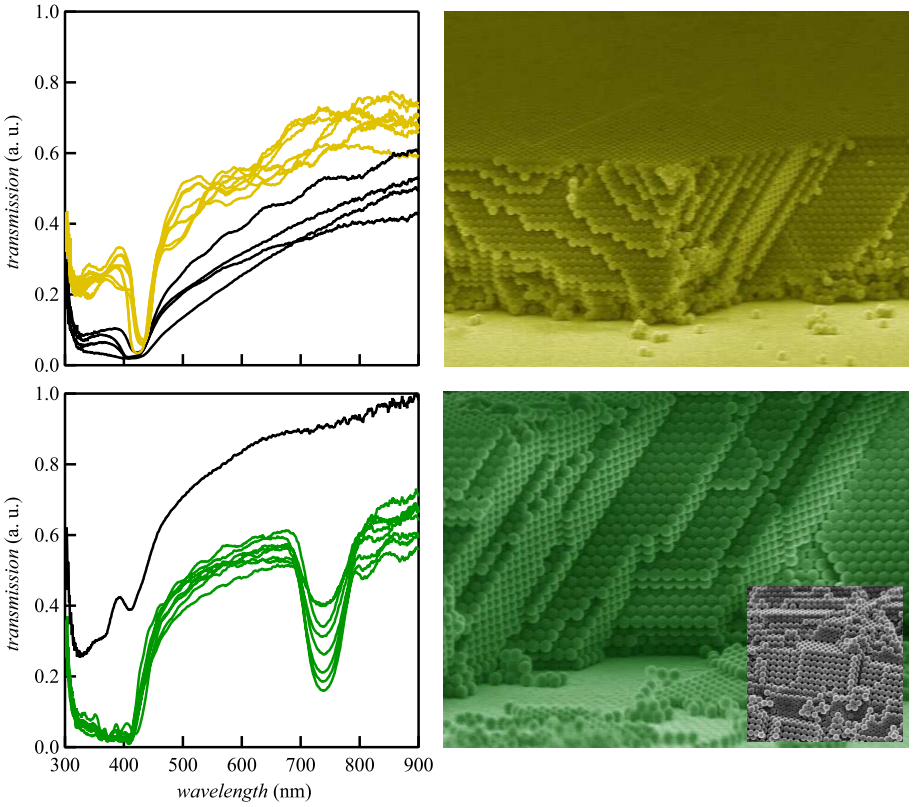

Figure 5.6: 3D assembly of polystyrene spheres. A f.c.c. opal-like structure is naturally formed. A photonic band gap exists in the Γ - L direction. For a proper size of spheres, the band gap can be centered in the visible range of wavelength. "Synthetic-opals" formed of 173 and 330 nm spheres exhibiting stop-bands centered at 430 and 740 nm (top and bottom plots, respectively). Normal incidence transmission spectroscopy was used to probe the optical properties of assemblies on glass substrates. Multiple areas have been scanned. In the crystalline areas only variations in the stop-band intensity was observed while in the amorphous or polycrystalline areas the peak disappeared (black curves). The SEM images are false-colored with the complementary color for the stop-band. Gray-scale inset show a mixed amorphous-polycrystalline area.

sphere size ratio of 1.91, respectively (calculated gaps for a perfect lattice are centered at 404 and 772 nm, respectively). The small deviations are due to the size variations for the used spheres ($\sim 5\%$ as specified by the productor[8]) and imperfections in the crystal structure. Transmission spectra of the amorphous or polycrystalline areas is free of the respective

[8]MicroParticlesGmbH.

stop-bands.

Though the obtained results are relatively modest compared to the advances in the respective field, the ability to manipulate the colloids assembly and to exploit the potential provided was encouraging for frontally attacking the domain[9]. 2D colloidal masks provides various ways of patterning vast surface areas with diverse functional nano-architectures that were and are to be further studied. Arrays of nanodiscs and oriented elliptical nanostructures, arrays of nanodisc pairs, nanocones shown to be excellent SERS substrates, and optically resonant nanodiscs embedded in a surrounding matrix, mono- and multi-layered SRR's are only few architectures to be cited that could be fabricated by physical deposition using shadow colloidal masking. Combined with RIE, simple pathways for realization of nanostructured or anti-reflective surfaces and 2D or 3D photonic crystals could be envisioned[10]. And many other ways to get usefulness of these structures are to be developed. As for the 3D assemblies, options are multiple as well. Controlled deposition, 3D defect engineering or inverting opals with "smart nano-materials" for intelligent optoelectronic devices are envisioned as future work. We are only at the beginning and as many people working in the field of photonic devices say - *the future looks bright.*

[9] After lots of unsuccessful trials in characterizing PMMA, AAO or PANI photonic crystals, it provided a great personal satisfaction the fabrication of the respective photonic crystals and the observation of a prohibited optical band making them nicely colored.

[10] A present study direction is to use a monolayered colloidal mask for 3D RIE of photonic structures in silicon operating in the near-infrared.

Conclusions and perspectives

> Nu scriem pentru că avem ceva de spus ci scriem pentru că simţim nevoia să spunem ceva.
>
> *Emil Cioran*

The main scientific outcomes in this thesis concern the advanced nanoengineering of porous materials for emerging optoelectronic technologies. The primary specific aim was bridging the gap between the nanoelectronic and nanophotonic applications; porous materials are excellent candidates for such innovative devices. The morphology of porous materials provides an intrinsic way for the control of the flow of light and at the same time an irreplaceable route for nanoscale structuring. Although, their co-integration seems obvious, the major obstacle is our technological incapability of processing reliably these materials to simultaneously exploit both functionalities. Our results may provide a starting point for further advances.

We showed how bulk silicon and aluminum can be fully processed to obtain cross-bar latches with cores composed of single, template-embedded nanowires. We demonstrated that statistical processing provides a simple and convenient way to resolve single features within nanoporous templates. By adjusting only the size of the lithographic mask, precise control over the patterning resolution can be achieved without any complex preliminary analysis or overlay alignment. The controllable yield is outstanding for advancing the design of the next generation defect-tolerant computer architectures. Although we focused on the phenomenology and on primary technological implications of the statistical patterning, the potential provided by this method is much broader. Statistical patterning can be extended to any processing approach that reduces to overlapping a given item with a nanoporous material.

If advanced processing of mass fabricated nanotemplates may look to heavy to handle, we proposed a *one-by-one* approach for individual processing of nanostructures providing single nanowire cross-bar el-

ements. The exemplification was done using polyaniline, a prototypical conjugated polymer that definitely settled the concept of synthetic metals. While the polyaniline is often considered the counterpart of the silicon in organic electronics and a plethora of macro and mesoscale systems having it at the heart of the operation are continuously developed, reliable nanoscale patterning of this material conspicuously misses. We showed how *ultimate* structuring of polyaniline nanostructures can be performed by converging top-down and bottom-up techniques (in occurrence, EBL and electroless polymerization of aniline on platinum). Single polyaniline nanowire patterning, growth, processing and device integration is demonstrated. The presented method will simplify and enhance the study of the extraordinary properties offered by the polyaniline derivatives at reduced dimensions and it may serve as a generic approach for nanoscale architecturing of other types of functional polymers.

As for the perspectives, many simple or difficult things could be done to continue this work. Downscaling and the study of the process scalability as well as switching form simple $1 \times n$ to $n \times n$ architectures are planned. More sophisticated materials than Ni could be envisioned to be grown and characterized using the AAO microprocessed devices. Multilayered magnetic nanowires with spin-transfer properties could be among the short term directions. Carbon nanotubes based materials are not to excluded as the field is exponentially evolving and the functionalities provided are endless. Also, the realization of $III - V$ light harvesting nanostructures embedded in highly ordered, photonic bandgap, alumina slabs for combined optoelectronic functioning seems not so far from our technological perspective. Statistical gambling is other possibility to further study and exploit. Statistical structuring reliability remains to be studied using other experimental approaches. As a free admittance to a *Millipede* is not granted to everyone, the co-integration of the cross-bar latch technology with the porous materials seems practically accessible. And not by using various masking protocols to access single structures, instead by directly criss-crossing properly dimensioned electrodes on both sides of a nanotemplate membrane. One possible option is to use block-copolymers thin films structured on top of arrays of word lines and then orthogonally define the second set of bit lines. Thus, the full block-copolymer lithography through stepwise processing seems possible now by statistically incorporating porous structures in-between two crisscrossed lamellae layers.

The fabricated 3D architectures (in AAO, PMMA, polyaniline, porous silicon and colloids) could be tested and improved to work properly as photonic structures. RDM-3D-EBL could be extended to other resist formulations to build even more complex 3D architectures and used to

template other materials than polyaniline. Reversely, the polyaniline confined growth could be done using other, more sophisticated templates. Moreover, the electroless polymerization is a scarcely studied synthesis protocol and there is a huge potential behind this approach. Doping physico-chemistry and functionalization in polyaniline can be now envisaged in configurations that where hard to access up to now. The provided simple fabrication schemes for the realization of single polyaniline nanowire based crossbar devices is also to be developed. Improving the ON/OFF ratio, write/erase speed as well as the retention and the endurance time characteristic of the erase-and-program cycles upon physico-chemical modification are among the primary tasks. Current-sensing AFM characterization of near Tb/inch^2 patterned structures, downscaling of the single-nanowire crossbar elements and building of multilevel architectures (for example, by exploiting the catalytic activity of a Pt or Pd top electrode that will serve subsequently as bottom electrode for the next circuit level) may provide lot of space for progress as well. And finally, we shall not forget that the ability to uniquely address well-structured, nanoscale amounts of matter is of great interest, at least, at the fundamental scientific level.

Appendix A

Process sheet

The Table below provides the detailed process sheet we used to micro- and nano-structure AAO templates. All of the fabrication steps, with the exception of those marked with asterisk are performed in a clean-room environment (implying the use of microelectronic grade chemicals and materials).

Step description	Products/Sub-steps	Parameters
Substrates	Si 3-inch wafers	<100>; 20 Ohm/sq
Standard cleaning	- H_2SO_4/H_2O_2 v:v=2:5 - H_2SO_4/H_2O_2 v:v=2:5 - HF 2% - rinser dryer	15 min boiling 5 min rinse water 15 min boiling 5 min rinse water 15 sec 5 min rinse water
Thermal oxidation	800 - 1000°C, O_2 post-annealing N_2	300 nm wet quality oxide
Inspection	Ellipsometry	check thickness
Metalization	5 nm Ti 50 nm Au	deposition rates $\sim$ 1 Å/s
Photolithography	- coating *AZ6612* thickness bake - exposure *i-line* mask - Development - rinser dryer	6600 rpm 1.1 μm 1 min at 110°C 200 - 350 mJ/cm^2 **AluminaSPR** - *AZ-MIF762* 1 min 1 min rinse water

Inspection	Optical microscope	check quality
Au wet-etch	- HNO_3/HCl v:v=1:3 *Aqua Regia* - *Acetone* - H_2SO_4/H_2O_2 v:v=2:5	1 - 3 min visual etch stop detection 5 min rinse water 10 min boiling remove photoresist remove Ti 5 - 10 sec 5 min rinse water
Inspection	Optical microscope	check quality
Al deposition* RF sputtering	- *Ar* plasma - Metal deposition 5 nm Ti 1 - 2 μm *Al*	pre-clean step deposition rates 1 Å/s 30 - 60 Å/s
Dicing	- Protective coating bake - Dicing	3000 rpm 1 min at 110°C chip size 6 × 10 mm
Al anodization*	- *Acetone* IPA N_2 - $H_2C_2O_4$ 0.3 M - pre-enlargement H_3PO_4 0.5 M N_2	strip protective resist rinse blown dry 2°C; 60 V; 5 min rinse water 70 nm pore diameter 30°C; 40 min; 5 min rinse water blown dry
Inspection	Optical microscope	check quality
Cleaning	*Acetone* *Acetone* IPA N_2	5 min boiling 1 min ultrasonic bath 5 min boling rinse blown dry
SiN deposition PECVD Oxford Plasmafab 100	- pre-clean N_2O - 100 sccm - SiN_x deposit SiH_4 5% - 500 sccm NH_3 - 2 sccm SiH_4 - 750 sccm	5 min; 20 W (13.56 MHz); 1 mTorr; thickness 400 nm 24 min; 20 W (13.56 MHz); 0.8 mTorr; 18 nm/min
Inspection	Ellipsometry	check thickness

Resist spin coating	$PMMA$ 950K 7% in *chlorobenzene* thickness	2000 rpm; 1800 rpm/s; 1 min $\sim$ 1 μm
Resist backing		2 min at 160°C over night at 60°C
EBL Al/AAO etch mask patterning		magnification: $\times$200 dose: 500 μC/cm^2 $I_{beam} \sim$ 20 nA
Development	- $MIBK/IPA$ v:v=1:3 - IPA - N_2	1 min 30 sec 30 sec rinse 5 min rinse water blown dry
Inspection	Optical microscope	check quality
SiN_x mask etch RIE-ICP Oxford Plasmafab 100	- pre-clean O_2 - 20 sccm - SiN_x etch SF_6 - 100 sccm	10 sec; 10 W (13.56 MHz); 10 mTorr 10 min; 20 W (13.56 MHz); 45 mTorr; 50 nm/min
Inspection	Optical microscope Ellipsometry	check quality 0 nm SiN_x and $\sim$ 1 μm $PMMA$
AAO/Al wet etch	- KOH 2 M etch - KOH 2 M rinse - KOH 2 M rinse - HF 2% etch	6 - 10 min 1 min 1 min 5 min rinse water 15 sec, strip Ti 5 min rinse water
PMMA striping	- *Acetone* - IPA - N_2	5 min boiling rinse blown dry
Inspection	Optical microscope Ellipsometry	check quality
SiN_x mask removal RIE-ICP Oxford Plasmafab 100	- SiN_x etch SF_6 - 100 sccm	9 min; 20 W (13.56 MHz); 45 mTorr; 50 nm/min
Inspection	Optical microscope Ellipsometry	check quality

Resist spin coating	- $PMMA(8.5)MAA$ 9% in $ethyl-lactate$ thickness bake each coating - $PMMA$ 950K 7% in *chlorobenzene* thickness bake total thickness soft bake	3 × at 3000 rpm; 1800 rpm/s; 1 min $\sim$ 600 nm each layer 1 min at 130°C 2000 rpm; 1800 rpm/s; 1 min $\sim$ 1 μm 1 min at 130°C $\sim$ 3 μm over night at 60°C
EBL SCL patterning	overexposed, with large negative undercut	magnification: ×2000 dose: 1000 μC/cm^2 $I_{beam} \sim$ 780 pA
Development	- $MIBK/IPA$ v:v=1:3 - IPA - N_2	2 min 30 sec 30 sec 1 min rinse water blown dry
Inspection	Optical microscope	check quality
Metal deposition SCL definition	- 2 nm Ti - 2 nm Ti - 20 nm Au - 20 nm Au	deposition rate $\sim$ 1 Å/s; +/- 45° tilt deposition rate $\sim$ 1 Å/s; +/- 45° tilt
Lift off	- *Acetone* - IPA - N_2	5 min boiling rinse blown dry
Inspection	Optical microscope Profilometer	check quality
SiN deposition PECVD Oxford Plasmafab 100	- pre-clean $N_2$0 - 100 sccm - SiN_x deposit SiH_4 5% - 500 sccm NH_3 - 2 sccm SiH_4 - 750 sccm	5 min; 20 W (13.56 MHz); 1 mTorr thickness 300 nm 17 min; 20 W (13.56 MHz); 0.8 mTorr; 18 nm/min
Inspection	Ellipsometry	check quality
Resist spin coating	- $PMMA$ 950K 2% in *chlorobenzene* thickness bake	3000 rpm; 1800 rpm/s; 1 min $\sim$ 200 nm 2 min at 160°C over night at 60°C

EBL selective plating mask definition	high resolution 40 - 150 nm dots	magnification: $\times$2000 dose: $\sim$ 220 μC/cm^2 $I_{beam} \sim$ 65 pA
Development	- $MIBK/IPA$ v:v=1:3 - IPA - N_2	1 min 30 sec 30 sec 1 min rinse water blown dry
SiN_x mask etch RIE-ICP Oxford Plasmafab 100	- pre-clean (ash) O_2 - 20 sccm - SiN_x etch SF_6 - 100 sccm	2 sec; 10 W (13.56 MHz); 10 mTorr 8 min; 20 W (13.56 MHz); 45 mTorr; 50 nm/min
Inspection	Optical microscope	check quality
Strip PMMA Emitech	- *Acetone* - O_2 ash 3 sccm	5 min boiling 3 mbar; 10 W 5 min
Electroplating*	- Post-enlargement H_3PO_4 0.5 M - Ni deposition $NiSO_4$ 0.5 M H_3BO_3 0.5 M	90 nm pore diameter 30°C; 5 min RT, 3-electrode cell Pt counter electrode $Ag/AgCl$ reference
Cleaning	- Acetone	5 min boiling
SiN_x mask strip RIE-ICP Oxford Plasmafab 100	- pre-clean (ash) O_2 - 20 sccm - SiN_x etch SF_6 - 100 sccm	30 sec; 10 W (13.56 MHz); 10 mTorr 10 min; 20 W (13.56 MHz); 45 mTorr; 50 nm/min
Inspection	Optical microscope Ellipsometry	check quality
Resist spin coating	- $PMMA(8.5)MAA$ 9% in $ethyl-lactate$ thickness bake each coating - $PMMA$ 950K 7% in *chlorobenzene* thickness bake total thickness soft bake	3 $\times$ at 3000 rpm; 1800 rpm/s; 1 min $\sim$ 600 nm each layer 1 min at 130°C 2000 rpm; 1800 rpm/s; 1 min $\sim$ 1 μm 1 min at 130°C $\sim$ 3 μm over night at 60°C

EBL top contact definition	overexposed, large negative undercut	magnification: $\times$200 dose: 1000 μC/cm^2 $I_{beam} \sim$ 3 nA
Development	- $MIBK/IPA$ v:v=1:3 - IPA - N_2	2 min 30 sec 30 sec rinse 5 min rinse water blown dry
Inspection	Optical microscope	check quality
Metal deposition top contact	- 1 μm Al, in steps of 20 nm	deposition rate $\sim$ 6 Å/s; +/- 45° tilt
Lift off	- *Acetone* - IPA - N_2	5 min boiling rinse blown dry
Inspection	Optical microscope	check quality

Table A.1: Process sheet for the micro- and nano-fabrication of AAO embedded single nanowire devices.

Appendix B

Statistical patterning simulation protocol

The experimental aspects of the statistical patterning behavior could be simply evaluated using a common image processing protocol. A detailed description is given bellow.

1. The surface morphology of AAO templates is analyzed using a SEM after the pre-enlargement step. The images (.tiff format) are acquired at a typical magnifications of × 10.000, × 20.000, × 30.000 and × 50.000. High-contrasting is enabled using low electron acceleration energies (1 - 5 keV). Areas with non-usual defects (dust, scratches, cracks, etc.) are avoided.

2. The picture is loaded in Igor Pro software (version 5.02) using the standard image loading procedure: `Data / Load waves / Load Image`. In the `Load Image` pop-up window, `File Type: .TIFF` is selected and, let's say, *original* for the `image name`. The image is loaded in the form of a 3D or 2D wave depending on the color mode. The pixel size in the loaded image is calibrated according to the acquired magnification. Next, the image data bar is removed.

3. If the image is loaded in other color format than gray scale, then it has to transformed for further analysis. For that, tape in the command line `ImageTransform rgb2gray original`. This operation applies a grays-scale transform if other color mode is present (caution: information can be lost during this transformation). A new image is created: *M_RGB2Gray*.

4. The next step is image binarization. For that, tape in the command line `ImageThreshold/C/T=value M_RGB2Gray`. A new image is created: *M_ImageThresh*. The `value` for the threshold operation is chosen to obtain a threshold correlation factor better than 0.8. The Figure B.1 shows an example of a gray-scale (left) and the corresponding binarized image (right). Eventually, a qualitative visual inspection is also performed to avoid loosing data during the binarization step. This operation is very important as the statistical patterning analysis is based on this type of plots.

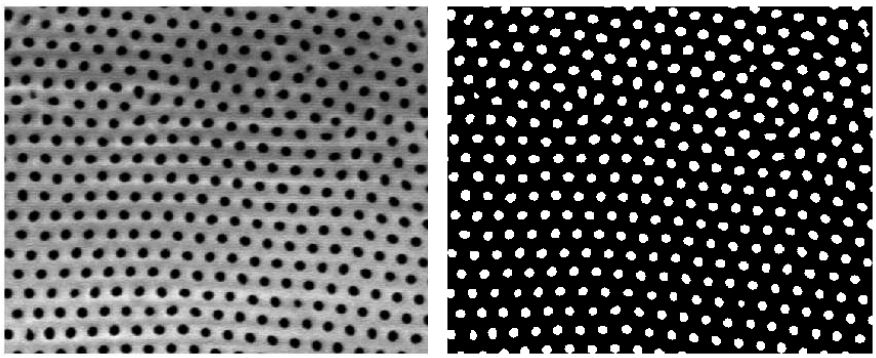

Figure B.1: The SEM image was acquired at × 50.000 magnification. The threshold correlation factor here is 0.87.

5. The simulation protocol is performed on the *M_ImageThresh* image. An automatic function was programmed for this operation. An example code is given bellow. For this case, the variable values are valid for a 1000 × 1000 pixels image. The variables (in units of pixels) and some of the operations have the following signification:

- `gridX` and `gridY` are the computation resolutions, maximum values are limited to the image size.

- `deltaD` and `gridD` are the increment and the number of iterations for the circular mask diameter; `D` being the actual size, here varying from `2` to `200`.

- `stat` is a 2D wave for storing the data in the form of probability *vs.* the mask diameter and the number of pores.

- `DrawOval left,top,right,bottom` draws an oval within the rectangle defined by `left, top, right, bottom` coordinates. Here, the size and the position are variable with the first and last value being

0,0,2,2 and 800,800,1000,1000. Other functions to draw various shapes in Igor are DrawPoly (used for the square mask definition) and DrawBezier.

- ImageGenerateROIMask operation creates a ROI mask on the active image, defined by the previously drawn shape.

- ImageAnalyzeParticles combined with the stats argument measures the particles in the image. Here, defined by the previous ROI. Results of the measurements are reported for all particles whose area exceeds the minimum area specified by the /A flag. This is the parameter which is used to set the counting threshold here being set to 0 (see main text for details). Another important parameter resulted from this operation is V_NumParticles - the number of particles that exceed the minimum area limit comprised in the ROI, or the *patterning resolution*.

The simulation code.

```
function stat()
variable i, j, D, gridX, gridY, n, k, deltaD, gridD
gridX=101
gridY=101
gridD=100
D=0
n=0
deltaD=2
make /O/N=(100, gridD) stat
stat=0
for (k=0; k<gridD; k+=1)
D=2+k*deltaD
  for (i=0; i<gridX; i+=1)
    for (j=0; j<gridY; j+=1)
      SetDrawLayer progFront
      SetDrawEnv xcoord= top,ycoord= left,fillpat=0
      DrawOval 8*i,8*j,8*i+D,8*j+D
      ImageGenerateROIMask/E=128/I=0 M_ImageThresh
      ImageAnalyzeParticles/Q/A=0/M=2/R=M_ROIMask stats M_ImageThresh
      stat[V_NumParticles][k]=stat[V_NumParticles][k]+1/(gridX*gridY)
      SetDrawLayer/K progFront
      n=n+1
    endfor
  endfor
endfor
end
```

The simulation time depends on the configuration of the PC, the size of the image and especially on the gridX, gridY and gridD values and may require few minutes up to several days for calculation.

Bibliography

[1] Vlad, A. *et al.* Controlled growth of single nanowires within a supported alumina template. *Nanotechnology* **17**, 4873 (2006).

[2] Vlad, A. *et al.* Nanowire-decorated microscale metallic electrodes. *Small* **4**, 557 (2008).

[3] Vlad, A. *et al.* Highly ordered conjugated polymer nanoarchitectures with three-dimensional structural control. *Nano Lett.* **9**, 2838 (2009).

[4] Binning, G., Rohrer, H., Gerber, C. & Weibel, E. Surface studies by scanning tunneling microscopy. *Phys. Rev. Lett.* **49**, 57 (1982).

[5] Eigler, D. M. & Schweizer, E. K. Positioning single atoms with a scanning tunneling microscope. *Nature* **344**, 524 (1990).

[6] Bachmann, G. Opportunities at the boundary from micro to nanotechnology. *MST News* **3**, 13 (2001).

[7] Lu, G. Q. & Zhao, X. S. *Nanoporous Materials - Science and Engineering* (Imperial College Press, London, 2005).

[8] Huo, Q. S., Margolese, D. I. & Stucky, G. D. Surfactant control of phases in the synthesis of mesoporous silica-based materials. *Chem. Mat.* **8**, 1147 (1996).

[9] Ying, J. Y., Mehnert, C. P. & Wong, M. S. Synthesis and applications of supramolecular-templated mesoporous materials. *Angew. Chem. - Intl. Ed.* **38**, 56 (1999).

[10] Corma, A. From microporous to mesoporous molecular sieve materials and their use in catalysis. *Chem. Rev.* **97**, 2373 (1997).

[11] Zhao, D. Y., Huo, Q. S., Feng, J. L., Chmelka, B. F. & Stucky, G. D. Nonionic triblock and star diblock copolymer and oligomeric

surfactant syntheses of highly ordered, hydrothermally stable, mesoporous silica structures. *J. Am. Chem. Soc.* **120**, 6024 (1998).

[12] Zhao, D. Y. *et al.* Triblock copolymer syntheses of mesoporous silica with periodic 50 to 300 angstrom pores. *Science* **279**, 548 (1998).

[13] Beck, J. S. *et al.* A new family of mesoporous molecular-sieves prepared with liquid-crystal templates. *J. Am. Chem. Soc.* **114**, 10834 (1992).

[14] Huo, Q. S., Leon, R., Petroff, P. M. & Stucky, G. D. Mesostructure design with gemini surfactants - supercage formation in a 3-dimensional hexagonal array. *Science* **268**, 1324 (1995).

[15] Moller, K. & Bein, T. Inclusion chemistry in periodic mesoporous hosts. *Chem. Mat.* **10**, 2950 (1998).

[16] Firouzi, A. *et al.* Cooperative organization of inorganic-surfactant and biomimetic assemblies. *Science* **267**, 1138 (1995).

[17] Wu, C. G. & Bein, T. Conducting polyaniline filaments in a mesoporous channel host. *Science* **264**, 1757 (1994).

[18] Wu, C. G. & Bein, T. Conducting carbon wires in ordered, nanometer-sized channels. *Science* **266**, 1013 (1994).

[19] Lodge, T. P. Block copolymers: Past successes and future challenges. *Macromol. Chem. Phys.* **204**, 265 (2003).

[20] Bates, F. S. & Fredrickson, G. H. Block copolymers - Designer soft materials. *Phys. Today* **52**, 32 (1999).

[21] Park, C., Yoon, J. & Thomas, E. L. Enabling nanotechnology with self assembled block copolymer patterns. *Polymer* **44**, 6725 (2003).

[22] Darling, S. B. Directing the self-assembly of block copolymers. *Prog. Polym. Sci.* **32**, 1152 (2007).

[23] Förster, S. & Plantenberg, T. From self-organizing polymers to nanohybrid and biomaterials. *Angew. Chem. Int. Ed.* **41**, 689 (2002).

[24] Guillet, P. *Metallo-Supramolecular Block Copolymers: From Synthesis to Smart Nanomaterials* (PhD thesis, Université catholique de Louvain, Louvain-la-Neuve, 2008).

[25] Lee, J. I. *et al.* Highly aligned ultrahigh density arrays of conducting polymer nanorods using block copolymer templates. *Nano Lett.* **8**, 2315 (2008).

[26] Thurn-Albrecht, T. *et al.* Ultrahigh-density nanowire arrays grown in self-assembled diblock copolymer templates. *Science* **290**, 2126 (2000).

[27] Silk, E. C. H. & Barnes, R. S. Examination of fission fragment tracks with an electron microscope. *Philos. Mag.* **4**, 970 (1959).

[28] Katz, R. & Kobetich, E. J. Formation of etchable tracks in dielectrics. *Phys. Rev.* **170**, 401 (1968).

[29] Piraux, L. *et al.* Giant magnetoresistance in magnetic multilayered nanowires. *Appl. Phys. Lett.* **65**, 2484 (1994).

[30] Blondel, A., Meier, J. P., Doudin, B. & Ansermet, J. P. Giant magnetoresistance of nanowires of multilayers. *Appl. Phys. Lett.* **65**, 3019 (1994).

[31] Liu, K., Nagodawithana, K., Searson, P. & Chien, C. Perpendicular giant magnetoresistance of multilayered Co/Cu nanowires. *Phys. Rev. B* **51**, 7381 (1995).

[32] Ferain, E. & Legras, R. Track-etch templates designed for micro- and nanofabrication. *Nucl. Instrum. Methods Phys. Res., Sect. B* **208**, 115 (2003).

[33] Xu, F., Wharton, J. & Martin, C. Template synthesis of carbon nanotubes with diamond-shaped cross sections. *Small* **3**, 1718 (2007).

[34] Li, J. L., Gershow, M., Stein, D., Brandin, E. & Golovchenko, J. A. DNA molecules and configurations in a solid-state nanopore microscope. *Nat. Mater.* **2**, 611 (2003).

[35] Dekker, C. Solid-state nanopores. *Nat. Nanotechnol.* **2**, 209 (2007).

[36] Joannopoulos, J. D., Johnson, S. G., Winn, J. N. & Meade, R. D. *Photonic crystals - Molding the flow of light* (Princeton University Press, Princeton, 2007).

[37] Novotny, L. & Hecht, B. *Principles of nano-optics* (Cambridge University Press, 2006).

[38] Johnson, S. G. & Joannopoulos, J. Block-iterative frequency-domain methods for Maxwell's equations in a planewave basis. *Opt. Express* **8**, 173 (2001).

[39] Poborchii, V. V., Tada, T. & Kanayama, T. Photonic-band-gap properties of two-dimensional lattices of *Si* nanopillars. *J. Appl. Phys.* **91**, 3299 (2002).

[40] Wang, D. Y. & Caruso, F. Fabrication of polyaniline inverse opals via templating ordered colloidal assemblies. *Adv. Mater.* **13**, 350 (2001).

[41] Johnson, S. G., Fan, S., Villeneuve, P. R., Joannopoulos, J. D. & Kolodziejski, L. A. Guided modes in photonic crystal slabs. *Phys. Rev. B* **60**, 5751 (1999).

[42] Nakamura, S., Saito, M., Huang, L. F., Miyagi, M. & Wada, K. Infrared optical-constants of anodic alumina films with micropore arrays. *Jpn. J. Appl. Phys. Part 1* **31**, 3589 (1992).

[43] Choi, J. *et al.* Perfect two-dimensional porous alumina photonic crystals with duplex oxide layers. *J. Appl. Phys.* **94**, 4757 (2003).

[44] Choi, J. *et al.* Large-area porous alumina photonic crystals via imprint method. *Mat. Res. Soc. Symp. Proc.* **722**, 417 (2002).

[45] Potyrailo, R. A. *et al.* Morpho butterfly wing scales demonstrate highly selective vapour response. *Nat. Photonics* **1**, 123 (2007).

[46] Vukusic, P., Sambles, J. R., Lawrence, C. R. & Wootton, R. J. Quantified interference and diffraction in single Morpho butterfly scales. *Proc. R. Soc. Lond. B* **266**, 1403 (1999).

[47] Kustandi, T. S., Low, H. Y., Teng, J. H., Rodriguez, I. & Yin, R. Mimicking domino-like photonic nanostructures on butterfly wings. *Small* **5**, 574 (2009).

[48] Ho, K. M., Chan, C. T. & Soukoulis, C. M. Existence of a photonic gap in periodic dielectric structures. *Phys. Rev. Lett.* **65**, 3152 (1990).

[49] Yablonovitch, E., Gmitter, T. J. & Leung, K. M. Photonic band-structure - the face-centered-cubic case employing nonspherical atoms. *Phys. Rev. Lett.* **67**, 2295 (1991).

[50] Ho, K. M., Chan, C. T., Soukoulis, C. M., Biswas, R. & Sigalas, M. Photonic band-gaps in 3-dimensions - new layer-by-layer periodic structures. *Solid State Comm.* **89**, 413 (1994).

[51] Sözüer, H. S. & Dowling, J. P. Photonic band calculations for woodpile structures. *J. Mod. Opt.* **41**, 231 (1994).

[52] Vlasov, Y. A., Bo, X. Z., Sturm, J. C. & Norris, D. J. On-chip natural assembly of silicon photonic bandgap crystals. *Nature* **414**, 289 (2001).

[53] Maier, A. M. *Plasmonics - fundamentals and applications* (Springer, New York, 2007).

[54] Johnson, P. B. & Christy, R. W. Optical constants of the noble metals. *Phys. Rev. B* **6**, 4370 (1972).

[55] Vial, A., Grimault, A.-S., Macías, D., Barchiesi, D. & de la Chapelle, M. L. Improved analytical fit of gold dispersion: Application to the modeling of extinction spectra with a finite-difference time-domain method. *Phys. Rev. B* **71**, 085416 (2005).

[56] Lee, K. *et al.* Metallic transport in polyaniline. *Nature* **441**, 65 (2006).

[57] Ditlbacher, H., Krenn, J. R., Schider, G., Leitner, A. & Aussenegg, F. R. Two-dimensional optics with surface plasmon polaritons. *Appl. Phys. Lett.* **81**, 1762 (2002).

[58] Bozhevolnyi, S. I., Erland, J., Leosson, K., Skovgaard, P. M. W. & Hvam, J. M. Waveguiding in surface plasmon polariton band gap structures. *Phys. Rev. Lett.* **86**, 3008 (2001).

[59] Bozhevolnyi, S. I., Volkov, V. S., Devaux, E., Laluet, J. Y. & Ebbesen, T. W. Channel plasmon subwavelength waveguide components including interferometers and ring resonators. *Nature* **440**, 508 (2006).

[60] Nordlander, P. The Ring: A Leitmotif in Plasmonics. *ACS Nano* **3**, 488 (2009).

[61] Shelby, R. A., Smith, D. R. & Schultz, S. Experimental verification of a negative index of refraction. *Science* **292**, 77 (2001).

[62] Smith, D. R., Pendry, J. B. & Wiltshire, M. C. K. Metamaterials and negative refractive index. *Science* **305**, 788 (2004).

[63] Yen, T. J. *et al.* Terahertz magnetic response from artificial materials. *Science* **303**, 1494 (2004).

[64] Liu, N. *et al.* Three-dimensional photonic metamaterials at optical frequencies. *Nat. Mater.* **7**, 31 (2008).

[65] Liu, N., Liu, H., Zhu, S. & Giessen, H. Stereometamaterials. *Nat. Photon.* **3**, 157 (2009).

[66] Martin, C. R. Nanomaterials - a membrane-based synthetic approach. *Science* **266**, 1961 (1994).

[67] Piraux, L. *et al.* Template-grown $NiFe/Cu/NiFe$ nanowires for spin transfer devices. *Nano Lett.* **7**, 2563 (2007).

[68] Fusil, S. *et al.* Nanolithography based contacting method for electrical measurements on single template synthesized nanowires. *Nanotechnology* **16**, 2936 (2005).

[69] Antohe, V. A. *et al.* Nanowire-templated microelectrodes for high-sensitivity *pH* detection. *Appl. Phys. Lett.* **94**, 073118 (2009).

[70] Mallet, J., Yu-Zhang, K., Mátéfi-Tempfli, S., Mátéfi-Tempfli, M. & Piraux, L. Electrodeposited Co_xPt_{1-x} nanowires. *J. Phys. D: Appl. Phys.* **38**, 909 (2005).

[71] Ou, F. S., Shaijumon, M. M. & Ajayan, P. M. Controlled manipulation of giant hybrid inorganic nanowire assemblies. *Nano Lett.* **8**, 1853 (2008).

[72] Park, S., Lim, J. H., Chung, S. W. & Mirkin, C. A. Self-assembly of mesoscopic metal-polymer amphiphiles. *Science* **303**, 348 (2004).

[73] Tian, S. J., Wang, J. J., Jonas, U. & Knoll, W. Inverse opals of polyaniline and its copolymers prepared by electrochemical techniques. *Chem. Mater.* **17**, 5726 (2005).

[74] Meng, G. W., Jung, Y. J., Cao, A. Y., Vajtai, R. & Ajayan, P. M. Controlled fabrication of hierarchically branched nanopores, nanotubes, and nanowires. *Proc. Natl. Acad. Sci.* **102**, 7074 (2005).

[75] Su, Y. W., Wu, C. S., Chen, C. C. & Chen, C. D. Fabrication of two-dimensional arrays of $CdSe$ pillars using e-beam lithography and electrochemical deposition. *Adv. Mater.* **15**, 49 (2003).

[76] Guowen, M. *et al.* Ordered Ni nanowire tip arrays sticking out of the anodic aluminum oxide template. *J. Appl. Phys.* **97**, 64303 (2005).

[77] Pan, L. *et al.* Synthesis of polyaniline nanotubes with a reactive template of manganese oxide. *Adv. Mater.* **19**, 461 (2007).

[78] Li, G. C. & Zhang, Z. K. Synthesis of dendritic polyaniline nanofibers in a surfactant gel. *Macromolecules* **37**, 2683 (2004).

[79] Wijnhoven, J. E. G. J. & Vos, W. L. Preparation of photonic crystals made of air spheres in titania. *Science* **281**, 802 (1998).

[80] Reddy, A. L. M., Shaijumon, M. M., Gowda, S. R. & Ajayan, P. M. Coaxial MnO_2/Carbon Nanotube Array Electrodes for High-Performance Lithium Batteries. *Nano Lett.* **9**, 1002 (2009).

[81] Shaijumon, M. M., Ou, F. S., Ci, L. & Ajayan, P. M. Synthesis of hybrid nanowire arrays and their application as high power supercapacitor electrodes. *Chem. Comm.* 2373 (2008).

[82] Johansson, A., Widenkvist, E., Lu, J., Boman, M. & Jansson, U. Fabrication of high-aspect-ratio Prussian blue nanotubes using a porous alumina template. *Nano Lett.* **5**, 1603 (2005).

[83] O'Carroll, D., Iacopino, D. & Redmond, G. Luminescent conjugated polymer nanowire Y-junctions with on-branch molecular anisotropy. *Adv. Mater.* **20**, 1 (2008).

[84] Lee, W. *et al.* Individually addressable epitaxial ferroelectric nanocapacitor arrays with near Tb inch^{-2} density. *Nat. Nanotechnol.* **3**, 402 (2008).

[85] Arsenault, A. C., Puzzo, D. P., Manners, I. & Ozin, G. A. Photonic-crystal full-colour displays. *Nat. Photonics* **1**, 468 (2007).

[86] Arsenault, A. C. *et al.* From color fingerprinting to the control of photoluminescence in elastic photonic crystals. *Nat. Mater.* **5**, 179 (2006).

[87] Robbie, K., Broer, D. J. & Brett, M. J. Chiral nematic order in liquid crystals imposed by an engineered inorganic nanostructure. *Nature* **399**, 764 (1999).

[88] Ai, S. F., Lu, G., He, Q. & Li, J. B. Highly flexible polyelectrolyte nanotubes. *J. Am. Chem. Soc.* **125**, 11140 (2003).

[89] Steinhart, M. *et al.* Liquid crystalline nanowires in porous alumina: geometric confinement versus influence of pore walls. *Nano Lett.* **5**, 429 (2005).

[90] Vinckx, W. *et al.* Vortex pinning in superconducting Nb thin films deposited on nanoporous alumina templates. *Eur. Phys. J. B* **53**, 199 (2006).

[91] Tang, C., Lennon, E. M., Fredrickson, G. H., Kramer, E. J. & Hawker, C. J. Evolution of block copolymer lithography to highly ordered square arrays. *Science* **322**, 429 (2008).

[92] Cheng, J. Y. *et al.* Formation of a cobalt magnetic dot array via block copolymer lithography. *Adv. Mater.* **13**, 1174 (2001).

[93] Zhang, Z. B., Sun, X. Z., Dresselhaus, M. S., Ying, J. Y. & Heremans, J. Electronic transport properties of single-crystal bismuth nanowire arrays. *Phys. Rev. B* **61**, 4850 (2000).

[94] Michotte, S., Mátéfi-Tempfli, S. & Piraux, L. Current-voltage characteristics of Pb and Sn granular superconducting nanowires. *Appl. Phys. Lett.* **82**, 4119 (2003).

[95] Soldano, C., Kar, S., Talapatra, S., Nayak, S. & Ajayan, P. M. Detection of Nanoscale Magnetic Activity Using a Single Carbon Nanotube. *Nano Lett.* **8**, 4498 (2008).

[96] Toimil-Molares, M. E. *et al.* Electrical characterization of electrochemically grown single copper nanowires. *Appl. Phys. Lett.* **82**, 2139 (2003).

[97] Zhong, Z. H., Wang, D. L., Cui, Y., Bockrath, M. W. & Lieber, C. M. Nanowire crossbar arrays as address decoders for integrated nanosystems. *Science* **302**, 1377 (2003).

[98] Hayamizu, Y. *et al.* Integrated three-dimensional microelectromechanical devices from processable carbon nanotube wafers. *Nat. Nanotechnol.* **3**, 289 (2008).

[99] Smith, P. A. *et al.* Electric-field assisted assembly and alignment of metallic nanowires. *Appl. Phys. Lett.* **77**, 1399 (2000).

[100] Kovtyukhova, N. I., Kelley, B. K. & Mallouk, T. E. Coaxially gated in-wire thin-film transistors made by template assembly. *J. Am. Chem. Soc.* **126**, 12738 (2004).

[101] Pauzauskie, P. J. *et al.* Optical trapping and integration of semiconductor nanowire assemblies in water. *Nat. Mater.* **5**, 97 (2006).

[102] Hangarter, C. M., Rheem, Y., Yoo, B., Yang, E.-H. & Myung, N. V. Hierarchical magnetic assembly of nanowires. *Nanotechnology* **18**, 205305 (2007).

[103] Gence, L. *et al.* Structural and electrical characterization of hybrid metal-polypyrrole nanowires. *Phys. Rev. B* **76**, 115415 (2007).

[104] Zhang, Z. B., Sun, X. Z., Dresselhaus, M. S., Ying, J. Y. & Heremans, J. P. Magnetotransport investigations of ultrafine single-crystalline bismuth nanowire arrays. *Appl. Phys. Lett.* **73**, 1589 (1998).

[105] Chtanko, N., Toimil Molares, M. E., Cornelius, T., Dobrev, A. & Neumann, R. Etched single-ion-track templates for single nanowire synthesis. *J. Phys. Chem. B* **108**, 9950 (2004).

[106] Park, H.-G. *et al.* A wavelength-selective photonic-crystal waveguide coupled to a nanowire light source. *Nat. Photon.* **2**, 622 (2008).

[107] Vila, L., Piraux, L., George, J. M. & Faini, G. Multiprobe magnetoresistance measurements on isolated magnetic nanowires. *Appl. Phys. Lett.* **80**, 3805 (2002).

[108] Tanase, M., Silevitch, D. M., Chien, C. L. & Reich, D. H. Magnetotransport properties of bent ferromagnetic nanowires. *J. Appl. Phys.* **93**, 7616 (2003).

[109] Huang, Y. *et al.* Logic gates and computation from assembled nanowire building blocks. *Science* **294**, 1313 (2001).

[110] Cui, Y., Wei, Q. Q., Park, H. K. & Lieber, C. M. Nanowire nanosensors for highly sensitive and selective detection of biological and chemical species. *Science* **293**, 1289 (2001).

[111] Cui, Y. & Lieber, C. M. Functional nanoscale electronic devices assembled using silicon nanowire building blocks. *Science* **291**, 851 (2001).

[112] Huang, Y., Duan, X. F., Wei, Q. Q. & Lieber, C. M. Directed assembly of one-dimensional nanostructures into functional networks. *Science* **291**, 630 (2001).

[113] Duan, X. F., Huang, Y., Cui, Y., Wang, J. F. & Lieber, C. M. Indium phosphide nanowires as building blocks for nanoscale electronic and optoelectronic devices. *Nature* **409**, 66 (2001).

[114] Hedberg, J., Dong, L. F. & Jiao, J. Air flow technique for large scale dispersion and alignment of carbon nanotubes on various substrates. *Appl. Phys. Lett.* **86** (2005).

[115] Bentley, A. K., Trethewey, J. S., Ellis, A. B. & Crone, W. C. Magnetic manipulation of copper-tin nanowires capped with nickel ends. *Nano Lett.* **4**, 487 (2004).

[116] Huang, Y., Duan, X. F. & Lieber, C. M. Nanowires for integrated multicolor nanophotonics. *Small* **1**, 142 (2005).

[117] Li, Y., Qian, F., Xiang, J. & Lieber, C. M. Nanowire electronic and optoelectronic devices. *Mater. Today* **9**, 18 (2006).

[118] Zhou, X. *et al.* Color detection using chromophore-nanotube hybrid devices. *Nano Lett.* **9**, 1028 (2009).

[119] Hu, Z. *et al.* High-throughput fabrication of organic nanowire devices with preferential internal alignment and improved performance. *Nano Lett.* **7**, 3639 (2007).

[120] Asakawa, K. *et al.* Photonic crystal and quantum dot technologies for all-optical switch and logic device. *New Journal of Physics* **8** (2006).

[121] Matthias, S., Muller, F., Jamois, C., Wehrspohn, R. B. & Gosele, U. Large-area three-dimensional structuring by electrochemical etching and lithography. *Adv. Mater.* **16**, 2166 (2004).

[122] Gruning, U., Lehmann, V., Ottow, S. & Busch, K. Macroporous silicon with a complete two-dimensional photonic band gap centered at 5 μm. *Appl. Phys. Lett.* **68**, 747 (1996).

[123] Seo, M. & Yamaya, T. Selective formation of porous layer on n-type InP by anodic etching combined with scratching. *Electrochem. Acta* **51**, 787 (2005).

[124] Choi, J. S., Wehrspohn, R. B., Lee, J. & Gosele, U. Anodization of nanoimprinted titanium: a comparison with formation of porous alumina. *Electrochem. Acta* **49**, 2645 (2004).

[125] Macak, J. M., Sirotna, K. & Schmuki, P. Self-organized porous titanium oxide prepared in Na_2SO_4/NaF electrolytes. *Electrochem. Acta* **50**, 3679 (2005).

[126] Sieber, I., Hildebrand, H., Friedrich, A. & Schmuki, P. Formation of self-organized niobium porous oxide on niobium. *Electrochem. Comm.* **7**, 97– (2005).

[127] Tsuchiya, H. & Schmuki, P. Self-organized high aspect ratio porous hafnium oxide prepared by electrochemical anodization. *Electrochem. Comm.* **7**, 49 (2005).

[128] Shin, H., Dong, J. & Liu, M. Porous tin oxides prepared using an anodic oxidation process. *Adv. Mater.* **16**, 237 (2004).

[129] Keller, F., Hunter, M. S. & Robinson, D. L. Structural features of oxide coatings on aluminum. *J. Electrochem. Soc.* **100**, 411 (1953).

[130] Thompson, G., Furneaux, R., Wood, G., Richardson, J. & Goode, J. Nucleation and growth of porous anodic films on aluminium. *Nature* **272**, 433 (1978).

[131] Furneaux, R. C., Rigby, W. R. & Davidson, A. P. The formation of controlled-porosity membranes from anodically oxidized aluminum. *Nature* **337**, 147 (1989).

[132] Zhu, X., Li, D., Song, Y. & Xiao, Y. The study on oxygen bubbles of anodic alumina based on high purity aluminum. *Mater. Lett.* **59**, 3160 (2005).

[133] Crossland, A. *et al.* Residual flaws due to formation of oxygen bubbles in anodic alumina. *Corros. Sci.* **41**, 1945 (1999).

[134] Shimizu, K., Habazaki, H., Skeldon, P., Thompson, G. & Wood, G. Role of metal ion impurities in generation of oxygen gas within anodic alumina. *Electrochem. Acta* **47**, 1225 (2002).

[135] Diggle, J. W., Downie, T. C. & Goulding, C. W. Anodic oxide films on aluminum. *Chem. Rev.* **69**, 365 (1969).

[136] Surganov, V., Morgen, P., Nielsen, J. G., Gorokh, G. & Mozalev, A. Study of the initial-stage of aluminum anodization in malonic-acid solution. *Electrochem. Acta* **32**, 1125 (1987).

[137] Surganov, V. F. & Gorokh, G. G. Anodic oxide cellular structure formation on aluminum films in tartaric acid electrolyte. *Mater. Lett.* **17**, 121 (1993).

[138] Ono, S., Saito, M., Ishiguro, M. & Asoh, H. Controlling factor of self-ordering of anodic porous alumina. *J. Electrochem. Soc.* **151**, B473 (2004).

[139] Mozalev, A., Mozaleva, I., Sakairi, M. & Takahashi, H. Anodic film growth on Al layers and $Ta - Al$ metal bilayers in citric acid electrolytes. *Electrochem. Acta* **50**, 5065 (2005).

[140] Chu, S. Z. *et al.* Large-scale fabrication of ordered nanoporous alumina films with arbitrary pore intervals by critical-potential anodization. *J. Electrochem. Soc.* **153**, B384 (2006).

[141] Zhou, X., Thompson, G. & Potts, G. Effects of chromic acid anodizing of aluminium on adhesion and durability of bonded joints. *Trans. I.M.F.* **78**, 210 (2000).

[142] Wang, H. & Wang, H. Analysis on porous aluminum anodic oxide film formed in Re-OA-H_3PO_4 solution. *Mater. Chem. Phys.* **97**, 213 (2006).

[143] Jia, Y. *et al.* Preparation and characteristics of well-aligned macroporous films on aluminum by high voltage anodization in mixed acid. *Surf. Coat. Technol.* **201**, 513 (2006).

[144] Mozalev, A., Poznyak, A., Mozaleva, I. & Hassel, A. The voltage-time behaviour for porous anodizing of aluminium in a fluoride-containing oxalic acid electrolyte. *Electrochem. Commun.* **3**, 299 (2001).

[145] Shingubara, S., Morimoto, K., Sakaue, H. & Takahagi, T. Self-organization of a porous alumina nanohole array using a sulfuric/oxalic acid mixture as electrolyte. *Electrochem. Solid State Lett.* **7**, E15 (2004).

[146] Thompson, G. Porous anodic alumina: Fabrication, characterization and applications. *Thin Solid Films* **297**, 192 (1997).

[147] Arrowsmith, D. J. & Moth, D. A. Chromic-acid anodizing of aluminum. *Trans. I.M.F.* **64**, 91 (1986).

[148] Sulka, G. D. & Jaskula, M. Defects analysis in self-organized nanopore arrays formed by anodization of aluminium at various temperatures. *J. Nanosci. Nanotechnol.* **6**, 3803 (2006).

[149] Palibroda, E., Farcas, T. & Lupsan, A. A new image of porous aluminum-oxide. *Mater. Sci. Eng. B* **32**, 1 (1995).

[150] O'Sullivan, J. P. & Wood, G. C. The morphology and mechanism of formation of porous anodic films on aluminium. *Proc. Roy. Soc. Lond. A: Math. Phys. Sci.* **317**, 511 (1970).

[151] Nielsch, K., Choi, J., Schwirn, K., Wehrspohn, R. B. & Gosele, U. Self-ordering regimes of porous alumina: The 10% porosity rule. *Nano Lett.* **2**, 677 (2002).

[152] Masuda, H. *et al.* Highly ordered nanochannel-array architecture in anodic alumina. *Appl. Phys. Lett.* **71**, 2770 (1997).

[153] Eftekhari, A. *Nanostructured Materials in Electrochemistry* (Wiley-VCH, 2008).

[154] Lee, W., Ji, R., Goesele, U. & Nielsch, K. Fast fabrication of long-range ordered porous alumina membranes by hard anodization. *Nat. Mater.* **5**, 741 (2006).

[155] Tian, M. L. *et al.* Penetrating the oxide barrier in situ and separating freestanding porous anodic alumina films in one step. *Nano Lett.* **5**, 697 (2005).

[156] Hale, G. Deposition from an R.F. induction source of aluminum-copper alloys onto laminated polyimide substrates **63**, 95 (1979).

[157] Mattsson, L., Le Page, Y. H. & Ericson, F. Real-time study of migration in aluminum films by means of subangstrom-sensitive scattering and profiling methods. *Thin Solid Films* **198**, 149 (1991).

[158] Matsumoto, F., Harada, M., Nishio, K. & Masuda, H. Nanometer-scale patterning of DNA in controlled intervals on a gold-disk array fabricated using ideally ordered anodic porous alumina. *Adv. Mater.* **17**, 1609 (2005).

[159] Antohe, V. A. *et al.* A versatile method to grow localized arrays of nanowires for highly sensitive capacitive devices. *J. Optoelectron. Adv. Mater.* **10**, 2936 (2008).

[160] Li, A., Muller, F., Birner, A., Nielsch, K. & Gosele, U. Fabrication and microstructuring of hexagonally ordered two-dimensional nanopore arrays in anodic alumina. *Adv. Mater.* **11**, 483 (1999).

[161] Ackaert, J. *et al.* MIMC reliability and electrical behavior defined by a physical layer property of the dielectric. *Microelectron. Reliability* **48**, 1553 (2008).

[162] Vamvakas, V., Vourdas, N. & Gardelis, S. Optical characterization of *Si*-rich silicon nitride films prepared by low pressure chemical vapor deposition. *Microelectron. Reliability* **47**, 794 (2007).

[163] Mátéfi-Tempfli, S., Mátéfi-Tempfli, M. & Piraux, L. Characterization of nanopores ordering in anodic alumina. *Thin Solid Films* **516**, 3735 (2008).

[164] Kuekes, P. J., Stewart, D. R. & Williams, R. The crossbar latch: Logic value storage, restoration, and inversion in crossbar circuits. *J. Appl. Phys.* **97** (2005).

[165] Masuda, H. *et al.* Square and triangular nanohole array architectures in anodic alumina. *Adv. Mater.* **13**, 189 (2001).

[166] Pomot, C., Mahi, B., Petit, B., Arnal, Y. & Pelletier, J. Anisotropic etching of silicon using an SF_6/Ar microwave multipolar plasma. *J. Vac. Sci. Technol. B* **4**, 1 (1986).

[167] Vettiger, P. *et al.* The "Millipede" - More than one thousand tips for future AFM data storage. *IBM J. Res. Develop.* **44**, 323 (2000).

[168] Heath, J. R., Kuekes, P. J., Snider, G. S. & Williams, R. S. A defect-tolerant computer architecture: Opportunities for nanotechnology. *Science* **280**, 1716 (1998).

[169] Green, J. E. *et al.* A 160-kilobit molecular electronic memory patterned at 10^{11} bits per square centimetre. *Nature* **445**, 414 (2007).

[170] Beckman, R., Johnston-Halperin, E., Luo, Y., Green, J. E. & Heath, J. R. Bridging dimensions: Demultiplexing ultrahigh-density nanowire circuits. *Science* **310**, 465 (2005).

[171] Melosh, N. A. *et al.* Ultrahigh-density nanowire lattices and circuits. *Science* **300**, 112 (2003).

[172] Gracias, D. H., Tien, J., Breen, T. L., Hsu, C. & Whitesides, G. M. Forming electrical networks in three dimensions by self-assembly. *Science* **289**, 1170 (2000).

[173] Collier, C. P. *et al.* Electronically configurable molecular-based logic gates. *Science* **285**, 391 (1999).

[174] Wu, W. *et al.* One-kilobit cross-bar molecular memory circuits at 30-nm half-pitch fabricated by nanoimprint lithography. *Appl. Phys. A Mater. Sci. & Proc.* **80**, 1173 (2005).

[175] Chen, Y. *et al.* Nanoscale molecular-switch crossbar circuits. *Nanotechnology* **14**, 462 (2003).

[176] Snider, G. Computing with hysteretic resistor crossbars. *Appl. Phys. A Mater. Sci. & Proc.* **80**, 1165 (2005).

[177] Dong, Y., Yu, G., McAlpine, M. C., Lu, W. & Lieber, C. M. *Si*/a-*Si* core/shell nanowires as nonvolatile crossbar switches. *Nano Lett.* **8**, 386 (2008).

[178] Luo, Y. *et al.* Two-dimensional molecular electronics circuits. *Chem. Phys. Chem.* **3**, 519 (2002).

[179] Lee, W., Alexe, M., Nielsch, K. & Gosele, U. Metal membranes with hierarchically organized nanotube arrays. *Chem. Mater.* **17**, 3325 (2005).

[180] Wi, J.-S. *et al.* Fabrication of silicon nanopillar teradot arrays by electron-beam patterning for nanoimprint molds. *Small* **4**, 2118 (2008).

[181] Yang, X. *et al.* Challenges in 1 teradot/inch^2 patterning using electron beam lithography for bit-patterned media. *J. Vac. Sci. & Techn. B* **25**, 2202 (2007).

[182] Hatzakis, M. Electron resists for microcircuit and mask production. *J. Electrochem. Soc.* **116**, 1033 (1969).

[183] Rai-Choudhury, P. *Handbook of Microlithography, micromachining, and microfabrication. Volume 1: Microlithography* (The international society for optical engineering, Bellingham, 1997).

[184] Chang, T. H. P. Proximity effect in electron-beam lithography. *J. Vac. Sci. & Technol. B* **12**, 1271 (1975).

[185] Drouin, D. *et al.* Casino v2.42 - a fast and easy-to-use modeling tool for scanning electron microscopy and microanalysis users. *Scanning* **29**, 92 (2007).

[186] Casnati, E., Tartari, A. & Baraldi, C. An empirical approach to *k*-shell ionisation cross section by electrons. *J. Phys. B: At. Mol. Phys.* **15**, 155 (1982).

[187] Tan, Z., Xia, Y., Liu, X. & Zhao, M. An empirical stopping power relationship for low-energy electrons. *Scanning* **11**, 176 (1989).

[188] Press, W. H., Teukolsky, S. A., Vetterling, W. T. & Flannery, B. P. *Numerical Recipes - The art of scientific computing.* First edition (Cambridge University Press, New York, 1986).

[189] Koller, D. M. *et al.* Direct fabrication of micro/nano fluidic channels by electron beam lithography. *Microelec. Eng.* (In Press).

[190] Parikh, M. & Kyser, D. F. Energy deposition functions in electron resist films on substrates. *J. Appl. Phys.* **50**, 1104 (1979).

[191] Yin, H.-L., Hu, J. & Yu, C.-S. The study on 3D electron beam lithography for sub-micrometer diffractive optics. *Optical MEMS and Nanophotonics, IEEE/LEOS Int. Conf.* 149 (2007).

[192] Oppliger, Y. *et al.* One-step 3D shaping using a gray-tone mask for optical and microelectronic applications. *Microelec. Eng.* **23**, 449 (1994).

[193] Wong, W. H. & Pun, E. Y. B. Exposure characteristics and three-dimensional profiling of SU-8C resist using electron beam lithography. *J. Vac. Sci. & Technol. B* **19**, 732 (2001).

[194] Takano, H. *et al.* Electron-beam/ultraviolet hybrid exposure combined with novel bilayer resist system for a 0.15 μm T-shaped gate fabrication process. *J. Vac. Sci. & Technol. B* **14**, 3483 (1996).

[195] Cui, B. & Veres, T. High resolution electron beam lithography of PMGI using solvent developers. *Microelec. Eng.* **85**, 810 (2008).

[196] Haller, I., Hatzakis, M. & Srinivasan, R. High-resolution positive resists for electron-beam exposure. *IBM J. Res. Develop.* **12**, 251 (1968).

[197] Bernstein, G. H. & Hill, D. A. On the attainment of optimum developer parameters for PMMA resist. *Superlattices and Microstructures* **11**, 237 (1992).

[198] der Gaag, B. P. V. & Scherer, A. Microfabrication below 10 nm. *Appl. Phys. Lett.* **56**, 481 (1990).

[199] Fischbein, M. D. & Drndic, M. Nanogaps by direct lithography for high-resolution imaging and electronic characterization of nanostructures. *Appl. Phys. Lett.* **88**, 063116 (2006).

[200] Zandbergen, H. W. *et al.* Sculpting nanoelectrodes with a transmission electron beam for electrical and geometrical characterization of nanoparticles. *Nano Lett.* **5**, 549 (2005).

[201] Ogawa, S. P., Imada, M., Yoshimoto, S., Okano, M. & Noda, S. Control of light emission by 3D photonic crystals. *Science* **305**, 227 (2004).

[202] Parker, A. R. & Townley, H. E. Biomimetics of photonic nanostructures. *Nat. Nanotechnol.* **2**, 347 (2007).

[203] Nie, Z. & Kumacheva, E. Patterning surfaces with functional polymers. *Nat. Mater.* **7**, 277 (2008).

[204] Li, C. *et al.* Fabrication of three-dimensional microfluidic channels in glass by femtosecond pulses. *Opt. Comm.* **282**, 657 (2009).

[205] Kumar, C. S. S. R., Hormes, J. & Leuschner, C. *Nanofabrication Towards Biomedical Applications: Techniques, Tools, Applications, and Impact* (Wiley-VCH, Oxford, 1963).

[206] Bärsch, N., Körber, K., Ostendorf, A. & Tönshoff, K. Ablation and cutting of planar silicon devices using femtosecond laser pulses. *Appl. Phys. A* **77**, 237 (2003).

[207] Lehmann, O. & Stuke, M. Laser-driven movement of 3-dimensional microstructures generated by laser rapid prototyping. *Science* **270**, 1644 (1995).

[208] Cumpston, B. H. *et al.* Two-photon polymerization initiators for three-dimensional optical data storage and microfabrication. *Nature* **398**, 51 (1999).

[209] Scrimgeour, J. *et al.* Three-dimensional optical lithography for photonic microstructures. *Adv. Mater.* **18**, 1557 (2006).

[210] Jeon, S. *et al.* Fabricating complex three-dimensional nanostructures with high-resolution conformable phase masks. *Proc. Natl. Acad. Sci.* **101**, 12428 (2004).

[211] Henke, W., Hoppe, W., Quenzer, H., Staudt-Fischbach, P. & Wagner, B. Simulation assisted design of processes for gray-tone lithography. *Microelec. Eng.* **27**, 267 (1995).

[212] Daschner, W., Long, P., Stein, R., Wu, C. & Lee, S. H. General aspheric refractive micro-optics fabricated by optical lithography using a high energy beam sensitive glass gray-level mask. *J. Vac. Sci. & Technol. B* **14**, 3730 (1996).

[213] Yamazaki, K. & Namatsu, H. Two-axis-of-rotation drive system in electron-beam lithography apparatus for nanotechnology applications. *Microelec. Eng.* **73-74**, 85 (2004).

[214] Romanato, F. *et al.* Fabrication of 3D metallic photonic crystals by X-ray lithography. *Microelec. Eng.* **67-8**, 479 (2003).

[215] Cheng, C. C. & Scherer, A. Fabrication of photonic band-gap crystals. *J. Vac. Sci. & Technol. B* **13**, 2696 (1995).

[216] Toader, O. & John, S. Proposed square spiral microfabrication architecture for large three-dimensional photonic band gap crystals. *Science* **292**, 1133 (2001).

[217] Noda, S., Tomoda, K., Yamamoto, N. & Chutinan, A. Full three-dimensional photonic bandgap crystals at near-infrared wavelengths. *Science* **289**, 604 (2000).

[218] Hynninen, A.-P., Thijssen, J. H. J., Vermolen, E. C. M., Dijkstra, M. & Van Blaaderen, A. Self-assembly route for photonic crystals with a bandgap in the visible region. *Nat. Mater.* **6**, 202 (2007).

[219] Velev, O. D., Lenhoff, A. M. & Kaler, E. W. A class of microstructured particles through colloidal crystallization. *Science* **287**, 2240 (2000).

[220] Fustin, C. A., Glasser, G., Spiess, H. W. & Jonas, U. Site-selective growth of colloidal crystals with photonic properties on chemically patterned surfaces. *Adv. Mater.* **15**, 1025 (2003).

[221] Rinne, S. A., Garcia-Santamaria, F. & Braun, P. V. Embedded cavities and waveguides in three-dimensional silicon photonic crystals. *Nat. Photon.* **2**, 52 (2008).

[222] Fredriksson, H. *et al.* Hole-mask colloidal lithography. *Adv. Mater.* **19**, 4297 (2007).

[223] Forster, S. & Plantenberg, T. From self-organizing polymers to nanohybrid and biomaterials. *Angew. Chem. Int. Ed.* **41**, 689 (2002).

[224] Lee, W. *et al.* Structural engineering of nanoporous anodic aluminium oxide by pulse anodization of aluminium. *Nat. Nanotechnol.* **3**, 234 (2008).

[225] Caroff, P. *et al.* Controlled polytypic and twin-plane superlattices in III - V nanowires. *Nat. Nanotechnol.* **4**, 50 (2009).

[226] Dick, K. A. *et al.* Synthesis of branched nanotrees by controlled seeding of multiple branching events. *Nat. Mater.* **3**, 380 (2004).

[227] Hatzakis, M. PMMA copolymers as high sensitivity electron resists. *J. Vac. Sci. Technol.* **16**, 1984 (1979).

[228] Wu, C.-S., Lin, C.-F., Lin, H.-Y., Lee, C.-L. & Chen, C.-D. Polymer-based photonic crystals fabricated with single-step electron-beam lithography. *Adv. Mater.* **19**, 3052 (2007).

[229] Weitz, R. T., Harnau, L., Rauschenbach, S., Burghard, M. & Kern, K. Polymer nanofibers via nozzle-free centrifugal spinning. *Nano Lett.* **8**, 1187 (2008).

[230] Malzbender, J. & de With, G. Cracking and residual stress in hybrid coatings on float glass. *Thin Solid Films* **359**, 210 (2000).

[231] Pease, L. F., III, Deshpande, P., Wang, Y., Russel, W. B. & Chou, S. Y. Self-formation of sub-60-nm half-pitch gratings with large areas through fracturing. *Nat. Nanotechnol.* **2**, 545 (2007).

[232] Letheby, H. XXIX. - On the production of a blue substance by the electrolysis of sulphate of aniline. *J. Chem. Soc.* **15**, 161 (1862).

[233] Bolto, B. A., McNeill, R. & Weiss, D. E. Electronic conduction in polymers. iii. electronic properties of polypyrrole. *Aust. J. Chem.* **16**, 1090 (1963).

[234] McNeill, R., Weiss, D. E. & Willis, D. Electronic conduction in polymers. iv. polymers from imidazole and pyridine. *Aust. J. Chem.* **18**, 477 (1965).

[235] Bolto, B. A., Weiss, D. E. & Willis, D. Electronic conduction in polymers. v. aromatic semiconducting polymers. *Aust. J. Chem.* **18**, 487 (1965).

[236] McGinness, J., Corry, P. & Proctor, P. Amorphous semiconductor switching in melanins. *Science* **183**, 853 (1974).

[237] Nature Solid State Physics Correspondent. Semiconductors in the human body? *Nature* **248**, 475 (1974).

[238] Chiang, J. C. & MacDiarmid, A. G. Polyaniline - protonic acid doping of the emeraldine form to the metallic regime. *Synth. Met.* **13**, 193 (1986).

[239] Li, D., Huang, J. & Kaner, R. B. Polyaniline nanofibers: A unique polymer nanostructure for versatile applications. *Acc. Chem. Res.* **42**, 135 (2009).

[240] Gurunathan, K., Murugan, A. V., Marimuthu, R., Mulik, U. P. & Amalnerkar, D. P. Electrochemically synthesised conducting polymeric materials for applications toward technology in electronics, optoelectronics and energy storage devices. *Mater. Chem. and Phys.* **61**, 173 (1999).

[241] Spinks, G. M., Dominis, A. J., Wallace, G. G. & Tallman, D. E. Electroactive conducting polymers for corrosion control - part 2. ferrous metals. *J. Sol. State Electrochem.* **6**, 85 (2002).

[242] McQuade, D. T., Pullen, A. E. & Swager, T. M. Conjugated polymer-based chemical sensors. *Chem. Rev.* **100**, 2537 (2000).

[243] Cosnier, S. Biomolecule immobilization on electrode surfaces by entrapment or attachment to electrochemically polymerized films. A review. *Biosensors & Bioelectronics* **14**, 443 (1999).

[244] Malinauskas, A. Electrocatalysis at conducting polymers. *Synth. Met.* **107**, 75 (1999).

[245] Genies, E. M., Boyle, A., Lapkowski, M. & Tsintavis, C. Polyaniline - a historical survey. *Synth. Met.* **36**, 139 (1990).

[246] MacDiarmid, A. G. Synthetic metals: A novel role for organic polymers (Nobel lecture). *Angew. Chem. Int. Ed.* **40**, 2581 (2001).

[247] Kang, E. T., Neoh, K. G. & Tan, K. L. Polyaniline: A polymer with many interesting intrinsic redox states. *Prog. Polym. Sci.* **23**, 277 (1998).

[248] Inzelt, G., Pineri, M., Schultze, J. W. & Vorotyntsev, M. A. Electron and proton conducting polymers: recent developments and prospects. *Electrochimica Acta* **45**, 2403 (2000).

[249] Huang, J. X. & Kaner, R. B. A general chemical route to polyaniline nanofibers. *J. Am. Chem. Soc.* **126**, 851 (2004).

[250] Zhang, X. Y., Goux, W. J. & Manohar, S. K. Synthesis of polyaniline nanofibers by nanofiber seeding. *J. Am. Chem. Soc.* **126**, 4502 (2004).

[251] Li, W. G. & Wang, H. L. Oligomer-assisted synthesis of chiral polyaniline nanofibers. *J. Am. Chem. Soc.* **126**, 2278 (2004).

[252] Liang, L., Liu, J., Windisch, C. F., Exarhos, G. J. & Lin, Y. Direct assembly of large arrays of oriented conducting polymer nanowires. *Angew. Chem. Int. Ed.* **41**, 3665 (2002).

[253] Chiou, N.-R., Lui, C., Guan, J., Lee, L. J. & Epstein, A. J. Growth and alignment of polyaniline nanofibres with superhydrophobic, superhydrophilic and other properties. *Nat. Nanotechnol.* **2**, 354 (2007).

[254] Pinto, N. J., Carrión, P. & Quiñones, J. X. Electroless deposition of nickel on electrospun fibers of 2-acrylamido-2-methyl-1-propanesulfonic acid doped polyaniline. *Mater. Sci. Eng. A* **366**, 1 (2004).

[255] Surville, R. D., Jozefowicz, M., Yu, L. T., Pepichon, J. & Buvet, R. Electrochemical chains using protolytic organic semiconductors. *Electrochimica Acta* **13**, 1451 (1968).

[256] MacDiarmid, A. G., Chiang, J. C., Richter, A. F. & Epstein, A. J. Polyaniline - a new concept in conducting polymers. *Synth. Met.* **18**, 285 (1987).

[257] Genies, E., Syed, A. & Tsintavis, C. Electrochemical study of polyaniline in aqueous and organic medium - redox and kinetic-properties. *Mol. Cryst. Liq. Cryst.* **121**, 181 (1985).

[258] Ohsaka, T., Ohnuki, Y., Oyama, N., Katagiri, G. & Kamisako, K. IR absorption spectroscopic identification of electroactive and electroinactive polyaniline films prepared by the electrochemical polymerization of aniline. *J. Electroanal. Chem.* **161**, 399 (1984).

[259] Reneker, D. H. & Chun, I. Nanometre diameter fibres of polymer, produced by electrospinning. *Nanotechnology* **7**, 216 (1996).

[260] Edmondson, S., Osborne, V. L. & Huck, W. T. S. Polymer brushes via surface-initiated polymerizations. *Chem. Soc. Rev.* **33**, 14 (2004).

[261] Gospodinova, N. & Terlemezyan, L. Conducting polymers prepared by oxidative polymerization: Polyaniline. *Prog. Polym. Sci.* **23**, 1443 (1998).

[262] Attout, A., Yunus, S. & Bertrand, P. Electroless deposition of polyaniline: synthesis and characterization. *Surf. Interface Anal.* **40**, 657 (2008).

[263] Chen, Y. J., Kang, E. T. & Neoh, K. G. Electroless polymerization of aniline on platinum and palladium surfaces. *Appl. Surf. Sci.* **185**, 267 (2002).

[264] Liao, C. P. & Gu, M. Y. Electroless deposition of polyaniline film via autocatalytic polymerization of aniline. *Thin Solid Films* **408**, 37 (2002).

[265] Dharmadhikari, C. V. *et al.* Dynamic scaling in growth of platinum films on $Si(100)$. *Solid State Comm.* **114**, 377 (2000).

[266] Mailley, S., Hyland, M., Mailley, P., McLaughlin, J. A. & McAdams, E. T. Thin film platinum cuff electrodes for neurostimulation: in vitro approach of safe neurostimulation parameters. *Bioelectrochemistry* **63**, 359 (2004).

[267] Li, Z., Beck, P., Ohlberg, D. A. A., Stewart, D. R. & Williams, R. S. Surface properties of platinum thin films as a function of plasma treatment conditions. *Surf. Sci.* **529**, 410 (2003).

[268] Tzamalis, G., Zaidi, N. A., Homes, C. C. & Monkman, A. P. Doping dependent optical properties of polyaniline films. *Synth. Met.* **135**, 369 (2003).

[269] Cho, G., Jung, M., Yang, H., Lee, B. & Song, J. H. Photonic crystals with tunable optical stop band through monodispersed silica-polypyrrole core-shell spheres. *Mater. Lett.* **61**, 1086 (2007).

[270] Stafström, S. *et al.* Polaron lattice in highly conducting polyaniline: Theoretical and optical studies. *Phys. Rev. Lett.* **59**, 1464 (1987).

[271] MacDiarmid, A. & Epstein, A. J. The concept of secondary doping as applied to polyaniline. *Synth. Metals* **65**, 103 (1994).

[272] Epstein, A. *et al.* Insulator-to-metal transition in polyaniline. *Synth. Metals* **18**, 303 (1987).

[273] Al-Attar, H. A., Al-Alawina, Q. H. & Monkman, A. P. Spectroscopic ellipsometry of electrochemically prepared thin film polyaniline. *Thin Solid Films* **429**, 286 (2003).

[274] Ramsdale, C. M. & Greenham, N. C. Ellipsometric determination of anisotropic optical constants in electroluminescent conjugated polymers. *Adv. Mater.* **14**, 212 (2002).

[275] Pei, Q., Inganas, O. & Lundstrom, I. Bending bilayer strips built from polyaniline for artificial electrochemical muscles. *Smart Mat. Struct.* **2**, 1 (1993).

[276] Jager, E., Smela, E. & Inganas, O. Microfabricating conjugated polymer actuators. *Science* **290**, 1540 (2000).

[277] Yunus, S., Attout, A. & Bertrand, P. Controlled aniline polymerization strategies for polyaniline micro- and nano self-assembling into practical electronic devices. *Langmuir* **25**, 1851 (2009).

[278] Halliday, D. P. *et al.* Electroluminescence from porous silicon using a conducting polyaniline contact. *Thin Solid Films* **276**, 299 (1996).

[279] Krauss, P. R. & Chou, S. Y. Nano-compact disks with 400 Gbit/in^2 storage density fabricated using nanoimprint lithography and read with proximal probe. *Appl. Phys. Lett.* **71**, 3174 (1997).

[280] Mallick, K., Witcomb, M. J. & Scurrell, M. S. Gold in polyaniline: Recent trends. *Gold Bull.* **39**, 166 (2006).

[281] Neoh, K. G., Young, T. T., Looi, N. T., Kang, E. T. & Tan, K. L. Oxidation-reduction interactions between electroactive polymer thin films and Au(III) ions in acid solutions. *Chem. Mater.* **9**, 2906 (1997).

[282] Smith, J. A. *Polyaniline gold nanocomposites. Thesis dissertation.* (Georgia Institute of Technology, 2004).

[283] Min, Y., Akbulut, M., Kristiansen, K., Golan, Y. & Israelachvili, J. The role of interparticle and external forces in nanoparticle assembly. *Nat. Mater.* **7**, 527 (2008).

[284] Kim, H. *et al.* Parallel patterning of nanoparticles via electrodynamic focusing of charged aerosols. *Nat. Nanotechnol.* **1**, 117 (2006).

[285] Liu, H. T. & Alivisatos, A. P. Preparation of asymmetric nanostructures through site selective modification of tetrapods. *Nano Lett.* **4**, 2397 (2004).

[286] Pokroy, B., Kang, S. H., Mahadevan, L. & Aizenberg, J. Self-organization of a mesoscale bristle into ordered, hierarchical helical assemblies. *Science* **323**, 237 (2009).

[287] Cohen, A. & Mahadevan, L. Kinks, rings, and rackets in filamentous structures. *Proc. Natl. Acad. Sci.* **100**, 12141 (2003).

[288] Anderson, M. R., Mattes, B. R., Reiss, H. & Kaner, R. Conjugated polymer-films for gas separations. *Science* **252**, 1412 (1991).

[289] Cai, L. T. *et al.* Reversible bistable switching in nanoscale thiol-substituted oligoaniline molecular junctions. *Nano Lett.* **5**, 2365 (2005).

[290] Tseng, R. J., Huang, J. X., Ouyang, J., Kaner, R. B. & Yang, Y. Polyaniline nanofiber/gold nanoparticle nonvolatile memory. *Nano Lett.* **5**, 1077 (2005).

[291] Tseng, R. J. *et al.* Charge transfer effect in the polyaniline-gold nanoparticle memory system. *Appl. Phys. Lett.* **90**, 053101 (2007).

[292] Serban, D. A. *et al.* Towards all-organic field-effect transistors by additive soft lithography. *Small* **5**, 1117 (2009).

[293] Tu, D. *et al.* Electrical bistable behavior of an organic thin film through proton transfer. *Appl. Phys. Lett.* **90**, 052111 (2007).

[294] Mueller, R. *et al.* Organic $CuTCNQ$ integrated in complementary metal oxide semiconductor copper back end-of-line for nonvolatile memories. *Appl. Phys. Lett.* **89**, 223501 (2006).

[295] Zhang, J. X., Liu, C. & Shi, G. Q. Raman spectroscopic study on the structural changes of polyaniline during heating and cooling processes. *J. Appl. Polym. Sci.* **96**, 732 (2005).

[296] Reddy, A. L. M., Shaijumon, M. M., Gowda, S. R. & Ajayan, P. M. Coaxial MnO_2/carbon nanotube array electrodes for high-performance lithium batteries. *Nano Lett.* **9**, 1002 (2009).

[297] Halliday, D., Eggleston, J., Adams, P., Holland, E. & Monkman, A. A visible large area light emitting diode fabricated from porous silicon using a conducting polyaniline contact. *IEE Seminar Digests* **1995**, 13 (1995).

[298] Cullis, A. G. & Canham, L. T. Visible-light emission due to quantum size effects in highly porous crystalline silicon. *Nature* **353**, 335 (1991).

[299] Lehmann, V. & Gosele, U. Porous silicon formation - a quantum wire effect. *Appl. Phys. Lett.* **58**, 856 (1991).

[300] Canham, L. T. Silicon quantum wire array fabrication by electrochemical and chemical dissolution of wafers. *Appl. Phys. Lett.* **57**, 1046 (1990).

[301] Doan, V. V. & Sailor, M. J. Luminescent color image generation on porous silicon. *Science* **256**, 1791 (1992).

[302] Li, X. & Bohn, P. W. Metal-assisted chemical etching in HF/H_2O_2 produces porous silicon. *Appl. Phys. Lett.* **77**, 2572 (2000).

[303] Peng, K. Q., Yan, Y. J., Gao, S. P. & Zhu, J. Synthesis of large-area silicon nanowire arrays via self-assembling nanoelectrochemistry. *Adv. Mater.* **14**, 1164 (2002).

[304] Chen, C.-Y., Wu, C.-S., Chou, C.-J. & Yen, T.-J. Morphological control of single-crystalline silicon nanowire arrays near room temperature. *Adv. Mater.* **20**, 3811 (2008).

[305] Sivakov, V. *et al.* Silicon nanowire-based solar cells on glass: Synthesis, optical properties, and cell parameters. *Nano Lett.* **9**, 1549 (2009).

[306] Orosco, M. M., Pacholski, C. & Sailor, M. J. Real-time monitoring of enzyme activity in a mesoporous silicon double layer. *Nature Nanotechnol.* **4**, 255 (2009).

[307] Bartlett, P. N., Birkin, P. R. & Ghanem, M. A. Electrochemical deposition of macroporous platinum, palladium and cobalt films using polystyrene latex sphere templates. *Chem. Comm.* 1671 (2000).

[308] Micheletto, R., Fukuda, H. & Ohtsu, M. A simple method for the production of a 2-dimensional, ordered array of small latex-particles. *Langmuir* **11**, 3333 (1995).

[309] Deckman, H. W. & Dunsmuir, J. H. Applications of surface textures produced with natural lithography. *J. Vac. Sci. Technol. B* **1**, 1109 (1983).

[310] Deckman, H. W. & Dunsmuir, J. H. Natural lithography. *Appl. Phys. Lett.* **41**, 377 (1982).

[311] Rossi, R., Tan, M. & Lewis, N. Size-dependent electrical behavior of spatially inhomogeneous barrier height regions on silicon. *Appl. Phys. Lett.* **77**, 2698 (2000).

[312] Fulda, K. U. & Tieke, B. Langmuir films of monodisperse 0.5 μm spherical polymer particles with a hydrophobic core and a hydrophilic shell. *Adv. Mater.* **6**, 288 (1994).

[313] Gwinner, M. C. *et al.* Periodic large-area metallic split-ring resonator metamaterial fabrication based on shadow nanosphere lithography. *Small* **5**, 400 (2009).

[314] Kosiorek, A., Kandulski, W., Chudzinski, P., Kempa, K. & Giersig, M. Shadow nanosphere lithography: Simulation and experiment. *Nano Lett.* **4**, 1359 (2004).

[315] Marczewski, D. & Goedel, W. The preparation of submicrometer-sized rings by embedding and selective etching of spherical silica particles. *Nano Lett.* **5**, 295 (2005).

[316] Rogach, A. L., Kotov, N. A., Koktysh, D. S., Ostrander, J. W. & Ragoisha, G. A. Electrophoretic deposition of latex-based 3D colloidal photonic crystals: A technique for rapid production of high-quality opals. *Chem. Mater.* **12**, 2721 (2000).

[317] Giersig, M. & Mulvaney, P. Preparation of ordered colloid monolayers by electrophoretic deposition. *Langmuir* **9**, 3408 (1993).

[318] Hoogenboom, J. P. *et al.* Template-induced growth of close-packed and non-close-packed colloidal crystals during solvent evaporation. *Nano Lett.* **4**, 205 (2004).

[319] Hulteen, J. C. & Vanduyne, R. P. Nanosphere lithography - a materials general fabrication process for periodic particle array surfaces. *J. Vac. Sci. Technol. A* **13**, 1553 (1995).

[320] Jiang, P. & McFarland, M. J. Wafer-scale periodic nanohole arrays templated from two-dimensional nonclose-packed colloidal crystals. *J. Am. Chem. Soc.* **127**, 3710 (2005).

[321] Sloane, N. J. A. Kepler's conjecture confirmed. *Nature* **395**, 435 (1998).

[322] Greer, R. Submicron structure of "amorphous" opal. *Nature* **224**, 1199 (1969).